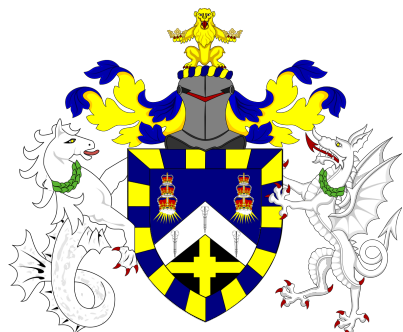


¹ ADVANCING NEUTRINO
² DETECTION AND TRIGGERING IN
³ DUNE



⁵ Francisco Martínez López

⁶ Submitted in partial fulfillment of the requirements
⁷ of the Degree of Doctor of Philosophy

⁸ School of Physical and Chemical Sciences

⁹ Queen Mary University of London

¹⁰ December 2023

¹¹ Statement of originality

- ¹² I, [insert name as recorded in QM records], confirm that the research included within
¹³ this thesis is my own work or that where it has been carried out in collaboration with, or
¹⁴ supported by others, that this is duly acknowledged below and my contribution indicated.
¹⁵ Previously published material is also acknowledged below.
- ¹⁶ I attest that I have exercised reasonable care to ensure that the work is original, and
¹⁷ does not to the best of my knowledge break any UK law, infringe any third party's
¹⁸ copyright or other Intellectual Property Right, or contain any confidential material.
- ¹⁹ I accept that the College has the right to use plagiarism detection software to check the
²⁰ electronic version of the thesis.
- ²¹ I confirm that this thesis has not been previously submitted for the award of a degree
²² by this or any other university.
- ²³ The copyright of this thesis rests with the author and no quotation from it or information
²⁴ derived from it may be published without the prior written consent of the author.
- ²⁵ Signature: [can be digital signature]
- ²⁶ Date:
- ²⁷ Details of collaboration and publications:
²⁸ [insert details here if applicable]

²⁹ Abstract

³⁰ Hello, here is some text without a meaning. This text should show what a printed text
³¹ will look like at this place. If you read this text, you will get no information. Really? Is
³² there no information? Is there a difference between this text and some nonsense like
³³ “Huardest gefburn”? Kjift – not at all! A blind text like this gives you information about
³⁴ the selected font, how the letters are written and an impression of the look. This text
³⁵ should contain all letters of the alphabet and it should be written in of the original
³⁶ language. There is no need for special content, but the length of words should match
³⁷ the language.

O time, thou must untangle this, not I.
It is too hard a knot for me to untie!

Twelfth Night

SHAKESPEARE

³⁸ Acknowledgements

³⁹ In principio fu la Maestra Manuela.

⁴⁰ A heartfelt thank you to . . . for accepting to be the referees of this thesis, and for
⁴¹ the thought-provoking discussions we shared. Their comments brought this manuscript
⁴² to a significant improvement.

⁴³ I feel privileged to have this many eminent researchers in my committee. A very big
⁴⁴ thank you for accepting to be part of it.

⁴⁵ Thank you to . . .

⁴⁶ Un ringraziamento va anche agli amici triestini di nascita, di adozione, o di passaggio,
⁴⁷ matematici, sballerine, o altro, oggi sparpagliati per il mondo a formare una famiglia
⁴⁸ grazie alla quale uno non si sente mai troppo solo e lontano da tutti. Tanto siamo
⁴⁹ dappertutto.

⁵⁰ In particolare grazie a . . .

⁵¹ Prima di giungere ai ringraziamenti più personali, . . .

52 Contents

53	Statement of originality	3
54	Abstract	5
55	Acknowledgements	9
56	List of Figures	15
57	List of Tables	29
58	List of Abbreviations	31
59	1 Introduction	33
60	2 Neutrino physics	35
61	2.1 Neutrinos in the SM	35
62	2.2 Neutrino oscillations	36
63	2.2.1 Oscillations in vacuum	37
64	2.2.2 Oscillations in matter	38
65	2.2.3 Current status of neutrino oscillations	39
66	2.3 Open questions in the neutrino sector	40
67	3 The Deep Underground Neutrino Experiment	43
68	3.1 Overview	43
69	3.2 Physics goals of DUNE	45
70	3.3 Far Detector	47

CONTENTS

71	3.3.1	Horizontal Drift	48
72	3.3.2	Vertical Drift	51
73	3.3.3	FD Data Acquisition System	53
74	3.4	Near Detector	54
75	3.4.1	ND-LAr	56
76	3.4.2	TMS/ND-GAr	57
77	3.4.3	PRISM	58
78	3.4.4	SAND	60
79	3.5	LBNF beamline	60
80	4	ND-GAr	63
81	4.1	Requirements	63
82	4.2	Reference design	64
83	4.2.1	HPgTPC	64
84	4.2.2	ECal	65
85	4.2.3	Magnet	66
86	4.2.4	Muon system	67
87	4.3	GArSoft	67
88	4.3.1	Event generation	67
89	4.3.2	Detector simulation	68
90	4.3.3	Reconstruction	69
91	5	FWTPG offline software	73
92	6	Matched Filter approach to induction wire Trigger Primitives	75
93	6.1	Motivation	75
94	6.2	Signal-to-noise ratio definition	77
95	6.3	Low-pass FIR filter design	79
96	6.4	Matched filters	82
97	6.5	Using simulated samples	88

CONTENTS

98	6.5.1 Angular dependence	94
99	6.5.2 Distortion and peak asymmetry	96
100	6.5.3 Hit sensitivity	99
101	7 DM searches with neutrinos from the Sun	109
102	7.1 Motivation	109
103	7.2 Gravitational capture of DM by the Sun	109
104	7.3 Neutrino flux from DM annihilations	116
105	7.4 Computing limits from solar neutrino fluxes	117
106	7.5 Example: Kaluza-Klein Dark Matter	121
107	7.6 High energy DM neutrino signals	125
108	7.6.1 DIS events	127
109	7.6.2 Single proton QEL events	132
110	7.6.3 Results	135
111	7.7 Example: Leptophilic Dark Matter	137
112	8 Particle ID in GArSoft	143
113	8.1 dE/dx measurement in the TPC	144
114	8.1.1 Energy calibration	146
115	8.1.2 Truncated dE/dx mean	156
116	8.1.3 Mean dE/dx parametrisation	159
117	8.1.4 Particle identification	163
118	8.2 Muon and pion separation in the ECal and MuID	163
119	8.2.1 Track-ECal matching	166
120	8.2.2 Classification strategy	170
121	8.2.3 Feature selection and importance	173
122	8.2.4 Hyperparameter optimisation	185
123	8.2.5 Probability calibration	188
124	8.2.6 Performance	188
125	8.3 ECal time-of-flight	188

CONTENTS

126	8.3.1 Arrival time estimations	188
127	8.3.2 Proton and pion separation	188
128	8.4 Charged pion decay in flight	188
129	8.4.1 Track breakpoints	195
130	8.5 Neutral particle identification	195
131	8.5.1 ECal clustering	195
132	8.5.2 π^0 reconstruction	199
133	9 Event selection in ND-GAr	203
134	9.1 CAFs and CAFAna	203
135	9.2 Event selection	203
136	9.2.1 ν_μ CC selection	203
137	9.2.2 Charged pion multiplicity	203
138	10 Conclusions	205
139	A An appendix	207
140	Bibliography	209

List of Figures

142	3.1 Schematic diagram of the DUNE experiment and the LBNF beamline [1].	44
143	3.2 Schematic diagram showing the operating principle of a LArTPC with	
144	wire readout	48
145	3.3 Proposed design for the FD-1 and FD-2 modules following the HD principle.	49
146	3.4 Schematic representation of an APA frames showing the U, V, X and G	
147	wires.	50
148	3.5 A PDS module containing 24 X-ARAPUCAs and the location of the	
149	modules on the APAs.	50
150	3.6 Proposed design for the FD-3 module following the VD principle.	51
151	3.7 Schematic representation of the electrode strip configuration for a top	
152	and bottom CRU.	52
153	3.8 Detailed diagram of the DUNE FD DAQ system. Figure taken from Ref.	
154	[2].	53
155	3.9 Representation of the ND hall in Phase II, showing the different subcomponents.	55
156	3.10 Schematic representation of the external components of ND-LAr, including	
157	the cryostat and the PRISM movable system and detailed drawing of one	
158	ArgonCube module.	56
159	3.11 Schematic view of the TMS detector, highlighting its main parts.	57
160	3.12 Cross section of the ND-GAr geometry, showing the HPgTPC, ECal and	
161	magnet.	58

LIST OF FIGURES

162	3.13	Predicted beam muon neutrino flux at the ND location for different off-axis positions.	59
163			
164	3.14	Schematic longitudinal section of the LBNF beamline at Fermilab.	60
165	3.15	Predicted neutrino fluxes at the FD in FHC mode and RHC mode.	61
166	4.1	Diagram of the ALICE TPC, showing the two drift chambers, inner and outer field cages and readout chambers.	65
167			
168	4.2	Diagram of the ALICE TPC, showing the two drift chambers, inner and outer field cages and readout chambers.	66
169			
170	6.1	<i>Schematic representation of an APA. The black lines represent the APA steel frame. The green and magenta lines correspond to the direction of the U and V induction wires respectively. The blue lines indicate the direction of the X collection wires and the wire shielding G.</i>	76
171			
172			
173			
174	6.2	<i>Left panel: Zoomed unfiltered waveform corresponding to channel 7840 from the ProtoDUNE-SP raw data capture <code>felix-2020-07-17-21:31:44</code> (blue line). The green dashed lines mark the region $\pm 3\sigma_{\text{raw}}$. The resulting noise waveform is also shown (red line). Top right panel: ADC distribution for channel 7840, where the green shaded region represents $\pm \sigma_{\text{raw}}$. Bottom right panel: noise ADC distribution for channel 7840, where the green shaded region represents $\pm \sigma_{\text{noise}}$.</i>	77
175			
176			
177			
178			
179			
180			
181	6.3	<i>Left panel: Zoomed filtered waveform corresponding to channel 7840 from the ProtoDUNE-SP raw data capture <code>felix-2020-07-17-21:31:44</code> (blue line). The filter used was the current implementation of the low-pass FIR filter in <code>dtp-firmware</code>. The green dashed lines mark the region $\pm 3\sigma_{\text{raw}}$. The resulting noise waveform is also shown (red line). Top right panel: ADC distribution for channel 7840 after filtering, where the green shaded region represents $\pm \sigma_{\text{raw}}$. Bottom right panel: noise ADC distribution for channel 7840 after filtering, where the green shaded region represents $\pm \sigma_{\text{noise}}$</i>	79
182			
183			
184			
185			
186			
187			
188			

LIST OF FIGURES

189	6.4 Power spectrum in decibels for the current implementation of the low-pass	
190	FIR filter in <code>dtp-firmware</code> (blue line), compared to the response of an	
191	optimal filter obtained using the Parks-McClellan algorithm for the same	
192	pass-band (red line). Also for comparison I include the spectrum of the	
193	optimal filter when taking only the integer part of the coefficients (red	
194	dashed line)	80
195	6.5 Relative change in the S/N for the ProtoDUNE-SP raw data capture	
196	<code>felix-2020-07-17-21:31:44</code> , using different values of the cutoff frequency	
197	f_c and the transition width δf . The optimal Chebyshev filters were applied	
198	using just the integer part of the coefficients given by the Parks-McClellan	
199	algorithm.	81
200	6.6 Distribution of the relative change of the S/N on the different wire planes	
201	from the ProtoDUNE-SP raw data capture <code>felix-2020-07-17-21:31:44</code>	
202	after the optimal Chebyshev filter was applied. The filter was computed	
203	with the Parks-McClellan algorithm using a cutoff of $f_c = 0.068 \text{ ticks}^{-1}$	
204	and a transition width $\delta f = 0.010 \text{ ticks}^{-1}$	82
205	6.7 Left panel: Zoomed match filtered waveform corresponding to channel 7840	
206	from the ProtoDUNE-SP raw data capture <code>felix-2020-07-17-21:31:44</code>	
207	(blue line). The filter used was directly extracted from the data, being	
208	the 32 values around the first peak in the original waveform. The green	
209	dashed lines mark the region $\pm 3\sigma_{\text{raw}}$. The resulting noise waveform is	
210	also shown (red line). Top right panel: ADC distribution for channel 7840	
211	after match filtering, where the green shaded region represents $\pm \sigma_{\text{raw}}$.	
212	Bottom right panel: noise ADC distribution for channel 7840 after match	
213	filtering, where the green shaded region represents $\pm \sigma_{\text{noise}}$	83
214	6.8 Relative improvement in the S/N for the raw data capture <code>felix-2020-07-17-21:31:44</code> ,	
215	using the matched filter following the parametrisation in Eq. (6.17). The	
216	black crosses in both panels denote the location of the maximum ratio value.	86

LIST OF FIGURES

217	6.9 Left panel: Optimal matched filter coefficients for the U (blue line) and V (red line) planes. The filters were computed with our parametrisation in Eq. (6.17) for the parameter values $\delta = 0.035$, $\sigma = 0.191$ and $\delta = 0.018$, $\sigma = 0.191$ respectively. Right panel: Distribution of the relative change of the S/N on the two induction wire planes from the ProtoDUNE-SP raw data capture <i>felix-2020-07-17-21:31:44</i> after their respective optimal matched filters were applied.	89
224	6.10 Left panel: distributions of the particles track length in the liquid argon for the generated $E_k = 100$ MeV monoenergetic samples, electrons (blue), muons (red), protons (green) and neutral pions (purple). Right panel: distribution of the length of the longest photon in the neutral pion sample after the decay process $\pi^0 \rightarrow \gamma\gamma$	90
229	6.11 Left panel: schematic representation of the two new rotated reference frames used in this analysis (denoted as prime and double prime), viewed from the yz plane. The magenta stack of lines represent the wires in the U plane, whereas the green lines correspond to the wires in the V plane. Right panel: 3D representation of the momentum of one of the generated monoenergetic muons (red arrow) in the original reference frame (black lines), along with the new reference frame used for the U plane waveforms (blue lines). In the yz plane I added the projection of these three.	92
237	6.12 Distributions of the mean S/N improvement per event for the corresponding sample after applying the matched filters. Here I separated the change in the U plane (blue) and the V plane (red) channels. From top left to the right: muon, electron, proton and neutral pion. All the events have a fixed kinetic energy of $E_k = 100$ MeV.	93

LIST OF FIGURES

LIST OF FIGURES

262	6.16 Left panel: peak asymmetry distribution for the case of the monoenergetic	
263	$E_k = 100$ MeV muon sample. Each value corresponds to a single bipolar	
264	signal peak from a channel in any event. The blue distribution represents	
265	the peaks on U plane channels, whereas the red corresponds to signal peaks	
266	in V wires. Right panel: relation between the mean peak asymmetry per	
267	event with the S/N for U channel waveforms from the $E_k = 100$ MeV	
268	muon sample. The top subplot shows the decimal logarithm of the mean	
269	S/N for the raw (red) and the matched filtered (blue) waveforms. The	
270	bottom subplot contains the mean S/N improvement ratio after the matched	
271	filter was applied.	98
272	6.17 Raw data display in the plane time (in firmware ticks) vs. offline channel	
273	number for an $E_k = 100$ MeV electron event. The produced true hits are	
274	superimposed (black boxes) as well as the hits comming from the standard	
275	hit finder chain (blue circles) and the hit finder using the matched filter	
276	(green triangles).	100
277	6.18 Dependence of the precision (blue), sensitivity (red) and F_1 (green) scores	
278	on the threshold values used in the hit finder, for the FIR (left panel)	
279	and matched filter (right panel) cases. The results were obtained after	
280	matching the hits to the true hits in the case of the isotropic muon sample	
281	with kinetic energy in the range 5 to 100 MeV, taking only into account	
282	the induction plane channels. The points represent the mean value while	
283	the error bars indicate one standard deviation around that mean value. . .	102

LIST OF FIGURES

- 284 6.19 *Dependence of the averaged hit sensitivity on the kinetic energy of the*
 285 *events for the matched filter (blue) and standard (red) hits, for the case of*
 286 *the muon (left panel) and electron (right panel) samples, separated between*
 287 *U (top plots) and V (bottom plots) induction wire planes. The top subplots*
 288 *contain the hit sensitivities for the two hit finder alternatives, while the*
 289 *bottom subplots show the ratio between the two. The horizontal lines sit at*
 290 *the mean value and represent the size of the energy bins, while the vertical*
 291 *error bars indicate one standard deviation around that mean value.* 104
- 292 6.20 *Distributions of the hit sensitivity in the U (top panels) and V (bottom*
 293 *panels) planes versus the hit sensitivity in the X plane, both for the*
 294 *standard hits (left panels) and the matched filter hits (right panels), in the*
 295 *case of the electron sample and a threshold of 30 ADC.* 105
- 296 6.21 *Top panels: standard residual plots of the hit sensitivities between the X*
 297 *and U planes. Bottom panels: quantile-quantile plots of the hit sensitivity*
 298 *standard residuals between the X and U planes. In all cases, the left*
 299 *panel corresponds to the standard hits while the right panel represents the*
 300 *matched filter case, all from the electron sample with a 30 ADC threshold.* 106
- 301 7.1 *Input solar parameters used in our capture rate computation as functions*
 302 *of the Sun's radius, from left to right: temperature (with respect to the*
 303 *temperature at the core), mass (in solar masses) and electron number*
 304 *density (with respect to the electron density at the core). All quantities*
 305 *shown correspond to the standard solar model BS2005-OP [3].* 113
- 306 7.2 *Capture rates as a function of the DM mass for the DM-electron interactions*
 307 *(red lines), SD DM-nucleons interactions (green lines) and SI DM-nucleons*
 308 *interactions (blue lines). Solid lines represent the values computed in this*
 309 *work while the dashed lines are the one given in Ref. [4]. All the rates*
 310 *are shown for a choice of scattering cross section of $\sigma_i = 10^{-40} \text{ cm}^2$.* . . 114

LIST OF FIGURES

311	7.3 <i>NuWro computed $\nu_\mu - {}^{40}\text{Ar}$ charged-current scattering cross section as a function of the neutrino energy E_μ. The black line shows to the total cross section, whereas the others correspond to the different contributions (in red quasi-elastic scattering, in green resonant pion exchange, in blue deep inelastic scattering and in purple meson exchange current).</i>	118
316	7.4 <i>Expected atmospheric neutrino flux as a function of the neutrino energy E_ν at Homestake at solar minimum, taken from Ref. [5]. The blue solid (dashed) line correspond to muon neutrinos (antineutrinos) and the red solid (dashed) line correspond to electron neutrinos (antineutrinos)</i>	120
320	7.5 Feynman diagrams for B^1B^1 annihilation into SM fermions.	122
321	7.6 Feynman diagrams for B^1B^1 annihilation into a Higgs boson pair.	122
322	7.7 <i>Computed spectra of muon neutrinos at the DUNE FD site from B^1 annihilations in the Sun for three different values of M_{LKP}, plotted in relative energy units for legibility.</i>	123
325	7.8 <i>Projected 90% confidence level upper limit for DUNE (400 kT yr) on the spin- dependent B^1-proton scattering cross section as a function of M_{LKP} (green dots). I also show the previous limits from IceCube [6] (blue line) and Antares [7] (red line) on the LKP cross section. The shaded area represents the disfavoured region (at 95% confidence level) on the mass of the LKP from LHC data [8]</i>	124
331	7.9 <i>Computed spectra of muon neutrinos at the DUNE FD site from $\tau^+\tau^-$ (left panel) and $b\bar{b}$ (right panel) annihilations in the Sun for the DM masses $m_{\text{DM}} = 10$ GeV (red line), 50 GeV (green line) and 100 GeV (blue line), plotted in relative energy units.</i>	125
335	7.10 <i>Distribution of the muon neutrino energies from the $\tau^+\tau^-$ (left panel) and $b\bar{b}$ (right panel) annihilation channels, for $m_{\text{DM}} = 10$ GeV, separated by CC interaction type: QEL (blue), MEC (orange), RES (green) and DIS (red)</i>	127

LIST OF FIGURES

<p>339 7.11 <i>Distributions of θ_μ (left panel), θ_j (central panel) and θ_{plane} (right panel)</i> 340 <i>for the $b\bar{b}$ sample with $m_{DM} = 10$ GeV (blue) and the atmospheric</i> 341 <i>background (red).</i></p> <p>342 7.12 <i>Left panel: signal efficiencies (blue lines) and background rejections (red</i> 343 <i>lines) for events passing the cuts $\theta < \theta_{cut}$ for the jet (solid lines) and</i> 344 <i>muon (dashed lines) angles. Right panel: signal efficiency (blue line) and</i> 345 <i>background rejection (red line) for events passing the cut $\theta_{plane} < \theta_{cut}$ for</i> 346 <i>the momentum conservation plane deviation.</i></p> <p>347 7.13 <i>Signal efficiencies for the $\tau^+\tau^-$ (blue line) and $b\bar{b}$ (red line) DIS samples</i> 348 <i>as functions of the DM mass, m_{DM}, obtained by applying the optimal</i> 349 <i>angular cuts $\theta_\mu < 27^\circ$, $4^\circ < \theta_j < 26^\circ$ and $\theta_{plane} < 3.5^\circ$.</i></p> <p>350 7.14 <i>Distributions of $\cos \theta_\mu$ (left panel), $\cos \theta_p$ (central panel) and $\cos \theta_N$</i> 351 <i>(right panel) for the $\tau^+\tau^-$ QEL sample with $m_{DM} = 5$ GeV (blue) and</i> 352 <i>the atmospheric background (red).</i></p> <p>353 7.15 <i>Left panel: value of the loss function for the training sample (blue line)</i> 354 <i>and accuracy for the validation sample (red line) versus the number of</i> 355 <i>iterations for the MLP classifier training. Right panel: distributions of the</i> 356 <i>predicted probabilities assigned by the MLP classifier to the test sample</i> 357 <i>for the $\tau^+\tau^-$ QEL signal with $m_{DM} = 5$ GeV (blue) and the atmospheric</i> 358 <i>background (red).</i></p> <p>359 7.16 <i>Signal efficiencies for the $\tau^+\tau^-$ (blue line) and $b\bar{b}$ (red line) single proton</i> 360 <i>QEL samples as functions of the DM mass, m_{DM}, obtained by requiring a</i> 361 <i>minimum predicted probability from the MLP classifier of 0.97 in order to</i> 362 <i>achieve a background rejection greater than 99.8%.</i></p>	<p>128</p> <p>129</p> <p>131</p> <p>132</p> <p>133</p> <p>134</p>
---	---

LIST OF FIGURES

363	7.17 Projected 90% confidence level upper limit for DUNE (400 kT yr) on 364 the spin-dependent DM-nucleon scattering cross section as a function of 365 m_{DM} , for the annihilation channels $\tau^+\tau^-$ (blue) and $b\bar{b}$ (red) separated 366 by interaction type (up triangles denote DIS interactions whereas down 367 triangles represent QEL interactions). I also show the previous limits 368 from IceCube [9] (solid lines) and the projected sensitivities for Pingu [10] 369 (dashed lines) and Hyper-Kamiokande [11] (dash-dotted lines), as well 370 as the direct detection limits from PICASSO [12] (solid green line) and 371 PICO-60 C ₃ F ₈ [13] (dashed green line).	136
372	7.18 Left panel: Projected 90% confidence level sensitivity of DUNE (400 kT 373 yr) to the scale Λ of an EFT containing only leptophilic DM axial-axial 374 interactions (blue line). Right panel: . In both cases the corresponding 375 limits from DarkSide-50 [14] (dotted green line) and XENON1T [15] 376 (dashed red line) are also shown, together with the configurations for which 377 the correct relic density is achieved (black line), all for the coupling values 378 $c_A^e = 10^3$ and $c_A^\nu = 10^{-2}$	140
379	8.1 Distribution of the fraction of energy deposits with residual range less 380 than 20% of the total track length, and distribution of the ionisation per 381 unit length after removing the tracks with less than 30% of their energy 382 deposits in the last 20% of the track.	147
383	8.2 Distribution of the reconstructed ionisation charge per unit length for 384 different reclustering values, and distribution of the median change in 385 dQ/dx per track for the $N_{\text{group}} = 4$ reclustering.	148
386	8.3 Distribution of the Geant4-simulated energy losses per unit length versus 387 residual range for the stopping proton sample.	150
388	8.4 Fitted most probable dQ/dx values for each dE/dx bin, together with 389 best fit to the logarithmic calibration function.	151

LIST OF FIGURES

390	8.5 Fitted most probable dQ/dx values for each dE/dx bin for three different	
391	ADC bit limits.	153
392	8.6 Area normalised dE/dx distributions for the true and the reconstructed	
393	energy deposits in the stopping proton sample, both after applying the	
394	calibration and the calibration and the normalisation correction.	154
395	8.7 Fractional residuals between the true and the corrected dE/dx means	
396	and the 60% truncated means, and fractional residuals between the true	
397	and the uncorrected, corrected and uncalibrated dE/dx 60% truncated	
398	means.	156
399	8.8 Estimated values of the mean dE/dx bias and resolution for the stopping	
400	proton sample at different values of the truncation factor.	157
401	8.9 Examples of the truncated mean dE/dx LanGauss fits for various $\beta\gamma$	
402	bins, from a simulated FHC neutrino sample.	159
403	8.10 Resulting one and two dimensional projections of the posterior probability	
404	distributions of the ALEPH $\langle dE/dx \rangle$ parameters obtained by fitting the	
405	60% truncated mean dE/dx values from a FHC neutrino sample.	160
406	8.11 Truncated mean dE/dx obtained for the FHC neutrino sample as a	
407	function of the $\beta\gamma$ product, together with the fitted most probable values	
408	for each $\beta\gamma$ bin and the best fit obtained using the ALEPH parametrisation.	161
409	8.12 Distribution of the 60% truncated mean dE/dx versus reconstructed	
410	momentum for the FHC neutrino sample.	162
411	8.13 Estimated values of the mean dE/dx bias and resolution obtained for the	
412	true protons in a FHC neutrino sample.	163
413	8.14 True momentum distribution for the primary muon in ν_μ CC $N\pi^\pm$	
414	interactions inside the fiducial volume of ND-GAr, compared to the	
415	post FSI charged pion spectrum.	164
416	8.15 Distributions of energy deposits in the ECal for a muon and a charged	
417	pion with similar momenta.	165

LIST OF FIGURES

418	8.16 Left panel: comparison between the precision (blue), sensitivity (yellow) and F_1 score (red) obtained for the default (horizontal lines) and new algorithms, both with the χ^2 -based direction estimator (squares) and cheating the directions (circles), for different values of the χ^2 cut. Right panel: comparison of the performance of the new algorithm when applying the cluster t_0 correction (squares) and when (circles).	167
424	8.17 Schematics of a possible option to deal with track-ECal associations in non-zero t_0 neutrino interaction events, trying to correct for the drift direction uncertainty in a cluster-by-cluster basis using the cluster time, $t_{cluster}$	169
428	8.18 Momentum distribution for the reconstructed muons (top panel) and charged pions (bottom panel) in a FHC neutrino sample, together with the fraction of them reaching the ECal (red) and MuID (blue). Each entry corresponds to a reconstructed track, backtracked to a true muon or pion which has not produced any other reconstructed track.	171
433	8.19 Predicted truncated mean dE/dx versus momentum, for electrons, muons, charged pions and protons, obtained using the ALEPH parametrisation. The vertical dashed lines represent the boundaries of the six regions used for the muon and pion classification training.	172
437	8.20 Example ECal feature distributions for muons and charged pions in the five different momentum ranges considered.	176
439	8.21 Example MuID feature distributions for muons and charged pions in the three different momentum ranges considered.	177
441	8.22 Left panel: cumulative explained variance for the first three principal components (top panel) and contribution of the different features to the principal axes in feature space (bottom panel). Right panel: Shapley (blue) and Gini (red) feature importances for the different input features. Both figures correspond to the samples in the momentum range $0.3 \leq p < 0.8 \text{ GeV}/c$	178

LIST OF FIGURES

447	8.23 Left panel: cumulative explained variance for the first three principal components (top panel) and contribution of the different features to the principal axes in feature space (bottom panel). Right panel: Shapley (blue) and Gini (red) feature importances for the different input features. Both figures correspond to the samples in the momentum range $0.8 \leq p < 1.5 \text{ GeV}/c$	179
448		
449		
450		
451		
452		
453	8.24 Evolution of the SHAP importance for the top six most important features across all five momentum ranges.	182
454		
455		
456		
457		
458		
459		
460	8.25 Permutation importances for the ten most important features in the different momentum ranges (from left to right, top to bottom, in increasing momentum order). The bars indicate the effect that permutations of each feature have on the purity (blue) and the sensitivity (yellow), the translucent regions representing one standard deviation around the central value.	184
461		
462		
463	8.26 Values of the precision and sensitivity obtained for 10000 BDT hyperparameter configurations, for the momentum regions I, III and V.	187
464		
465		
466		
467		
468	8.27 Left panel: number of non-decaying, decaying and decaying in the fiducial volume pions for a MC sample of 10^5 , $p = 500 \text{ MeV}$ isotropic positively charged pions inside the TPC. Right panel: event display for a positive pion decaying inside the fiducial volume, with a single reconstructed track for the pion and muon system.	189
469		
470		
471		
472	8.28 Values of $\chi_k^{2(FB)}$ (top left panel), F_k (top right panel), $D_k^{1/R}$ (bottom left panel) and D_k^ϕ (bottom right panel) versus position along the drift direction for a reconstructed track in a positive pion decay event. The vertical red dashed line indicates the true location of the decay point.	190
473		
474		
475		
476	8.29 Fractional residual distributions of the true and reconstructed decay position along the drift coordinate, using the position of the maximum of $\chi_k^{2(FB)}$ (left panel) and F_k (right panel) as estimates of the decay position. Also shown are double Gaussian fits to these points (red lines).	192
477		

LIST OF FIGURES

476	8.30 Distributions of the extreme values of $\chi_k^{2(FB)}$ (top left panel), F_k (top right panel), $D_k^{1/R}$ (bottom left panel) and D_k^ϕ (bottom right panel) for non-decaying reconstructed pion tracks (blue) and tracks which include the decay inside the fiducial volume (red).	193
480	8.31 Left panel: distributions of the predicted probabilities assigned by the BDT classifier to a test sample of decaying pion+muon tracks (blue) and non-decaying pion tracks (red). Left: signal efficiency versus background acceptance (ROC curve) obtained from the BDT for the test sample. . .	194
484	8.32 Left panel: dependence of the decay position finding resolution on the true value of the decay angle for the $\chi_k^{2(FB)}$ (red) and F_k (blue) methods. Right panel: signal efficiency (blue line) and background rejection (red line) from the BDT classifier versus true decay angle.	194
488	8.33 Mean values of the F_1 -score marginal distributions for the different free parameters of the new clustering algorithm, with the error bars representing one standard deviation around the mean. The F_1 -score values were computed for the 6561 possible parameter configurations using 1000 ν_μ CC interaction events.	197
493	8.34 Left panel: distributions of the number of ECal clusters per photon from π^0 decays for the standard (red) and new (blue) clustering algorithms. Right panel: reconstructed invariant mass distributions for photon pairs from single π^0 events using the standard (red) and new (blue) ECal clustering algorithms.	199

List of Tables

499	2.1	Summary of neutrino oscillation parameters determined in the Neutrino Global Fit of 2020 [16]	40
500			
501	3.1	Summary of the two-phased plan for DUNE	45
502	3.2	Exposure and time required to achieve the different physics milestones of the two phases	46
503			
504	6.1	<i>Characteristic parameters of the two monoenergetic muon events selected, relative to the U plane: projected angles in the xz' and $y'z'$ planes, S/N values for the raw and filtered waveforms, mean improvement of the S/N and peak asymmetry.</i>	97
505			
506			
507			
508	8.1	Calibration parameters obtained from the fit of the ND-GAr simulated stopping proton sample to the calibration function, for different ADC limits.	153
509			
510	8.2	Momentum ranges and description of the PID approach assumed for the muon and pion classification task.	173
511			
512	8.3	Optimal values of the hyperparameters used by the BDT, for each momentum range.	187
513			
514	8.4	Summary of parameters and sampled values used in the optimisation of the clustering algorithm.	198
515			
516			

⁵¹⁷ List of Abbreviations

ADC	Analog to Digital Converter.
ALEPH	Apparatus for LEP PHysics.
ALICE	A Large Ion Collider Experiment.
BDT	Boosted Decision Tree.
CC	Charged Current.
DM	Dark Matter.
DUNE	Deep Underground Neutrino Experiment.
ECal	Electromagnetic Calorimeter.
FD	Far Detector.
FHC	Forward Horn Current.
HPgTPC	High Pressure gaseous Time Projection Chamber.
LBL	Long BaseLine.

List of Abbreviations

MuID	Muon IDentification system.
NC	Neutral Current.
ND	Near Detector.
ND-GAr	Near Detector Gaseous Argon.
ND-LAr	Near Detector Liquid Argon.
PDG	Particle Data Group.
RHC	Reverse Horn Current.

⁵¹⁸ Chapter 1

⁵¹⁹ Introduction

520 Chapter 2

521 Neutrino physics

522 Ever since they were postulated in 1930 by Wolfgang Pauli to explain the continuous
523 β decay spectrum [17] and later found by Reines and Cowan at the Savannah River
524 reactor in 1953 [18], neutrinos have had a special place among all other elementary
525 particles. They provide a unique way to probe a wide range of quite different physics,
526 from nuclear physics to cosmology, from astrophysics to colliders. Moreover, there is
527 compelling evidence to believe that the study of neutrinos may be key to unveil different
528 aspects of physics beyond the SM, difficult to test elsewhere.

529 In this Chapter I will review the basics of neutrino physics, from its role within the
530 SM to the main open questions related to the neutrino sector, paying special attention
531 to the phenomenology of neutrino oscillations.

532 2.1 Neutrinos in the SM

533 By definition, in the SM there are no right-handed neutrino fields. A direct implication
534 of this fact is that neutrinos are strictly massless within the SM. This follows from the
535 experimental observation that all neutrinos produced via weak interactions are pure
536 left-handed helicity states (and similarly antineutrinos are pure right-handed states).
537 The hypothetical existence of right-handed neutrinos could be indirectly inferred from
538 the observation of non-zero neutrino masses, nevertheless the existence neutrino masses

Chapter 2. Neutrino physics

539 is not a sufficient condition for the existence of such fields.

540 In the SM neutrinos appear in three flavours, namely ν_e , ν_μ and ν_τ . These are
541 associated with the corresponding charged leptons e , μ and τ , in such a way that the
542 charged current part of the Lagrangian coupling them is diagonal. As in the electroweak
543 theory neutrinos are coupled to the Z boson in a universal way, by measuring the so-called
544 invisible decay width of the Z we have an estimate of the number of light (i.e. lighter
545 than the Z boson) neutrino flavours. This number was measured by LEP in a combined
546 analysis of $e^+e^- \rightarrow \mu^+\mu^-$ and $e^+e^- \rightarrow$ hadrons to be $N_\nu = 2.9840 \pm 0.0082$ [19].

547 2.2 Neutrino oscillations

548 The evidence for neutrino oscillation [20], and therefore the existence of non-zero neutrino
549 masses, constitutes one of the groundbreaking discoveries of modern Physics and has
550 acted as driving force for Beyond the Standard Model (BSM) Physics. The minimal
551 extension of the Standard Model (SM) we can do to address these phenomena is
552 introducing distinct masses for at least two of the neutrinos. This way, we are left with
553 three neutrino mass eigenstates ν_1 , ν_2 and ν_3 , with masses m_1 , m_2 and m_3 respectively,
554 which in general will not coincide with the flavour eigenstates ν_e , ν_μ and ν_τ .

555 The way to relate these two sets of neutrino eigenstates is via a 3×3 unitary matrix,
556 called the Pontecorvo-Maki-Nakagawa-Sakata (PMNS) matrix [21, 22], as:

$$|\nu_\alpha\rangle = \sum_{i=1}^3 U_{\alpha i}^* |\nu_i\rangle, \quad (2.1)$$

557 where the Greek index α denotes the flavour $\{e, \mu, \tau\}$ and the Latin index i the associated
558 masses $\{1, 2, 3\}$. This leptonic mixing matrix may be parametrized in terms of 6
559 parameters, 3 of which are mixing angles θ_{12} , θ_{13} and θ_{23} , one CP-violating phase δ_{CP}

2.2. Neutrino oscillations

560 and 2 Majorana phases α and β :

$$U = \begin{pmatrix} 1 & 0 & 0 \\ 0 & c_{23} & s_{23} \\ 0 & -s_{23} & c_{23} \end{pmatrix} \begin{pmatrix} c_{13} & 0 & s_{13}e^{-i\delta_{CP}} \\ 0 & 1 & 0 \\ -s_{13}e^{-i\delta_{CP}} & 0 & c_{13} \end{pmatrix} \begin{pmatrix} c_{12} & s_{12} & 0 \\ -s_{12} & c_{12} & 0 \\ 0 & 0 & 1 \end{pmatrix} \begin{pmatrix} 1 & 0 & 0 \\ 0 & e^{i\alpha} & 0 \\ 0 & 0 & e^{i\beta} \end{pmatrix}, \quad (2.2)$$

561 where $c_{ij} \equiv \cos \theta_{ij}$ and $s_{ij} \equiv \sin \theta_{ij}$. This matrix is analogous to the Cabibbo-Kobayashi-
562 Maskawa (CKM) matrix in the quark sector. If neutrinos are Dirac fermions, we can
563 drop the Majorana phases in the PMNS matrix. But, in any case, these phases play no
564 role on the neutrino oscillations.

565 2.2.1 Oscillations in vacuum

566 Consider the case where a neutrino of flavour α is produced at $t = 0$, and then it
567 propagates through vacuum. Such a state will evolve in time according to the relation:

$$|\nu_\alpha(t)\rangle = \sum_{i=1}^3 U_{\alpha i}^* e^{-iE_i t} |\nu_i(t=0)\rangle, \quad (2.3)$$

568 as the mass eigenstates are also eigenstates of the free Hamiltonian. Now, if we express
569 the mass eigenstates as a superposition of flavour eigenstates, the last expression can be
570 rewritten as:

$$|\nu_\alpha(t)\rangle = \sum_{i=1}^3 U_{\beta i} e^{-iE_i t} U_{\alpha i}^* |\nu_\beta\rangle. \quad (2.4)$$

571 This way, the probability for the neutrino to transition from flavour α to flavour β
572 will be given by:

$$P(\nu_\alpha \rightarrow \nu_\beta) = |\langle \nu_\beta | \nu_\alpha(t) \rangle|^2 = \left| \sum_{i=1}^3 U_{\beta i} e^{-iE_i t} U_{\alpha i}^* \right|^2. \quad (2.5)$$

573 A usual approximation to take at this point is to consider ultra-relativistic neutrinos,
574 i.e. $E \approx |\vec{p}|$, so we can write the dispersion relations as:

$$E_i = \sqrt{p^2 + m_i^2} \approx E + \frac{m_i^2}{2E}, \quad (2.6)$$

Chapter 2. Neutrino physics

575 so we can write the oscillation probability as:

$$\begin{aligned} P(\nu_\alpha \rightarrow \nu_\beta) &= \sum_{i,j} U_{\alpha i}^* U_{\beta i} U_{\alpha j} U_{\beta j}^* e^{-i \frac{\Delta m_{ij}^2}{2E} t} \\ &= \delta_{\alpha\beta} - 4 \sum_{i < j} \Re [U_{\alpha i}^* U_{\beta i} U_{\alpha j} U_{\beta j}^*] \sin^2 \left(\frac{\Delta m_{ij}^2}{4E} t \right) \\ &\quad + 2 \sum_{i < j} \Im [U_{\alpha i}^* U_{\beta i} U_{\alpha j} U_{\beta j}^*] \sin \left(\frac{\Delta m_{ij}^2}{2E} t \right), \end{aligned} \quad (2.7)$$

576 where Δm_{ij}^2 is the difference of the squared masses of the j th and i th neutrino mass
 577 eigenvalues. At this point, it is usual to write the phase responsible for the oscillations
 578 as (under the approximate assumption $t \approx L$):

$$\Delta_{ij} \equiv \frac{\Delta m_{ij}^2}{4E} L \simeq 1.27 \frac{\Delta m_{ij}^2}{(\text{eV}^2)} \frac{L}{(\text{km})} \frac{(\text{GeV})}{E}. \quad (2.8)$$

579 Notice that, in the case of antineutrinos the only difference would be the sign of the
 580 last term in the oscillation probability. This way, one can write the CP asymmetry as:

$$\begin{aligned} A_{CP}^{\alpha\beta} &= P(\nu_\alpha \rightarrow \nu_\beta) - P(\bar{\nu}_\alpha \rightarrow \bar{\nu}_\beta) \\ &= 4 \sum_{i < j} \Im [U_{\alpha i}^* U_{\beta i} U_{\alpha j} U_{\beta j}^*] \sin 2\Delta_{ij}. \end{aligned} \quad (2.9)$$

581 2.2.2 Oscillations in matter

582 When neutrinos propagate through matter, their oscillation can be affected in mainly
 583 two ways. First, neutrinos can inelastically scatter with nuclei, thus destroying the
 584 coherent propagation of their quantum state. Nevertheless, in most cases this effect is
 585 negligible (even in very dense mediums like the core of the Sun). Second, neutrinos can
 586 also experience coherent or forward scatterings, that can affect their oscillation but not
 587 lose the coherent propagation of the state.

588 The first proposed model to account for neutrino oscillations in matter was proposed
 589 by Mikhaev, Smirnov and Wolfenstein (MSW) [23]. It relies on the fact that, as the
 590 only charged lepton present in ordinary matter is the electron, electron neutrinos can

2.2. Neutrino oscillations

undergo both charged and neutral-current interactions with matter whereas for muon and tau neutrinos just neutral currents are possible.

2.2.3 Current status of neutrino oscillations

A wide range of neutrino experiments provide experimental input to the neutrino oscillation framework, both using natural or synthetic neutrino sources. The results from one of the neutrino global fit analyses, shown in Tab. 2.1¹, summarise well our current understanding of the different oscillation parameters.

Solar neutrino experiments detect neutrinos produced in thermonuclear reactions inside the Sun, mainly from the so-called *pp* chain and the CNO cycle. These neutrinos have a typical energy in the range from 0.1 to 20 MeV. These experiments (Homestake [24], GALLEX [25], SAGE [26], Borexino [27], Super-Kamiokande [28] and SNO [29]) provide the best sensitivities to θ_{12} and Δm_{21}^2 .

Atmospheric neutrino experiments detect the neutrino flux produced when cosmic rays scatter with particles in Earth's atmosphere. These collisions generate particle showers that eventually produce electron and muon neutrinos (and antineutrinos). Their energies range from few MeV to about 10^9 GeV. Experiments, like Super-Kamiokande [30] and IceCube [31] use atmospheric neutrinos to measure oscillations and are specially sensitive to θ_{23} and Δm_{32}^2 .

Reactor neutrino experiments look for the $\bar{\nu}_e$ spectrum produced by nuclear reactors, with energies in the MeV scale. Depending on the distance to the source, long-baseline experiments like KamLAND [32] are sensitive to the solar mass splitting Δm_{21}^2 whereas much shorter baseline experiment such as RENO [33] or DayaBay [34] measure θ_{13} and Δm_{31}^2 .

Accelerator experiments measure neutrino fluxes generated in particle accelerators. Usually mesons are produced in the accelerator to be focused into a beam, then some decay to muon neutrinos and the rest are absorbed by a target. Depending on the

¹These are the results reported during M. Tórtola's talk at Neutrino 2024 (see this link). I need to keep an eye and see if they publish these or other updated results in the near future.

Chapter 2. Neutrino physics

Table 2.1: Summary of neutrino oscillation parameters determined in the Neutrino Global Fit of 2020 [16].

Parameter	Best fit $\pm 1\sigma$	3σ range
Δm_{21}^2 [eV $^2 \times 10^{-5}$]	$7.55^{+0.22}_{-0.20}$	6.98 – 8.19
$ \Delta m_{31}^2 $ [eV $^2 \times 10^{-3}$] (NO)	$2.51^{+0.02}_{-0.03}$	2.43 – 2.58
$ \Delta m_{31}^2 $ [eV $^2 \times 10^{-3}$] (IO)	$2.41^{+0.03}_{-0.02}$	2.34 – 2.49
$\sin^2 \theta_{12}/10^{-1}$	3.04 ± 0.16	2.57 – 3.55
$\sin^2 \theta_{23}/10^{-1}$ (NO)	$5.64^{+0.15}_{-0.21}$	4.23 – 6.04
$\sin^2 \theta_{23}/10^{-1}$ (IO)	$5.64^{+0.15}_{-0.18}$	4.27 – 6.03
$\sin^2 \theta_{13}/10^{-2}$ (NO)	$2.20^{+0.05}_{-0.06}$	2.03 – 2.38
$\sin^2 \theta_{13}/10^{-2}$ (IO)	$2.20^{+0.07}_{-0.04}$	2.04 – 2.38
δ_{CP}/π (NO)	$1.12^{+0.16}_{-0.12}$	0.76 – 2.00
δ_{CP}/π (IO)	$1.50^{+0.13}_{-0.14}$	1.11 – 1.87

617 configuration one can obtain a beam made of mostly neutrinos or antineutrinos. The
 618 typical energies of these neutrinos are in the GeV range. Experiments such as NOvA
 619 [35], T2K [36], MINOS [37], OPERA [?] and K2K [38] (and in the future DUNE [39])
 620 are primarily sensitive to θ_{13} , θ_{23} and Δm_{32}^2 . Also, in the coming years DUNE [39] and
 621 Hyper-Kamiokande [40] will be sensitive to δ_{CP} .

622 2.3 Open questions in the neutrino sector

623 A crucial question that remains open these days, and is of vital importance for oscillation
 624 phenomena, is whether the mass eigenvalue ν_3 is the heaviest (what we call normal
 625 ordering) or the lightest (referred to as inverted ordering) of the mass eigenstates. In
 626 other words, this means that we do not know the sign of Δm_{32}^2 , so we can either have
 627 $m_1 < m_2 < m_3$ (NO) or $m_3 < m_1 < m_2$ (IO).

628 Another big puzzle is related to the value of δ_{CP} . Nowadays it is poorly constrained,
 629 with all values between π and 2π being consistent with data. A prospective measurement
 630 different from $\delta_{CP} = 0, \pi$ will predict CP-violation in the leptonic sector, and thus

2.3. Open questions in the neutrino sector

631 contribute along with the one measured in the quark sector to the total amount of
632 CP-violation. Although it is true that these two contributions by themselves are not
633 enough to explain the matter anti-matter asymmetry in our universe, the amount of
634 CP-violation in the leptonic sector can be key to explain such imbalance.

635 Both of these questions, because of their nature, could be understood thanks to
636 future oscillation experiments.

637 Notwithstanding, there are other mysteries that can not be unveiled just by conducting
638 oscillation experiments, as certain quantities do not influence these phenomena. Among
639 these there is the question of the absolute values of the neutrino masses. Depending
640 on the value of the lightest of the neutrino masses we can have different mass spectra,
641 from hierarchical $m_1 \ll m_2 < m_3$ (NO) or $m_3 \ll m_1 < m_2$ (IO) to quasi-degenerate
642 $m_1 \simeq m_2 \simeq m_3$.

643 Other open question concerns the nature itself of the neutrinos. If neutrinos are Dirac
644 particles then their mass term can be generated through the usual Higgs mechanism
645 by adding right-handed neutrino fields. However, if they are Majorana particles and
646 therefore their own antiparticles, there is no need to add extra fields to have the mass
647 term in the Lagrangian. Experiments like SuperNEMO [?], SNO+ [?] and NEXT [?],
648 which search for neutrino-less double beta decay, will be able to determine whether
649 neutrinos are Dirac or Majorana.

650 Chapter 3

651 The Deep Underground Neutrino
652 Experiment

653 The Deep Underground Neutrino Experiment (DUNE) is a next generation long-baseline
654 neutrino experiment [1]. It will aim to address several questions in neutrino physics,
655 study neutrinos from astrophysical sources and search for beyond the standard model
656 physics.

657 This chapter reviews the main goals of the DUNE experiment, the design of the far
658 detector modules and their data acquisition (DAQ) system, and the role that the near
659 detector plays in the physics program of DUNE.

660 3.1 Overview

661 The main physics goals of DUNE are:

- 662 • measure the neutrino mass hierarchy, the amount of CP violation in the leptonic
663 sector and the θ_{23} octant,
- 664 • detect rare low energy neutrino events, like neutrinos from supernova bursts, and
- 665 • search for proton decay and other beyond the standard model phenomena.

Chapter 3. The Deep Underground Neutrino Experiment

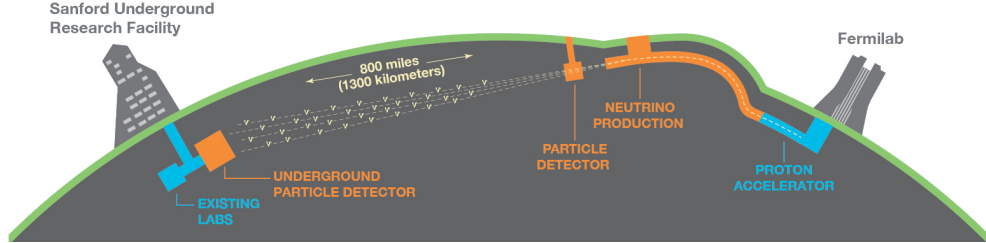


Figure 3.1: Schematic diagram of the DUNE experiment and the LBNF beamline [1].

The design of DUNE has been tailored with these goals in mind. It will consist of two neutrino detectors. A near detector (ND) complex will be placed in Fermilab, 574 m downstream of the neutrino production point, whereas a larger far detector (FD) will be built in the Sandford Underground Research Facility (SURF), South Dakota, approximately 1300 km away. Fig. 3.1 shows a simplified view of the various components of DUNE (not to scale).

The beam neutrinos to be used in DUNE will be provided by the LBNF beamline, the multi-megawatt wide-band neutrino beam planned for Fermilab. First, an intense proton beam is extracted from the Fermilab Main Injector. Then, these protons with energies between 60 GeV and 120 GeV collide with a high-power production target and produce charged mesons. Two magnetic horns allow to focus the mesons and perform a sign selection (thus having the capability to switch between neutrino and antineutrino mode). Soon after that, the mesons decay and produce neutrinos (or antineutrinos) which are then aimed to SURF.

Before arriving to the FD, the neutrino beam meets the ND complex, which serves as the experiment's control. Its role is to measure the unoscillated neutrino energy spectra. From these we can predict the unoscillated spectra at the FD, which can be compared to the spectra measured at the FD in order to extract the oscillation parameters. Therefore, the design of the DUNE ND is mainly driven by the needs of the oscillation physics program.

The liquid Argon time projection chamber (LArTPC) technology has been chosen for

3.2. Physics goals of DUNE

Table 3.1: Summary of the two-phased plan for DUNE. Adapted from Ref. [41].

Parameter	Phase I	Phase II	Benefit
FD mass	20 kt fiducial	40 kt fiducial	FD statistics
Beam power	up to 1.2 MW	2.4 MW	FD statistics
ND config.	ND-LAr, TMS, SAND	ND-LAr, ND-GAr, SAND	Systematic constraints

the FD modules of DUNE. Its four modules will record neutrino interactions from the accelerator-produced beam arriving at predictable times. As it also aims at recording rare events, the FD requires trigger schemes which can deal with both kinds of physics, and also maximum uptime.

DUNE is planned to be built using a staged approach consisting on two phases, which are summarised in Tab. 3.1. Phase I consists of a FD with 50% of the total fiducial mass, a reduced version of the ND complex and a 1.2 MW proton beam. It will be sufficient to achieve some early physics goals, like the determination of the neutrino mass ordering. For its Phase II, DUNE will feature the full four FD modules, a more capable ND and a 2.4 MW proton beam. The physics milestones for the two phases are given in Tab. 3.2, in a staging scenario which assumes that Phase II is completed after 6 years of operation.

A summary of the DUNE science program can be found in the DUNE FD Technical Design Report (TDR) Volume I [1]. For a detailed discussion on the two-phased approach the reader is referred to the DUNE Snowmass 2021 report [41].

3.2 Physics goals of DUNE

As noted in the literature (see for instance Ref. [16] for a review), the parameter space of the neutrino oscillation phenomena within the three-flavour picture is quite constrained by current experimental data. However, there are still crucial open questions, like the mass ordering, the value of δ_{CP} or the θ_{13} octant. One of the main goals of DUNE is to shed some light on the values of these parameters [42].

To address these questions DUNE can look to the subdominant oscillation channel

Chapter 3. The Deep Underground Neutrino Experiment

Table 3.2: Exposure and time required to achieve the different physics milestones of the two phases. The predictions assume a Phase II staging scenario where FD modules 3 and 4 are deployed in years 4 and 6 and both the beam and ND are upgraded after 6 years. Adapted from Ref. [41].

Stage	Physics milestone	Exposure (kt-MW-years)	Years (staged)
Phase I	5σ MO ($\delta_{CP} = -\pi/2$)	16	1-2
	5σ MO (100% of the δ_{CP} values)	66	3-5
	3σ CPV ($\delta_{CP} = -\pi/2$)	100	4-6
Phase II	5σ CPV ($\delta_{CP} = -\pi/2$)	334	7-8
	δ_{CP} resolution of 10 degrees ($\delta_{CP} = 0$)	400	8-9
	5σ CPV (50% of the δ_{CP} values)	646	11
	3σ CPV (75% of the δ_{CP} values)	936	14
	$\sin^2(2\theta_{13})$ resolution of 0.004	1079	16

709 $\nu_\mu \rightarrow \nu_e$ ($\bar{\nu}_\mu \rightarrow \bar{\nu}_e$) and study the energy dependence of the ν_e ($\bar{\nu}_e$) appearance probability.

710 When we focus on the antineutrino channel $\bar{\nu}_\mu \rightarrow \bar{\nu}_e$ there is a change in the sign of δ_{CP} ,
711 thus introducing CP-violation. Moreover, due to the fact that there are no positrons in
712 the composition of Earth, there is a sign difference for the matter effect contribution
713 when looking to the antineutrino channel. This asymmetry is proportional to the baseline
714 length L and is sensitive to the sign of Δ_{31} , and thus to the neutrino mass ordering.

715 Another of the main physics goals of DUNE is the search for baryon-number violating
716 processes. Specifically, it will try to answer the question of whether protons are stable
717 or not. There is no symmetry argument that forbids protons from decaying, but its
718 apparent stability seems to suggest that baryon number is conserved [43]. However,
719 proton decay is a usual feature of grand-unified theories, where electromagnetic, weak
720 and strong interactions are unified above a certain energy scale [44].

721 As the energy deposition scale for this kind of searches is nearly the same as the one
722 for long-baseline neutrino oscillations, DUNE will be able to look for them. It has several
723 advantages over other experiments, such as excellent imaging and particle identification,
724 which can be translated to lower backgrounds.

725 The last of the main objectives of DUNE is the detection of neutrinos originated in
726 supernovae explosions, what is called a supernova neutrino burst (SNB). These neutrinos
727 carry with them information about the core-collapse process, from the progenitor to the

3.3. Far Detector

explosion and the remnant; but also may have information about new exotic physics. So far, the only neutrino events ever recorded from such a process were a few dozens of $\bar{\nu}_e$ events from the 1987A supernova located in the Magellanic Cloud, 50 kpc away from Earth [45, 46].

DUNE aims to collect also some SNB events. Although these are quite rare, as the expected supernovae explosion events are about one every few decades for our galaxy and Andromeda, the long lifetime of the experiment (around a few decades as well) makes it reasonable to expect some. Nowadays the main sensitivity to SNB of most experiments is to the $\bar{\nu}_e$ through inverse beta decay. One of the advantages of DUNE is its expected sensitivity to ν_e , since the dominant channel will be ν_e CC scattering.

Moreover, due to the stringent requirements that the main physics goals set for DUNE, it will allow also to perform searches for all kind of BSM physics. Among others, DUNE will be able to look for: active-sterile neutrino mixing, non-unitarity of the PMNS matrix, non-standard interactions, Lorentz and CPT violations, neutrino trident production, light-mass DM, boosted DM and heavy neutral leptons. The reader is referred to the DUNE FD TDR Volume II [42] for a full discussion of the physics scope of DUNE.

3.3 Far Detector

The so-called DUNE FD complex will sit 1.5 km underground at SURF, South Dakota. Two caverns will host the four FD modules, two of them per cavern, each embedded in cryostats of dimensions 18.9 m (w) \times 17.8 m (h) \times 65.8 m (l). A central, smaller cavern will host the cryogenic system.

Three out of the four modules will be liquid argon (LAr) time projection chamber detectors, often refer to as LArTPCs, with a LAr fiducial mass of at least 10 kt each. The first and second FD modules, FD-1 and FD-2, will use a Horizontal Drift (HD) technology, whereas the third module, FD-3, will have a Vertical Drift (VD) direction. The technology for the fourth module is still to be decided,

Chapter 3. The Deep Underground Neutrino Experiment

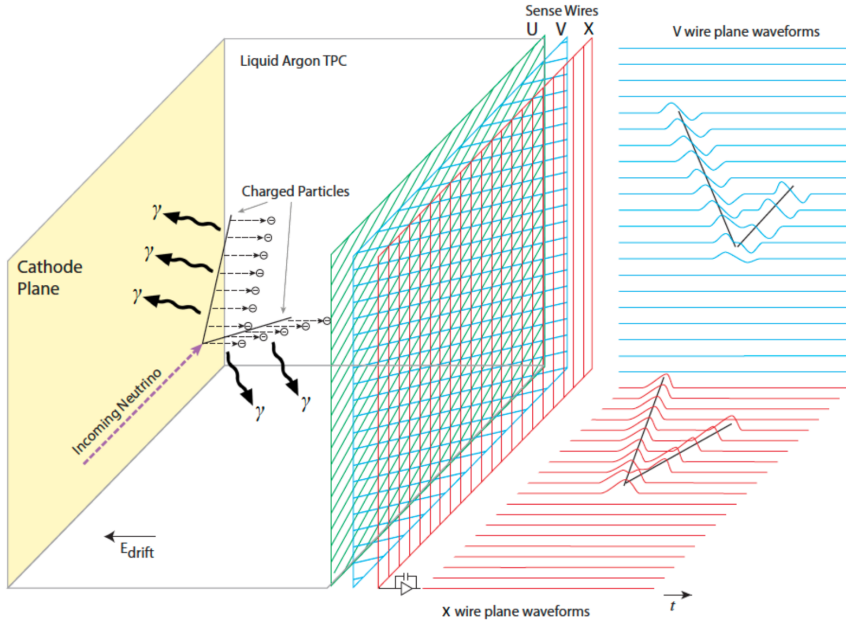


Figure 3.2: Schematic diagram showing the operating principle of a LArTPC with wire readout. Figure taken from Ref. [1].

For each event, with energies ranging from a few MeV to several GeV, these detectors collect both the scintillation light and the ionisation electrons created when the charged particles produced in neutrino-nucleus interactions ionise the argon nuclei. In both HD and VD designs the characteristic 128 nm scintillation light of argon is collected by a photon detection system (PDS). This light will indicate the time at which electrons start to drift, thus enabling reconstruction over the drift coordinate when compared to the time when the first ionisation electron arrives to the anode. Reconstruction of the topology in the transverse direction is achieved using the charge readout. Fig. 3.2 illustrates the detection principle described, for the case of a HD detector with a wire readout.

3.3.1 Horizontal Drift

Within the HD design the ionisation electrons produced as charged particles traverse the LAr drift horizontally towards the anode planes, made out of three layers of wire readout, due to the effect of an electric field. This design, previously known as single-phase (SP), was tested by the ProtoDUNE-SP detector at CERN. The prototype collected data from

3.3. Far Detector

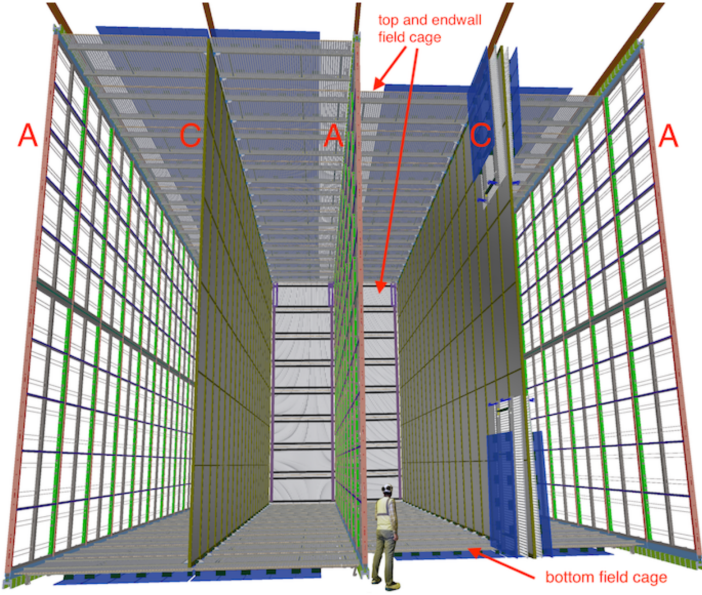


Figure 3.3: Proposed design for the FD-1 and FD-2 modules following the HD principle. Figure taken from Ref. [1].

770 a hadron beam and cosmic rays, providing high-quality data sets for calibration studies
771 and proving the excellent performance of this design.

772 Each FD HD detector module is divided in four drift regions, with a maximum drift
773 length of 3.5 m, by alternating anode and cathode walls. The surrounding field cage
774 ensures the uniformity of the 500 V/cm horizontal electric field across the drift volumes.
775 The three anode walls, which constitute the charge readout of the detector, are built by
776 stacking anode plane assemblies (APAs), 2 high times 25 wide. The design of the HD
777 modules is shown in Fig. 3.3.

778 Each APA is made of 2560 active wires arranged in three layers, plus an extra grid
779 layer, wrapped around a metal frame. The two induction wire planes, U and V, sit at
780 $\pm 35.7^\circ$ to the vertical on each side of the APA. The collection and shielding plane wires,
781 X and G, run parallel to the vertical direction. The ionisation electrons drift past the
782 induction planes, generating bipolar signals on those wires, and are collected by the
783 collection plane, producing a monopolar positive signal. The spacing between the wires
784 is ~ 5 mm, and it defines the spatial resolution of the APA.

785 The front-end readout electronics, or cold electronics as they are immerse in the LAr,

Chapter 3. The Deep Underground Neutrino Experiment

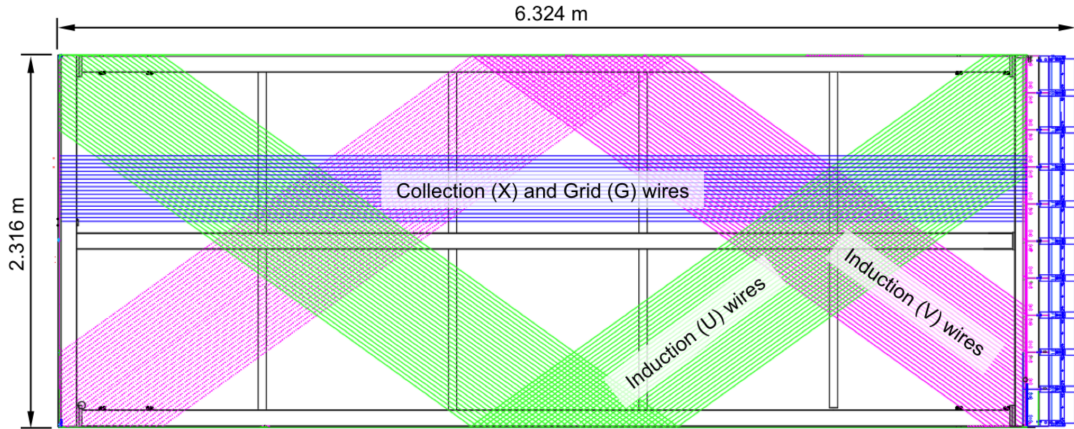


Figure 3.4: Schematic representation of an APA. The black lines represent the APA steel frame. The green and magenta lines correspond to the direction of the U and V induction wires respectively. The blue lines indicate the direction of the X collection wires and the wire shielding G. Figure taken from Ref. [1].

786 are attached to the top of the up APAs and the bottom of the down APAs. Mounted on
 787 the front-end mother boards we have a series of ASICs that digitize the signals from the
 788 collection and induction planes. Each wire signal goes to a charge-sensitive amplifier,
 789 then there is a pulse-shaping circuit and this is followed by the analogue-to-digital
 790 converter. This part of the process happens inside the LAr to minimise the number of
 791 cables penetrating the cryostat. The digitised signals come out finally via a series of
 792 high-speed serial links to the warm interface boards (WIBs), from where the data is sent
 793 to the back-end DAQ through optical fibers.

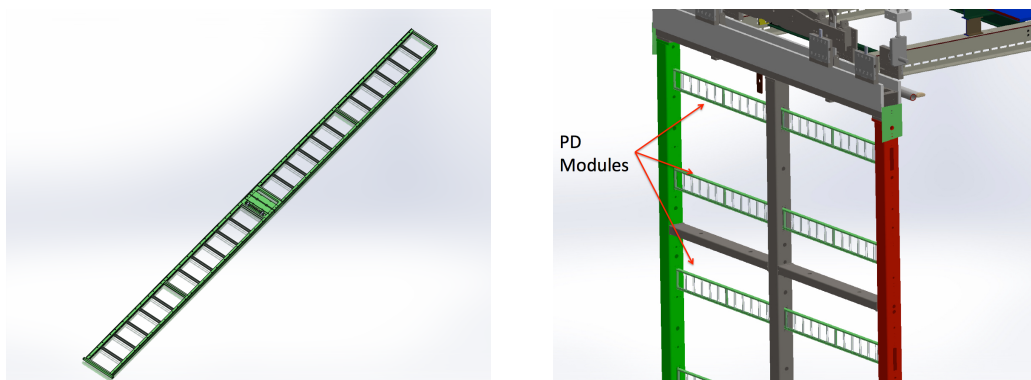


Figure 3.5: A PDS module containing 24 X-ARAPUCAs (left) and the location of the modules on the APAs (right). Figure taken from Ref. [1].

3.3. Far Detector

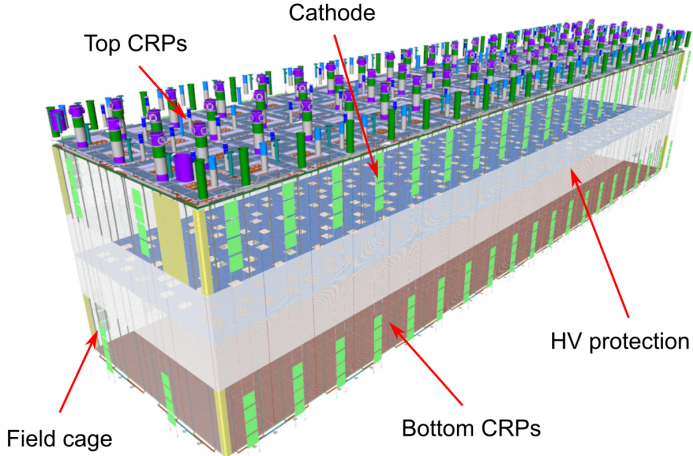


Figure 3.6: Proposed design for the FD-3 module following the VD principle. Figure adapted from Ref. [47].

794 The PDS uses modules of X-ARAPUCA devices, mounted on the APA frames
 795 between the wire planes. Each X-ARAPUCA consists of layers of dichroic filter and
 796 wavelength-shifter. They shift the VUV scintillation light into the visible spectrum,
 797 sending then the visible photons to silicon photomultiplier (SiPM) devices. The PDS
 798 modules are $209\text{ cm} \times 12\text{ cm} \times 2\text{ cm}$ bars, containing 24 X-ARAPUCAs. There are 10
 799 of these PDS modules per APA. Fig. 3.5 shows a PDS module (left) and the placement
 800 of the modules on the APAs (right).

801 **3.3.2 Vertical Drift**

802 In the VD case the ionisation electrons will drift vertically until they meet a printed
 803 circuit board-based (PCB) readout plane. It is based on the original dual-phase (DP)
 804 design deployed at CERN, known as ProtoDUNE-DP, used a vertical drift design with
 805 an additional amplification of the ionization electrons using a gaseous argon (GAr) layer
 806 above the liquid phase. The VD module incorporates the positive features of the DP
 807 design without the complications of having the LAr-GAr interface.

808 The current design of the FD VD module counts with two drift chambers with a
 809 maximum drift distance of 6.5 cm. A cathode plane splits the detector volume along the

Chapter 3. The Deep Underground Neutrino Experiment

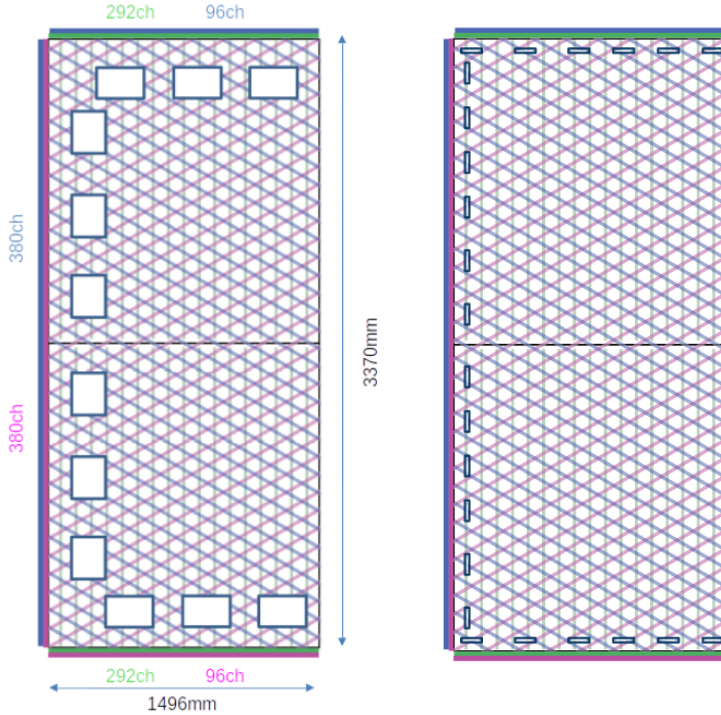


Figure 3.7: Schematic representation of the electrode strip configuration for a top (left) and bottom (right) CRU. Figure taken from Ref. [47].

drift direction while the two anode planes are connected to the bottom and top walls of the detector. The layout of the VD module is shown in Fig. 3.6. Compared with the HD design, the VD option offers a slightly larger instrumented volume and a more cost-effective solution for the charge readout.

As in the HD design, each drift volume features a 500 V/cm electric field and a field cage that ensures its uniformity. The anode planes are arrays of $3.4\text{ m} \times 3\text{ m}$ charge-readout planes (CRPs). These are formed by a pair of charge-readout units (CRUs), which are built from two double-sided perforated PCBs, with their perforations aligned. The perforations allow the drift electrons to pass between the layers.

The PCB face opposite to the cathode has a copper guard plane which acts as shielding, while its reverse face is etched with electrode strips forming the first induction plane. The outer PCB has electrode strips on both faces, the ones facing the inner PCB form the second induction plane while the outermost ones form the collection plane. Fig. 3.7 shows the layout of the electrode strips for the top (left) and bottom (right) CRUs.

3.3. Far Detector

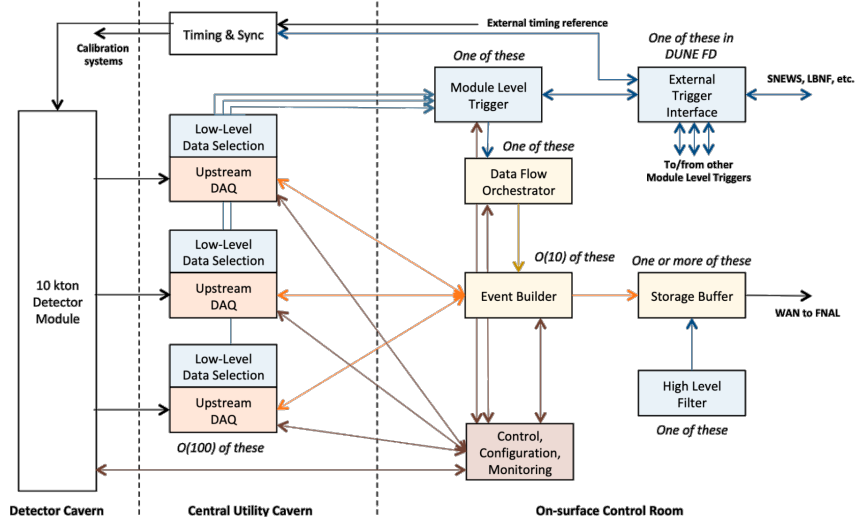


Figure 3.8: Detailed diagram of the DUNE FD DAQ system. Figure taken from Ref. [2].

824 The magenta and blue lines represent the first and second induction planes respectively,
 825 and the green lines correspond to the collection plane.

826 The PDS in the VD module will use the same X-ARAPUCA technology developed
 827 for the HD design. The plan is to place the PDS modules on the cryostat walls and on
 828 the cathode, in order to maximise the photon yield.

829 3.3.3 FD Data Acquisition System

830 The task of the data acquisition (DAQ) system is to receive, process and store data from
 831 the detector modules. In the case of DUNE the DAQ architecture is designed to work
 832 for all FD modules interchangeably, except some aspects of the upstream part which
 833 may depend on the specific module technology.

834 The enormous sample rate and the number of channels in TPC and PD readouts
 835 will produce a very large volume of data. These pose really strong requirements and
 836 challenges to the DUNE FD DAQ architecture. It will be required to read out data of
 837 the order of ten thousand or more channels at rates of a few MHz. In order to cope
 838 with the huge data volume, segmented readouts and compression algorithms are used to
 839 reduce the data rate to manageable levels.

Chapter 3. The Deep Underground Neutrino Experiment

840 The DAQ system of the DUNE FD is composed of five different subsystems. The
841 first one is the upstream DAQ, which receives the raw data from the detector, buffers it
842 and perform some low-level pre-processing. The minimally processed data is then fed
843 into a hierarchical data selection system, which then performs a module level trigger
844 decision. In case of a positive decision a trigger command is produced and executed by
845 the data flow orchestrator, located in the back-end (BE) DAQ subsystem. Subsequently
846 the DAQ BE retrieves the relevant data from the buffers located in the upstream DAQ,
847 adds all the data into a cohesive record and saves it to permanent storage. Watching
848 over all the other subsystems we also have the control, configuration and monitoring
849 subsystem and the time and synchronization subsystem. Fig. 3.8 shows a schematic
850 diagram of the DAQ system, showing the different subsystems and their relations.

851 A notorious challenge for the DUNE DAQ system comes from its broad physics
852 goals. We must be prepared to process events spanning a wide range of time windows
853 (from 5 ms in the case of beam and cosmic neutrinos and nucleon decay to 100 s in the
854 case of SNBs) and therefore this requires a continuous readout of the detector modules.
855 Moreover, because of the off-beam measurements we need to ensure the capabilities
856 of online data processing and self-triggering. Having this into account, together with
857 the technical constraints, the DUNE FD DAQ faces a series of challenges: it needs to
858 be fault tolerant and redundant to reduce downtime, accommodate new components
859 while it keeps serving the operational modules, have large upstream buffers to handle
860 SNB physics, be able to support a wide range of readout windows and last reduce the
861 throughput of data to permanent storage to be at most 30 PB/year.

862 3.4 Near Detector

863 In order to estimate the oscillation parameters we measure the neutrino energy spectra
864 at the FD. This reconstructed energy arises from a convolution of the neutrino flux, cross
865 section, detector response and the oscillation probability. Using theoretical and empirical
866 models to account for the other effects, one can extract the oscillation probability using

3.4. Near Detector

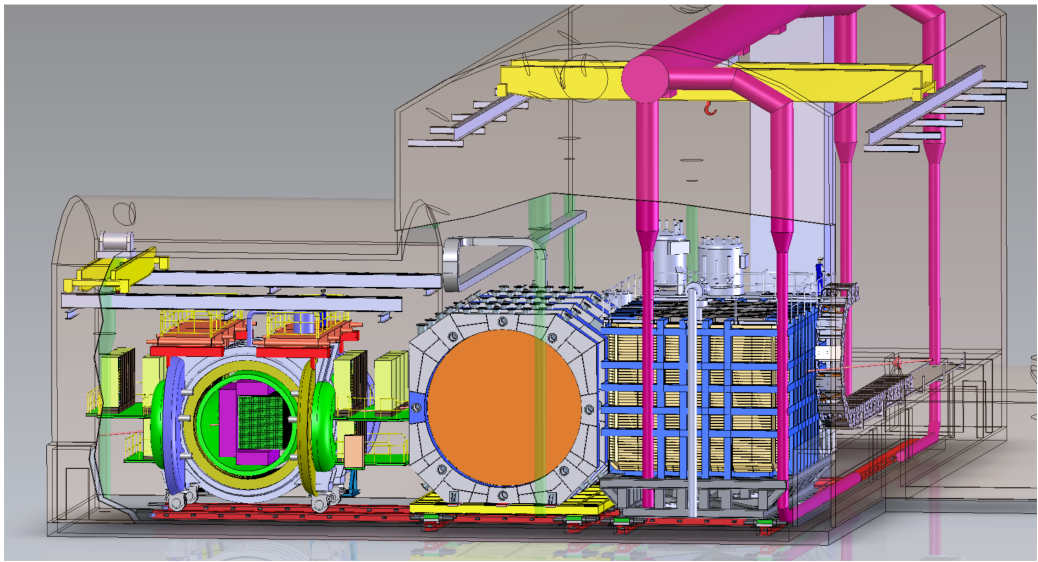


Figure 3.9: Representation of the ND hall in Phase II, showing the different subcomponents. From right to left, in the direction of the beam, we have ND-LAr, ND-GAr and SAND. Figure taken from Ref. [48].

867 the measurement. However, these models have associated a number of uncertainties that
868 are then propagated to the oscillation parameters.

869 One of the main roles of the ND is to measure the neutrino interaction rates before
870 the oscillation effects become relevant, i.e. close to the production point. By measuring
871 the ν_μ and ν_e energy spectra, and that of their corresponding antineutrinos, at the ND
872 we can constrain the model uncertainties. A complete cancellation of the uncertainties
873 when taking the ratio between the FD and ND measurements is not possible, as that
874 would require both detectors to have identical designs and the neutrino fluxes to be
875 the same. Because of the distance, the flux probed by the FD will have a different
876 energy and flavour composition than that at the ND, as neutrinos oscillate and the beam
877 spreads. The differences in the flux also determine the design of the detectors, therefore
878 the ND is limited in its capability to match the FD design.

879 Nevertheless, having a highly capable ND DUNE can minimise the systematic
880 uncertainties affecting the observed neutrino energy. The ND data can be used to
881 tune the model parameters by comparison with the prediction. Then, one uses the
882 tuned model to predict the unoscillated FD spectra. Comparing the prediction with the

Chapter 3. The Deep Underground Neutrino Experiment

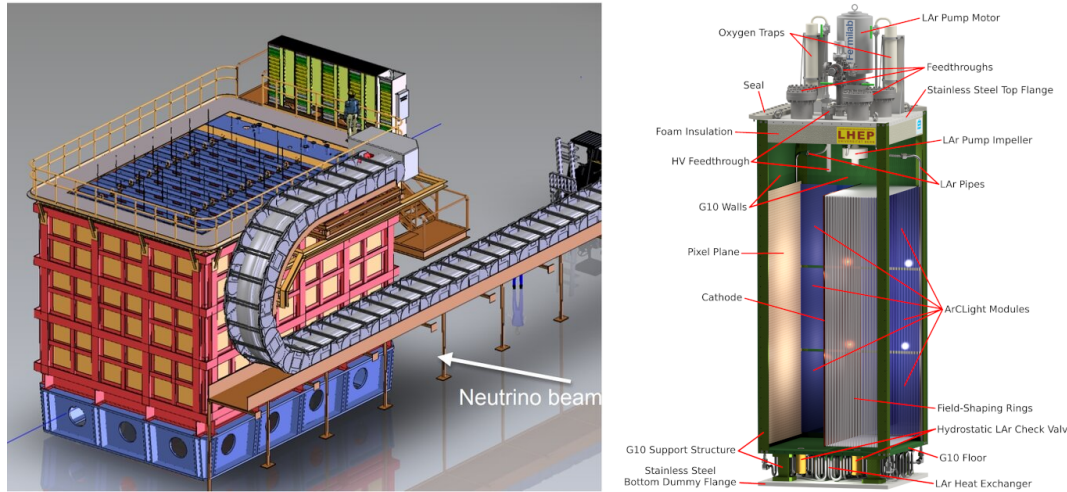


Figure 3.10: Schematic representation of the external components of ND-LAr, including the cryostat and the PRISM movable system (left) and detailed drawing of one ArgonCube module (right). Figure adapted from Ref. [1].

883 measured spectra it is possible to extract the oscillation parameters.

884 Additionally, the ND will have a physics program of its own. In particular, it will
 885 measure neutrino cross sections that will then be used to constrain the model used in
 886 the long-baseline oscillation analysis. It will also be used to search for BSM phenomena
 887 such as heavy neutral leptons, dark photons, millicharged particles, etc.

888 The DUNE ND can be divided in three main components, a LArTPC known as ND-
 889 LAr, a magnetised muon spectrometer, which will be the Temporary Muon Spectrometer
 890 (TMS) in Phase I and ND-GAr in Phase II, and the System for on-Axis Neutrino
 891 Detection (SAND). The layout of the Phase II DUNE ND can be seen in Fig. 3.9. The
 892 first two components of the ND will be able to move off-axis, in what is called the
 893 Precision Reaction-Independent Spectrum Measurement (PRISM) concept. More details
 894 on the purpose and design of the ND can be found in the DUNE ND Conceptual Design
 895 Report (CDR) [48].

896 3.4.1 ND-LAr

897 ND-LAr is a LArTPC, as the ND needs a LAr component in order to reduce cross
 898 section and detector systematic uncertainties in the oscillation analysis. However, its

3.4. Near Detector

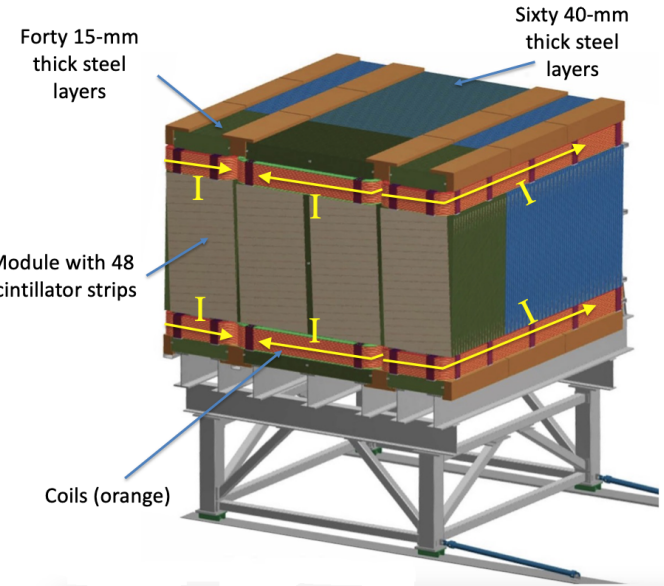


Figure 3.11: Schematic view of the TMS detector, highlighting its main parts. Figure adapted from Ref. [1].

899 design differs significantly from those proposed for the FD modules. Because of the
900 high event rates at the ND, approximately 55 neutrino interaction events per $10 \mu\text{s}$ spill,
901 ND-LAr will be built in a modular way. Each of the modules, based on the ArgonCube
902 technology, is a fully instrumented, optically isolated TPC with a pixelated readout.
903 The pixelisation allows for a fully 3D reconstruction and the optical isolation reduces
904 the problems due to overlapping interactions. Fig. 3.10 shows a representation of the
905 external parts of ND-LAr (left) and a detailed diagram of an ArgonCube module (right).

906 With a fiducial mass of 67 t and dimensions $7 \text{ m} (\text{w}) \times 3 \text{ m} (\text{h}) \times 5 \text{ m} (\text{l})$, ND-LAr
907 will be able to provide high statistics and contain the hadronic systems from the beam
908 neutrino interactions, but muons with a momentum higher than 0.7 GeV will exit the
909 detector.

910 3.4.2 TMS/ND-GAr

911 In order to accurately estimate the neutrino energy, the momentum of the outgoing
912 muons needs to be determined. That is the reason why a muon spectrometer is needed
913 downstream of ND-LAr.

Chapter 3. The Deep Underground Neutrino Experiment

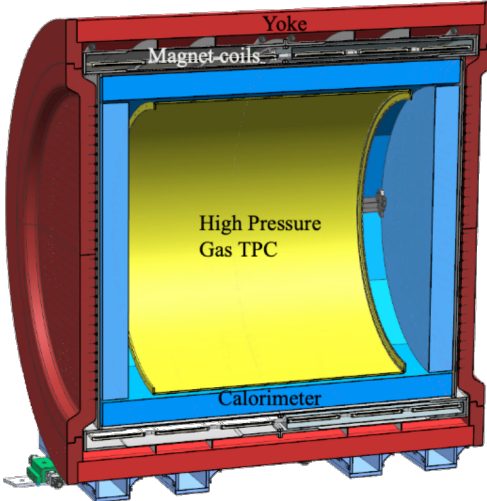


Figure 3.12: Cross section of the ND-GAr geometry, showing the HPgTPC, ECal and magnet. Figure adapted from Ref. [1].

914 In Phase I that role will be fulfilled by TMS. It is a magnetised sampling calorimeter,

915 with alternating steel and plastic scintillator layers. Fig. 3.11 shows a schematic view of
916 the TMS detector. The magnetic field allows a precise measurement of the sign of the
917 muon, so one can distinguish between neutrino and antineutrino interactions.

918 After the Phase II upgrade, TMS will be replaced with ND-GAr. This detector is

919 a magnetised, high-pressure GAr TPC (often denoted as HPgTPC) surrounded by an
920 electromagnetic calorimeter (ECal) and a muon tagger. A cross section of its geometry
921 can be seen in Fig. 3.12. ND-GAr will be able to measure the momenta of the outgoing
922 muons while also detect neutrino interactions inside the GAr volume. This allows
923 ND-GAr to constrain the systematic uncertainties even further, as it will be able to
924 accurately measure neutrino interactions at low energies thanks to the lower tracking
925 thresholds of GAr.

926 3.4.3 PRISM

927 In general, the observed peak neutrino energy of a neutrino beam decreases as the
928 observation angle with respect to the beam direction increases. This feature has been
929 used in other long-baseline neutrino experiments, like T2K (2.5° off-axis) and NOvA

3.4. Near Detector

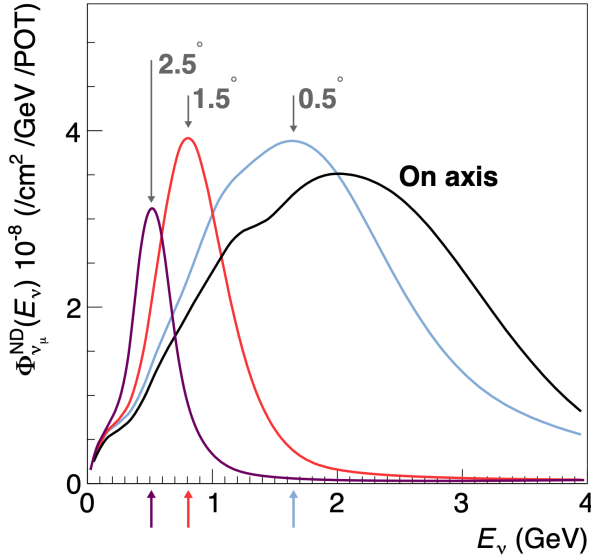


Figure 3.13: Predicted beam muon neutrino flux at the ND location for different off-axis positions. Figure taken from Ref. [48].

(0.8° off-axis), in order to achieve narrower energy distributions. The DUNE PRISM concept exploits this effect using a movable ND. Within PRISM both ND-LAr and the muon spectrometer (TMS in Phase I and ND-GAr in Phase II) can be moved up to 3.2° off-axis, equivalent to move the detectors 30.5 m laterally through the ND hall.

This allows to record additional data samples with different energy compositions. Fig. 3.13 compares the on-axis muon neutrino flux at the ND with the fluxes at different off-axis positions. As the off-axis position increases the neutrino flux becomes closer to a monoenergetic beam with a lower peak energy. These samples can be used to perform a data-driven determination of the relation between true and reconstructed neutrino energy, in order to reduce the dependence on the interaction model. The off-axis samples are linearly combined to produce a narrow Gaussian energy distribution centered on a target true energy. From the combination coefficients one can build a sample of reconstructed neutrino events that will determine the energy mapping.

The PRISM samples can also be used to form a flux at the ND location similar in shape to the oscillated flux measured by the FD. This method can be used to extract the oscillation parameters with minimal input from the neutrino interaction model.

Chapter 3. The Deep Underground Neutrino Experiment

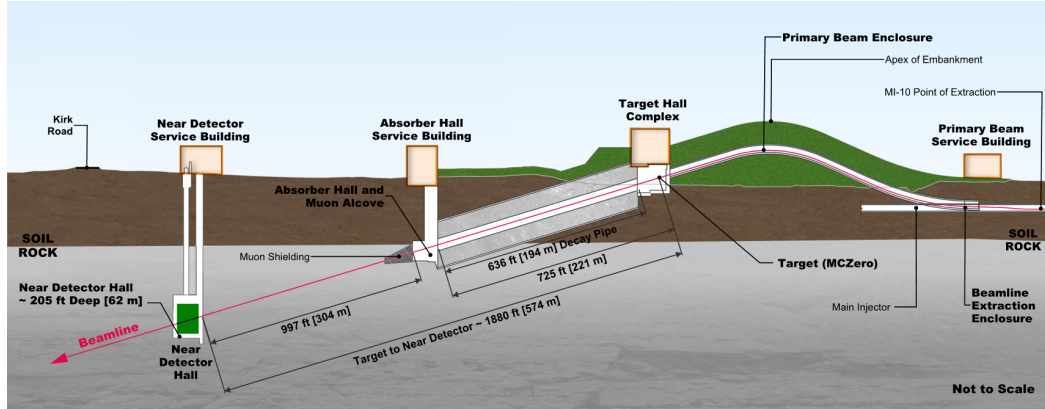


Figure 3.14: Schematic longitudinal section of the LBNF beamline at Fermilab (not to scale). Figure taken from Ref. [49].

946 3.4.4 SAND

947 The role of SAND is to monitor the beam stability by measuring the on-axis neutrino
 948 energy spectra. As the PRISM program requires that ND-LAr and its downstream
 949 muon spectrometer spend about half of the time in off-axis positions, it is not possible
 950 to monitor the stability with the movable detectors. Moreover, for the success of PRISM
 951 it is essential to have a stable beam configuration, or, at least, a quick assessment and
 952 modeling of the distortions.

953 The SAND detector is magnetised, and it counts with an inner low density tracker,
 954 a LAr target with optical readout and surrounding sampling calorimeter.

955 3.5 LBNF beamline

956 The Long-Baseline Neutrino Facility (LBNF) project is responsible for producing the
 957 neutrino beam for the DUNE detectors. A detailed discussion of the LBNF program
 958 can be found in the DUNE/LBNF CDR Volume III [49].

959 The LBNF beamline will provide a high-intensity neutrino beam within the adequate
 960 energy range in order to meet the long-baseline oscillation physics goals of DUNE. A
 961 schematic diagram of the longitudinal section of the LBNF beamline is shown in Fig.
 962 3.14. First, a beam of $60 - 120$ GeV protons is extracted from the Fermilab Main

3.5. LBNF beamline

963 Injector. This beam is aimed towards the target area, where it collides with a cylindrical
 964 graphite target to produce pions and kaons.

965 The diffuse, secondary beam of particles is focused by a pair of magnetic horns.
 966 These select the positively charged particles when operated in Forward Horn Current
 967 (FHC) mode, or the negatively charged ones when the current is reversed, also known as
 968 Reverse Horn Current (RHC) mode. The focused secondary beam then enters a 194 m
 969 decay pipe where the pions and kaons will predominantly produce $\mu^+\nu_\mu$ pairs when in
 970 FHC mode (or $\mu^-\bar{\nu}_\mu$ in RHC mode).

971 At the end of the decay pipe a hadron absorber removes the undecayed hadrons and
 972 muons from the beam, which reduces the ν_e ($\bar{\nu}_e$) and $\bar{\nu}_\mu$ (ν_μ) contamination coming
 973 from the μ^+ (μ^-) decays. The resulting neutrino flux at the FD is shown in Fig. 3.15,
 974 both for FHC (left) and RHC (right) modes. These predictions show the intrinsic $(\bar{\nu}_e)$
 975 contamination and wrong sign component from wrong sign and neutral meson decays,
 976 as well as muons decaying before reaching the absorber.

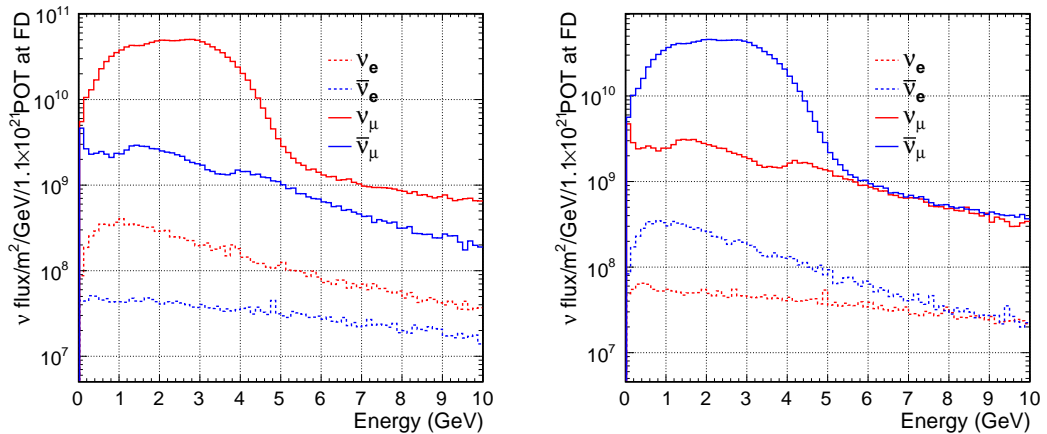


Figure 3.15: Predicted neutrino fluxes at the FD in FHC mode (left panel) and RHC mode (right panel). Figures taken from Ref. [42].

977 **Chapter 4**

978 **ND-GAr**

979 ND-GAr is a magnetised, high-pressure gaseous argon TPC (HPgTPC), surrounded by
980 an electromagnetic calorimeter (ECal) and a muon detector (commonly refer to as μ ID).
981 A detailed discussion on the requirements, design, performance and physics of ND-GAr
982 can be found in the DUNE ND CDR [48] and the ND-GAr whitepaper (cite).

983 In DUNE Phase II ND-GAr will fulfill the role of TMS, measuring the momentum
984 and sign of the charged particles exiting ND-LAr. Additionally, it will be able to measure
985 neutrino interactions inside the HPgTPC, achieving lower energy thresholds than those
986 of the ND and FD LArTPCs. By doing so ND-GAr will allow to constrain the relevant
987 systematic uncertainties for the LBL analysis even further.

988 The goal of the present chapter is to review the requirements that the physics program
989 of DUNE impose on ND-GAr, present the current status of its design and describe the
990 GArSoft package, its simulation and reconstruction software.

991 **4.1 Requirements**

992 The primary requirement for ND-GAr is to the measure the momentum and charge of
993 muons from ν_μ and $\bar{\nu}_\mu$ CC interactions in ND-LAr, in order to measure their energy
994 spectrum. To achieve the sensitivity to the neutrino oscillation parameters described
995 in the DUNE FD TDR Volume II [42] ND-GAr should be able to constrain the muon

Chapter 4. ND-GAr

996 energy within a 1% uncertainty or better. The main constraint will come from the
997 calibration of the magnetic field, performed using neutral kaon decays in the HPgTPC.

998 Another requirement for ND-GAr is the precise measurement of neutrino interactions
999 on argon for the energies relevant to the neutrino oscillation program. The goal is to
1000 constrain the cross section systematic uncertainties in the regions of phase space that
1001 are not accessible to ND-LAr. This requires the kinematic acceptance for muons in
1002 ND-GAr to exceed that of ND-LAr, being comparable to the one observed in the FD.

1003 ND-GAr should also be able to the relationship between true and reconstructed energy
1004 from neutrino interactions on argon with low thresholds, being sensitive to particles that
1005 are not observed or may be misidentified in ND-LAr. In particular, ND-GAr needs to
1006 have low tracking thresholds in order to measure the spectrum of pions and protons
1007 produced in final-state interactions (FSI). It also must be able to accurately measure
1008 the pion multiplicity in 1, 2 and 3 pions final states, to inform the pion mass correction
1009 in the LArTPCs.

1010 4.2 Reference design

1011 The final design of ND-GAr is still under preparation. However, a preliminary baseline
1012 design was in place at the time of the ND CDR. This section summarises the main
1013 features of that design, as it is also the one used for the default geometry in our simulation.
1014 A DUNE Phase II whitepaper, discussing the different options under consideration for
1015 the ND-GAr design, is in progress.

1016 4.2.1 HPgTPC

1017 The reference design for the ND-GAr HPgTPC follow closely that of the ALICE TPC.
1018 It is a cylinder with a central high-voltage cathode, generating the electric field for
1019 the two drift volumes, with a maximum drift distance of 2.5 m each. The anodes will
1020 be instrumented with charge readout chambers. The original design repurposed the
1021 multi-wire proportional readout chambers of ALICE, however the current R&D efforts

4.2. Reference design

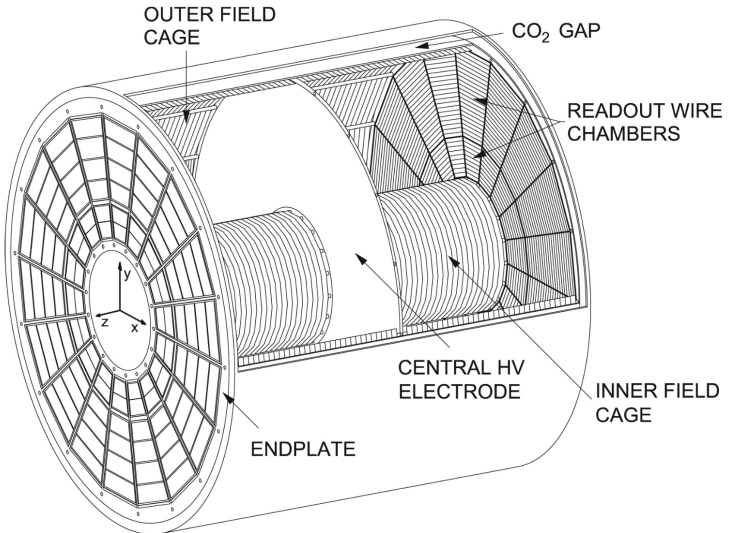


Figure 4.1: Diagram of the ALICE TPC, showing the two drift chambers, inner and outer field cages and readout chambers. Figure taken from Ref. [1].

1022 focus on a gas electron multiplier option instead. Fig. 4.1 shows a schematic diagram of
 1023 the ALICE TPC design. The basic ND-GAr geometry will resemble this, except for the
 1024 inner field cage.

1025 It will use a 90-10 molar fraction argon-CH₄ mixture at 10 bar. With this baseline
 1026 gas mixture light collection is not possible, as the quenching gas absorbs most of the
 1027 VUV photons. Additional R&D efforts are underway, to understand if different mixtures
 1028 allow for the light signal to be used to provide a t_0 while maintaining stable charge gain.

1029 4.2.2 ECal

1030 The main role of the ND-GAr ECal is the calorimetric measurement of the electron
 1031 energies and the reconstruction of photons, in particular those from neutral pion decays.
 1032 Also, the ECal is able to provide a t_0 timestamp for neutrino interactions, by associating
 1033 its activity to the tracks in the HPgTPC. The ECal will also be able to perform
 1034 neutron reconstruction using time of flight and reject external backgrounds, thanks to
 1035 its sub-nanosecond time resolution.

1036 The ECal design features three independent subdetectors, two end caps at each side
 1037 and a barrel surrounding the HPgTPC. Each of the detectors is divided in modules,

Chapter 4. ND-GAr

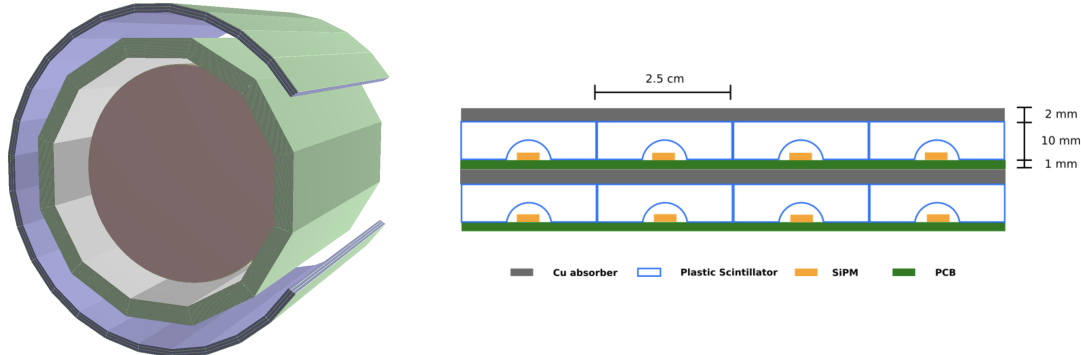


Figure 4.2: View of the 12-sided ECal barrel and outer muon tagger geometries (left) and layout of the ECal tile layers for the 2 mm Cu, 10 mm scintillator option (right). Figure adapted from Ref. [1].

1038 which combine alternating layers of plastic scintillator and absorber material readout
 1039 by SiPMs. The inner scintillator layers consist of $2.5 \times 2.5 \text{ cm}^2$ high-granularity tiles,
 1040 whereas the outer ones are made out of 4 cm wide cross-strips spanning the whole
 1041 module length. The current barrel geometry consists of 8 tile layers and 34 strip layers,
 1042 while the end caps feature 6 and 36 respectively. The thickness of the scintillator layers
 1043 is 7 mm and 5 mm for the Pb absorber layers. The 12-sided geometry of the ECal barrel
 1044 (left) and the layout of the tile layers (left)¹ can be seen in Fig. 4.2.

1045 4.2.3 Magnet

1046 The ND-GAr magnet design, known as the Solenoid with Partial Yoke (SPY), consists of
 1047 two coupled solenoids with an iron return yoke. The idea behind the design is to have a
 1048 solenoid as thin as possible, as well as a return yoke mass distribution that minimises
 1049 the material budget between ND-LAr and ND-GAr. The magnet needs to provide a
 1050 0.5 T field in the direction perpendicular to the beam, parallel to the drift electric field.
 1051 It needs to host the pressure vessel and the surrounding ECal, which points to an inner
 1052 diameter of ~ 6.4 m.

1053 The solenoid is a single layer coil, based on niobium titanium superconducting

¹The figure shows the layout of the tile layers for a previous design with 2 mm Cu absorber and 10 mm plastic scintillator, as mentioned in the text the current choice is 5 mm Pb absorber and 7 mm scintillator.

4.3. GArSoft

1054 Rutherford cable. The total length of the coil is 7.5 m. The bobbin will be split in four
1055 segments grouped in pairs with two identical cryostats, connected in series. The iron
1056 yoke features an aperture in the upstream side to allow the muons coming from ND-LAr.
1057 Still, its material will be enough to reduce the magnetic field reaching SAND, and also
1058 stop the charged pions produced inside the HPgTPC.

1059 4.2.4 Muon system

1060 The design of the ND-GAr muon system is still in a preliminary stage. Its role is to
1061 distinguish between muons and pions punching through the ECal. This is especially
1062 important for wrong-sign determination, to separate these from neutral current events.

1063 In its current form, the muon system consists of three layers of longitudinal sampling
1064 structures. It alternates 10 cm Fe absorber slabs with 2 cm plastic scintillator strips.
1065 The transverse granularity required is still under study.

1066 4.3 GArSoft

1067 GArSoft is a software package developed for the simulation and reconstruction of events
1068 in ND-GAr. It is inspired by the LArSoft toolkit used for the simulation of LArTPC
1069 experiments, like the DUNE FD modules. It is based on `art`, the framework for event
1070 processing in particle physics experiments [?]. Other of its main dependencies are `ROOT`,
1071 `NuTools`, `GENIE` and `Geant4`. It allows the user to run all the steps of a generation-
1072 simulation-reconstruction workflow using FHiCL configuration files.

1073 4.3.1 Event generation

1074 The standard generator FHiCLs in GArSoft run the event generation and particle
1075 propagation simulation (i.e. Geant4) in the same job by default. However, it is possible
1076 to split them up if needed. The current version of GArSoft provides five different event
1077 generators, each of them producing `simb::MCTruth` products defined in `NuTools`. The
1078 available modules are:

Chapter 4. ND-GAr

- 1079 • **SingleGen**: particle gun generator. It produces the specified particles with a given
1080 distribution of momenta, initial positions and angles.
- 1081 • **TextGen**: text file generator. The input file must follow the `hepevt` format², the
1082 module simply copies this to `simb::MCTruth` data products.
- 1083 • **GENIEGen**: GENIE neutrino event generator. The module runs the neutrino-nucleus
1084 interaction generator using the options specified in the driver FHiCL file (flux file,
1085 flavour composition, number of interactions per event, t_0 distribution, ...). Current
1086 default version is `v3_04_00`.
- 1087 • **RadioGen**: radiological generator. It produces a set list of particles to model
1088 radiological decays. Not tested.
- 1089 • **CRYGen**: cosmic ray generator. The module runs the CRY event generator with a
1090 configuration specified in the FHiCL file (latitude and altitude of detector, energy
1091 threshold, ...). Not tested.

1092 The module `GArG4` searches for all the generated `simb::MCTruth` data products, using
1093 them as inputs to the Geant4 simulation with the specified detector geometry. A constant
1094 0.5 T magnetic field along the drift coordinate is assumed. The main outputs of this step
1095 are `simb::MCParticle` objects for the generated Geant4 particles, `gar::EnergyDeposit`
1096 data products for the energy deposits in the HPgTPC and `gar::CaloDeposit` data
1097 products for the energy deposits in the ECal and muon system.

1098 4.3.2 Detector simulation

1099 The standard detector simulation step in GArSoft is all run with a single FHiCL, but
1100 the different modules can be run independently as well. First the `IonizationReadout`

²In brief, each event contains at least two lines. The first line contains two entries, the event number and the number of particles in the event. Each following line contains 15 entries to describe each particle. The entries are: status code, pdg code for the particle, entry of the first mother for this particle, entry of the second mother for this particle, entry of the first daughter for this particle, entry of the second daughter for this particle, x component of the particle momentum, y component of the particle momentum, z component of the particle momentum, energy of the particle, mass of the particle, x component of the particle initial position, y component of the particle initial position, z component of the particle initial position and time of the particle production.

4.3. GArSoft

1101 module simulates the charge readout of the HPgTPC, and later the `SiPMReadout` module
1102 runs twice, once for the ECal and then for the muon system, with different configurations.

1103 The `IonizationAndScintillation` module collects all the `gar::EnergyDeposit`
1104 data products, to compute the equivalent number of ionization electrons for each energy
1105 deposit. The `ElectronDriftAlg` module simulates the electron diffusion numerically
1106 both in the longitudinal and transverse directions and applies an electron lifetime
1107 correction factor. The induced charge on the nearest and neighbouring readout pads
1108 is modeled using the provided pad response functions. The digitisation of the data is
1109 then simulated with the `TPCReadoutSimAlg` module. By default, the ADC sampling
1110 rate used is 50.505 MHz. The resulting raw waveforms for each channel are stored with
1111 zero-suppression, in order to save memory and CPU time. The algorithms keep blocks
1112 of ADC values above a certain threshold, plus some adjustable additional early and late
1113 tick counts. The results of these three steps are `gar::raw::RawDigit` data products.

1114 For the ECal and the muon system the `SiPMReadout` module calls either the
1115 `ECALReadoutSimStandardAlg` or `MuIDReadoutSimStandardAlg` modules. These take
1116 all the `gar::CaloDeposit` data products in the corresponding detector and do the
1117 digitisation depending on whether the hit was in a tile or strip layer. They include single
1118 photon statistics, electronic noise, SiPM saturation and time smearing. The resulting
1119 objects are `gar::raw::CaloRawDigit` data products.

1120 4.3.3 Reconstruction

1121 The reconstruction in GArSoft is also run as a single job by default. It first runs the hit
1122 finding, clustering, track fitting and vertex identification in the HPgTPC, followed by
1123 the hit finding and clustering in the ECal and muon system. After those it produces the
1124 associations between the associations between the tracks and the ECal clusters.

1125 Focusing first on the HPgTPC reconstruction, the `CompressedHitFinder` module
1126 takes the zero-suppressed ADCs from the `gar::raw::RawDigit` data products. The
1127 reconstructed hits largely correspond to the above threshold blocks, however the hit
1128 finder identifies waveforms with more than one maximum, diving them in multiple hits

Chapter 4. ND-GAr

1129 if they dip below a certain threshold. The data products produced are of the form
1130 `gar::rec::Hit`. These are the inputs to the clustering of hits in the `TPCHitCluster`
1131 module. Hits close in space and time are merged, and the resulting centroids are found.
1132 This module outputs `gar::rec::TPCClusters` objects and associations to the input
1133 hits.

1134 The following step prior to the track fitting is pattern recognition. The module
1135 called `tpcvecchitfinder2` uses the `gar::rec::TPCClusters` data products to find track
1136 segments, typically called vector hits. They are identified by performing linear 2D fits
1137 to the positions of the clusters in a 10 cm radius, one fit for each coordinate pair. A
1138 3D fit defines the line segment of the vector hit, using as independent variable the one
1139 whose sum of (absolute value) slopes in the 2D fits is the smallest. The clusters are
1140 merged to a given vector hit if they are less than 2 cm away from the line segment. The
1141 outputs are `gar::rec::VecHit` data products, as well as associations to the clusters. The
1142 `tpcpatrec2` module takes the `gar::rec::VecHit` objects to form the track candidates.
1143 The vector hits are merged together if their direction matches, their centers are within
1144 60 cm and their direction vectors point roughly to their respective centers. Once
1145 the clusters of vector hits are formed they are used to make a first estimation of the
1146 track parameters, simply taking three clusters along the track. The module produces
1147 `gar::rec::Track` data products and associations between these tracks and the clusters
1148 and vector hits.

1149 The track is fitted by means of a Kalman filter in the `tpctrackfit2` module, using
1150 the position along the drift direction as the independent variable. Two different fits are
1151 performed per track, a forward and a backwards fit, each starting from one of the track
1152 ends. The Kalman filter state vector ($y, z, R, \phi, \tan\lambda$) is estimated at each point along
1153 the track using a Bayesian update. The track parameters reported in the forward and
1154 backwards fits are the ones computed at the opposite end where the fit started. The
1155 main outputs of the track fit are the `gar::rec::Track` objects. Additionally, the module
1156 stores the fitted 3D positions along the track in the `gar::rec::TrackTrajectory` data
1157 products and the total charge and step sizes for each point also get stored in the form of

4.3. GArSoft

1158 `gar::rec::TrackIonization` objects.

1159 After the tracking step, the `vertexfinder1` module looks at the reconstructed
1160 `gar::rec::Track` products, creating vertex candidates with the track ends that are
1161 within 12 cm of each other. The vertices are then fitted using linear extrapolations from
1162 the different track ends associated. The results are `gar::rec::Vertex` data products,
1163 and associations to the tracks and corresponding track ends.

1164 For the ECal and muon tagger, the `SiPMHitFinder` module runs twice with different
1165 configurations, adapted to the particular capabilities of both. The module simply takes
1166 the `gar::raw::CaloRawDigit` products, applies a calibration factor to convert the ADC
1167 counts to MeV and for the strip layer hits it calculates the position along the strip using
1168 the times recorded of both SiPMs. This module produces `gar::rec::CaloHit` data
1169 products. Next, these objects are used as inputs to the `CaloClustering` module. It
1170 merges the hits based on a simple nearest neighbours (NN) algorithm. For the resulting
1171 clusters it also computes the total energy and position of the centroid. The results are
1172 stored as `gar::rec::Cluster` data products, with associations to the hits.

1173 The last step in the reconstruction is associating the reconstructed tracks in the
1174 HPgTPC to the clusters formed in the ECal and muon system. The `TPCECALAssociation`
1175 module checks first the position of the track end points, considering only the points
1176 that are at least 215 cm away from the cathode or have a radial distance to the center
1177 greater than 230 cm. The candidates are propagated up to the radial position, in the
1178 case of clusters in the barrel, or the drift coordinate position, for the end cap cluster, of
1179 the different clusters in the collection using the track parameters computed at the end
1180 point. The end point is associated to the cluster if certain proximity criteria are met.
1181 This module creates associations between the tracks, the end points and the clusters.
1182 The criteria for the associations are slightly different for the ECal and the muon tagger.

₁₁₈₃ Chapter 5

₁₁₈₄ FWTPG offline software

1185 Chapter 6

1186 Matched Filter approach to
1187 induction wire Trigger Primitives

1188 6.1 Motivation

1189 The filter implemented in the firmware of the upstream DUNE FD DAQ is a 32nd-order
1190 low-pass finite impulse-response (FIR) filter. The output of such filter for a discrete
1191 system can be written as:

$$y[i] = \sum_{j=0}^N h[j]x[i-j], \quad (6.1)$$

1192 where N is the order of the filter, y is the output sequence, x is the input sequence and h
1193 is the set of coefficients of the filter. The current implementation within `dtp-firmware`
1194 [50] uses a set of 16 non-zero integer coefficients.

1195 Filtering is a vital step in the hit finder chain. It helps to suppress the noise and
1196 enhance the signal peaks with respect to the noiseless baseline. A good filtering strategy
1197 allows us to use lower thresholds when forming the trigger primitives (TPs) and thus
1198 increasing the sensitivity of our detector to low energy physics events. In such events,
1199 the hits produced by the ionisation electrons tend to have lower amplitudes than those
1200 of interest to the baseline physics programme of the DUNE experiment.

1201 This is particularly important for the induction planes. In general, signal peaks in

Chapter 6. Matched Filter approach to induction wire Trigger Primitives

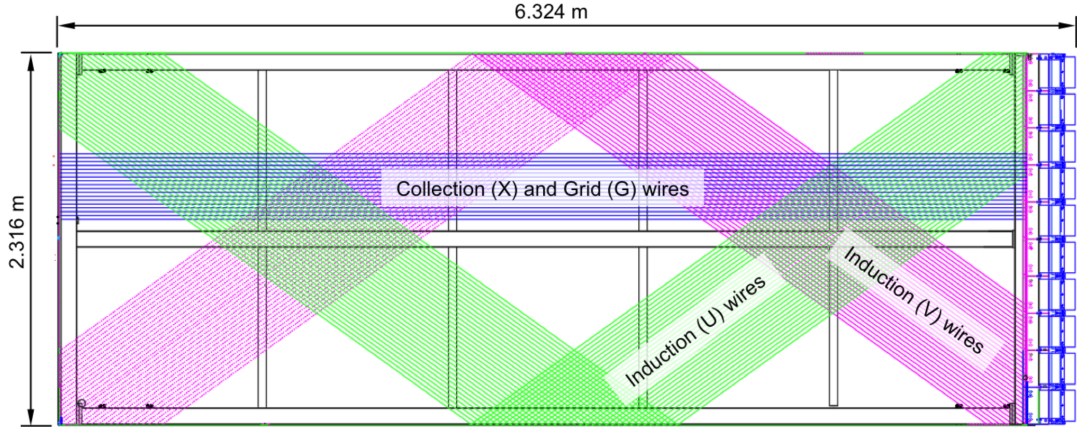


Figure 6.1: Schematic representation of an APA. The black lines represent the APA steel frame. The green and magenta lines correspond to the direction of the U and V induction wires respectively. The blue lines indicate the direction of the X collection wires and the wire shielding G.

the induction wires have smaller amplitude than the ones in the induction plane. This, together with the fact that the pulse shapes are bipolar, reduces our capacity to detect the hits on these channels. The inefficiency of detecting TPs in the induction planes (denoted as U and V planes) lead trigger algorithms to focus mainly on the TPs from the collection plane (so-called X plane). As a result, the possibility of making trigger decisions based on the coincidence of TPs across the three wire planes remains nowadays unexploited in DUNE. Fig. 6.1 shows a schematic view of an anode plane assembly (APA), with the different wire plane orientations highlighted.

A possible improvement of the current hit finder chain could require optimising the existing or choosing a new filter implementation. A filter strategy which improves the induction signals may be able to enhance the detection efficiency of TPs from the induction planes and ideally make it comparable to that of the collection plane.

The goal is to implement a better finite-impulse response filter design and to evaluate its performance relative to the current filter. To do so, we need to take into account the limitations of the firmware: the FIR filter shall have maximum 32 coefficients (so-called taps) whose values are 12-bit unsigned integers. Although it is technically possible to include non-integer coefficients, it would be a technical challenge as we have 40 FIR

6.2. Signal-to-noise ratio definition

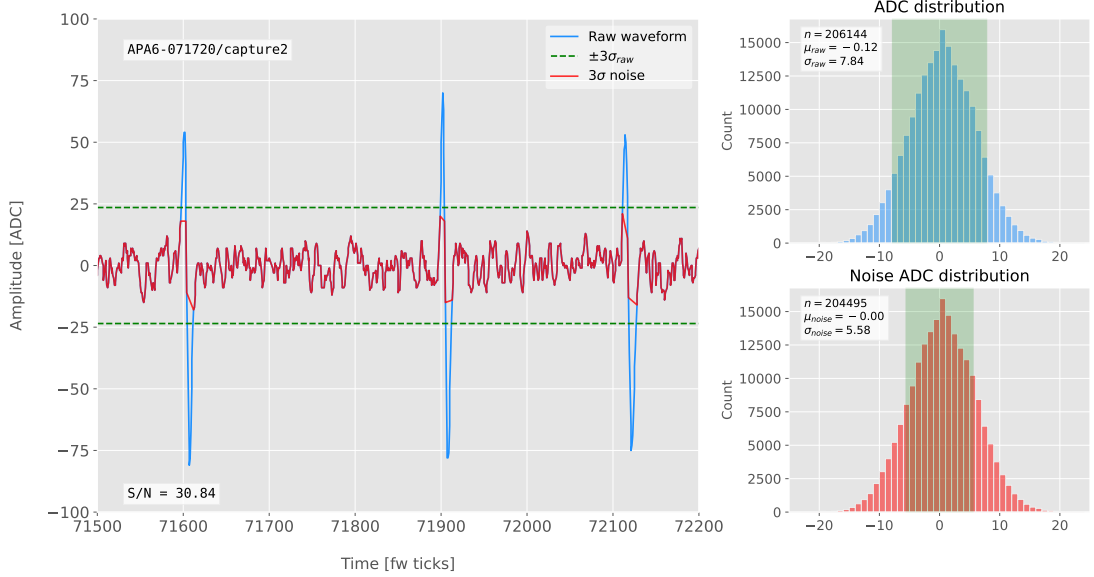


Figure 6.2: Left panel: Zoomed unfiltered waveform corresponding to channel 7840 from the ProtoDUNE-SP raw data capture `felix-2020-07-17-21:31:44` (blue line). The green dashed lines mark the region $\pm 3\sigma_{\text{raw}}$. The resulting noise waveform is also shown (red line). Top right panel: ADC distribution for channel 7840, where the green shaded region represents $\pm \sigma_{\text{raw}}$. Bottom right panel: noise ADC distribution for channel 7840, where the green shaded region represents $\pm \sigma_{\text{noise}}$.

1219 instances per APA, as there are 4 FIR per optical link and 10 optical links per APA.
 1220 With these restrictions, the task is to provide a set of 32 coefficients which yield an
 1221 optimal filter performance for the induction wires.

1222 6.2 Signal-to-noise ratio definition

1223 I introduce the signal to noise ratio (S/N) as a measure of the FIR filter performance
 1224 and demonstrate how to extract its value for a set of ProtoDUNE-SP data. The S/N
 1225 metrics allow us to compare different filter implementations and serve as a basis for more
 1226 detailed studies presented later in this document. Specifically, I use the ADC capture
 1227 `felix-2020-07-17-21:31:44` (data capture taken for firmware validation purposes). I
 1228 defined S/N as the height of the signal peaks relative to the size of the noise peaks.
 1229 To quantify this quantity channel by channel one first need to estimate the standard
 1230 deviation of the ADC data for each channel, σ_{ADC} . Then, I define the corresponding

Chapter 6. Matched Filter approach to induction wire Trigger Primitives

noise waveform to be the ADC values in the range $\pm 3\sigma_{ADC}$. From this new noise data one can estimate again the mean and standard deviation, μ_{noise} and σ_{noise} , so I can write the S/N for any given channel as:

$$S/N = \frac{\max [ADC] - \mu_{noise}}{\sigma_{noise}}, \quad (6.2)$$

where $\max [ADC]$ is simply the maximum ADC value found in the corresponding channel.

One can apply this definition of the S/N with a waveform from one of the channels of the data capture¹. Fig. 6.2 shows a zoomed region of the waveform corresponding to channel 7840 (blue line), where one can clearly see three signal peaks and continuous additive noise (we actually see 6 peaks, 3 positive and 3 negative, but, because by design for induction channels the expected signal pulse shapes are bipolar, I treat them as a collection of 3 individual signal peaks). I estimated the standard deviation of this raw waveform to be $\sigma_{raw} = 7.84$ ADC, so I am able to define the noise waveform (red line) as the ADC values in the range ± 23.52 ADC. This way one obtains $\mu_{noise} = 0$ and $\sigma_{noise} = 5.58$ ADC, which gives $S/N = 30.84$.

We can repeat this calculation now for the corresponding filtered waveform (using the current firmware FIR filter). In Fig. 6.3 I plotted the same time window for the filtered waveform from channel 7840 (blue line). In this case, the standard deviation of the waveform is larger than before, giving $\sigma_{raw} = 10.99$ ADC. The resulting noise waveform (red line) results from selection the ADC values in the range ± 32.91 ADC, giving now $\mu_{noise} = -0.47$ ADC and $\sigma_{noise} = 7.03$ ADC. Finally, one obtains $S/N = 24.68$. Notice that the value of S/N decreases after the filtering. Clearly, one can see that the noise baseline has increased by a factor of 1.35 when we applied the FIR filter and at the same time the amplitude of the signal peaks has remained almost unchanged, leading to this poorer S/N value.

¹All the original work was done within the `dtp-simulation` package [51], which offers a variety of tools to read raw data and emulate the TPG block (pedestal subtraction, filtering and hit finder). However, the results shown in this report were re-worked later using the C++ based `dtpemulator` package [52]. Its main purpose is the emulation of the TPG block and, in the same way as its predecessor, it has been cross-checked against the current firmware implementation.

6.3. Low-pass FIR filter design

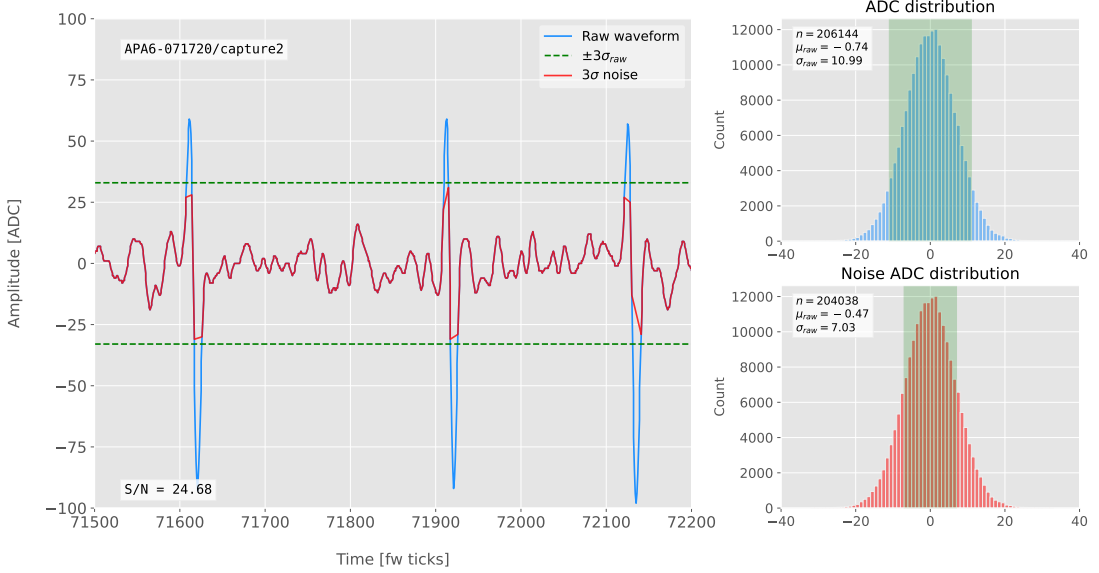


Figure 6.3: Left panel: Zoomed filtered waveform corresponding to channel 7840 from the ProtoDUNE-SP raw data capture `felix-2020-07-17-21:31:44` (blue line). The filter used was the current implementation of the low-pass FIR filter in `dtp-firmware`. The green dashed lines mark the region $\pm 3\sigma_{\text{raw}}$. The resulting noise waveform is also shown (red line). Top right panel: ADC distribution for channel 7840 after filtering, where the green shaded region represents $\pm \sigma_{\text{raw}}$. Bottom right panel: noise ADC distribution for channel 7840 after filtering, where the green shaded region represents $\pm \sigma_{\text{noise}}$

1254 6.3 Low-pass FIR filter design

1255 In general, when one uses a method to optimize the frequency response of a digital filter,
 1256 such as the Parks-McClellan algorithm, one finds a set of N real coefficients that give
 1257 the best response for the specified pass-band and order of the filter [53].

1258 In our case, as the sampling frequency is defined as 1 ticks^{-1} , the Nyquist frequency
 1259 will simply be $1/2 \text{ ticks}^{-1}$. The current implementation of the filter seems to have as
 1260 pass-band the range $[0, 0.1] \text{ ticks}^{-1}$. This can be seen in Fig. 6.4, where I show the
 1261 power spectrum, in decibels, of such filter implementation (blue solid line). For instance,
 1262 the Park-McClellan algorithm finds the optimal Chebyshev FIR filter taking as input
 1263 the boundaries of the target pass-band and stop-band, which can be written in the form:

$$\left\{ \begin{array}{l} [0, f_c] \\ [f_c + \delta f, f_N] \end{array} \right. , \quad (6.3)$$

Chapter 6. Matched Filter approach to induction wire Trigger Primitives

where f_c is the cut-off frequency, δf is the transition width and f_N is the aforementioned Nyquist frequency. A similar behaviour to the one in the current filter can be obtained by setting $f_c = 0$ and $\delta f = 0.1 \text{ ticks}^{-1}$. The response of the resulting filter is also shown in Fig. 6.4 (blue solid line). Notice that the suppression of the stop-band is enhanced for this optimal filter. For comparison I included the power response of the filter obtained by taking the integer part of the coefficients resulting from the Parks-McClellan method (red dashed line). One can see that it does not suppress that much the stop-band, in a similar way to the current implementation of the filter.

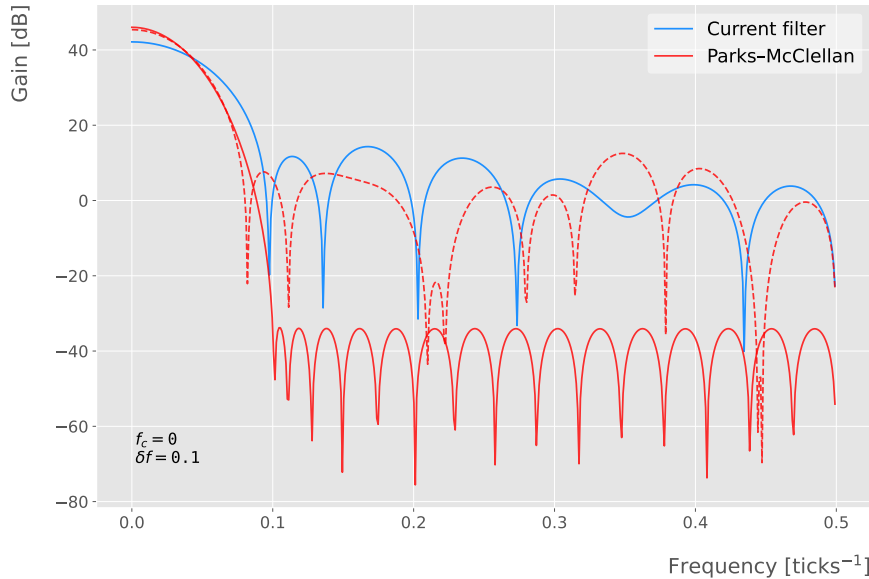


Figure 6.4: Power spectrum in decibels for the current implementation of the low-pass FIR filter in `dtp-firmware` (blue line), compared to the response of an optimal filter obtained using the Parks-McClellan algorithm for the same pass-band (red line). Also for comparison I include the spectrum of the optimal filter when taking only the integer part of the coefficients (red dashed line).

At this point, I tried to improve the performance of the FIR filter using the Parks-McClellan method, i.e. maximize the overall S/N, using the available data captures. I did so by varying the values of the two quantities that parametrize the pass-band and stop-band, the cut-off frequency f_c and the transition width δf .

Fig. 6.5 shows the average relative change in the S/N (i.e. the ratio between the value of the S/N after and before the filtering) for capture `felix-2020-07-17-21:31:44`,

6.3. Low-pass FIR filter design

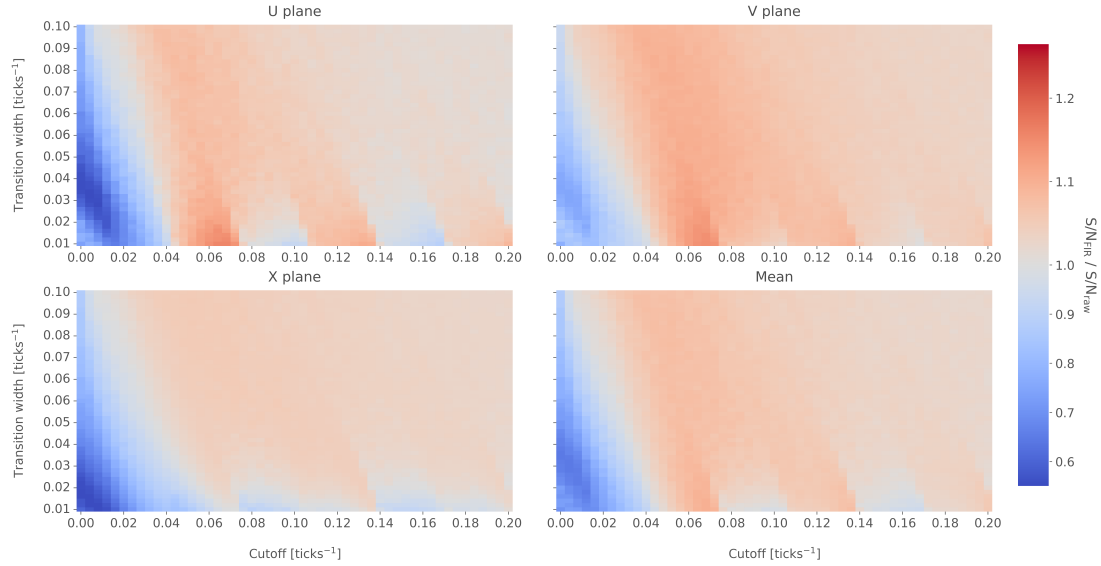


Figure 6.5: Relative change in the S/N for the ProtoDUNE-SP raw data capture `felix-2020-07-17-21:31:44`, using different values of the cutoff frequency f_c and the transition width δf . The optimal Chebyshev filters were applied using just the integer part of the coefficients given by the Parks-McClellan algorithm.

when using filters designed with the Parks-McClellan algorithm for the specified values of the cut-off frequency f_c and the transition width δf , restricted to integer values for the filter coefficients. One can clearly distinguish different regions where we get an improvement of up to a factor of 1.35 for the U plane. For large values of $f_c + \delta f$ the ratio tends to 1, as expected (in that limit the width of the stop-band goes to 0, meaning that no frequencies are filtered out and thus the waveform remains the same).

Using the configuration which gives the best mean performance for the three planes (see bottom right panel of Fig. 6.5), i.e. $f_c = 0.068 \text{ ticks}^{-1}$ and $\delta f = 0.010 \text{ ticks}^{-1}$, we can see how such filter affects the different channels. Fig. 6.6 shows the distribution of the S/N improvement values for all the channels in the raw ADC capture `felix-2020-07-17-21:31:44`, separated by wire plane, after the optimal Chebyshev filter was applied. One can see that there is a clear improvement for both U and V induction wire planes, obtaining a mean change of 1.25 and 1.30 for them respectively. However, in the case of the collection plane X the mean of this distribution is roughly 1, meaning that a good fraction of channels in that plane get a slightly worse S/N after the

Chapter 6. Matched Filter approach to induction wire Trigger Primitives

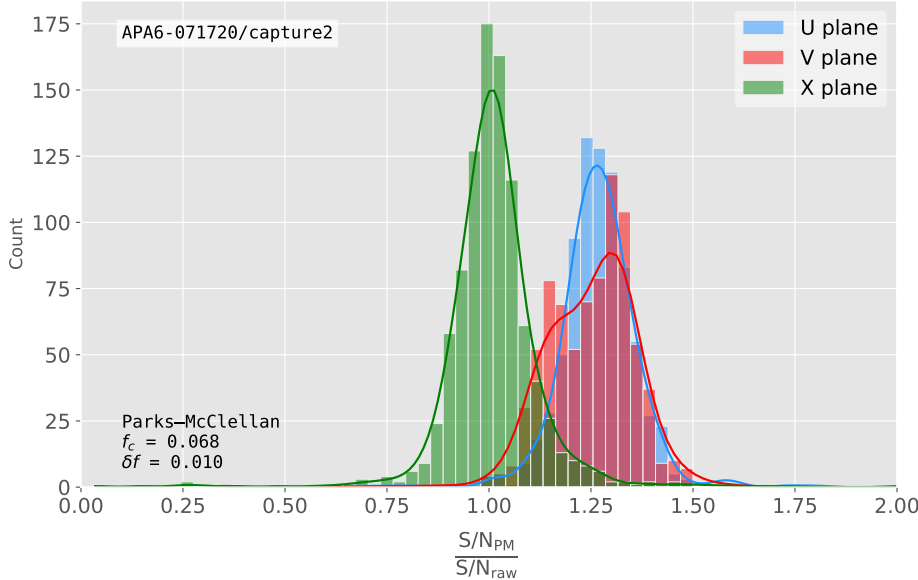


Figure 6.6: Distribution of the relative change of the S/N on the different wire planes from the ProtoDUNE-SP raw data capture *felix-2020-07-17-21:31:44* after the optimal Chebyshev filter was applied. The filter was computed with the Parks-McClellan algorithm using a cutoff of $f_c = 0.068 \text{ ticks}^{-1}$ and a transition width $\delta f = 0.010 \text{ ticks}^{-1}$.

filter is applied. In any case, this is not a big issue as the S/N for collection channels is usually much higher than the one for induction channels.

The results I obtained optimising the low pass filter with the Parks-McClellan method are promising. Nonetheless, the improvement found is rather marginal so I wondered if there could be an alternative approach to the filtering problem which yields better outputs. At this point, I found a possible alternative in matched filters. By construction, this kind of filters offer the best improvement on the S/N.

6.4 Matched filters

In the context of signal processing, a matched filter is the optimal linear filter for maximising the signal-to-noise ratio (S/N) in the presence of additive noise, obtained by convolving a conjugated time-reversed known template with an unknown signal to detect the presence of the template in the signal [54].

Given a known signal sequence $s(t)$ and another (a priori unknown) noise sequence

6.4. Matched filters

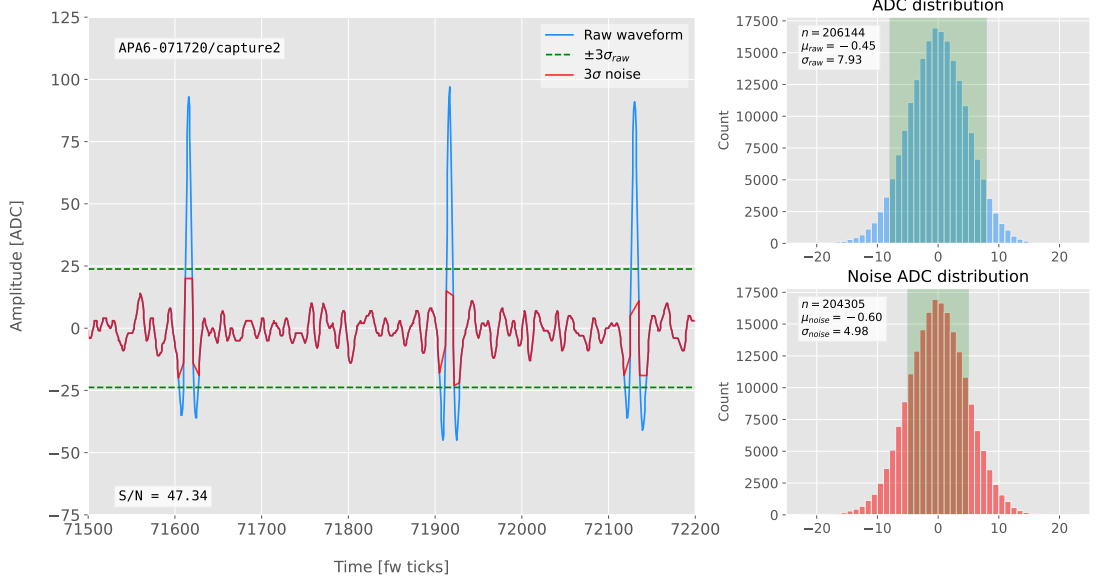


Figure 6.7: Left panel: Zoomed match filtered waveform corresponding to channel 7840 from the ProtoDUNE-SP raw data capture felix-2020-07-17-21:31:44 (blue line). The filter used was directly extracted from the data, being the 32 values around the first peak in the original waveform. The green dashed lines mark the region $\pm 3\sigma_{\text{raw}}$. The resulting noise waveform is also shown (red line). Top right panel: ADC distribution for channel 7840 after match filtering, where the green shaded region represents $\pm \sigma_{\text{raw}}$. Bottom right panel: noise ADC distribution for channel 7840 after match filtering, where the green shaded region represents $\pm \sigma_{\text{noise}}$

1306 $n(t)$, the input signal can be written as:

$$x(t) = s(t) + n(t). \quad (6.4)$$

1307 Now, considering a linear time-invariant filter, whose impulse-response function I
1308 will refer to as $h(t)$, one can write the output signal as:

$$\begin{aligned} y(t) &= x(t) * h(t) \\ &= (s(t) + n(t)) * h(t) \\ &= y_s(t) + y_n(t), \end{aligned} \quad (6.5)$$

1309 where $y_s(t)$ and $y_n(t)$ are simply the outputs of the filter due to the signal and the noise
1310 components respectively.

Chapter 6. Matched Filter approach to induction wire Trigger Primitives

1311 The goal of the matched filter is to detect the presence of the signal $s(t)$ in the input
 1312 sample $x(t)$ at a certain time t_0 , which effectively means we need to maximise the S/N.
 1313 This way, what one wants is to have a filter which gives a much bigger output when the
 1314 known signal is present than when it is not. Putting it in other words, the instantaneous
 1315 power of the signal output $y_s(t)$ should be much larger than the average power of the
 1316 noise output $y_n(t)$ at some time t_0 .

1317 For the case of the filtered signal, one can easily re-write it as an inverse Fourier
 1318 transform:

$$y_s(t) = \frac{1}{2\pi} \int_{-\infty}^{\infty} d\omega H(\omega)S(\omega)e^{i\omega t}, \quad (6.6)$$

1319 where $H(\omega)$ and $S(\omega)$ are the Fourier transforms of the impulse-response function (i.e.
 1320 the transfer function of the filter) and of the input signal, respectively.

1321 Now focusing on the noise, we can use the Wiener-Khinchin theorem [55] to write
 1322 the mean power of the noise after filtering as:

$$E|y_n(t)|^2 = \frac{1}{2\pi} \int_{-\infty}^{\infty} d\omega |H(\omega)|^2 S_n(\omega), \quad (6.7)$$

1323 where $S_n(\omega)$ is the power spectral density of the noise.

1324 Having these, one can write the instantaneous S/N at time t_0 as:

$$\begin{aligned} \left(\frac{S}{N} \right)_{t_0} &= \frac{|y_s|^2}{E|y_n(t)|^2} \\ &= \frac{1}{2\pi} \frac{\left| \int_{-\infty}^{\infty} d\omega H(\omega)S(\omega)e^{i\omega t_0} \right|^2}{\int_{-\infty}^{\infty} d\omega |H(\omega)|^2 S_n(\omega)}. \end{aligned} \quad (6.8)$$

1325 Once we have this expression, we need to find the upper limit of it to determine what
 1326 would be the optimal choice for the transfer function. One can use the Cauchy-Schwarz
 1327 inequality, which in the present case takes the form:

$$\left| \int_{-\infty}^{\infty} dx f(x)g(x) \right|^2 \leq \int_{-\infty}^{\infty} dx |f(x)|^2 + \int_{-\infty}^{\infty} dx |g(x)|^2, \quad (6.9)$$

6.4. Matched filters

1328 for any two analytical functions $f(x)$ and $g(x)$. One can prove that making the choice:

$$\begin{aligned} f(x) &= H(\omega) \sqrt{S_n(\omega)} e^{i\omega t_0}, \\ g(x) &= \frac{S(\omega)}{\sqrt{S_n(\omega)}}, \end{aligned} \quad (6.10)$$

1329 leads to the following upper bound for the S/N:

$$\left(\frac{S}{N} \right)_{t_0} \leq \frac{1}{2\pi} \int_{-\infty}^{\infty} d\omega \frac{|S(\omega)|^2}{S_n(\omega)}. \quad (6.11)$$

1330 From Eqs. (6.8), (6.9) and (6.10) one can also derive the form of the transfer function

1331 such that the upper bound is exactly reached [56]:

$$H(\omega) \propto \frac{S^*(\omega) e^{-i\omega t_0}}{S_n(\omega)}. \quad (6.12)$$

1332 From this last expression we can clearly see the way the matched filter acts. As the

1333 transfer function is proportional to the Fourier transform of the signal it will try to only

1334 pick the frequencies present in the signal [57].

1335 The matched filter transfer function can be greatly simplified if the input noise is

1336 Gaussian. In that case, the power spectral density of the noise is a constant, so it can be

1337 re-absorbed in the overall normalisation of the transfer function. Moreover, considering

1338 that the input signal is a real function, one can simply set $S^*(\omega) = S(-\omega)$, which gives:

$$H(\omega) \propto S(-\omega) e^{-i\omega t_0}. \quad (6.13)$$

1339 For a discrete signal, one can think of the input and impulse-response sequences as

1340 vectors of \mathbb{R}^N . Then, the matched filter tries to maximise the inner product of the signal

1341 and the filter while minimising the output due to the noise by choosing a filter vector

1342 orthogonal to the later. In the case of additive noise, that leads to the impulse-response

1343 vector:

$$h = \frac{1}{\sqrt{s^\dagger R_n^{-1} s}} R_n^{-1} s, \quad (6.14)$$

Chapter 6. Matched Filter approach to induction wire Trigger Primitives

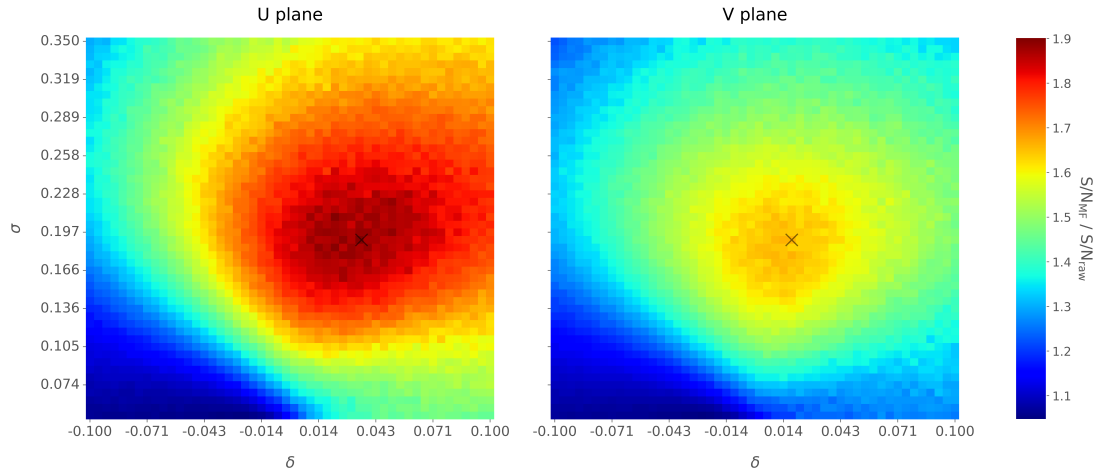


Figure 6.8: Relative improvement in the S/N for the raw data capture `felix-2020-07-17-21:31:44`, using the matched filter following the parametrisation in Eq. (6.17). The black crosses in both panels denote the location of the maximum ratio value.

1344 where s is a reversed signal template sequence of length N equal to the order of the filter
 1345 and R_n is the covariance matrix associated with the noise sequence n . For the Gaussian
 1346 noise case, the covariance matrix is simply the unit matrix, so the above expression
 1347 simplifies again to:

$$h = \frac{s}{|s|}. \quad (6.15)$$

1348 For this first stage of the study, I use a definition of the S/N per channel given by:

$$\text{S/N} = \frac{\max [ADC] - \mu_{noise}}{\sigma_{noise}}, \quad (6.16)$$

1349 where the subscript *noise* refers to a subset of the data obtained by only taking into
 1350 account waveform values within a $\pm 3\sigma$ range around the mean of the data and $\max [ADC]$
 1351 is the maximum of the original waveform. This definition is further discussed in App.
 1352 6.2, where I also show examples of its application to raw data and to a waveform filtered
 1353 with the current low-pass FIR filter.

1354 To test whether this choice of filter is appropriate one needs to choose a signal
 1355 template. As an example of how a matched filter would affect our signal, I simply took
 1356 the filter coefficients to be the 32 ADC values around a signal peak present in the data.

6.4. Matched filters

1357 In Fig. 6.7 (left panel) I plotted a zoomed region for channel 7840 in the raw data capture
1358 `felix-2020-07-17-21:31:44`, after applying the matched filter described before (blue
1359 line). When compared to the raw and FIR filtered case (see App. 6.2), after applying
1360 the match filter the standard deviation of the noise waveform (red line) decreases and at
1361 the same time the signal peaks are enhanced. This leads to an improvement of the S/N
1362 by a factor of 1.92 when compared to the raw waveform.

1363 In order to obtain the matched filter that is more suitable for our data, I explored
1364 different configurations of signal templates. In order to perform this exploration, I
1365 parametrised the signal using the bipolar function:

$$f(x) = -A(x + \delta) e^{-x^2/\sigma^2}, \quad (6.17)$$

1366 where the parameter δ controls the asymmetry between the positive and negative peaks
1367 and σ controls their width. The amplitude parameter A is set such that it keeps the
1368 height of the biggest peak to be less than 200 ADC in absolute value.

1369 As this parametrisation is only adequate for bipolar signals I will focus exclusively
1370 on the induction channels. Also, the optimal configurations I found for the U and V
1371 plane will be kept separate, i.e. I will have two sets of coefficients that will be applied to
1372 either the U and V planes of wires. I do so as I found this was the choice giving the
1373 best performance. Even so, as I will discuss, the differences are not very pronounced. In
1374 case it is not technically possible to separate channels in the firmware according to the
1375 wire plane they come from and use different sets of filter coefficients for them, we can
1376 just find a common unique set of coefficients. In such case, I do not expect our results
1377 to change dramatically.

1378 In Fig. 6.8 I present the results of our parameter scan, for channels in the induction
1379 planes U (left panel) and V (right panel). For each configuration of σ and δ the resulting
1380 matched filter was applied to all channels in the corresponding plane within the data
1381 capture `felix-2020-07-17-21:31:44`, the S/N improvement was computed with respect
1382 to the raw waveforms and then the S/N mean value was kept as a score for such filter.

Chapter 6. Matched Filter approach to induction wire Trigger Primitives

1383 One can see that the improvement obtained for the U plane is in general higher than the
1384 one for the V plane. In any case, I got substantially higher ratios than the ones obtained
1385 for the low-pass FIR filters. For the optimal configurations I attained improvements up
1386 to a factor of 1.85 for the U plane and 1.65 for the V plane.

1387 The sets of optimal matched filter coefficients were obtained for the parameters
1388 $\delta = 0.035$, $\sigma = 0.191$ for the U plane and $\delta = 0.018$, $\sigma = 0.191$ for the V plane. I
1389 show these two sets of coefficients in Fig. 6.9 (left panel). Also in Fig. 6.9 (right
1390 panel) I plot the distribution of the S/N improvement after the optimal match filters
1391 for the U and V were applied to the corresponding channels in the raw data capture
1392 `felix-2020-07-17-21:31:44`. As mentioned before, the mean improvement achieved
1393 for the U plane channels is slightly bigger than the one for the V channels. Note, however,
1394 that the spread of the distribution for the V plane is also smaller than the one for the U
1395 plane.

1396 I also performed a similar scan for the case of a low-pass FIR filter using the Parks-
1397 McClellan algorithm. In that case, the parameters to check were the cutoff frequency
1398 and the transition width of the filter. A summary of the results is given in App. 6.3.

1399 Overall, one can see that the improvements on the S/N are much more significant in
1400 the case of the matched filter than it is for the low-pass FIR filters. The analysis of this
1401 and other raw data captures from ProtoDUNE-SP suggest that matched filters increase
1402 the S/N of induction channels by a factor of 1.5 more than the optimal low-pass FIR
1403 filters.

1404 Although these results are by themselves great points in favour of the matched
1405 filter, more studies are needed to completely assess the robustness of this approach. I
1406 proceeded then to test the matched filter with simulated data samples.

1407 6.5 Using simulated samples

1408 In order to further test the matched filter, the next step was to generate and process
1409 data samples using *LArSoft* [58]. In this way, one can control the particle content of

6.5. Using simulated samples

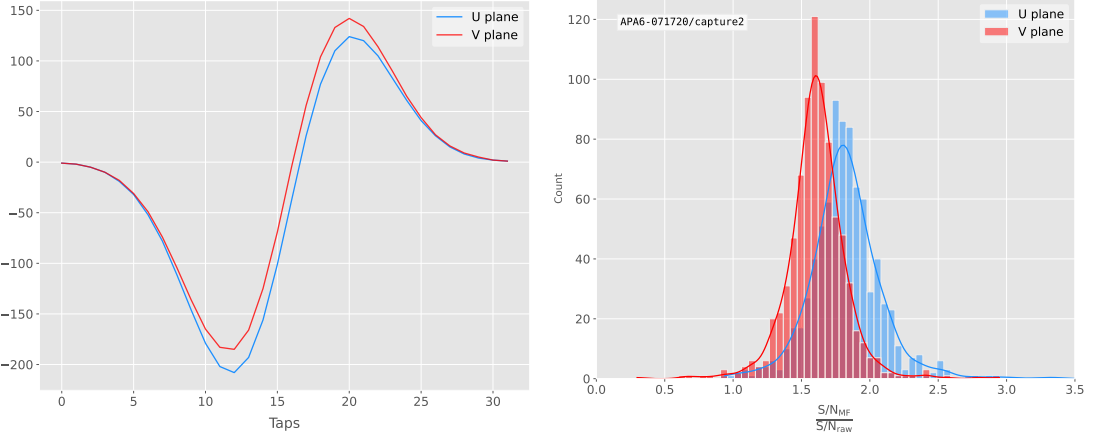


Figure 6.9: Left panel: Optimal matched filter coefficients for the U (blue line) and V (red line) planes. The filters were computed with our parametrisation in Eq. (6.17) for the parameter values $\delta = 0.035$, $\sigma = 0.191$ and $\delta = 0.018$, $\sigma = 0.191$ respectively. Right panel: Distribution of the relative change of the S/N on the two induction wire planes from the ProtoDUNE-SP raw data capture *felix-2020-07-17-21:31:44* after their respective optimal matched filters were applied.

1410 the samples, the orientation of the tracks and their energy, and therefore see how the
1411 matched filter behaves in various situations.

1412 To begin with, I prepared different monoenergetic and isotropic samples containing
1413 a single particle per event. Each sample contains a different particle species, namely
1414 electrons, muons, protons and neutral pions all with a kinetic energy of $E_k = 100$ MeV.
1415 I chose these because of the fairly different topologies they generate in the liquid argon,
1416 ranging from shower-like to track-like. The procedure I followed to generate the samples
1417 and process them is discussed in detail in App. ??.

1418 These were generated with the single particle gun and the Geant4 stage of the
1419 *LArSoft* simulation [58] was performed with the standard configuration for the DUNE
1420 FD 10kt module.

1421 For simplicity, I restricted the particles to start drifting in a single TPC volume
1422 (in this case TPC 0), so I can focus exclusively on the signals coming from one APA.
1423 The chosen kinetic energy for all the particles in my first trial is $E_k = 100$ MeV, so a
1424 necessary check is to see if all our tracks will be typically contained in one TPC volume.
1425 Fig. 6.10 (left panel) shows the distributions of the track lengths in the liquid argon

Chapter 6. Matched Filter approach to induction wire Trigger Primitives

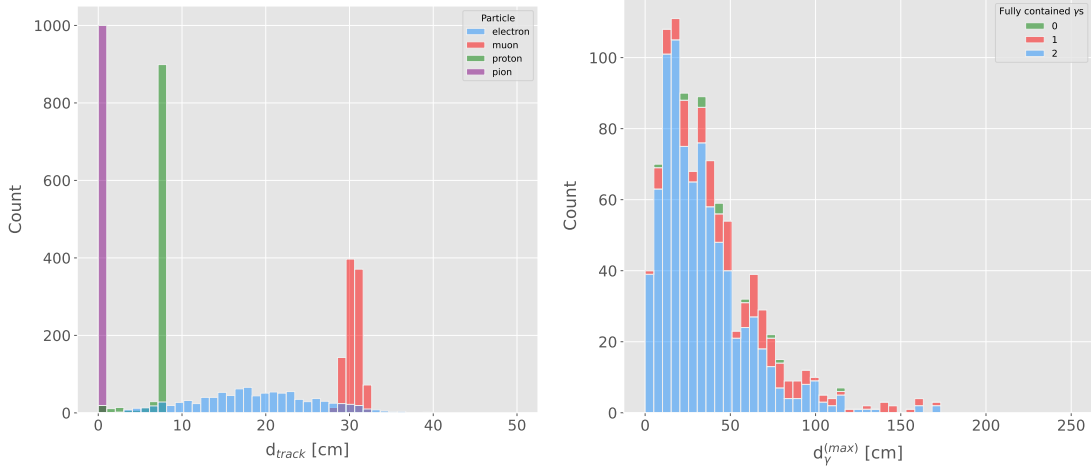


Figure 6.10: Left panel: distributions of the particles track length in the liquid argon for the generated $E_k = 100$ MeV monoenergetic samples, electrons (blue), muons (red), protons (green) and neutral pions (purple). Right panel: distribution of the length of the longest photon in the neutral pion sample after the decay process $\pi^0 \rightarrow \gamma\gamma$.

of all generated particles with $E_k = 100$ MeV. One can see that, in the case of the track-like particles (i.e. muons and protons), their length distributions are quite sharp and centered at relatively low distances (30 and 8 cm, respectively). For electrons, the distribution is quite broad but it does not extend past ~ 30 cm. The case of neutral pions can be misleading, as they decay promptly the track length associated with the true Monte Carlo particle is always < 1 cm. In Fig. 6.10 (right panel) I show the effective length distribution of the longest photon after the pion decays as $\pi^0 \rightarrow \gamma\gamma$, highlighting the number of fully contained photons in the TPC volume per event (either zero, one or both). One can see that the vast majority of events has both photons contained and that just a negligible number of them has none of them contained in the TPC volume. In any case, for the sake of caution, I will only keep the pion events with both photons contained.

Once I have prepared a sample at the Geant4 level, I need to process it through the detector simulation. In order to make adequate estimations of the noise levels and run the filtering and hit finder as I did with the ProtoDUNE data, one needs to turn off the default zero-suppression of the waveforms produced by the simulation. At this first stage I am only concerned with the waveforms with the noise added, so I keep the noise

6.5. Using simulated samples

addition option as true in the configuration. However, for studies related to the hit finder performance one will also need to store the noiseless waveforms in order to retrieve the truth information of the hits. I will discuss this approach next.

After the detector simulation stage, one needs to extract the no zero-suppressed noisy waveforms, along with their offline channel numbers, and store them in a certain format to be analysed later. To reduce the amount of data that will go for processing, I used the information from the Geant4 step of the simulation to select only the active channels, i.e. the channels where some ionisation electrons arrive. Moreover, as said previously, I only extract the waveforms from APA 0 and exclusively the ones coming from induction channels. The resulting ROOT file contains a tree with two branches, one containing the waveforms for each event and channel and the other with the corresponding offline channel numbers.

Finally, to extract the truth values for the orientation of the tracks and the energies of the particles I used a modified analysis module. This gives a ROOT file with a single tree, containing several branches with different information such as the components of the initial momentum of the particles, initial and final xyz location, track length, etc.

For the analysis of the resulting waveforms and truth values I used a custom set of Python libraries (available at [??]). Among other functionalities, these enable the user to read the ROOT files, export the raw data as pandas objects, apply the filters and compute the S/N of both the raw and filtered signals. So far, the default configuration for the filtering uses the set of optimal matched filter coefficients that I found using the ProtoDUNE data samples.

Additionally, for the analysis of the samples it was necessary to use two different reference frames, to study separately the signals coming from the U and V induction wire planes. As I am focussing on a single APA, the U and V wires have a different orientation in the yz plane. In the case of U wires, these are tilted 35.7° clockwise from the vertical (y direction), whereas the V wires are at the same angle but in the counter clockwise direction. Because of this, the best option is to deal with two new coordinate systems rotated by $\pm 35.7^\circ$ along the x axis, so the new y' and y'' directions are aligned with the

Chapter 6. Matched Filter approach to induction wire Trigger Primitives

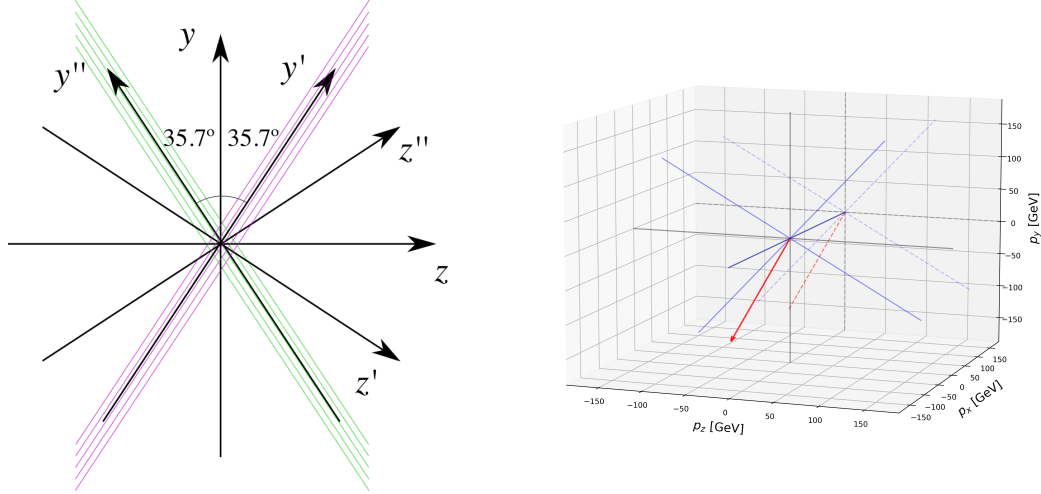


Figure 6.11: Left panel: schematic representation of the two new rotated reference frames used in this analysis (denoted as prime and double prime), viewed from the yz plane. The magenta stack of lines represent the wires in the U plane, whereas the green lines correspond to the wires in the V plane. Right panel: 3D representation of the momentum of one of the generated monoenergetic muons (red arrow) in the original reference frame (black lines), along with the new reference frame used for the U plane waveforms (blue lines). In the yz plane I added the projection of these three.

1472 U and V induction wires. Fig. 6.11 (left panel) shows a schematic representation of
 1473 the original reference frame together with the two rotated ones (denoted by primed and
 1474 double primed). This way, one can easily understand how parallel was a track to the
 1475 wires in the two induction planes. Fig. 6.11 (right panel) shows a 3D representation of
 1476 the momentum of a track (red arrow) in the original reference frame (black lines), along
 1477 with the new reference frame for U wires (blue lines). I added the projection in the yz
 1478 plane of this three, to show the usefulness of the new reference frame to tell whether a
 1479 track is parallel or normal to the wires in the induction plane.

1480 Fig. 6.12 shows the distribution of the average S/N improvement per event when one
 1481 applies the optimal matched filters. I produced separate distributions for the channels
 1482 in the U (red) and V (blue) induction wire planes. Notice that the S/N distributions
 1483 for the track-like particles, i.e. muons (top left panel) and protons (bottom left panel),
 1484 have significantly larger mean values than the distributions of the shower like particles,
 1485 i.e. electrons (top right panel) and neutral pions (bottom right panel). An important

6.5. Using simulated samples

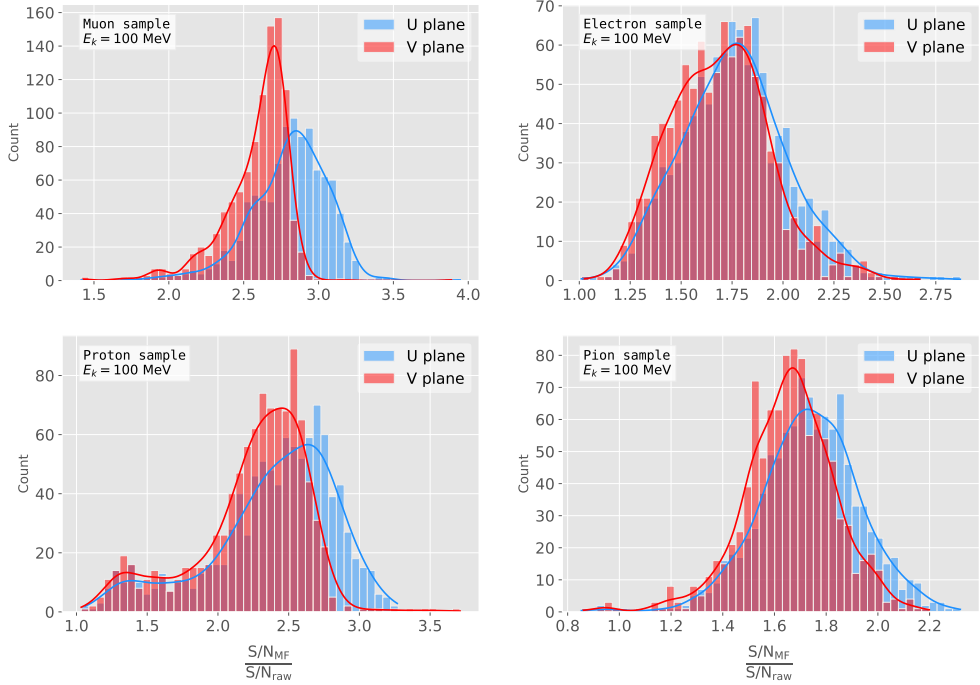


Figure 6.12: Distributions of the mean S/N improvement per event for the corresponding sample after applying the matched filters. Here I separated the change in the U plane (blue) and the V plane (red) channels. From top left to the right: muon, electron, proton and neutral pion. All the events have a fixed kinetic energy of $E_k = 100$ MeV.

difference between these results and the ones seen before for ProtoDUNE data is that, overall, the improvements that I get for simulated data are bigger. This could be due either to the default noise model used in the *LArSoft* simulation or to the simulated hits having higher energy than the ones in the recorded data. Nonetheless, the concluding message is that the previously optimised matched filters give an overall significant improvement of the S/N for the different samples.

About the convention I followed for the plots and results, in the case of the raw and filtered S/N of each event in the sample I simply took the average of the quantities over all the active channels in the event. That is, if a certain event has N_{chan} active channels these two quantities are computed as:

$$(S/N_{fir})_{event} = \frac{\sum_{i=0}^{N_{chan}} (S/N_{fir})_i}{N_{chan}},$$

$$(S/N_{raw})_{event} = \frac{\sum_{i=0}^{N_{chan}} (S/N_{raw})_i}{N_{chan}}.$$
(6.18)

Chapter 6. Matched Filter approach to induction wire Trigger Primitives

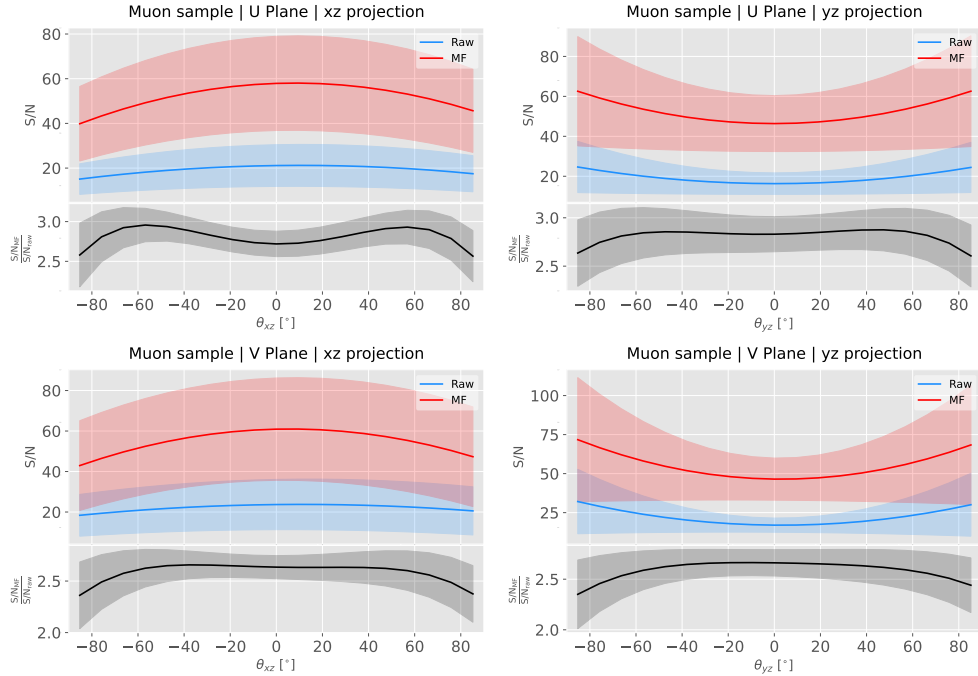


Figure 6.13: Angular dependence of the mean S/N and the S/N improvement, for the different monoenergetic samples considered (from top to bottom: electrons, muons, protons and neutral pions). The two columns on the left represent the values for the U plane waveforms. The top subplots show the mean S/N for raw (green) and filtered (red) waveforms whereas the bottom subplots depict the averaged S/N improvement (black).

1496 However, for the ratio of the raw and filtered S/N (what I called the S/N improvement)
 1497 per event I am not just taking the ratio of the previous two quantities but computing
 1498 the average of the individual ratios per channel in the event:

$$\left(\frac{S/N_{fir}}{S/N_{raw}} \right)_{event} = \frac{\sum_{i=0}^{N_{chan}} \left(\frac{S/N_{fir}}{S/N_{raw}} \right)_i}{N_{chan}}, \quad (6.19)$$

1499 and so:

$$\left(\frac{S/N_{fir}}{S/N_{raw}} \right)_{event} \neq \frac{(S/N_{fir})_{event}}{(S/N_{raw})_{event}}. \quad (6.20)$$

1500 6.5.1 Angular dependence

1501 Having these monoenergetic samples, one can also study the angular dependence of the
 1502 performance of the matched filter. This is an important point, as it is a well established
 1503 fact that for certain configurations (an extreme case configuration being signals normal

6.5. Using simulated samples

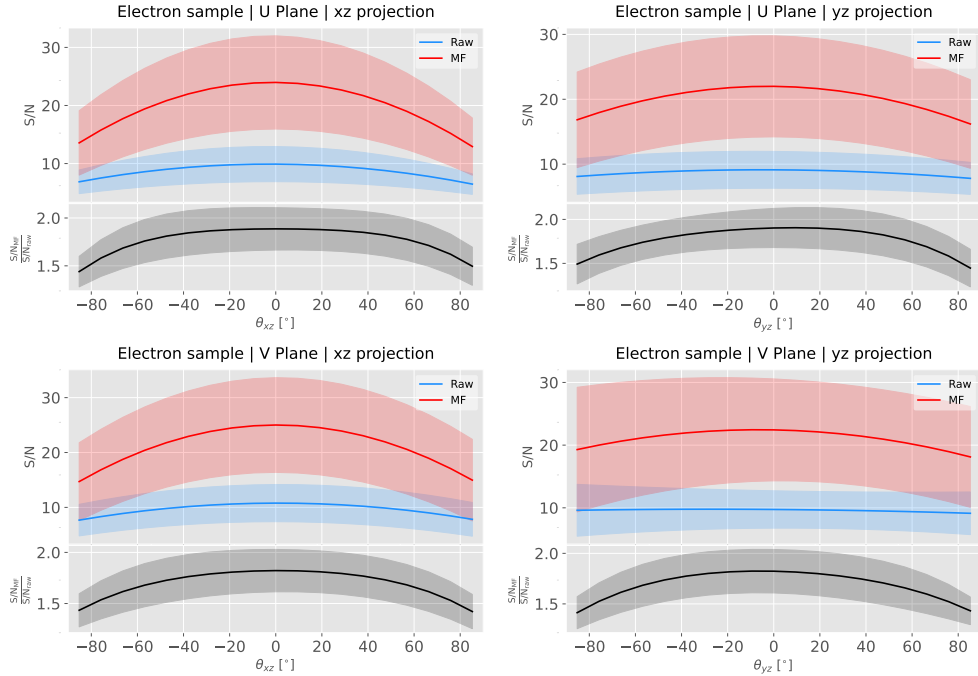


Figure 6.14: Angular dependence of the mean S/N and the S/N improvement, for the different monoenergetic samples considered (from top to bottom: electrons, muons, protons and neutral pions). The two columns on the left represent the values for the U plane waveforms. The top subplots show the mean S/N for raw (green) and filtered (red) waveforms whereas the bottom subplots depict the averaged S/N improvement (black).

1504 to the wire plane and perpendicular to the induction wires at the same time) the S/N is
 1505 much lower than average as the corresponding waveforms are severely distorted. In this
 1506 sense, I am interested to see how the matched filter behaves for these cases and how the
 1507 S/N improvement on those compare to the average.

1508 Fig. 6.13 shows the angular dependence of the S/N for the monoenergetic $E_k =$
 1509 100 MeV isotropic muons, for the different induction wire planes and projections. The
 1510 angles for each event are given by the components of the initial value of the momentum
 1511 of the particles, taking the angles of the projections on the xz and yz planes with respect
 1512 to the z axis (more accurately, one needs to compute these angles twice for each event, a
 1513 pair for the $xy'z'$ coordinate system and the other for the $xy''z''$). The top row shows the
 1514 dependence on the angles corresponding to the U plane, i.e. $\theta_{xz'}$ and $\theta_{y'z'}$, whereas the
 1515 bottom row shows the angular dependence viewed from the V plane, $\theta_{xz''}$ and $\theta_{y''z''}$. In
 1516 each plot, the top subplot represents the mean values of the S/N for the raw (blue) and

Chapter 6. Matched Filter approach to induction wire Trigger Primitives

1517 matched filtered (red) signals, and the bottom subplot the averaged S/N improvement
1518 (black). The solid lines represent the mean value obtained for the corresponding angular
1519 value, whereas the semitransparent bands represent one standard deviation around the
1520 mean at each point.

1521 As expected, the S/N is in general higher when tracks are parallel to the APA (i.e.
1522 $\theta_{xz} \sim 0$) and lower when it is normal to the plane ($\theta_{xz} \sim \pm 90^\circ$). In the same way, tracks
1523 parallel to the wires ($\theta_{yz} \sim \pm 90^\circ$) tend to have higher S/N than those perpendicular to
1524 these ($\theta_{yz} \sim \pm 0$).

1525 Fig. 6.14 shows the corresponding angular dependence information for the $E_k =$
1526 100 MeV electrons sample. Notice that, in this case, the S/N behaviour discussed above
1527 does not hold. A possible explanation can be that, because most hits in these events
1528 are produced by the secondary particles generated in the EM shower, the signal peaks
1529 whose S/N ratios were computed do not correspond to the directional information of
1530 the primary electron.

1531 6.5.2 Distortion and peak asymmetry

1532 As a little case of study, I selected two of the simulated $E_k = 100$ MeV monoenergetic
1533 muon events. With respect to the U induction plane, one is parallel to the APA (low
1534 $\theta_{xz'}$) and to the wires (high $\theta_{y'z'}$) and the other is normal to the APA plane (high $\theta_{xz'}$)
1535 and perpendicular to the wires (low $\theta_{y'z'}$). As expected from the results on the angular
1536 dependence discussed above, the former has a higher S/N (before and after the filtering)
1537 when compared to the latter. An interesting thing to notice about these two samples
1538 is that, even though one has a much bigger S/N than the other, it is the one with the
1539 smallest S/N the one that got the biggest averaged S/N improvement. In Table 6.1
1540 I included all the relevant parameters of these two $E_k = 100$ MeV muon events I am
1541 considering, namely, the angles with respect to the $xy'z'$ reference frame, the values of
1542 the S/N, the S/N improvement and also the so-called peak asymmetry Δ_{peak} that I will
1543 discuss next.

1544 One can try to understand better what is going on with these two events by looking

6.5. Using simulated samples

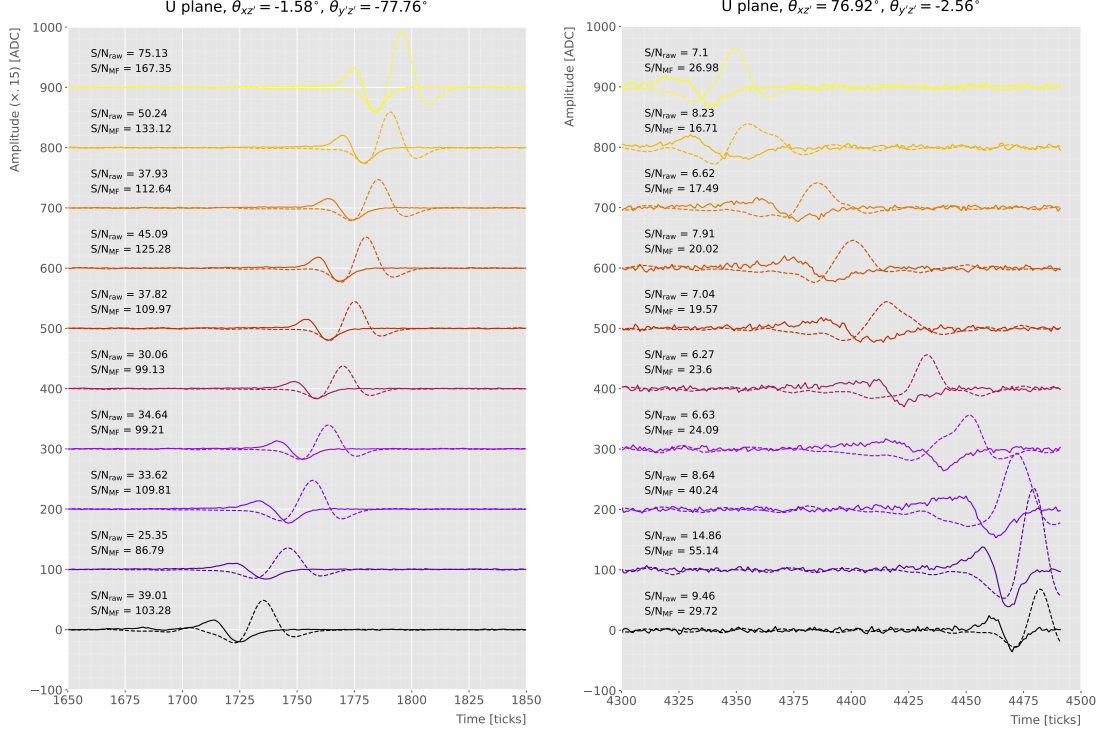


Figure 6.15: Selected consecutive waveforms corresponding to two monoenergetic $E_k = 100$ MeV muon events, one is parallel to the APA and to the wires in the U plane (left panel) and the other is normal to the APA plane and perpendicular to the U plane wires (right panel). The solid lines represent the raw waveforms whereas the dashed lines correspond to the waveforms after the matched filter was applied. The waveforms on the left panel have been scaled by a factor of 0.15 to have similar amplitude to the ones on the right panel.

Table 6.1: Characteristic parameters of the two monoenergetic muon events selected, relative to the U plane: projected angles in the xz' and $y'z'$ planes, S/N values for the raw and filtered waveforms, mean improvement of the S/N and peak asymmetry.

	$\theta_{xz'} (\circ)$	$\theta_{y'z'} (\circ)$	S/N _{raw}	S/N _{MF}	$\frac{S/N_{MF}}{S/N_{raw}}$	Δ_{peak} (ADC)
High ("parallel")	-1.58	-77.76	41.65	112.44	2.83	-35.73
Low ("normal")	76.92	-2.56	8.07	25.46	3.12	-10.38

at the raw and filtered data from some of their active channels. Fig. 6.15 shows a selection of consecutive raw and filtered U plane waveforms from the event with high S/N (left panel) and the one with low S/N (right panel). Notice that to show both collections of waveforms at a similar scale I had to apply a factor of 0.15 to the waveforms with high S/N. Additionally, next to each waveform I included the values of the raw and

Chapter 6. Matched Filter approach to induction wire Trigger Primitives

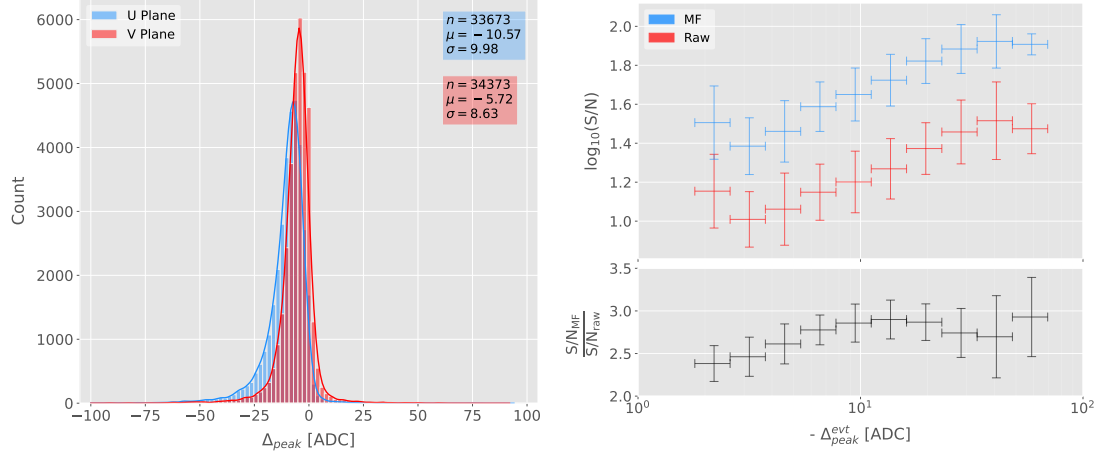


Figure 6.16: Left panel: peak asymmetry distribution for the case of the monoenergetic $E_k = 100$ MeV muon sample. Each value corresponds to a single bipolar signal peak from a channel in any event. The blue distribution represents the peaks on U plane channels, whereas the red corresponds to signal peaks in V wires. Right panel: relation between the mean peak asymmetry per event with the S/N for U channel waveforms from the $E_k = 100$ MeV muon sample. The top subplot shows the decimal logarithm of the mean S/N for the raw (red) and the matched filtered (blue) waveforms. The bottom subplot contains the mean S/N improvement ratio after the matched filter was applied.

1550 matched filtered S/N for the corresponding channel. The first thing to notice in this plot
 1551 is that the amplitude of the signal peaks from the normal track have a much smaller
 1552 amplitude, and also appear quite distorted when compared to the others. On the other
 1553 hand, although the matched filtered S/N is still smaller, the relative improvement is
 1554 bigger than in the parallel case.

1555 A way I found to quantify the difference between the shapes within these two events
 1556 is their different peak asymmetry. One can define the peak asymmetry as the (signed)
 1557 difference between the positive and the negative peaks of the bipolar shape, i.e.:

$$\Delta_{peak} \equiv h_+ - h_-, \quad (6.21)$$

1558 where both heights h_+ and h_- are positive defined. Fig. 6.16 (left panel) shows the
 1559 distribution of this peak asymmetry for all the waveforms corresponding to channels
 1560 in the U (blue) and V (red) planes for the monoenergetic muon sample. One can
 1561 see that these distributions are clearly shifted to negative values (with mean values

6.5. Using simulated samples

1562 $\mu_{\Delta}^U = -10.57$ ADC and $\mu_{\Delta}^V = -5.72$ ADC respectively). It is interesting to notice
1563 that the peak asymmetry value of the sample with high S/N sits at the left tail of the
1564 distribution whereas the corresponding value of the sample with low S/N lies around
1565 the mean.

1566 Now, one can try to correlate the peak asymmetry with the S/N and the S/N change
1567 per event. Fig. 6.16 (right panel) shows the result of comparing (minus) the mean
1568 peak asymmetry per event to the averaged raw (red) and matched filtered (blue) S/N
1569 per event (top subplot). The horizontal lines sit at the mean value obtained in the fit
1570 and represent the width of the $-\Delta_{peak}$ bins used, while the vertical lines indicate one
1571 standard deviation around that mean value. Notice that, when taking decimal logarithm
1572 on both, there is an approximate linear relation between these quantities, except for
1573 peak asymmetry values bigger than -5 ADC where the S/N remains constant.

1574 Also, in the bottom subplot of Fig. 6.16 (right panel) I show the relation between
1575 the peak asymmetry and the mean S/N improvement. In this case, one see that there is
1576 a maximum at $\Delta_{peak} \sim -10$ ADC. As mentioned previously, this is also the value of the
1577 mean of the peak asymmetry distribution. In fact, it is expected that our filter favours
1578 the signal peaks with the most common values of the peak asymmetry, as this was one
1579 of the features I target in our filter coefficient optimisation through the parameter δ .

1580 These results suggest that events with poorer values of the mean S/N, usually
1581 associated to non-favourable track orientations, tend to have smaller values of the mean
1582 peak asymmetry (in absolute value). Nonetheless, because our matched filters have
1583 been optimised to account for these asymmetries, the improvement on the S/N for these
1584 events is sizeable if not better than the one for events which already had a high S/N.

1585 6.5.3 Hit sensitivity

1586 One of the advantages of the matched filter, directly related to increasing the S/N, is
1587 the capability of picking hits that before fell below the threshold. For instance, Fig. 6.17
1588 shows the raw ADC data from an example event (electron, $E_k = 100$ MeV) with the
1589 produced true hits superimposed (black boxes), together with the hits produced by the

Chapter 6. Matched Filter approach to induction wire Trigger Primitives

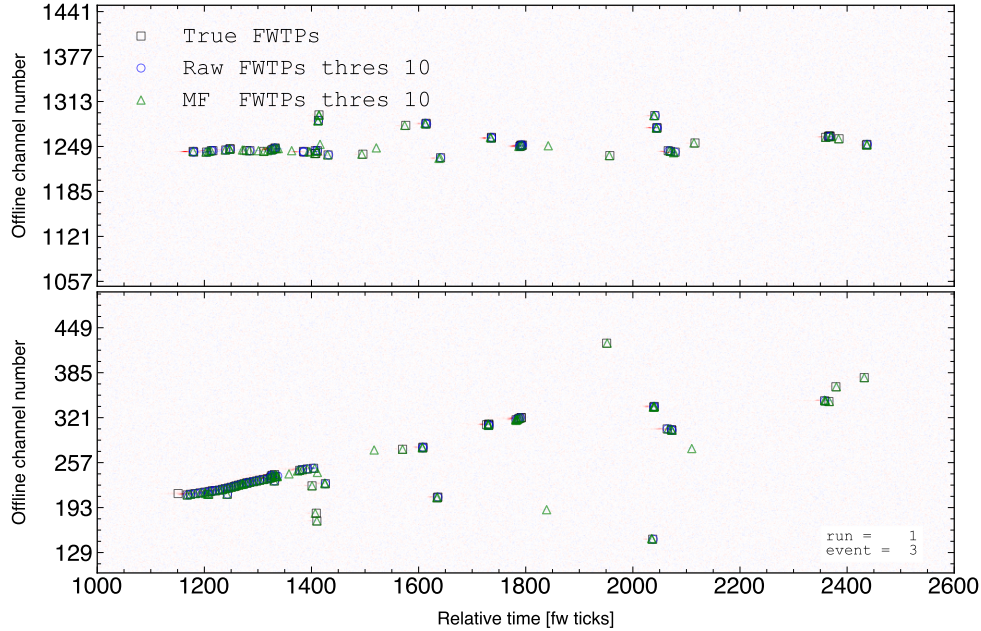


Figure 6.17: Raw data display in the plane time (in firmware ticks) vs. offline channel number for an $E_k = 100$ MeV electron event. The produced true hits are superimposed (black boxes) as well as the hits coming from the standard hit finder chain (blue circles) and the hit finder using the matched filter (green triangles).

standard hit finder chain (blue circles), i.e. using the current FIR filter, and the hits obtained using the matched filters (green triangles). Both the standard and the matched filter hit finders were run with a threshold of 10 ADC. Notice that the standard hits match well the true ones at the initial part of the event (where we have a track-like object), but they miss most of the hits produced by the EM shower at later times. On the other hand, the hits produced with the matched filter have a better agreement with the true hits even for the more diffuse shower activity.

Notwithstanding that now I get more hits with this combination of matched filter and low threshold as a results of the enhancement of the signal peaks relative to the noise level, it is also true that I pick some spurious hits not related to any real activity if one lowers the thresholds too much. Therefore, some optimisation of the threshold is needed. Basically one will need to make a trade-off between precision and sensitivity.

Having this in mind, I tried to compare the produced hits one gets from the standard hit finder and the ones resulting from applying the matched filter with the true hits.

6.5. Using simulated samples

1604 By running the hit finders on our samples with different values of the threshold one
1605 can understand, for instance, how low one can set the threshold without getting mostly
1606 spurious hits and then evaluate the gains obtained from this.

1607 Because now I am also interested in seeing how the hit sensitivity changes with the
1608 energy, I prepared new isotropic samples with the same types of particles as before
1609 (muons, electrons, protons and neutral pions) but with a flat kinetic energy distribution
1610 ranging from 5 to 100 MeV.

1611 In order to estimate the hit sensitivity, given a certain sample, one needs to recover
1612 the set of true hits to be able to compare these with the ones produced. To do so,
1613 a modification in the procedure I was using to extract the raw waveforms is needed.
1614 For this kind of study I run the detector simulation in two steps, first I produce the
1615 waveforms without noise and extract them in the same format I used for the raw data,
1616 then the noise is added and the noisy waveforms are then written to a file as well.

1617 To have a better comparison between the true hits and the ones produced from
1618 the raw waveforms after applying the two filters, I applied also the FIR filter and the
1619 matched filters to the noiseless waveforms and then I run the hit finder with a minimal
1620 threshold (in this case I used 1 ADC) on these noiseless filtered waveforms. In this way
1621 I generated two sets of true hits, I will refer to them as standard true hits (with the
1622 current/default FIR filter) and matched filter true hits respectively. This allows a more
1623 precise matching between the different groups of hits produced, as it will account for
1624 any delays and distortions introduced by the FIR and the matched filters.

1625 In the case of the raw waveforms (with noise), I run the hit finder on them, with
1626 different values of the threshold, after applying either the FIR or the matched filters. I
1627 will name them simply standard hits and matched filter hits respectively. Then, I match
1628 the generated hits to the true hits (the standard hits with the standard true hits and
1629 the matched filter hits with the matched filter true hits). The matching is performed by
1630 comparing the channel number and the timestamp of the hits. To count as a match,
1631 I require that all hits with the same channel number and timestamp have overlapping
1632 hit windows, i.e. the time windows between their hit end and hit start times need to

Chapter 6. Matched Filter approach to induction wire Trigger Primitives

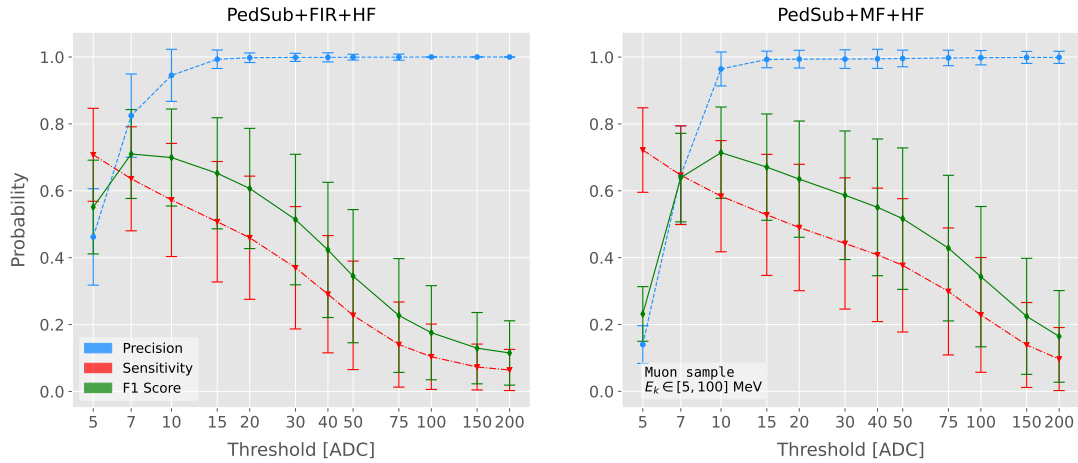


Figure 6.18: Dependence of the precision (blue), sensitivity (red) and F_1 (green) scores on the threshold values used in the hit finder, for the FIR (left panel) and matched filter (right panel) cases. The results were obtained after matching the hits to the true hits in the case of the isotropic muon sample with kinetic energy in the range 5 to 100 MeV, taking only into account the induction plane channels. The points represent the mean value while the error bars indicate one standard deviation around that mean value.

overlap. If more than one hit in one of the groups have hit overlap with the same hit in the other group I only count the hit with closer hit peak time value.

The generation of the samples, the procedure to produce the standard hits (with the default FIR filter) and matched filter hits and the matching of these with the true hits is described in detail in App. ??.

To quantify the performance of the two hit finder approaches, I use a classical method from statistical classification known as confusion matrix [59]. This is basically a way of sorting the outputs of a binary classifier, considering the true values of the classification and the predicted values. It divides the outputs in four categories: true positive (TP, both true and predicted values are 1), false negative (FN, true value is 1 but predicted is 0), false positive (FP, true value is 0 but predicted is 1) and true negative (TN, both true and predicted values are 0)).

The contents of the confusion matrix allow us to compute other derived scores to judge the performance of our classifiers. In this study, I will make use of three of these

6.5. Using simulated samples

1647 metrics, namely the precision or positive predictive value:

$$\text{PPV} = \frac{\text{TP}}{\text{TP} + \text{FP}}, \quad (6.22)$$

1648 the sensitivity or true positive rate:

$$\text{TPR} = \frac{\text{TP}}{\text{TP} + \text{FN}}, \quad (6.23)$$

1649 and the F_1 score [60]:

$$F_1 = \frac{2\text{TP}}{2\text{TP} + \text{FP} + \text{FN}}, \quad (6.24)$$

1650 which is the harmonic mean of the precision and the sensitivity.

1651 In our specific case I am not going to make use of the true negative value, as its
1652 definition in this context can be ambiguous because one does not have clear instances in
1653 the classification process. This way, I will only count the number of true positives as the
1654 total amount of hits I can match between true and raw populations, the number of false
1655 negatives will be the number of missing true hits and the false positive the number of
1656 hits which do not match any true hit.

1657 In Fig. 6.18 I show the precision (blue), sensitivity (red) and F_1 (green) scores I
1658 obtained for different values of the threshold used in the hit finder for the case of the
1659 muon sample. Because the matched filters are only applied to induction channels, I only
1660 consider here hits coming from the U and V planes. The panel on the left corresponds
1661 to the scores I got when I ran the hit finder on the FIR filtered waveforms, whereas the
1662 right panel contains the scores for the matched filter case. The points are centered at
1663 the threshold value used and represent the mean value obtained for each score using all
1664 the generated events, while the error bars indicate one standard deviation around the
1665 mean value.

1666 One can see that the precision for the matched filter case is lower when the thresholds
1667 are very low, as the noise baseline is slightly amplified, but then rises to high values
1668 quicker than for the FIR case. The other difference one can spot is that the sensitivity

Chapter 6. Matched Filter approach to induction wire Trigger Primitives

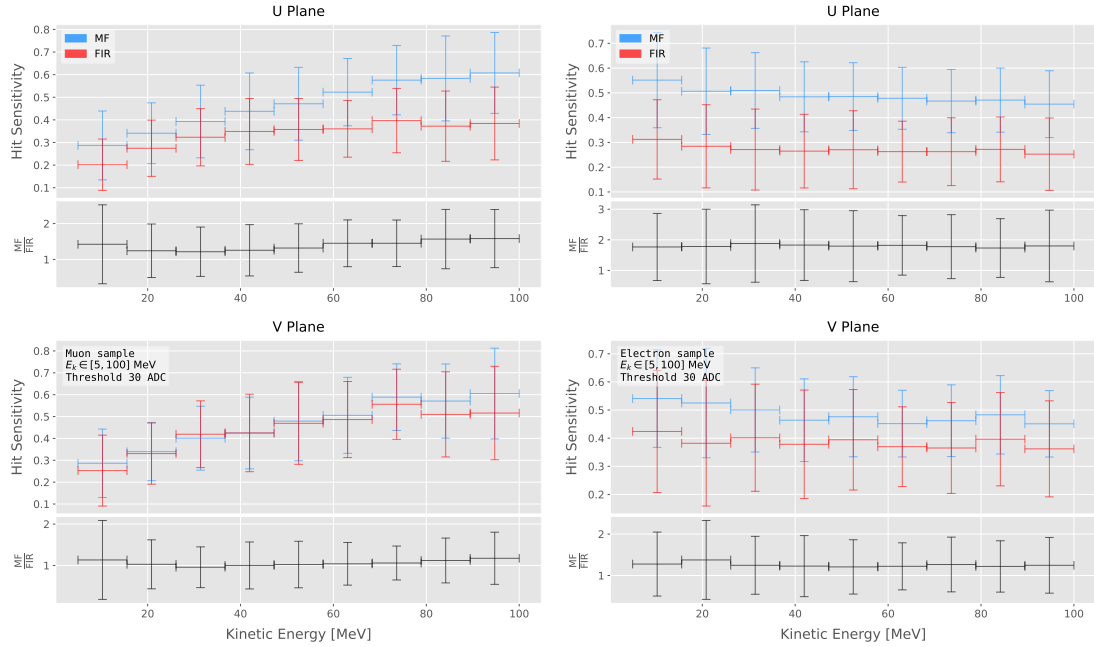


Figure 6.19: Dependence of the averaged hit sensitivity on the kinetic energy of the events for the matched filter (blue) and standard (red) hits, for the case of the muon (left panel) and electron (right panel) samples, separated between U (top plots) and V (bottom plots) induction wire planes. The top subplots contain the hit sensitivities for the two hit finder alternatives, while the bottom subplots show the ratio between the two. The horizontal lines sit at the mean value and represent the size of the energy bins, while the vertical error bars indicate one standard deviation around that mean value.

in the FIR case starts dropping faster at around the same threshold values where the precision stabilizes around 1, while in contrast for the matched filter this rapid decrease starts at higher threshold values. A similar scan for the same thresholds was performed for the electron sample in the same energy range, yielding similar results.

In Fig. 6.19 I show the averaged hit sensitivity versus the kinetic energy of the events, both for the matched filter hits (blue) and the standard hits (red). The left panel corresponds to the muon sample, whereas the one on the right corresponds to the electron sample, both with kinetic energies between 5 and 100 MeV. In each panel the top plot corresponds to hits in the U plane, while the bottom plot contains the same information for the V plane. Each plot contains two subplots, the one on the top shows the hit sensitivity values for the matched filter and standard hits separate, while the bottom subplot depicts the ratio between the matched filter and standard sensitivities.

6.5. Using simulated samples

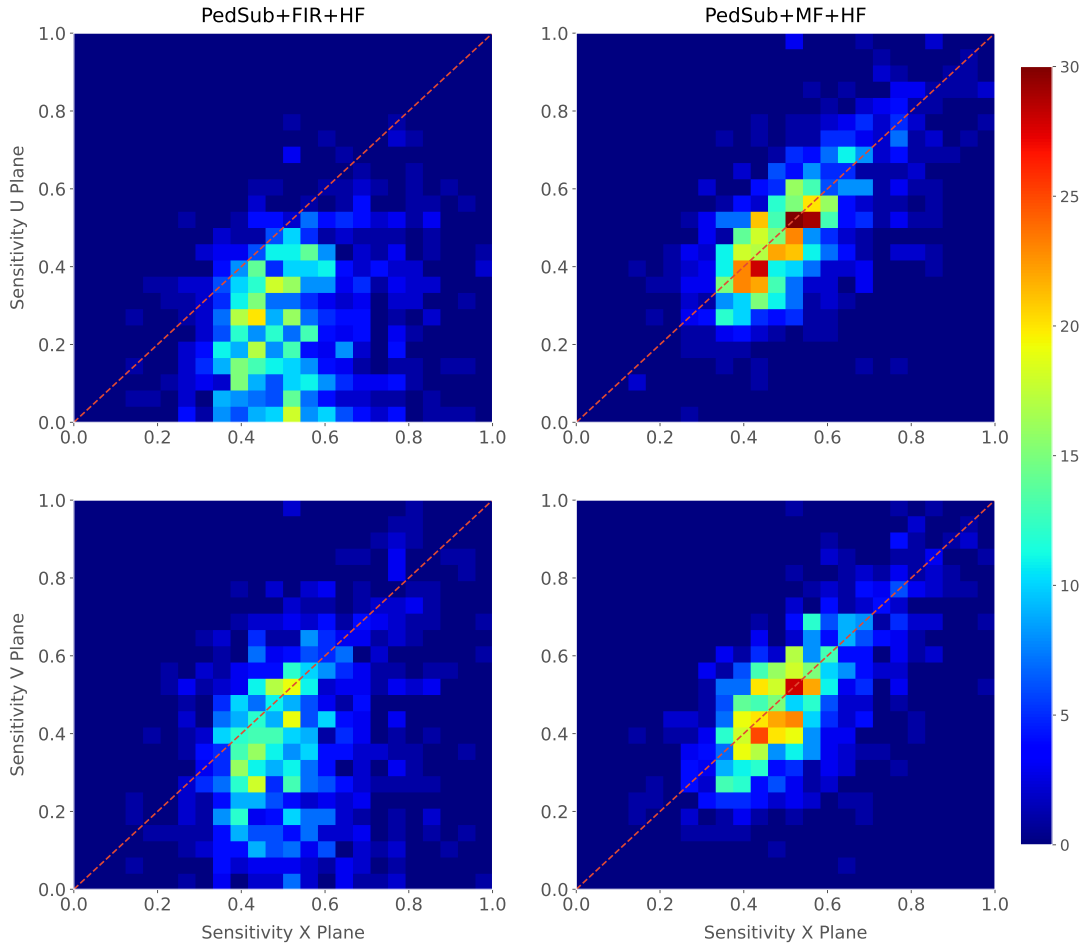


Figure 6.20: Distributions of the hit sensitivity in the U (top panels) and V (bottom panels) planes versus the hit sensitivity in the X plane, both for the standard hits (left panels) and the matched filter hits (right panels), in the case of the electron sample and a threshold of 30 ADC.

1681 The horizontal lines are placed at the mean value obtained in the fit and represent the
 1682 width of the E_k bins used, while the vertical error bars indicate one standard deviation
 1683 around that mean value. In both cases the threshold used was 30 ADC, as I required
 1684 the precision to be higher than 0.99 for both matched filter and standard cases.

1685 One can see that, in general, the improvements are better for the U than for the V
 1686 plane. While for the U channels I achieved a mean improvement of 50% and 80% for
 1687 muons and electrons respectively, the improvement in the V plane is stalled at 10% and
 1688 25%. Nevertheless, if I look at the sensitivities for the matched filter hits in both planes
 1689 one can see these have similar mean values for each energy bin, while on the contrary

Chapter 6. Matched Filter approach to induction wire Trigger Primitives

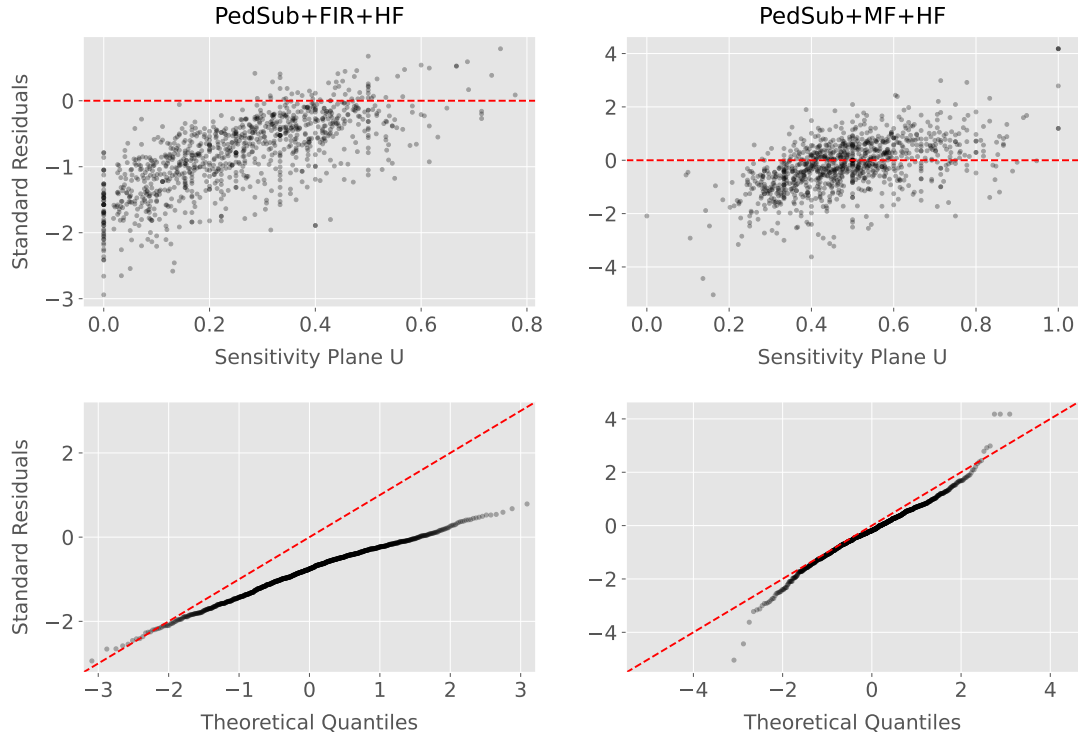


Figure 6.21: Top panels: standard residual plots of the hit sensitivities between the X and U planes. Bottom panels: quantile-quantile plots of the hit sensitivity standard residuals between the X and U planes. In all cases, the left panel corresponds to the standard hits while the right panel represents the matched filter case, all from the electron sample with a 30 ADC threshold.

for the standard hits the sensitivity remains relatively high for the V plane. This way, it looks there was a less significant gain because the hit sensitivity was already high.

Another interesting observation is the different behaviors for muons and electrons. While hit sensitivity for muons grows significantly with energy, in the case of electrons this slightly decreases the higher the kinetic energy of the event is. In any case, when it comes to the improvement on the sensitivities, this remains almost constant in all cases.

Furthermore, we can look at how the concurrence of hits between the different wire planes has changed. For any given event, I expect to have a similar number of hits in the three planes. As the ionisation electrons need to cross the U and V planes prior to reach the collection plane X they will induce current in those wire planes. A way to check the concurrence of hits across planes is looking at the relation between the hit sensitivities for each individual event. One cannot expect the sensitivities to be exactly equal across

6.5. Using simulated samples

1702 planes, but ideally they should be normally distributed around the diagonal.

1703 Fig. 6.20 shows the hit sensitivity in the U (top panels) and V (bottom panels)
1704 planes versus the hit sensitivity in the X plane, for the case of the standard hits (left
1705 panels) and the matched filter hits (right panels). All plots were generated for the
1706 electron sample and a threshold of 30 ADC. From these one can see a clear trend,
1707 when I use the standard hit finder chain the sensitivities in the induction planes are
1708 systematically lower than the hit sensitivity in the X plane, i.e. most of the points sit
1709 below the diagonal (red dashed line). In contrast, when the matched filters are applied,
1710 the majority of the events are distributed around the diagonal. This points out that the
1711 concurrence of hits across planes has improved.

1712 To exemplify the improvement I obtained, one can consider the residuals of the hit
1713 sensitivities for the X and U planes. Assuming the diagonal hypothesis, i.e. given a
1714 dataset of the form (x, y) for any x I take the predicted y value to be equal to the value
1715 of x , I can compute the standard residuals for the hit sensitivities in U given the ones for
1716 X. In Fig. 6.21 (top panels) I show these standard residuals against the corresponding
1717 values of the hit sensitivity in the U plane, for our electron sample with kinetic energy
1718 between 5 and 100 MeV. If I compare the scatter points in the case of the standard
1719 hits (left panel) and the matched filter hits (right panel), I see that the residuals of the
1720 standard hit finder case follow a certain pattern and their mean deviates from 0.

1721 To see clearly if the residuals are normally distributed, in Fig. 6.21 (bottom panels)
1722 I plot the corresponding quantile-quantile plot for both the standard (left panel) and
1723 matched filter (right panel) standard residuals. One can clearly see that the points for
1724 the standard case follow a strongly non-linear pattern, suggesting that the residuals
1725 do not follow a normal distribution. In contrast, for the matched filter hits the points
1726 conform to a roughly linear path, implying that in this case the normality condition is
1727 fulfilled.

1728 All these results hint at the fact that the concurrence of hits across the wire planes
1729 can be strengthened by applying the matched filters.

₁₇₃₀ **Chapter 7**

₁₇₃₁ **DM searches with neutrinos from
₁₇₃₂ the Sun**

₁₇₃₃ **7.1 Motivation**

₁₇₃₄ The idea of detecting neutrino signals coming from the Sun’s core to probe DM is not new.
₁₇₃₅ The main focus of these searches has usually been high-energy neutrinos originated from
₁₇₃₆ DM annihilations into heavy particles [61–64], although recent studies have proposed to
₁₇₃₇ look at the low-energy neutrino flux arising from the decay of light mesons at rest in the
₁₇₃₈ Sun [65–68] previously thought undetectable.

₁₇₃₉ In this chapter I try to demonstrate the capability of DUNE to constrain different
₁₇₄₀ DM scenarios. I used the neutrino fluxes arising from DM annihilations in the core
₁₇₄₁ of the Sun to compute the projected limits that DUNE would be able to set on the
₁₇₄₂ annihilation rates in the Sun and the DM scattering cross sections.

₁₇₄₃ **7.2 Gravitational capture of DM by the Sun**

₁₇₄₄ The Sun and the centre of the Earth are possible sources of DM annihilations, specially
₁₇₄₅ interesting because of their proximity. Their gravitational attraction ensured the capture
₁₇₄₆ of DM from the local halo through repeated scatterings of DM particles crossing them.

Chapter 7. DM searches with neutrinos from the Sun

1747 Only neutrinos produced from DM annihilations can escape the dense interior of these
1748 objects. Therefore, neutrino telescopes are the most useful experimental layouts to
1749 pursue DM searches from their cores.

1750 The neutrino flux from DM annihilations inside the Sun depends on the DM capture
1751 rate, which is proportional to the DM scattering cross section, and the annihilation rate,
1752 which is proportional to the velocity-averaged DM annihilation cross-section. The total
1753 number of DM particles inside the Sun follows the Boltzmann equation [65]:

$$\frac{dN_{DM}}{dt} = C_{\odot} - A_{\odot} N_{DM}^2, \quad (7.1)$$

1754 where C_{\odot} and A_{\odot} are the total Sun DM capture and annihilation rates respectively.
1755 In this expression I neglected the evaporation term, proportional to N_{DM} , which only
1756 contribute for $m_{DM} \lesssim 4$ GeV [69]. As the current threshold of neutrino telescopes is
1757 a few GeV, this region falls below the probed range but can be important in future
1758 low-energy projects.

1759 This equation has an equilibrium solution:

$$N_{DM}^{eq} = \sqrt{\frac{C_{\odot}}{A_{\odot}}}, \quad (7.2)$$

1760 which represents the amount of DM inside the Sun if the capture and annihilation have
1761 reached equilibrium. As the Sun is approximately 4.6 Gyr old, it is usually assumed that
1762 equilibrium has been achieved. Therefore, the anomalous neutrino flux from the Sun
1763 would only depend on the DM scattering cross section, enabling us to set limits on this
1764 quantity. If one does not assume equilibrium, some assumptions on the DM annihilation
1765 cross section are necessary to extract predictions from neutrino signals.

1766 Here, I am going to consider three possible scenarios for the DM interactions: DM
1767 scattering off electrons, spin-dependent (SD) and spin-independent interactions off nuclei.
1768 For the case of these last two, the cross sections will be given in terms of the SD and
1769 SI elastic scattering DM cross section off protons (assuming that DM interactions off

7.2. Gravitational capture of DM by the Sun

1770 protons and neutrons are identical), σ_p^{SD} and σ_p^{SI} , as [4, 65]:

$$\sigma_i^{\text{SD}} = \left(\frac{\tilde{\mu}_{A_i}}{\tilde{\mu}_p} \right)^2 \frac{4(J_i + 1)}{3J_i} |\langle S_{p,i} \rangle + \langle S_{n,i} \rangle|^2 \sigma_p^{\text{SD}}, \quad (7.3)$$

$$\sigma_i^{\text{SI}} = \left(\frac{\tilde{\mu}_{A_i}}{\tilde{\mu}_p} \right)^2 A_i^2 \sigma_p^{\text{SI}}, \quad (7.4)$$

1771 where $\tilde{\mu}_{A_i}$ is the reduced mass of the DM-nucleus i system, $\tilde{\mu}_p$ is the reduced mass of
 1772 the DM-proton system, A_i and J_i the mass number and total angular momentum of
 1773 nucleus i and $\langle S_{p,i} \rangle$ and $\langle S_{n,i} \rangle$ the expectation value of the spins of protons and neutrons
 1774 averaged over all nucleons, respectively (see Ref. [70] for a review on spin expectation
 1775 values).

1776 Since the Sun is mainly composed of Hydrogen, the capture of DM from the halo
 1777 is expected to occur mainly through spin-dependent scattering. However, since the
 1778 spin-independent cross section is proportional to the square of the atomic mass, heavy
 1779 elements can contribute to the capture rate (even though they constitute less than 2%
 1780 of the mass of the Sun). Heavy elements can also contribute to the spin-dependent cross
 1781 section if the DM has also momentum-dependent interactions.

1782 DM particles can get captured by the Sun if after repeated scatterings off solar
 1783 targets their final velocity is lower than the escape velocity of the Sun. In the limit of
 1784 weak cross sections, this capture rate can be approximately written as [4]:

$$C_{\odot}^{\text{weak}} = \sum_i \int_0^{R_{\odot}} dr 4\pi r^2 \int_0^{\infty} du_{\chi} \frac{\rho_{\chi}}{m_{\chi}} \frac{f_{v_{\odot}}(u_{\chi})}{u_{\chi}} \omega(r) \int_0^{v_e(r)} dv R_i^-(\omega \rightarrow v) |F_i(q)|^2, \quad (7.5)$$

1785 where the summation extends over all possible nuclear targets. In this expression, R_{\odot}
 1786 is the radius of the Sun, ρ_{χ} is the local DM density, m_{χ} the mass of the DM particle,
 1787 $f_{v_{\odot}}(u_{\chi})$ the DM velocity distribution seen from the Sun's reference frame, $R_i^-(\omega \rightarrow v)$
 1788 is the differential rate at which a DM particle with velocity v scatters a solar target of
 1789 mass m_i to end up with a velocity ω and $|F_i(q)|$ is the nuclear form factor of target i .

1790 The differential scattering rate takes a rather simple form when considering velocity-

Chapter 7. DM searches with neutrinos from the Sun

1791 independent and isotropic cross sections. In that case, this quantity is given by [4, 71]:

$$R_i^-(\omega \rightarrow v) = \frac{2}{\sqrt{\pi}} \frac{\mu_{i,+}^2}{\mu_i} \frac{v}{\omega} n_i(r) \sigma_i \left[\chi(-\alpha_-, \alpha_+) + \chi(-\beta_-, \beta_+) e^{\mu_i(\omega^2 - v^2)/u_i^2(r)} \right], \quad (7.6)$$

1792 where μ_i is the ratio between the DM mass and the mass of target i , $\mu_{i,\pm}$ is defined as:

$$\mu_{i,\pm} \equiv \frac{\mu_i \pm 1}{2}, \quad (7.7)$$

1793 $n_i(r)$ is the density profile of target i in the solar medium, $u_i(r)$ is the most probable

1794 velocity of target i given by:

$$u_i(r) = \sqrt{\frac{2T_\odot(r)}{m_i}}, \quad (7.8)$$

1795 where $T_\odot(r)$ is the temperature of the Sun, the quantities α_\pm and β_\pm are defined as:

$$\alpha_\pm \equiv \frac{\mu_{i,+}v \pm \mu_{i,-}\omega}{u_i(r)}, \quad (7.9)$$

$$\beta_\pm \equiv \frac{\mu_{i,-}v \pm \mu_{i,+}\omega}{u_i(r)}, \quad (7.10)$$

1796 and the function $\chi(a, b)$ is a Gaussian integral of the form:

$$\chi(a, b) \equiv \int_a^b dx e^{-x^2}. \quad (7.11)$$

1797 Finally, if one assumes the DM halo velocity distribution in the galactic rest frame

1798 to be a Maxwell-Boltzmann distribution, one can write the halo velocity distribution for

1799 an observer moving at the speed of the Sun with respect to the DM rest frame as:

$$f_{v_\odot}(u_\chi) = \sqrt{\frac{3}{2\pi}} \frac{u_\chi}{v_\odot v_d} \left(e^{-\frac{3(u_\chi - v_\odot)^2}{2v_d^2}} - e^{-\frac{3(u_\chi + v_\odot)^2}{2v_d^2}} \right), \quad (7.12)$$

1800 where:

$$\omega^2 = u_\chi + v_e(r)^2, \quad (7.13)$$

1801 is the DM velocity squared, v_\odot the relative velocity of the Sun from the DM rest frame

7.2. Gravitational capture of DM by the Sun

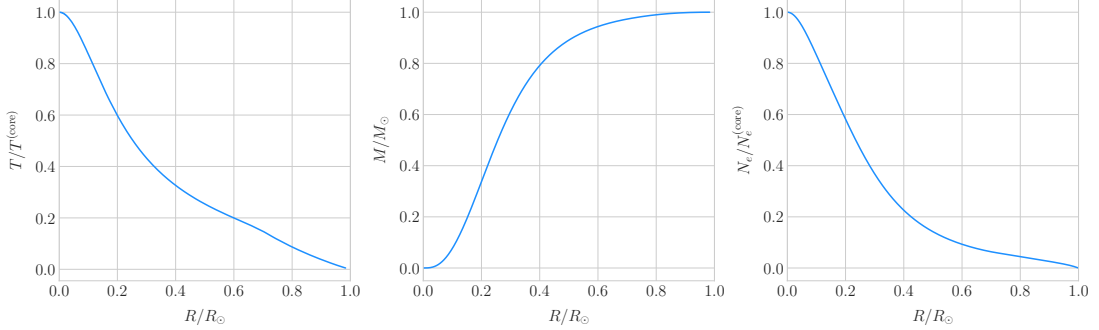


Figure 7.1: Input solar parameters used in our capture rate computation as functions of the Sun's radius, from left to right: temperature (with respect to the temperature at the core), mass (in solar masses) and electron number density (with respect to the electron density at the core). All quantities shown correspond to the standard solar model BS2005-OP [3].

1802 and $v_d \simeq \sqrt{3/2}v_\odot$ the velocity dispersion.

1803 For the case of strong scattering cross section, Eq. (7.5) ceases to be valid, as it
 1804 escalates indefinitely with the cross section. In that limit, the capture rate saturates to
 1805 the case where the probability of interaction is equal to one, which can be written as:

$$C_\odot^{\text{geom}} = \pi R_\odot^2 \left(\frac{\rho_\chi}{m_\chi} \right) \langle v \rangle \left(1 + \frac{3}{2} \frac{v_e^2(R_\odot)}{v_d^2} \right) \xi(v_\odot, v_d), \quad (7.14)$$

1806 where $v_d = \sqrt{8/3\pi}v_d$ is the mean velocity in the DM rest frame and the factor $\xi(v_\odot, v_d)$
 1807 accounts for the suppression due to the motion of the Sun:

$$\xi(v_\odot, v_d) = \frac{v_d^2 e^{-\frac{3v_\odot^2}{2v_d^2}} + \sqrt{\frac{\pi}{6}} \frac{v_d}{v_\odot} (v_d^2 + 3v_e^2(R_\odot) + 3v_\odot^2) \text{Erf} \left(\sqrt{\frac{3}{2}} \frac{v_\odot}{v_d} \right)}{2v_d^2 + 3v_e^2(R_\odot)}. \quad (7.15)$$

1808 Having these into account, one can write the total capture rate as a combination of
 1809 both contributions, allowing a smooth transition between the two, as:

$$C_\odot = C_\odot^{\text{weak}} \left(1 - e^{C_\odot^{\text{geom}}/C_\odot^{\text{weak}}} \right). \quad (7.16)$$

1810 I computed the capture rate from Eq. (7.16) in the case of interactions with
 1811 electrons. To do so, I used the standard solar model BS2005-OP [3]. Fig. 7.1 shows the

Chapter 7. DM searches with neutrinos from the Sun

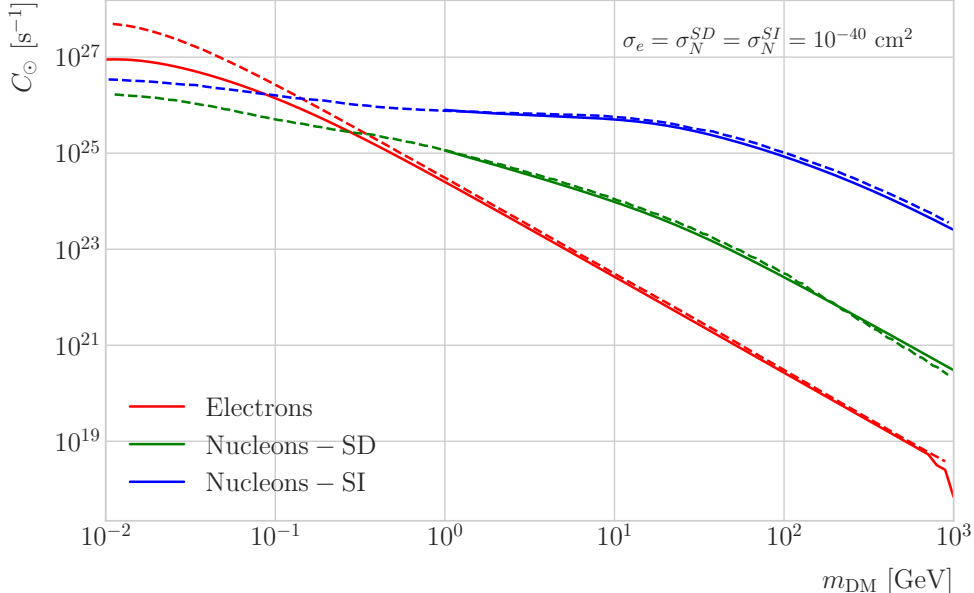


Figure 7.2: Capture rates as a function of the DM mass for the DM-electron interactions (red lines), SD DM-nucleons interactions (green lines) and SI DM-nucleons interactions (blue lines). Solid lines represent the values computed in this work while the dashed lines are the one given in Ref. [4]. All the rates are shown for a choice of scattering cross section of $\sigma_i = 10^{-40} \text{ cm}^2$.

1812 three parameters from the solar model that are needed for the computation, the solar

1813 temperature (left panel), mass (central panel) and electron density (right panel) profiles.

1814 For the case of the interactions off nuclei, the computations are more convoluted

1815 as one needs to add up the contributions of the different most abundant nuclei in

1816 the Sun. Also, in contrast to the electron scenario where the form factor is trivially

1817 $|F_e(q)|^2 = 1$, for any nucleus i one would need to consider some appropriate nuclear

1818 density distribution (either a Gaussian approximation, a Woods-Saxon distribution, etc)

1819 which would complicate the calculations even further.

1820 That is the reason why, at this stage of our study, I decided to take an alternative

1821 approach to the computation of the DM-nucleus capture rates. I used the **DarkSUSY**

1822 software, that allows us to compute these quantities performing a full numerical

1823 integration over the momentum transfer of the form factors. The default standard

1824 solar model used by **DarkSUSY** is BP2000¹ [72].

¹This is what they say in their manual, but I fear it is somewhat outdated. It appears to me this

7.2. Gravitational capture of DM by the Sun

1825 In Fig. 7.2 I show the results I obtained for the capture rates, for the case of
 1826 interactions off electrons (red solid line), SD (green solid line) and SI (blue solid line)
 1827 interactions of nucleons. In all cases I used a value of the scattering cross sections of
 1828 $\sigma_i = 10^{-40} \text{ cm}^2$. Note here one of the limitations of the **DarkSUSY** approach, one can
 1829 not extend the computation below $m_{\text{DM}} = 1 \text{ GeV}$. Nevertheless, this is not something
 1830 to worry about in this case, as I will discuss next. As a comparison, I added also the
 1831 values computed in Ref. [4] (same color scheme, dashed lines). One can see there is good
 1832 agreement between these and the **DarkSUSY** computation of the SD and SI interactions
 1833 for $m_{\text{DM}} \geq 1 \text{ GeV}$. In this regime their computations also matches quite well our
 1834 result for the electron capture rate. However, these start to differ significantly below
 1835 $m_{\text{DM}} = 1 \text{ GeV}$, being their estimate up to a factor of 5 bigger than ours for low masses.

1836 Let us comment briefly about the assumption I made before about not including
 1837 an evaporation term in the Boltzmann equation. If I include this term in the equation
 1838 (which will be proportional to the number of DM particles) the equilibrium solution
 1839 takes the form:

$$N_{\text{DM}}^{eq} = \sqrt{\frac{C_{\odot}}{A_{\odot}}} \frac{1}{\kappa + \frac{1}{2} E_{\odot} \tau_{eq}}, \quad (7.17)$$

1840 where E_{\odot} is the total evaporation rate, τ_{eq} is the equilibrium time in the absence of
 1841 evaporation:

$$\tau_{eq} = \frac{1}{\sqrt{C_{\odot} A_{\odot}}}, \quad (7.18)$$

1842 and κ is defined as:

$$\kappa \equiv \sqrt{1 + \left(\frac{E_{\odot} \tau_{eq}}{2} \right)^2}. \quad (7.19)$$

1843 Now, it is easy to proof that in case evaporation dominates $\kappa \gg 1$ and therefore:

$$N_{\text{DM}}^{eq} \simeq \frac{C_{\odot}}{E_{\odot}}. \quad (7.20)$$

1844 In contrast, if evaporation is irrelevant $\kappa \simeq 1$ and one recovers Eq. (7.2).

model is relatively old and do not see why they are not using others like [3]. Maybe one can double-check in the code to make sure.

Chapter 7. DM searches with neutrinos from the Sun

1845 In this way, one can define the evaporation mass as the mass for which the number
1846 of DM particles in equilibrium approaches Eq. (7.20) at 10% level:

$$\left| N_{DM}^{eq}(m_{\text{evap}}) - \frac{C_{\odot}(m_{\text{evap}})}{E_{\odot}(m_{\text{evap}})} \right| = 0.1 N_{DM}^{eq}(m_{\text{evap}}). \quad (7.21)$$

1847 This can be regarded as the minimum testable mass one can reach using the annihilation
1848 products of the DM in the Sun.

1849 It was reported in Ref. [4] that, in the case of both SD and SI DM interactions
1850 off nuclei, this value ranges from 2 to 4 GeV depending on the specific scattering
1851 cross section value, compatible with the usual assumptions in the literature. What is
1852 interesting is the case of the electron capture. It was found that, when one applies a
1853 cutoff in the velocity distribution of the DM trapped in the Sun slightly below the escape
1854 velocity, the evaporation mass for the DM-electron interaction decreases remarkably. For
1855 a moderate choice of $v_c(r) = 0.9v_e(r)$ one gets an evaporation mass of around 200 to
1856 600 MeV. This possibility opens a region of the parameter space that could be tested
1857 with neutrino detectors.

1858 7.3 Neutrino flux from DM annihilations

1859 When WIMPs annihilate inside the Sun a flux of high-energy neutrinos is expected from
1860 heavy quarks, gauge bosons and $\tau^+\tau^-$ final states, which decay before losing energy
1861 in the dense solar medium, as they will produce a continuum spectra up to $E_{\nu} \sim m_{\chi}$
1862 (in the case of direct annihilation to neutrinos one would have a line at $E_{\nu} = m_{\chi}$) [66].
1863 This kind of signal has been extensively studied in the literature, allowing to put strong
1864 limits on the SD WIMP-proton cross section for large m_{χ} . However, the number of
1865 high-energy neutrinos per WIMP annihilation is small and the spectrum depends on the
1866 unknown final state. Moreover, background rejection is easier for large m_{χ} but neutrinos
1867 with $E_{\nu} \gtrsim 100$ GeV are significantly attenuated by interactions in the Sun.

1868 Nevertheless, most WIMP annihilation final states eventually produce a low-energy
1869 neutrino spectrum. In this case one does not just consider the more massive final

7.4. Computing limits from solar neutrino fluxes

1870 states but also annihilations into e^+e^- , $\mu^+\mu^-$ and light quarks [65]. In particular, light
 1871 mesons would be produced and stopped in the dense medium, thus decaying at rest and
 1872 producing a monoenergetic neutrino signal. The decay-at-rest of kaons will produce
 1873 a $E_\nu = 236$ MeV ν_μ while in the case of pions one would have a $E_\nu = 29.8$ MeV ν_μ .
 1874 In practice only K^+ and π^+ contribute to these signals, as K^- and π^- are usually
 1875 Coulomb-captured in an atomic orbit and get absorbed by the nucleus. There is also a
 1876 low-energy neutrino signal coming from muon decays, which are produced in kaon or
 1877 pion decays, leptonic decays of other hadrons and heavy leptons or even directly from
 1878 WIMP annihilations, which can decay at rest and contribute to the previous low-energy
 1879 neutrino flux with a well known spectrum below 52.8 MeV.

1880 These monoenergetic MeV neutrinos were previously considered undetectable but,
 1881 due to the large yield, the known spectra and the modern advances in the detector
 1882 technology, these low-energy neutrino flux can be a good probe of the SD WIMP-proton
 1883 cross-section in standard solar WIMP capture scenario, as it is sensitive to low WIMP
 1884 masses and insensitive to the particular final state. A good place to look for these signals
 1885 are next-generation neutrino experiments such as DUNE.

1886 7.4 Computing limits from solar neutrino fluxes

1887 In order to use the neutrino fluxes from DM annihilations in the Sun, the first thing I
 1888 need to do is to determine the expected number of atmospheric background events, for
 1889 a given exposure, after directionality selection has been applied. I can write this number
 1890 as:

$$N_B = \eta_B \int d\Omega \int_{E_{min}}^{E_{max}} dE_\nu \frac{d^2\Phi_{atm}^\mu}{dE_\nu d\Omega} \times \left(A_{eff}^{(\mu)}(E_\nu) T \right), \quad (7.22)$$

1891 where η_B is the background efficiency, E_{min} and E_{max} the minimum and maximum
 1892 energies to integrate over, $d^2\Phi_{atm}^\mu/dE_\nu d\Omega$ the differential flux of atmospheric muon
 1893 neutrinos, $A_{eff}^{(\mu)}$ is the effective area of DUNE to muon neutrinos and T is the exposure
 1894 time. The effective area can be expressed as the product of the neutrino-nucleus scattering
 1895 cross section and the number of nuclei in the fiducial volume of the detector. This way

Chapter 7. DM searches with neutrinos from the Sun

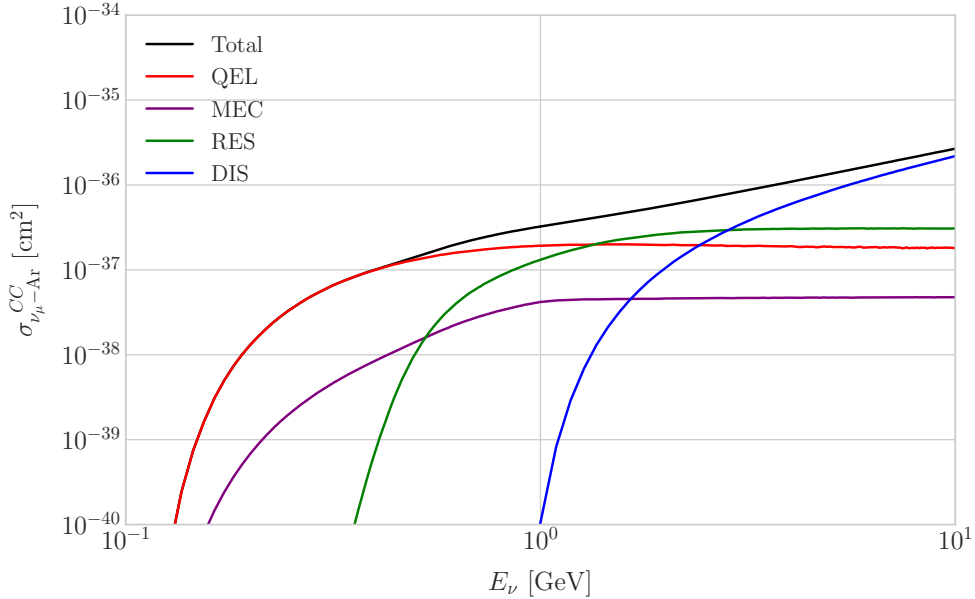


Figure 7.3: *NuWro* computed $\nu_\mu - {}^{40}\text{Ar}$ charged-current scattering cross section as a function of the neutrino energy E_μ . The black line shows to the total cross section, whereas the others correspond to the different contributions (in red quasi-elastic scattering, in green resonant pion exchange, in blue deep inelastic scattering and in purple meson exchange current).

1896 for DUNE I can write:

$$A_{eff}^{(\mu)}(E_\nu) = (6.0 \times 10^{-10} \text{ m}^2) \left(\frac{\sigma_{\nu - \text{Ar}}^{(\mu)}(E_\nu)}{10^{-38} \text{ cm}^2} \right) \left(\frac{M_{target}}{40 \text{ kT}} \right), \quad (7.23)$$

1897 where $\sigma_{\nu - \text{Ar}}^{(\mu)}$ is the $\nu_\mu - {}^{40}\text{Ar}$ charged-current scattering cross section. In Fig. 7.3 I
 1898 show the computed value of this cross section as a function of the neutrino energy E_ν ,
 1899 in the range of interest both for the atmospheric background and signal events. It was
 1900 computed using the NuWro Monte Carlo neutrino event generator [73], including the
 1901 charged-current contributions of the quasi-elastic scattering (red line), resonant pion
 1902 exchange (green line), deep inelastic scattering (blue line) and meson exchange current
 1903 (purple line).

1904 The background rejection will depend on the resolution of the detector and the
 1905 selection one applies on the events. A geometry argument can be used to estimate
 1906 the maximum background rejection one can achieve in this case, considering one can

7.4. Computing limits from solar neutrino fluxes

1907 efficiently discriminate all events coming from a direction different from that of the
 1908 Sun. In that case, the optimal background efficiency will simply be the relative angular
 1909 coverage of the Sun. Taking the angular diameter of the Sun as seen from the Earth to
 1910 be 0.5° , I have:

$$\eta_B^{(opt)} \approx \frac{\pi \left(\frac{0.5}{2}\right)^2}{360 \times 180} \simeq 3.03 \times 10^{-6}. \quad (7.24)$$

1911 This value will give a very optimistic estimate of the number of background events.
 1912 However, it can be regarded as a lower limit, as it represents the best case scenario.

1913 In Fig. 7.4 I show the fluxes of atmospheric neutrinos at the Homestake mine during
 1914 solar minimum, taken from Ref. [5]. The values are averaged over the two angular
 1915 directions. In blue I have the flux of muon neutrinos while in red I indicate the flux
 1916 of electron neutrinos. Additionally, the dashed lines correspond to both antineutrino
 1917 species.

1918 Using these values for the muon neutrino and the corresponding total CC cross
 1919 section, one can compute the number of expected background events by integrating over
 1920 the given energy range (as in this case the angular integral is trivial). As for the energy
 1921 range to integrate over, I choose the range for DUNE specified in [42], $E_{min} = 10^{-1}$ GeV
 1922 and $E_{max} = 10$ GeV. Taking all these into account, I found the number of background
 1923 events to be:

$$N_B \simeq \eta_B \times (3.827 \times 10^4) \times \left(\frac{\text{exposure}}{400 \text{ kT yr}} \right). \quad (7.25)$$

1924 In order to estimate the sensitivity of DUNE to this kind signal, one can consider a
 1925 hypothetical data set where the number of observed neutrinos is taken to be the expected
 1926 number of background events rounded to the nearest integer, $N_{obs} = \text{round}(N_B)$ [74].
 1927 Now, if I assume that the number of signal and background events seen by DUNE are
 1928 given by Poisson distributions with means equal to the expected number of signal and
 1929 background events, N_S and N_B , one can denote by N_S^{90} to the number of expected
 1930 signal events such that the probability of having an experimental run with a number of
 1931 events greater than N_{obs} is 90%. This number can be obtained as the numerical solution

Chapter 7. DM searches with neutrinos from the Sun

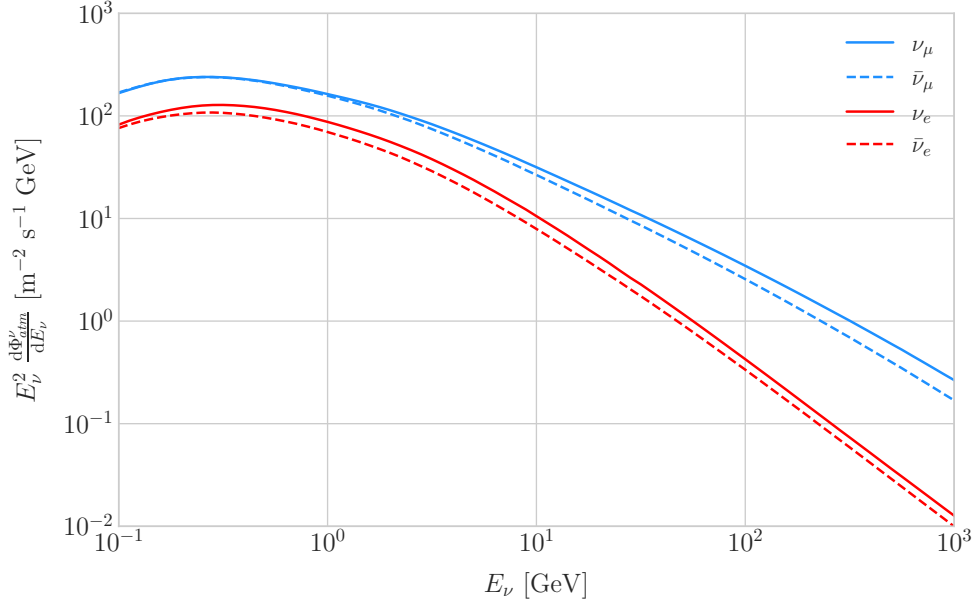


Figure 7.4: Expected atmospheric neutrino flux as a function of the neutrino energy E_ν at Homestake at solar minimum, taken from Ref. [5]. The blue solid (dashed) line correspond to muon neutrinos (antineutrinos) and the red solid (dashed) line correspond to electron neutrinos (antineutrinos).

¹⁹³² to the equation:

$$1 - \frac{\Gamma(N_{obs} + 1, N_S^{90} + N_B)}{N_{obs}!} = 0.9, \quad (7.26)$$

¹⁹³³ where $\Gamma(x, y)$ is the upper incomplete gamma function.

¹⁹³⁴ The number of signal events is related to the neutrino flux from DM annihilations in
¹⁹³⁵ a similar way as the background events to the atmospheric neutrino flux. In this case I
¹⁹³⁶ have:

$$N_S = \eta_S \Gamma_A^{eq} \int_{z_{min}}^{z_{max}} dz \frac{dN_\nu}{dAdN_Adz} \times (A_{eff}^\mu(z)T), \quad (7.27)$$

¹⁹³⁷ where η_S is the signal efficiency, Γ_A^{eq} is the total annihilation rate of DM particles at
¹⁹³⁸ equilibrium, $\Gamma_A^{eq} = A_\odot (N_{DM}^{eq})^2$, z_{min} and z_{max} the minimum and maximum relative
¹⁹³⁹ energies to integrate over (in such a way that $z_{min,max} \leq E_{min,max}/m_{DM}$ for each m_{DM})
¹⁹⁴⁰ and $dN_\nu/dAdN_Adz$ the muon neutrino flux per DM annihilation in the Sun.

¹⁹⁴¹ Knowing N_S^{90} one can use the relation in Eq. (7.27) to obtain $\Gamma_A^{eq,90}$ for different
¹⁹⁴² values of the DM mass. From there I can directly translate those values into the

7.5. Example: Kaluza-Klein Dark Matter

1943 upper limits for DUNE on the DM scattering cross sections, for a given exposure. The
1944 relation between the annihilation rate and the DM-nucleon cross section comes from the
1945 equilibrium condition through the solar DM capture rate. The details of the evolution
1946 of the number of DM particles inside the Sun and the computation of the capture rates
1947 are discussed in App. 7.2.

1948 7.5 Example: Kaluza-Klein Dark Matter

1949 Even though there are plenty of BSM theories which provide viable dark matter
1950 candidates, Kaluza-Klein type of models [75, 76] within the universal extra dimensions
1951 (UED) paradigm naturally predict the existence of a massive, stable particle that can
1952 play the role of the dark matter. In the UED scenario all the SM fields can propagate
1953 in one or more compact extra dimensions [77], as opposed to the idea of brane worlds
1954 [78, 79], where just gravity can propagate in the bulk while SM particles live at fixed
1955 points.

1956 Furthermore, in UED there is no violation of the translational invariance along the
1957 extra dimensions, thus leading to degenerate KK modes masses and also the conservation
1958 of the KK number in the effective four dimensional theory. At loop level, radiative
1959 corrections and boundary terms shift the masses of the KK modes and break KK
1960 number conservation into a KK parity. As a result, this theory only contains interactions
1961 between an even number of odd KK modes and therefore the lightest among the first KK
1962 excitations will be stable. This particle is usually denoted as the lightest Kaluza-Klein
1963 particle (LKP) and its mass is proportional to $1/R$, being R the size of the extra
1964 dimension.

1965 A viable DM candidate needs to be electrically neutral and non-baryonic, therefore
1966 good candidates among the first Kaluza-Klein excitations would be the KK neutral
1967 gauge bosons and the KK neutrinos [80]. Another possible candidate is the first KK
1968 excitation of the graviton, which receives negligible radiate contributions and therefore
1969 has a mass almost equal to $1/R$, but it has been shown that the lightest eigenstate from

Chapter 7. DM searches with neutrinos from the Sun

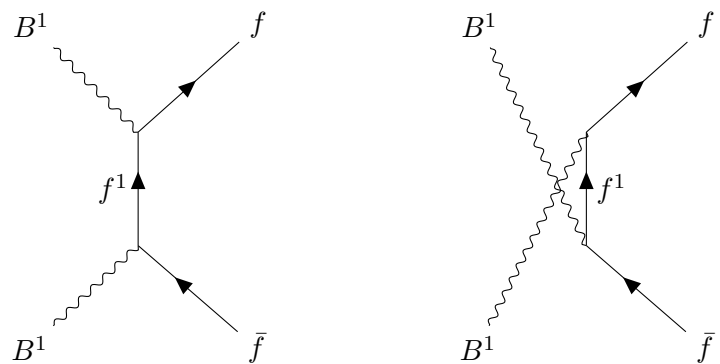


Figure 7.5: Feynman diagrams for $B^1 B^1$ annihilation into SM fermions.

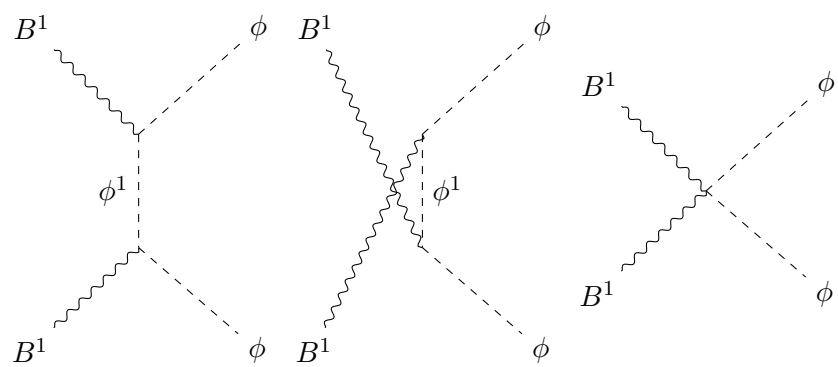


Figure 7.6: Feynman diagrams for $B^1 B^1$ annihilation into a Higgs boson pair.

7.5. Example: Kaluza-Klein Dark Matter

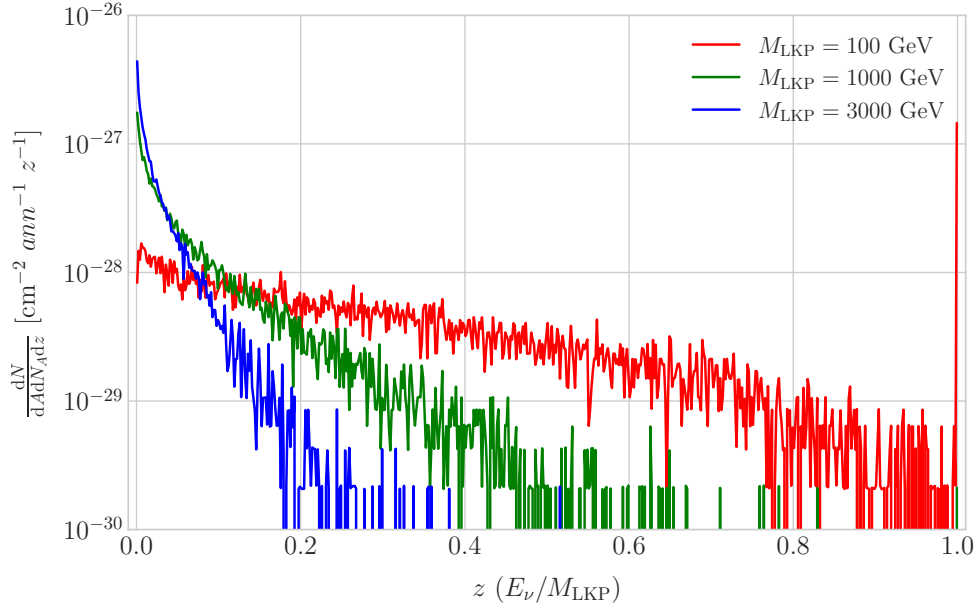


Figure 7.7: Computed spectra of muon neutrinos at the DUNE FD site from B^1 annihilations in the Sun for three different values of M_{LKP} , plotted in relative energy units for legibility.

the mixing of the gauge mass states (B^1, W_3^1) would be lighter, as B^1 and W_3^1 receive negative radiative corrections [81]. It is also understood that, when these corrections become sizeable, the eigenstates become approximately pure B^1 and W_3^1 states as the Weinberg mixing angle grows small with the KK number [81]. In that case, the LKP can be well-approximated as being entirely B^1 .

I need to compute the neutrino flux produced by the annihilations of the LKP in the core of the Sun, taking into account their propagation in the solar medium, as well as neutrino oscillations. To this end I used `WimpSim` [82, 83] to generate one million annihilation events in the Sun over a time span of four years and propagate them to the DUNE FD location ($44^\circ 20' \text{ N}, 103^\circ 45' \text{ W}$), for different values of M_{LKP} . In Fig. 7.7 I show the obtained muon neutrino spectra arriving to the detector from LKP annihilations in the Sun, per unit area and per annihilation, plotted in relative energy units for different values of the mass. As one could expect the spectra get steeper the higher is the mass, due to the absorption of high-energy neutrinos in the solar medium. Also, one can see the peak at $z = 1$ due to the direct annihilation into neutrinos $\chi\chi \rightarrow \nu\bar{\nu}$.

Chapter 7. DM searches with neutrinos from the Sun

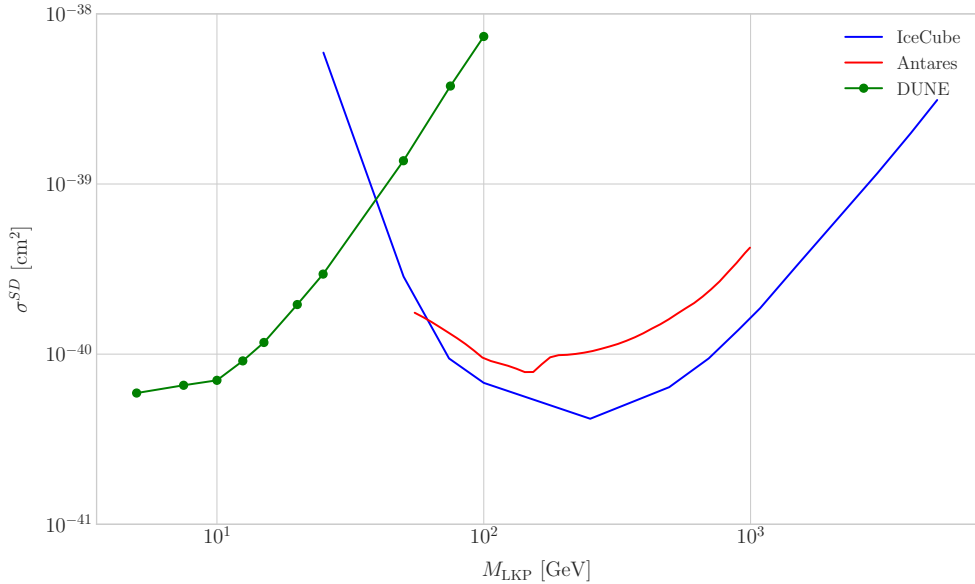


Figure 7.8: Projected 90% confidence level upper limit for DUNE (400 kT yr) on the spin-dependent B^1 -proton scattering cross section as a function of M_{LKP} (green dots). I also show the previous limits from IceCube [6] (blue line) and Antares [7] (red line) on the LKP cross section. The shaded area represents the disfavoured region (at 95% confidence level) on the mass of the LKP from LHC data [8].

Now, one can estimate the sensitivity of DUNE to this particular model by using the methods I previously discussed. To begin with, I will use the optimistic estimation of the background efficiency in Eq. (7.24) to get our upper bound. Using it, one can directly compute the number of expected background events to be $N_B = 0.1101$ for an exposure of 400 kT yr. Then, Eq. (7.26) give us a value of $N_S^{90} = 2.20$ for the 90% exclusion number of expected signal events. By using the NuWro generated cross sections and the computed neutrino fluxes from B^1 annihilations in the Sun I can estimate the limits on the SD and SI DM-nucleus cross section using the relation in Eq. (7.2) and the capture rates I computed with DarkSUSY.

In Fig. 7.8 I show the projected sensitive for DUNE on the spin-dependent B^1 -proton scattering cross section versus the mass of the DM particle, for a exposure of 400 kT yr (green dots). I also include the previous results from IceCube [6] (blue line) and Antares [7] (red line). The shaded area represents the disfavoured region from combined searches for UED by ATLAS and CMS [8].

7.6. High energy DM neutrino signals

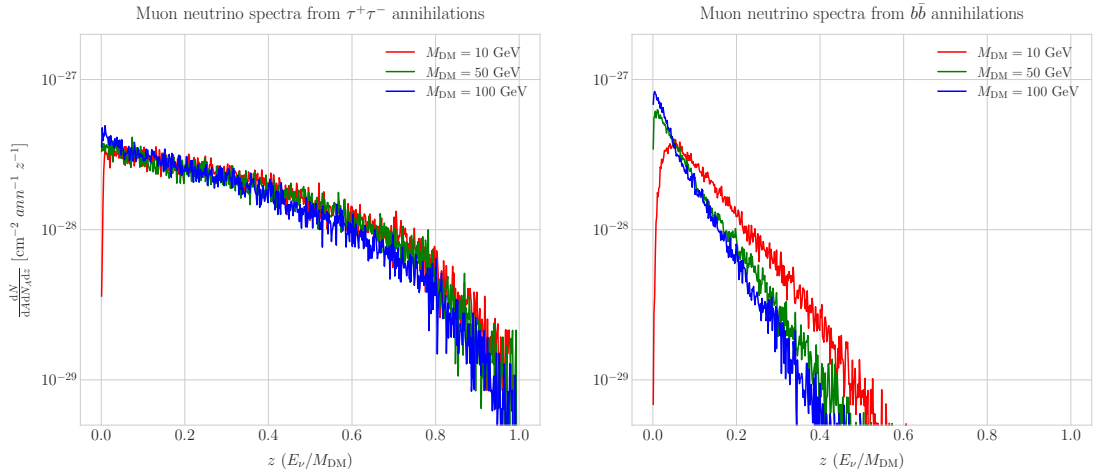


Figure 7.9: Computed spectra of muon neutrinos at the DUNE FD site from $\tau^+\tau^-$ (left panel) and $b\bar{b}$ (right panel) annihilations in the Sun for the DM masses $m_{\text{DM}} = 10 \text{ GeV}$ (red line), 50 GeV (green line) and 100 GeV (blue line), plotted in relative energy units.

From the experimental point of view, this estimation lacked a detailed simulation of the detector response and thus this must be consider as a mere optimistic sensitivity computation. However, it shows the potential of DUNE to constrain this kind of exotic scenarios, showing the region where it will be in a position to compete with other neutrino telescopes. A more detailed analysis is needed if I am to make a realistic estimation. Even though the region of the parameter space where DUNE would be sensitive to this particular model is quite constrained by collider searches [8] and other rare decay measurements [84, 85], it still constitutes an alternative indirect probe.

7.6 High energy DM neutrino signals

To have better estimates on the capability of the DUNE FD to constrain the parameter space of DM using solar neutrino fluxes, I need to start accounting for the detector resolution effects and the topologies of the different signatures. As a starting point, I will focus on specific annihilation channels. For the case of DUNE, the relevant ones are mainly the hard channels $\tau^+\tau^-$ and $\nu\bar{\nu}$ and the soft channel $b\bar{b}$. These are the open annihilation channels for relatively low mass WIMPs that will actually give neutrino fluxes. Other channels, like W^+W^- and ZZ , are open for more massive WIMPs, but

Chapter 7. DM searches with neutrinos from the Sun

2015 those will produce usually a higher energy neutrino flux that will be out of reach for
2016 DUNE (usually the maximum neutrino energy is taken to be $E_{max} = 10$ GeV).

2017 In Fig. 7.9 I show the `WimpSim` [82, 83] generated muon neutrino spectra at the
2018 DUNE FD location ($44^\circ 20' N, 103^\circ 45' W$) from $\tau^+\tau^-$ (left panel) and $b\bar{b}$ (right panel)
2019 annihilations in the core of the Sun, for different DM masses. Here, one can clearly see
2020 the meaning of the previous distinction between hard and soft channels. For the same
2021 DM mass value, the muon neutrino spectrum from the $\tau^+\tau^-$ channel is more flat and
2022 reaches higher energies than the one from the $b\bar{b}$ channel, which drops faster.

2023 In this case, I prepared two sets of files, one for $\tau^+\tau^-$ and the other for $b\bar{b}$, for DM
2024 masses in the range from 5 to 100 GeV (actually for $b\bar{b}$ the first mass point I took is
2025 7.5 GeV, as a WIMP with $m_{DM} = 5$ GeV can not kinematically self annihilate into $b\bar{b}$).
2026 Then, I prepared the `WimpSim` output fluxes in a specific way to use them as inputs to
2027 `NuWro`, which simulates the neutrino interaction with the argon.

2028 Because `WimpSim` outputs an event list together with the fluxes, I can use the former
2029 to generate the events. The direction of these is given in terms of the azimuth and
2030 altitude angles viewed from the specified location, so first I need to convert these into the
2031 DUNE FD coordinates. Once I have done it, each event can be processed with `NuWro`.
2032 To increase the number of samples and optimise the computation time, I generate 100
2033 interactions (i.e. `NuWro` events) for each `WimpSim` event². I restrict the event generation
2034 to charged current interactions, but I allow all the different contributions to the CC
2035 cross section, i.e. quasielastic scattering (QEL), meson exchange current process (MEC),
2036 resonant pion production (RES) and deep inelastic scattering (DIS). I just take into
2037 account the CC contribution because I am only interested in final states with charged
2038 leptons, as we have better chances of reconstructing the kinematics of CC events.

2039 For the atmospheric fluxes I follow a similar procedure, only that this time I do not
2040 have a set of events but the fluxes binned in azimuth and altitude angles. This way, I
2041 transform these to DUNE coordinates and process the fluxes for each bin separated with

²This also solves a problem related with the generation of the neutrino interactions in `NuWro`, as if you only produce one event each time you launch `NuWro` it will always produce an interaction of the dominant interaction type for that particular energy.

7.6. High energy DM neutrino signals

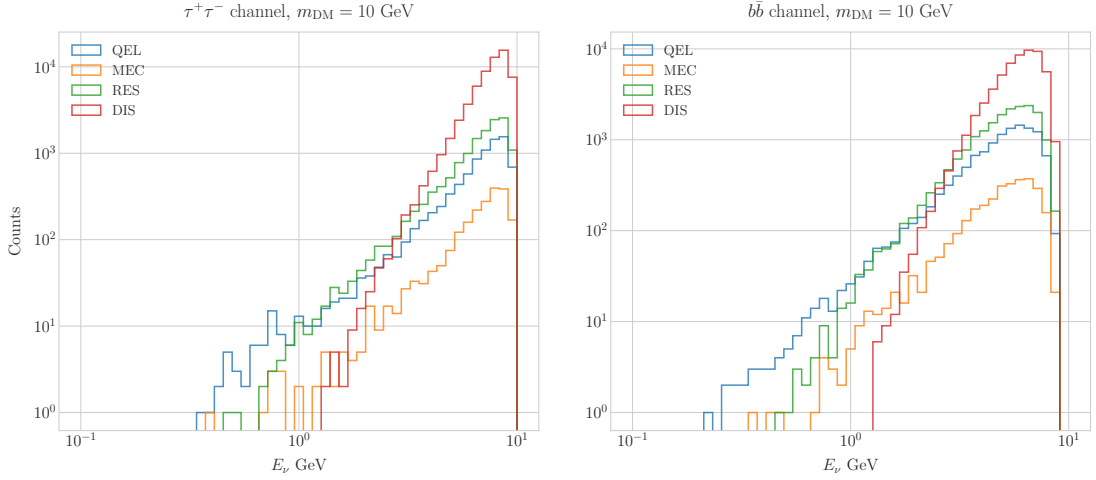


Figure 7.10: Distribution of the muon neutrino energies from the $\tau^+\tau^-$ (left panel) and $b\bar{b}$ (right panel) annihilation channels, for $m_{\text{DM}} = 10 \text{ GeV}$, separated by CC interaction type: QEL (blue), MEC (orange), RES (green) and DIS (red).

2042 NuWro.

2043 At this point, I have two sets of events with different energies and final states.
 2044 In Fig. 7.10 one can see the distribution of the muon neutrino energies for the case
 2045 $m_{\text{DM}} = 10 \text{ GeV}$, both for the $\tau^+\tau^-$ (left panel) and $b\bar{b}$ (right panel) channels, separated
 2046 by interaction. One can clearly see that there are different energy regimes where the
 2047 primary interaction type is different. This leads to a plurality of event topologies,
 2048 therefore making it difficult to implement a general approach to the selection of events
 2049 in detriment of the background. As a way to proceed, I decided to split our samples,
 2050 based on the different interaction modes and contents of the final state, into a CC DIS
 2051 sample and a single proton CC QEL sample.

2052 **7.6.1 DIS events**

2053 To begin with, I consider the high energy part of the spectrum. In this region DIS events
 2054 dominate, i.e. interactions of the form $\nu_\mu + q_d(\bar{q}_u) \rightarrow \mu^- + q_u(\bar{q}_d)$. Therefore, our final
 2055 estates will contain a muon and a hadronic jet from the fragmentation of the outgoing
 2056 quark. As all these events have $E_\nu \gtrsim 1 \text{ GeV}$ the momentum transfer to the remnant
 2057 nucleus is negligible, for this reason the neutrino energy can be effectively reconstructed

Chapter 7. DM searches with neutrinos from the Sun

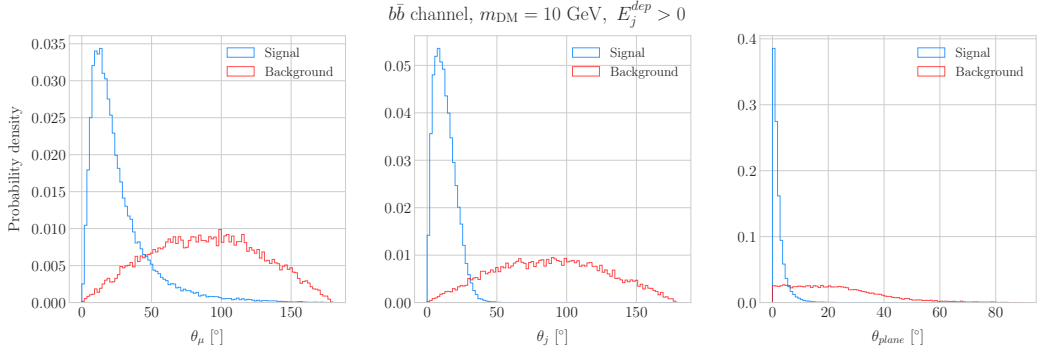


Figure 7.11: Distributions of θ_μ (left panel), θ_j (central panel) and θ_{plane} (right panel) for the $b\bar{b}$ sample with $m_{\text{DM}} = 10$ GeV (blue) and the atmospheric background (red).

just taking into account the momenta of the muon and the jet. This technique was successfully used in Ref. [86] to select monoenergetic DM solar neutrino events from $\nu\bar{\nu}$ annihilation channels.

Using momentum conservation one sees that the plane generated by the momenta of the muon and the jet needs to also contain the momentum of the neutrino. As we are interested in neutrinos coming from the Sun, the momentum of the neutrino can be regarded as known beforehand. This will allow us to define the angle of the outgoing muon and jet with respect to the incoming neutrino. Moreover, one can also use that information to reject poorly reconstructed jets, checking for deviations of these from the momentum conservation plane.

To account for the limited angular resolution of the detector, I smeared the momenta of the muons and hadrons. In a liquid argon TPC muons are expected to be tracked with high precision, therefore I take the associated angular resolution to be 1° . In the case of jets, it is expected that for the hadrons dominating the cascade a detector like DUNE has an angular resolution between 1° to 5° [42], so I take the latter, more conservative, estimate.

As a first selection step, I will just take into account particles with kinetic energies above the detection threshold of DUNE. For muons and photons the specified threshold energy is 30 MeV, for charged pions 100 MeV and for other hadrons 50 MeV [42]. This way, if the outgoing muon in a certain event has an energy lower than the required

7.6. High energy DM neutrino signals

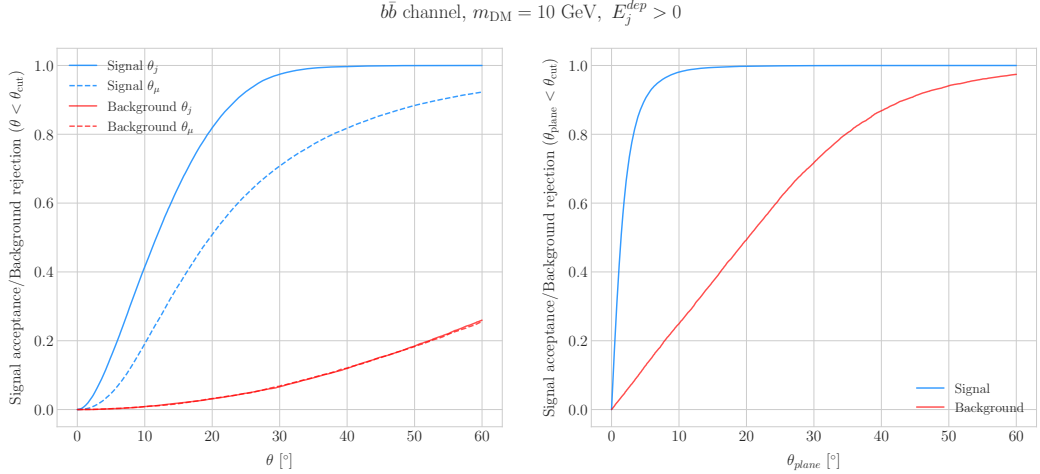


Figure 7.12: Left panel: signal efficiencies (blue lines) and background rejections (red lines) for events passing the cuts $\theta < \theta_{\text{cut}}$ for the jet (solid lines) and muon (dashed lines) angles. Right panel: signal efficiency (blue line) and background rejection (red line) for events passing the cut $\theta_{\text{plane}} < \theta_{\text{cut}}$ for the momentum conservation plane deviation.

threshold I will drop such event. For the case of hadrons and photons, I will only require to have at least one particle above the energy threshold, so then one can compute the jet momentum using the (smeared) momenta of the N particles above threshold as:

$$\vec{p}_j = \sum_{i=1}^N \vec{p}_i. \quad (7.28)$$

Additionally, I will also define an estimation of the deposited hadronic energy as:

$$E_j^{\text{dep}} = m_{^{39}\text{Ar}} - m_{^{40}\text{Ar}} + \sum_{i=1}^N \sqrt{|\vec{p}_i|^2 + m_i^2}. \quad (7.29)$$

This quantity is useful to select events with enough hadronic visible energy in the detector. For events where most of the hadronic energy is scattered across plenty of hadrons with individual energies below the detection threshold, this estimation will give $E_j^{\text{dep}} \leq 0$. In these cases it could be expected that the jet momentum is poorly reconstructed, and therefore I require events to pass the cut $E_j^{\text{dep}} > 0$.

For the events I can compute the angles for the muon and jet with respect to the

Chapter 7. DM searches with neutrinos from the Sun

2088 incoming neutrino as:

$$\cos \theta_\mu = \hat{p}_\nu \cdot \hat{p}_\mu, \quad (7.30)$$

$$\cos \theta_j = \hat{p}_\nu \cdot \hat{p}_j, \quad (7.31)$$

2089 and the deviation from the momentum conservation plane as:

$$\sin \theta_{plane} = \left| \frac{\hat{p}_\mu \times \hat{p}_\nu}{|\hat{p}_\mu \times \hat{p}_\nu|} \cdot \hat{p}_j \right|. \quad (7.32)$$

2090 In Fig. 7.11 I show some distributions of these quantities for the case of the $b\bar{b}$ sample
 2091 with $m_{DM} = 10$ GeV (blue histograms) and for the atmospheric backgrounds (red).
 2092 In order to select the atmospheric events I followed the same criteria as for the signal
 2093 events. However, because in the signal case I used the true direction of the neutrino
 2094 as input, as it should be that of the Sun at that time and therefore known, in the
 2095 atmospheric case I used a set of solar positions as our ansatz for the neutrino direction.
 2096 From the distributions, one can see that the muon and the jet for the signal events are
 2097 predominantly forward and also that the deviations from the momentum conservation
 2098 plane are peaked at zero, as one should expect.

2099 Now, I can start applying cuts to maximise our signal selection efficiency while at
 2100 the same time I try to minimise the amount of atmospheric background events passing
 2101 the selection. To this end, I will need to find some lower and upper cuts for θ_j and
 2102 θ_μ and an upper bound for θ_{plane} . In Fig. 7.12 I show how upper bound cuts in the
 2103 different angular variables affect the signal efficiency (blue lines) and the background
 2104 rejection (red lines). Notice that the signal efficiency behaves in a quite different way
 2105 when I apply cuts in the jet and the muon angles. On the contrary, the cuts on both
 2106 variables have a similar effect on the background rejection.

2107 In order to obtain the optimal set of cuts, I perform a multidimensional scan. I
 2108 do this separately for the $\tau^+\tau^-$ and the $b\bar{b}$ samples. For each case, I scan the possible
 2109 cuts for each mass point and then I take the mean value of the signal efficiency for

7.6. High energy DM neutrino signals

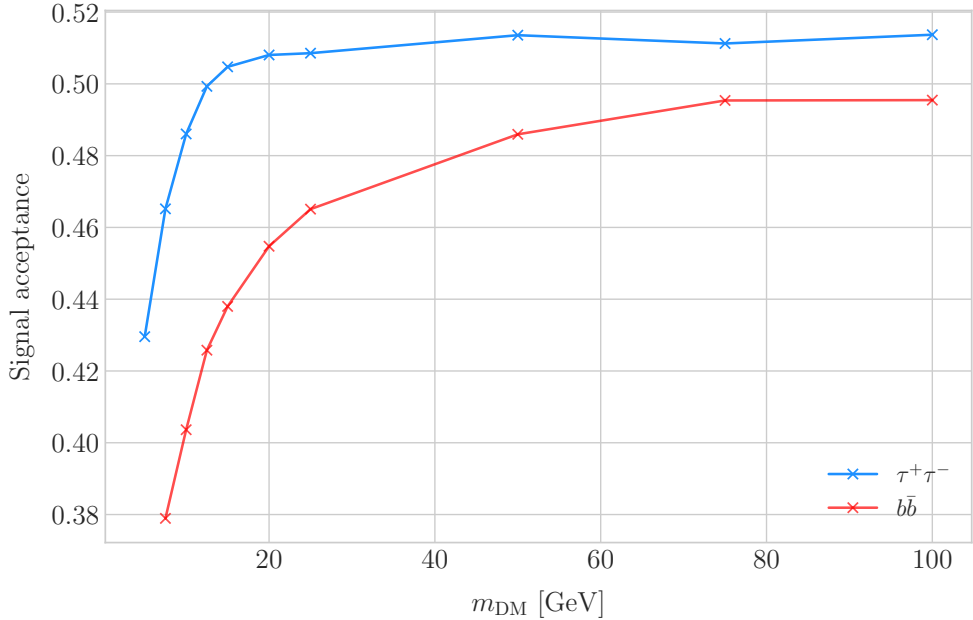


Figure 7.13: Signal efficiencies for the $\tau^+\tau^-$ (blue line) and $b\bar{b}$ (red line) DIS samples as functions of the DM mass, m_{DM} , obtained by applying the optimal angular cuts $\theta_\mu < 27^\circ$, $4^\circ < \theta_j < 26^\circ$ and $\theta_{\text{plane}} < 3.5^\circ$.

2110 each configuration, to get the mean efficiency for each set of cuts. I do a similar scan
 2111 for the atmospheric sample independently. Then, I take the sets of cuts such that
 2112 the background rejection achieved is greater than 99.8% and search for the one which
 2113 maximises the $\tau^+\tau^-$ and $b\bar{b}$ sample mean efficiencies. I found that with the cuts $\theta_\mu < 27^\circ$,
 2114 $4^\circ < \theta_j < 26^\circ$ and $\theta_{\text{plane}} < 3.5^\circ$ I get a background rejection of 99.80% while achieving
 2115 a 49.40% and 44.92% mean signal efficiencies for the $\tau^+\tau^-$ and $b\bar{b}$ signals respectively.

2116 In Fig. 7.13 I show the signal efficiencies as a function of the DM mass for the $\tau^+\tau^-$
 2117 (blue line) and the $b\bar{b}$ (red line) DIS events, after applying the cuts discussed above, as
 2118 well as the energy threshold and hadronic visible energy selections. One can see that
 2119 the efficiency grows with the mass, as annihilations of more massive DM particles will
 2120 produce a neutrino spectrum centered at higher energies, where DIS events dominate.
 2121 Notice also that the efficiency is higher for the $\tau^+\tau^-$ case at every mass point, as in
 2122 general this channel produces neutrinos at higher energies than the corresponding $b\bar{b}$
 2123 channel.

Chapter 7. DM searches with neutrinos from the Sun

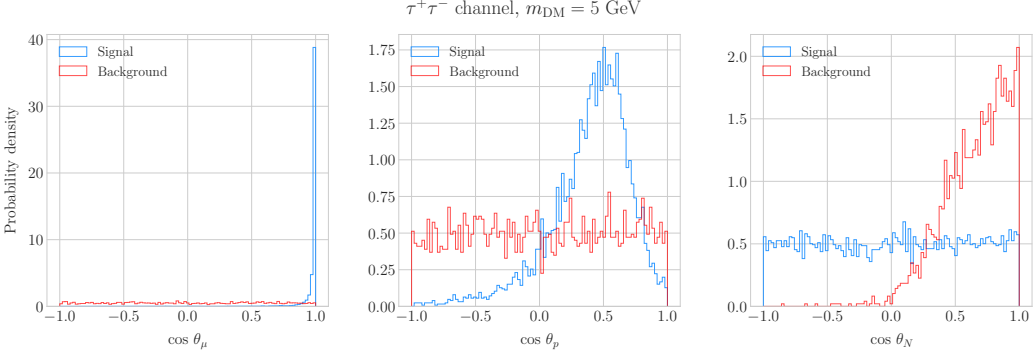


Figure 7.14: Distributions of $\cos \theta_\mu$ (left panel), $\cos \theta_p$ (central panel) and $\cos \theta_N$ (right panel) for the $\tau^+\tau^-$ QEL sample with $m_{\text{DM}} = 5$ GeV (blue) and the atmospheric background (red).

2124 7.6.2 Single proton QEL events

2125 Now, one can try to explore the low energy tail of the neutrino energy distributions. This
 2126 regime is dominated by the QEL interactions, i.e. events of the type $\nu_\mu + n \rightarrow \mu^- + p$.
 2127 In this case, as the typical energies are $E_\nu \lesssim 1$ GeV, the momentum transfer to the
 2128 remnant nucleus is sizeable. Therefore, I can not make the approximation I did before
 2129 and assume that the momentum of the muon and the proton will give an adequate
 2130 estimation of the reconstructed neutrino energy.

2131 In any case, as before, I can take the direction of the incoming neutrino as known.
 2132 That way, one can estimate the energy of the neutrino as:

$$E_\nu^{reco} = E_\mu + E_p + m_{^{39}\text{Ar}} - m_{^{40}\text{Ar}}, \quad (7.33)$$

2133 and using momentum conservation I can write the momentum of the remnant nucleus
 2134 as:

$$\vec{p}_N = \hat{p}_\nu (E_\mu + E_p + m_{^{39}\text{Ar}} - m_{^{40}\text{Ar}}) - \vec{p}_\mu - \vec{p}_p. \quad (7.34)$$

2135 As in the previous case, I need to drop the events where the muon or the proton fall
 2136 below the kinetic energy detection threshold [42]. Also, I again apply a smearing to the
 2137 momenta of the particles, a 1% for muons and 5% for protons.

2138 Having done that, one can compute the following angular variables for our selected

7.6. High energy DM neutrino signals

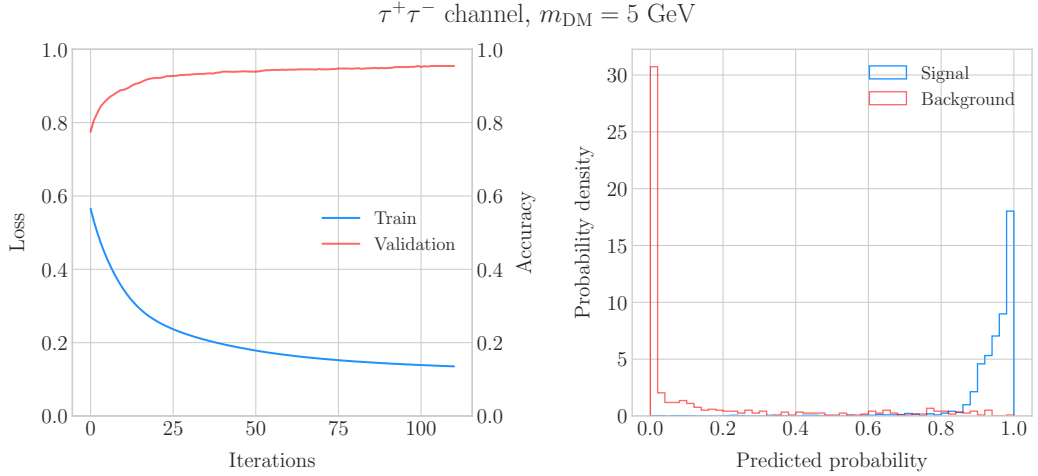


Figure 7.15: Left panel: value of the loss function for the training sample (blue line) and accuracy for the validation sample (red line) versus the number of iterations for the MLP classifier training. Right panel: distributions of the predicted probabilities assigned by the MLP classifier to the test sample for the $\tau^+\tau^-$ QEL signal with $m_{\text{DM}} = 5 \text{ GeV}$ (blue) and the atmospheric background (red).

2139 events:

$$\cos \theta_\mu = \hat{p}_\nu \cdot \hat{p}_\mu, \quad (7.35)$$

$$\cos \theta_p = \hat{p}_\nu \cdot \hat{p}_p, \quad (7.36)$$

$$\cos \theta_N = \hat{p}_\nu \cdot \hat{p}_N. \quad (7.37)$$

2140 Fig. 7.14 shows the distributions of these angular variables for the $\tau^+\tau^-$ QEL
 2141 sample with $m_{\text{DM}} = 5 \text{ GeV}$ (blue) and the atmospheric background (red). Again, for
 2142 the atmospheric events I used a random solar position as the ansatz for the incoming
 2143 neutrino direction. Notice that now, opposed to the DIS case where the signal had very
 2144 sharp distributions for the variables considered, the shapes of the angular distributions
 2145 for signal and background are not that much different.

2146 This effectively means that the usual approach of applying simple angular cuts would
 2147 not work as well as in the previous situation. Therefore, as a possible solution, I tried to
 2148 use a multilayer perceptron (MLP) classifier to separate between signal and background
 2149 events. Thus, the power of the hypothesis test will serve as an estimate of the signal

Chapter 7. DM searches with neutrinos from the Sun

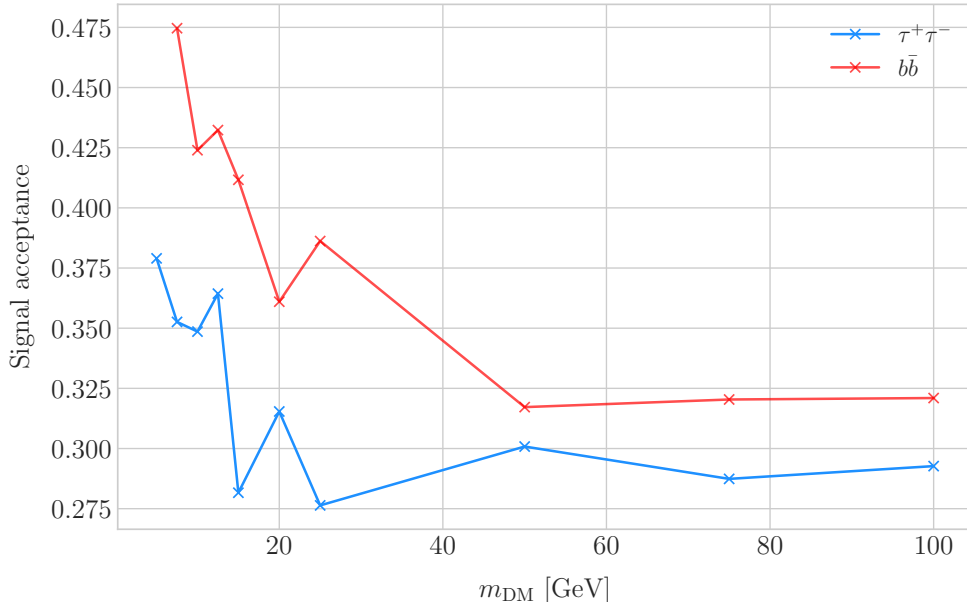


Figure 7.16: Signal efficiencies for the $\tau^+\tau^-$ (blue line) and $b\bar{b}$ (red line) single proton QEL samples as functions of the DM mass, m_{DM} , obtained by requiring a minimum predicted probability from the MLP classifier of 0.97 in order to achieve a background rejection greater than 99.8%.

efficiency, and in the same way one can take the size of the test to be our background rejection.

For each DM mass value and channel, as well as for the background sample, I divide our events into training, validation and test samples. The input variables for the classifier were the reconstructed neutrino energy from Eq. (7.33) and the angular variables defined in Eqs. (7.35 - 7.37). I used the MLP classifier implemented in `scikit-learn` [87], with a total of five hidden layers, the rectified linear unit activation function and adaptive learning rate. In order to account for fluctuations due to artifacts in the training process I repeated the training a thousand times for each sample, redefining each time the training, validation and test subsets, so one can take as our signal efficiency and background rejection the mean values of the powers and sizes of the tests.

The results of one of these training processes for the $\tau^+\tau^-$ QEL signal with $m_{\text{DM}} = 5$ GeV is shown in Fig. 7.15. On the left panel I show the loss function values (blue) and accuracy (red) at each iteration for the training and the validation samples respectively.

7.6. High energy DM neutrino signals

2164 The training stops either when the maximum number of iterations is reached (1000 in
2165 this case) or when the accuracy for the validation sample reaches a certain tolerance
2166 (I chose 10^{-4} as our tolerance). On the right panel I have the distributions for the
2167 predicted probability by the model, separated in true signal (blue) and background
2168 (red) events, for the test sample. One can see that both populations are well separated,
2169 obtaining a power of 44.97% and a size of 0.17% when I require a predicted probability
2170 greater than 0.97.

2171 Applying this criteria for each sample, I obtain the mean signal efficiencies shown in
2172 Fig. 7.16. Notice that the efficiencies for the channel $\tau^+\tau^-$ (blue line) are consistently
2173 lower than the ones for the $b\bar{b}$ channel (red line). This can be due to the fact that, for
2174 each DM mass point, the neutrino spectrum coming from the $b\bar{b}$ annihilation channel is
2175 centered at lower energies when compared to the $\tau^+\tau^-$ spectrum. This directly translates
2176 into more low energy neutrinos undergoing QEL interactions, which give signals that
2177 can be easily separated from the atmospheric background. This explanation also help us
2178 understand why in both cases the signal acceptance drops when the DM mass increases.
2179 In all cases, the background rejection took values between 99.8% to 99.9%. I will assume
2180 a 99.8% background rejection value in all cases to keep our estimation conservative.

2181 7.6.3 Results

2182 In order to estimate the DM-nucleon cross section sensitivities in the present case I need
2183 again to compute the expected number of background events. As I am now separating
2184 events by interaction type Eq. (7.25) does not hold anymore, as in that case I integrated
2185 over the total neutrino-argon cross section. In this instance, the expected background
2186 events for DIS events is approximately given by:

$$N_B^{DIS} \simeq \eta_B^{DIS} \times (4.655 \times 10^3) \times \left(\frac{\text{exposure}}{400 \text{ kT yr}} \right), \quad (7.38)$$

Chapter 7. DM searches with neutrinos from the Sun

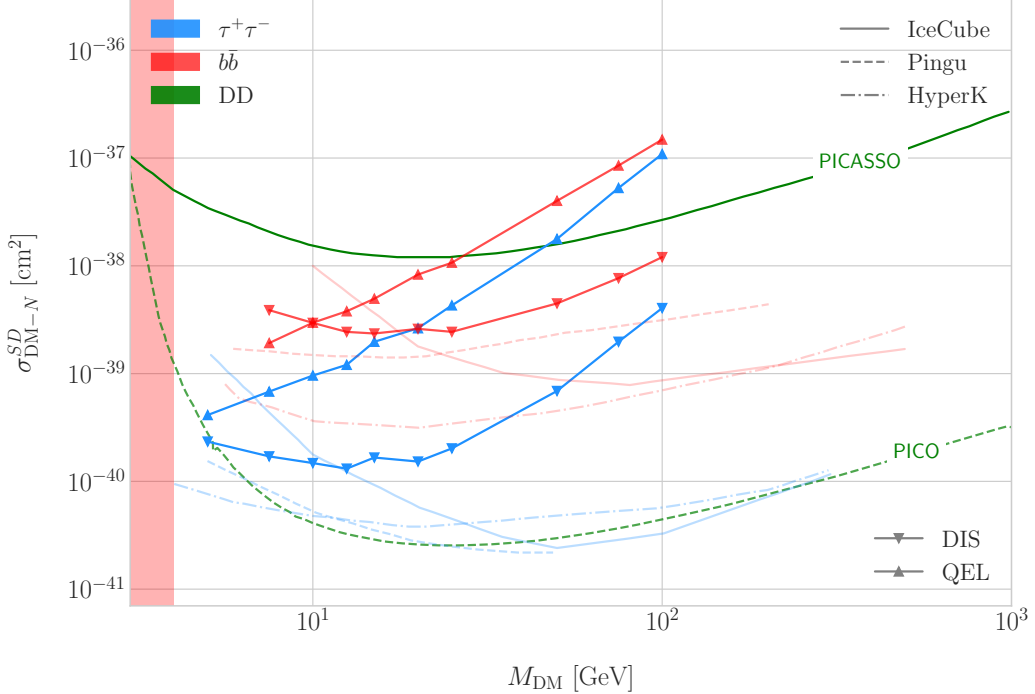


Figure 7.17: Projected 90% confidence level upper limit for DUNE (400 kT yr) on the spin-dependent DM-nucleon scattering cross section as a function of m_{DM} , for the annihilation channels $\tau^+\tau^-$ (blue) and $b\bar{b}$ (red) separated by interaction type (up triangles denote DIS interactions whereas down triangles represent QEL interactions). I also show the previous limits from IceCube [9] (solid lines) and the projected sensitivities for Pingu [10] (dashed lines) and Hyper-Kamiokande [11] (dash-dotted lines), as well as the direct detection limits from PICASSO [12] (solid green line) and PICO-60 C₃F₈ [13] (dashed green line).

2187 whereas for QEL events we have:

$$N_B^{QEL} \simeq \eta_B^{QEL} \times (2.248 \times 10^4) \times \left(\frac{\text{exposure}}{400 \text{ kT yr}} \right). \quad (7.39)$$

2188 Now, using these together with Eqs. (7.26) and (7.27) one can obtain the 90% C.L.
 2189 upper limit on the total annihilation rate at equilibrium for both kind of events. Then,
 2190 applying the computed DM-nucleons capture rates I can translate these into limits on
 2191 the DM-nucleon cross section by means of Eqs. (7.2), (7.5) and (7.6).

2192 Fig. 7.17 shows the obtained limits on the SD DM-nucleon cross section for DUNE,
 2193 using the DIS (up triangles) and QEL (down triangles) events both for the $\tau^+\tau^-$ (blue)
 2194 and the $b\bar{b}$ (red) samples, for an exposure of 400 kT yr. I also include the corresponding

7.7. Example: Leptophilic Dark Matter

2195 current limits from IceCube [9] (solid lines), as well as the projected sensitivities of Pingu
2196 [10] (dashed lines) and Hyper-Kamiokande [11] (dash-dotted lines). For comparison, I
2197 also show the reported direct detection limits from PICASSO [12] (solid green line) and
2198 PICO-60 C₃F₈ [13] (dashed green line).

2199 Notice that, for most of the mass range, the limits one can set by using the DIS
2200 events are stronger than those of the QEL interactions, except for the low mass part
2201 of both the $\tau^+\tau^-$ and the $b\bar{b}$ curves where the QEL events dominate. In general, the
2202 expected sensitivity of DUNE for DM masses $\lesssim 25$ GeV surpasses the stronger current
2203 indirect limits. However, experiments like Hyper-Kamiokande are foreseen to have an
2204 overall better sensitivity in this kind of searches, as they have a bigger active volume
2205 and accept a broader energy range.

2206 A pending question is what happens when we add the RES and MEC charged-current
2207 interaction contributions. In that case it would probably be more convenient to split
2208 the samples by final state interaction topologies. Also, another necessary improvement
2209 would be adding a full detector simulation and reconstructions. This will also require
2210 considering the effect of poorly reconstructed events or final states containing neutral
2211 particles such that they mimic the desired topology at the reconstruction level.

2212 7.7 Example: Leptophilic Dark Matter

2213 In general, the capture rate of DM particles by the Sun via interactions with electrons is
2214 several orders of magnitude smaller than the capture via DM-nucleus scattering. Thus,
2215 it would be sub-leading even when nucleon capture is loop suppressed. As I showed in
2216 Fig. 7.2, the capture rate via scattering off electrons only surpasses the capture rates
2217 via DM-nucleons interactions for DM masses $\lesssim 100 - 500$ MeV.

2218 However, if one considers a model where DM-nucleon interactions are forbidden even
2219 at loop level, then electron interactions will be the sole contributor to DM capture in
2220 the Sun. One can describe such scenario where the DM particles couple to leptons but
2221 not to the quark sector using effective operators.

Chapter 7. DM searches with neutrinos from the Sun

2222 In general, assuming that the DM particle is a Dirac fermion, the dimension six
 2223 operators describing the interaction between two DM particles and two leptons can be
 2224 written as:

$$\mathcal{L}_{eff} = G \sum_i (\bar{\chi} \Gamma_\chi^i \chi) (\bar{\ell} \Gamma_\ell^i \ell), \quad (7.40)$$

2225 where $G = 1/\Lambda^2$ is the effective coupling strength, Λ the cut-off of the effective field
 2226 theory and ℓ denotes any lepton. In principle, one should consider all the possible
 2227 Lorentz structures Γ_f^i in order to have a complete set of effective operators.

2228 However, some combinations will induce interactions with nucleons at loop level. As
 2229 we are specifically interested in interactions which forbid any communication with the
 2230 quark sector, I will not consider those [88]. In addition, some of the effective operators
 2231 give rise to velocity-suppressed scattering cross sections between DM particles and
 2232 leptons. I will also neglect those, as the suppression goes with the square of the DM
 2233 halo velocity which in units of the speed of light is $\sim 10^{-6}$.

2234 This way, the only Lorentz tensor structure that do not induce interactions with
 2235 quarks at loop level and gives a contribution to the scattering cross section that is not
 2236 velocity suppress is the axial-axial interaction. The effective Lagrangian is then given
 2237 by:

$$\mathcal{L}_{eff} = \frac{c_A^\chi c_A^\ell}{\Lambda^2} (\bar{\chi} \gamma^\mu \gamma^5 \chi) (\bar{\ell} \gamma_\mu \gamma^5 \ell), \quad (7.41)$$

2238 where c_A^χ and c_A^ℓ are the couplings for the different species. As the DM coupling appears
 2239 as a common factor for any lepton choice, I will redefine the corresponding coupling c_A^ℓ
 2240 to absorb c_A^χ . Also, for simplicity, I will assume that the couplings between the DM
 2241 particles and the leptons are flavour independent, i.e. I have just two couplings, c_A^e for
 2242 charged leptons and c_A^v for neutrinos.

2243 In the case of a scalar DM particle, the lowest order effective interaction with
 2244 leptons happens through a dimension five operator, generating scalar and pseudoscalar
 2245 interactions. However, the former induces interactions with quarks at two loop level
 2246 whereas the latter gives a velocity suppressed scattering cross section.

2247 From the effective Lagrangian in Eq. (7.41) it can be shown that the axial-axial

7.7. Example: Leptophilic Dark Matter

2248 contribution to the scattering cross section for the fermionic DM and a charged lepton
2249 is given by:

$$\sigma_{\text{DM}-e}^{AA} = 3(c_A^e)^2 \frac{m_e^2}{\pi \Lambda^4}. \quad (7.42)$$

2250 If the DM interacts exclusively with fermions, then the only annihilation channels
2251 that will give us a measurable neutrino flux coming out of the Sun are $\tau^+\tau^-$ and $\nu\bar{\nu}$. The
2252 former channel, already explored previously in the more mainstream scenario of the DM
2253 capture via scattering off nucleons, is open only for $m_{\text{DM}} > m_\tau \simeq 1776.86 \pm 0.12$ MeV
2254 [89], a mass region where the solar DM capture by electrons is at least one order of
2255 magnitude smaller than the capture via interactions with nucleons. On the contrary, the
2256 latter allows us to explore a region where the capture rate via scattering off electrons
2257 dominates over the rest.

2258 One downside of focusing in such low mass range is that it falls below the usual
2259 limit of $m_{\text{evap}} \sim 4$ GeV usually explored in the literature. The pretext to explore this
2260 region is the result discussed previously reported in Ref. [4], where DM evaporation in
2261 the Sun for the case of capture via electron scattering could be negligible for masses
2262 as low as $m_{\text{evap}} \sim 200$ MeV. This result is quite sensitive to the high velocity tail of
2263 the DM velocity distribution in equilibrium inside the Sun, and therefore full numerical
2264 simulations would be needed to assess the impact of this effect. However, this falls out of
2265 the scope of our work.

2266 In this case, as I have a specific realisation of the interaction between the DM
2267 and leptons, one can estimate the relic density of our DM for different values of the
2268 couplings and the effective field theory scale Λ . The first step to do so is compute the
2269 self-annihilation cross section. Because I consider cold relics, at the freeze-out time our
2270 DM particles were non-relativistic and so one can expand the annihilation cross section
2271 in terms of the relative velocity v between two annihilating DM particles as [90]:

$$\sigma_{\text{ann}}^{AA}|v| \approx \frac{1}{2\pi\Lambda^4} \sum_\ell \left(c_A^\ell\right)^2 m_\chi^2 \sqrt{1 - \frac{m_\ell^2}{m_\chi^2} \left[\frac{m_\ell^2}{m_\chi^2} + \frac{1}{12} \left(2 - \frac{m_\ell^2}{m_\chi^2}\right) v^2 \right]}, \quad (7.43)$$

Chapter 7. DM searches with neutrinos from the Sun

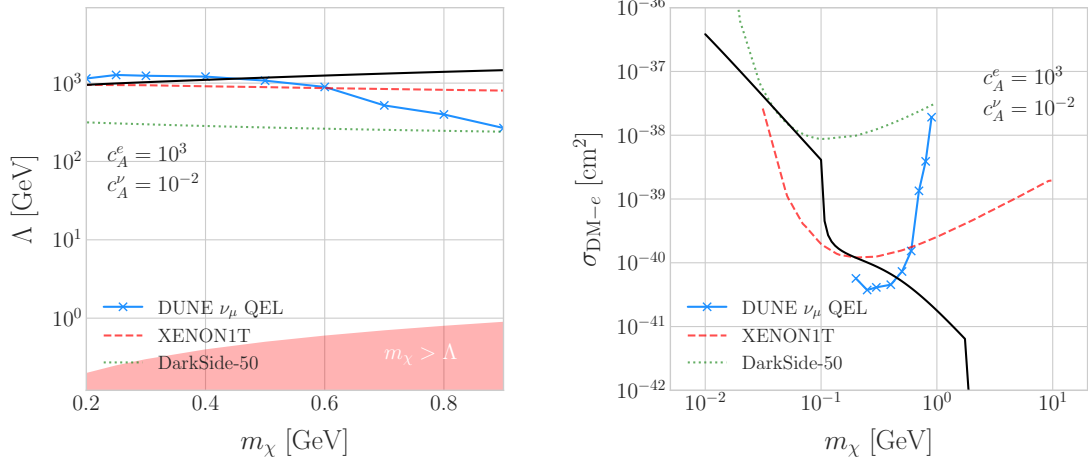


Figure 7.18: Left panel: Projected 90% confidence level sensitivity of DUNE (400 kT yr) to the scale Λ of an EFT containing only leptophilic DM axial-axial interactions (blue line). Right panel: In both cases the corresponding limits from DarkSide-50 [14] (dotted green line) and XENON1T [15] (dashed red line) are also shown, together with the configurations for which the correct relic density is achieved (black line), all for the coupling values $c_A^e = 10^3$ and $c_A^\nu = 10^{-2}$.

2272 where the sum includes all the possible lepton final states with mass m_ℓ .
 2273 Solving the Boltzmann equation for the evolution of the DM density gives as a
 2274 solution a relic density of:

$$\Omega_\chi h^2 \approx \frac{(1.04 \times 10^9) x_F}{M_{Pl} \sqrt{g_*} (a + 3b/x_F)}, \quad (7.44)$$

2275 where $x_F = m_\chi/T_F$ being T_F the freeze-out temperature, g_* the number of relativistic
 2276 degrees of freedom at freeze-out and a and b the terms in the annihilation cross section
 2277 expansion $\sigma_{ann}|v| \approx a + bv^2 + \mathcal{O}(v^4)$. Using the current best fit for the relic DM density
 2278 $\Omega_\chi h^2 = 0.1198 \pm 0.0012$ [91] one can use these relations to compute the required effective
 2279 theory scale Λ at which the correct density is achieved for any combinations of m_χ and
 2280 c_A^ℓ .

2281 As discussed before, in the low DM mass region QEL interactions dominate. Moreover,
 2282 if I focus on direct annihilation to neutrinos, the energy of the muon neutrino flux is
 2283 known as it must be equal to the mass of the DM particle, $E_\nu = m_\chi$. That way, now
 2284 I do not need to use Eq. (7.33) in order to estimate the momentum transfer to the

7.7. Example: Leptophilic Dark Matter

2285 remnant nucleus, I can simply take:

$$\vec{p}_N = \hat{p}_\nu m_\chi - \vec{p}_\mu - \vec{p}_p. \quad (7.45)$$

2286 To estimate the signal efficiency and background rejection for this case I used again
2287 the MLP classifier from `scikit-learn`, using the same specifications as before. The
2288 only difference now is that I add also the reconstructed neutrino energy as one of the
2289 features to train the classifier with, because the characteristic monoenergetic flux for
2290 each m_χ value will help to distinguish between signal and background events.

2291 In this case, for masses below ~ 500 MeV I obtain a signal efficiency close to unity
2292 while keeping a background rejection of 99.9%. For bigger values of the mass, the signal
2293 efficiency drops significantly if I require to keep the background acceptance under 0.01%.
2294 However, because this kind of search is dominated by the background, sacrificing the
2295 signal acceptance to keep the background rejection to a minimum enhances the reach
2296 of the analysis. This way, for DM masses of the order of $m_\chi \sim 1$ GeV I end up with
2297 efficiencies as low as 1%.

2298 Now, estimating the number of background events using Eq. (7.39) one can go on
2299 and apply Eqs. (7.26) and (7.27) together with Eq. (7.42) to derive the sensitivity of
2300 DUNE to this kind of model. Fig. 7.18 (left panel) shows the potential reach of DUNE
2301 to constrain the EFT scale Λ this model containing only leptophilic DM axial-axial
2302 interactions (blue line), for a choice of couplings $c_A^e = 10^3$ and $c_A^\nu = 10^{-2}$. I also included
2303 the current limits on the DM-electron scattering cross section from DarkSide-50 [14]
2304 (dotted green line) and XENON1T [15] (dashed red line), reworked with Eq. (7.42) to
2305 show their implications for the EFT scale. The values of Λ for which the correct DM relic
2306 density value is achieved for each mass are also shown (black line). This tells us that,
2307 for that specific choice of couplings, DUNE would be sensitive to DM configurations
2308 allowed by the relic density constraint up to a mass of $m_\chi \sim 400$ MeV.

2309 In Fig. 7.18 (right panel) I show the same upper limits but for the DM-electron
2310 scattering cross section. From this view one can see that DUNE would be able to

Chapter 7. DM searches with neutrinos from the Sun

2311 offer complementary information to the low energy DM-electron interaction searches
2312 performed by direct detection experiments, in a slightly higher mass range.

2313 With the present example, although it focuses on a very specific realisation of the DM
2314 interactions, I show the potential of DUNE to constrain exotic DM scenarios. Thanks
2315 to its low backgrounds and superb angular resolution DUNE will be able to help with
2316 the systematic searches for dark sectors physics.

2317 Chapter 8

2318 Particle ID in GArSoft

2319 ND-GAr is a magnetised, high-pressure gaseous argon TPC (HPgTPC), surrounded by
2320 an electromagnetic calorimeter (ECal) and a muon detector (commonly refer to as μ ID).
2321 A detailed discussion on the requirements, design, performance and physics of ND-GAr
2322 can be found in the DUNE ND CDR [48] and the ND-GAr whitepaper (cite).

2323 In DUNE Phase II ND-GAr will fulfill the role of TMS, measuring the momentum
2324 and sign of the charged particles exiting ND-LAr. Additionally, it will be able to measure
2325 neutrino interactions inside the HPgTPC, achieving lower energy thresholds than those
2326 of the ND and FD LArTPCs. By doing so ND-GAr will allow to constrain the relevant
2327 systematic uncertainties for the LBL analysis even further.

2328 The goal of the present chapter is to review the requirements that the physics program
2329 of DUNE impose on ND-GAr, present the current status of its design and describe the
2330 GArSoft package, its simulation and reconstruction software.

2331 As decided during the DUNE Phase II workshop in June 2023 [reference], we want
2332 to build ND-GAr physics case by showing:

- 2333 • That ND-GAr can constrain systematic uncertainties that ND-LAr might miss.
- 2334 • The impact on the neutrino oscillation results if such systematic uncertainties are
2335 missed.
- 2336 • That ND-GAr is necessary to reach DUNE's main physics goals.

Chapter 8. Particle ID in GArSoft

2337 This way, the design of ND-GAr will be physics driven.

2338 In order to study the effects of final state interactions (FSI) in CC interactions,
2339 ND-GAr should be able to measure the spectrum of protons and charged pions at low
2340 energies. ND-GAr also needs to be able to measure the pion multiplicity, specially for
2341 energies above 100 MeV as at these energies the pions shower in the LAr, to inform the
2342 pion mass correction in the ND and FD LArTPCs.

2343 In order to correctly identify electrons, muons, pions, kaons and protons ND-GAr
2344 can use a combination of: dE/dx measurements in the HPgTPC, E_{ECAL}/p using the
2345 ECAL total energy and the momentum obtained from magnetic spectroscopy in the
2346 HPgTPC and penetration information through the ECAL and muon tagger.

2347 8.1 dE/dx measurement in the TPC

2348 Among the parameters extracted from the track fitting, ionisation is particularly useful
2349 for particle identification, as it is a function of the particle velocity. Although for the
2350 case of relativistic particles this dependence is not very strong, measuring the track on
2351 a large number of points may allow us to estimate the amount of ionisation accuratel.
2352 This, paired with a measurement of the momentum, may allow us to identify the particle
2353 type.

2354 The first calculation of the energy loss per unit length of relativistic particles using
2355 a quantum-mechanical treatment is due to Bethe [?]. Using this approach, the mean
2356 ionisation rate of a charged particle traveling through a material medium is (using
2357 natural units $G = \hbar = c = 1$):

$$\left\langle \frac{dE}{dx} \right\rangle = \frac{4\pi Ne^4}{m_e \beta^2} z^2 \left(\log \frac{2m_e \beta^2 \gamma^2}{I} - \beta^2 \right), \quad (8.1)$$

2358 where N is the number density of electrons in the medium, e the elementary charge, m_e
2359 is the electron mass, z the charge of the particle in units of e , β is the velocity of the
2360 particle, $\gamma = (1 - \beta^2)^{-1}$ and I denotes the effective ionisation potential averaged over
2361 all electrons. This relation is known as the Bethe-Bloch formula.

8.1. dE/dx measurement in the TPC

From Eq. (8.1) one can see that the ionisation loss does not depend explicitly on the mass of the charged particle, that for non-relativistic velocities it falls as β^{-2} , then goes through a minimum and increases as the logarithm of γ . This behaviour at high velocities is commonly known as the relativistic rise. The physical origin of this effect is partly due to the fact that the transverse electromagnetic field of the particle is proportional to γ , therefore as it increases so does the cross section.

It was later understood that the relativistic rise could not grow indefinitely with γ . A way to add this feature in the Bethe-Bloch formula is by introducing the so-called density effect term. It accounts for the polarisation effect of the atoms in the medium, which effectively shield the electromagnetic field of the charged particle halting any further increase of the energy loss [?]. Denoting the correction as $\delta(\beta)$, one can rewrite Eq. (8.1) as:

$$\left\langle \frac{dE}{dx} \right\rangle = \frac{4\pi Ne^4}{m_e \beta^2} z^2 \left(\log \frac{2m_e \beta^2 \gamma^2}{I} - \beta^2 - \frac{\delta(\beta)}{2} \right). \quad (8.2)$$

In general, the form of $\delta(\beta)$ depends on the medium and its state of aggregation, involving the usage of tabulated parameters and implicit relations [?].

Another standard method to compute the amount of ionisation a charged particle produces is the so-called photo-absorption ionisation (PAI) model proposed by Allison and Cobb [?]. Within their approach, the mean ionisation is evaluated using a semiclassical calculation in which one characterises the continuum material medium by means of a complex dielectric constant $\epsilon(k, \omega)$. However, in order to model the dielectric constant they rely on the quantum-mechanical picture of photon absorption and collision. Therefore, in the PAI model the computation of the ionisation loss involves a numerical integration of the measured photo-absorption cross-section for the relevant material.

In a particle physics experiment, the typical way of determining the energy loss per unit length as a function of the particle velocity is studying identified particles over a range of momenta. Once we have established this relation we can use it for other, unknown particles. In this sense, it makes sense to have a regular mathematical expression for this relation that one can use.

Chapter 8. Particle ID in GArSoft

2389 It happens that neither the Bethe-Bloch theory nor the PAI model from Allison and
2390 Cobb offer a close mathematical form for the ionisation curve. This is the reason why a
2391 full parametrisation of the ionisation curves can be useful. A parametrisation originally
2392 proposed for the ALEPH TPC [?] and later used by the ALICE TPC [?] group that
2393 manages to capture the features of the ionisation energy loss is:

$$f(\beta\gamma) = \frac{P_1}{\beta^{P_4}} \left(P_2 - \beta^{P_4} - \log \left[P_3 + \frac{1}{(\beta\gamma)^{P_5}} \right] \right), \quad (8.3)$$

2394 where P_i are five free parameters. Hereafter, we will refer to Eq. (8.3) as the ALEPH
2395 dE/dx parametrisation.

2396 8.1.1 Energy calibration

2397 In order to obtain the amount of energy loss by a charged particle due to ionisation
2398 in our TPC we need to determine the conversion between the charge deposited in our
2399 readout planes and the actual energy depositions. This procedure is known as energy
2400 calibration.

2401 In a general, the first step of the calibration involves a non-uniformity correction,
2402 to make sure that the detector response is uniform throughout the TPC. These are
2403 typically divided into three categories, non-uniformities in the transverse YZ plane,
2404 non-uniformities along the drift direction X and variations of the detector response
2405 over time (would not apply to us as the detector is not built yet). These would correct
2406 for effects such as electron diffusion and attenuation, space charge effects or channel
2407 misconfiguration. However, because at the moment I am only interested in making sure
2408 we recover a sensible result from our simulation, I will not apply uniformity corrections
2409 to our charge deposits.

2410 Other effects, like electron-ion recombination or ADC saturation, lead to a non-linear
2411 relation between the observed charge and the deposited energy in the detector, with the
2412 observed readout charge saturating at high ionisation energies. In this case, because we
2413 are dealing with gaseous argon and therefore recombination is not as important as in

8.1. dE/dx measurement in the TPC

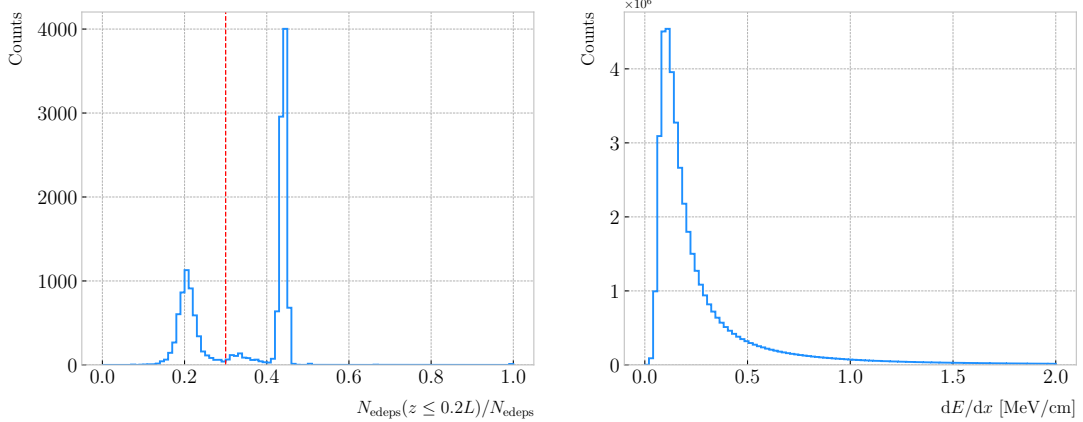


Figure 8.1: Left panel: distribution of the fraction of Geant4-level energy deposits per track with residual range less than 20% of the total track length, for the isotropic proton sample. Right panel: distribution of the ionisation per unit length of the energy deposits in the proton sample after removing the tracks with less than 30% of their energy deposits in the last 20% of the track.

2414 liquid, we do not simulate recombination effects in the TPC. Even so, the simulation of
 2415 the electronic response will still introduce charge saturation, and one needs to correct
 2416 for it in order to obtain the exact amount of energy loss due to ionisation.

2417 By default, the track fitting algorithm in GArSoft provides a `TrackIonization`
 2418 object associated to each reconstructed track. It contains two collections of charge
 2419 deposits, one for each fitting direction, consisting on pairs of charge values (dQ , in ADC)
 2420 and step sizes (dx , in cm).

2421 In order to estimate the ionisation loss in the ND-GAr TPC, I have used an MC
 2422 sample consisting of single, isotropic protons propagating in the TPC. The starting points
 2423 of the protons were sampled inside a $50 \times 50 \times 25$ cm box centered at $(100, -150, 1250)$,
 2424 and their momenta are uniformly distributed in the range $0.25 - 1.75$ GeV. I ran the
 2425 simulated sample through GArSoft's default detector simulation and reconstruction, and
 2426 then a custom analyser module that extracts the ionisation data together with other
 2427 reconstructed track information from the Kalman fit.

2428 For studying the energy loss of the protons I select the reconstructed tracks that
 2429 range out (i.e. slow down to rest) inside the TPC. A characteristic feature of the energy
 2430 loss profile of any stopping ionising particle is the so-called Bragg peak, a pronounced

Chapter 8. Particle ID in GArSoft

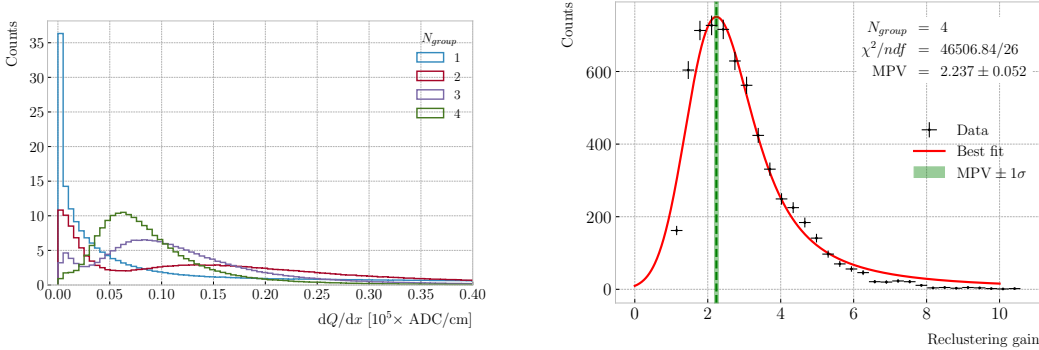


Figure 8.2: Left panel: distribution of the reconstructed ionisation charge per unit length for our MC stopping proton sample. The different colors indicate how many consecutive dQ/dx pairs were grouped together. Right panel: distribution of the median change in dQ/dx per track after $N_{group} = 4$ clusters were reclustered together.

peak that occurs immediately before the particle comes to rest. From Eq. (8.1) we can see that this behaviour is expected, as the energy loss for non-relativistic particles is inversely proportional to β^2 . In data, a way of identifying the Bragg peak, and thus select the stopping particles, is checking the number of energy deposits towards the end of the track. In this case, I count the fraction of the Geant4 simulated energy deposits with a residual range value (the distance from a given energy deposit to the last deposit in the track trajectory) less than a 20% of the corresponding track length¹. The distribution of this fraction of energy deposits for our proton sample is shown in Fig. 8.1 (left panel). We can clearly see two well separated peaks in this distribution, one centered at 0.2 and another, narrower, one centered at a higher value. The first one corresponds to non-stopping protons, as in that case the number of energy deposits towards the end of the track is uniformly distributed due to the absence of the Bragg peak. In that way, I apply a cut in this distribution, requiring that at least 30% of the simulated energy deposits sit in the last 20% of the tracks, to ensure that the Bragg peak is present.

Figure 8.1 (right panel) shows the distribution of the energy loss per unit length for the Geant4 simulated energy deposits of the selected stopping protons. We can see that

¹As we are applying this selection at the Geant4 level we could have simply selected the stopping protons using the `EndProcess` labels from the simulation. However, the Bragg peak identification method displayed here could serve as a starting point for a selection of stopping protons in real data.

8.1. dE/dx measurement in the TPC

it follows the expected shape of a Landau distribution, which describes the fluctuations of the ionisation energy losses [?]. This distribution has a characteristic asymmetric PDF, with a long right tail that translates into a high probability for high-energy ionisation losses. The origin of these fluctuations is mainly the possibility of transferring a high enough energy to an electron, so it becomes a ionising particle itself.

Now, from the point of view of the reconstruction, the objects that we have available to extract the ionisation information for the different reconstructed tracks are the collections of dQ and dx pairs, as stated before. The dQ values come from adding up the amplitude of all the reconstructed hits in a cluster, which is the input object to the Kalman fit.

Figure 8.2 (left panel) shows the distribution of the ionisation charge deposits per unit length for the track in the stopping proton sample (blue line). As one can notice, this distribution does not resemble the expected shape of the Landau PDF. This distribution peaks sharply at 0 and has a heavy tailed behaviour. Notice, however, how the distribution changes its shape as we group together N_{group} consecutive charge deposit pairs (red, purple and green lines). The distribution in the $N_{group} = 4$ case already has a shape which resembles that of the Geant4-level ionisation per unit length, so I will proceed using this amount of reclustering for the reconstruction-level depositions.

An extra factor I need to account for, when reclustering is applied, is how the overall dQ/dx per track changes. To do so, we can look at the ratio between the median dQ/dx after and before the reclustering. Figure 8.2 (right panel) shows the median enhancement in dQ/dx per track for the stopping proton sample in the case $N_{group} = 4$. Fitting a Landau distribution convolved with a Gaussian², I estimate the most probable value of this ratio to be $G_{group} = 2.24 \pm 0.05$.

At this point, I am left with determining the conversion between the charge deposits per unit length dQ/dx and the energy deposits per unit length dE/dx . To this end, we need a way of comparing the two. I can use the residual range z to get a prediction of

²In the literature, this distribution is often referred to as Landau+Gaussian or langau. In the following, I will use LanGauss to refer to such PDF.

Chapter 8. Particle ID in GArSoft

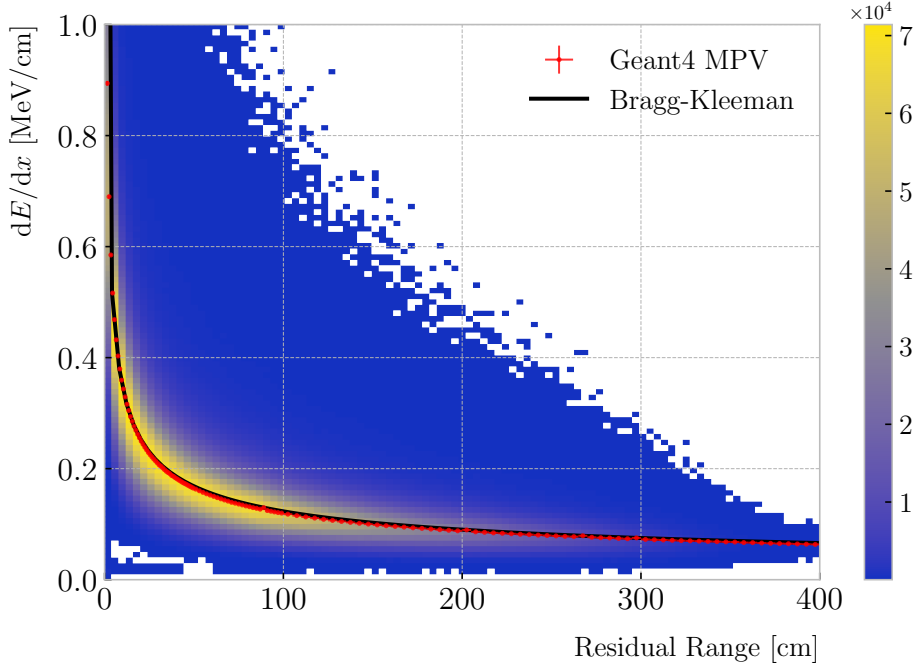


Figure 8.3: Distribution of the Geant4-simulated energy losses per unit length versus residual range for the stopping proton sample. The overlaid points represent the fitted most probable value of the dE/dx distribution in each residual range bin, whereas the curve is their best fit to the Bragg-Kleeman formula from Eq. (8.4).

2475 the most probable dE/dx by using the following empirical parametrisation [?]:

$$\frac{dE}{dx}(z) = \frac{z^{\frac{1}{p}-1}}{p\Lambda^{\frac{1}{p}}}, \quad (8.4)$$

2476 which is quoted in the literature as the Bragg-Kleeman formula. In order to obtain the
 2477 p and Λ parameters I perform a fit using the energy losses and the residual ranges given
 2478 by the Geant4 stage of our proton sample.

2479 Within our simulation, the residual range is sampled with a maximum size of
 2480 5 mm. Therefore, to perform the fit to the Bragg-Kleeman formula, we can use a
 2481 fine-grained residual range binning. For each of the residual range bins I extract the
 2482 dE/dx distribution and fit it to a LanGauss distribution, to obtain the value of the
 2483 most probable dE/dx in the bin together with a statistical uncertainty. I then fit Eq.
 2484 (8.4) to these most probable values and the centres of the residual range bins. This

8.1. dE/dx measurement in the TPC

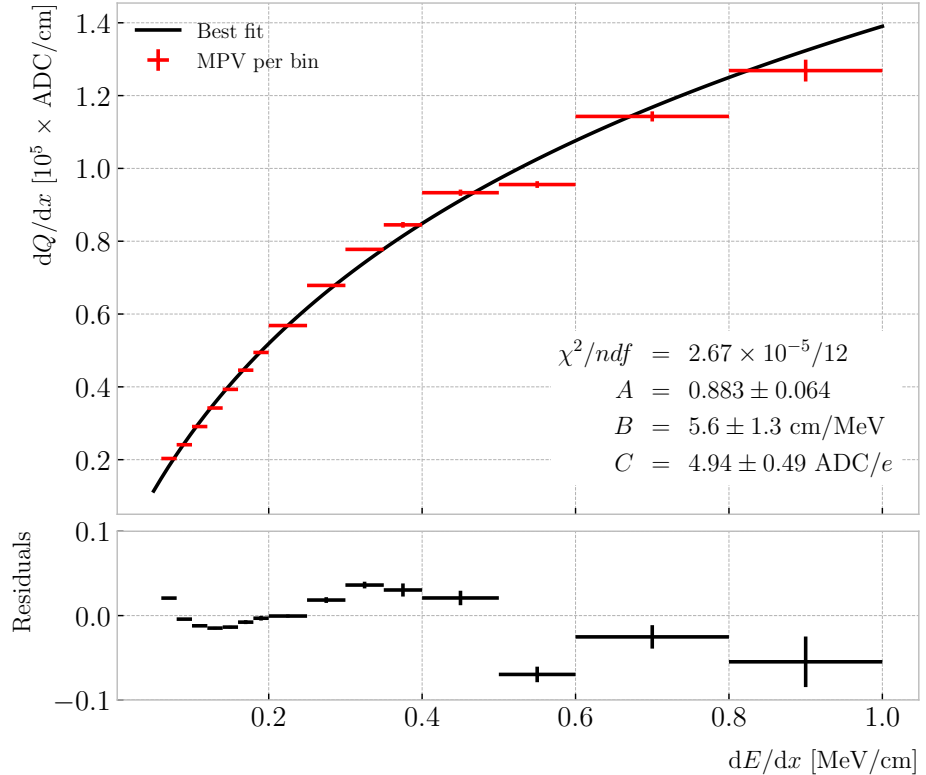


Figure 8.4: Fitted most probable dQ/dx values for each dE/dx bin (red points), obtained from the stopping proton sample. The overlaid curve (black line) represents the best fit to the logarithmic calibration function from Eq. (8.5).

procedure is depicted in Fig. 8.3, where I show the distribution of the energy loss per unit length versus the residual range, together with the most probable dE/dx values and their uncertainty in each bin (red points) and the curve with the best fit of the Bragg-Kleeman relation to those values (black line). The best fit is obtained for the parameter values $p = 1.8192 \pm 0.0005$ and $\Lambda = 0.3497 \pm 0.0008$ cm/MeV³.

Having an analytical expression that relates the residual range to dE/dx , I can take our reconstruction-level residual ranges from the stopping proton sample and compute the most probable energy loss associated.

In order to parametrise the charge saturation, we can use the following logarithmic

³These strange units for Λ come from dimensional analysis, just to keep the Bragg-Kleeman formula (8.4) consistent.

Chapter 8. Particle ID in GArSoft

2494 function inspired by the modified box model for recombination:

$$\frac{dE}{dx} = \frac{e^{\frac{dQ}{dx}B\frac{W_{ion}}{G_{group}C}} - A}{B}, \quad (8.5)$$

2495 where A and B are the calibration parameters we need to determine, W_{ion} is the average
2496 energy to produce an electron-ion pair, G_{group} is the gain from the reclustering discussed
2497 above and C is the calibration constant to convert number of electrons to ADC counts,
2498 commonly refer to as gain (also to be obtained in the fit). In this case, I use a value for the
2499 electron-ion production energy of $W_{ion} = 26.4$ eV [?]. This value, used in our simulation
2500 as well, was measured for gaseous argon in normal conditions, and therefore should
2501 be checked in the future to describe correctly the high-pressure argon-CH₄ mixture of
2502 ND-GAr.

2503 For the calibration fit I follow a procedure similar to the previous one for Eq. (8.4).
2504 Binning the dE/dx range, I fit a LanGauss distribution to the corresponding dQ/dx
2505 distribution to obtain the most probable value. The resulting data points (red bars) are
2506 shown in Fig. 8.4 (top panel), the horizontal error bars depict the width of the dE/dx
2507 bin whereas the vertical bars represent the error associated to the most probable value
2508 estimation. A fit to the logarithmic function in Eq. (8.5) is also shown (black line).
2509 For this I weighted the data points using the inverse of their relative error, obtaining
2510 a reduced chi-square value of $\chi^2/ndf = 2.22 \times 10^{-6}$. The best fit parameters I found
2511 from this fit are $A = 0.883 \pm 0.064$, $B = 5.6 \pm 1.3$ cm/MeV and $C = 4.94 \pm 0.49$ ADC/e.
2512 Figure 8.4 (bottom panel) shows the residuals between the data points and the fit.

2513 The value for the gain I obtained from the fit is in reasonable agreement with our
2514 expectation. This value is set in GArSoft to 5 ADC/e by default.

2515 One interesting thing to check is what induces this non-linear relation between charge
2516 and energy. The only effects that modify the amount of electrons reaching the readout
2517 planes in the simulation are the transverse diffusion and the finite electron lifetime.
2518 Once the electrons reach the readout chambers, the pad response functions are applied,
2519 together with an electrons-to-ADC conversion and the ADC saturation limit.

8.1. dE/dx measurement in the TPC

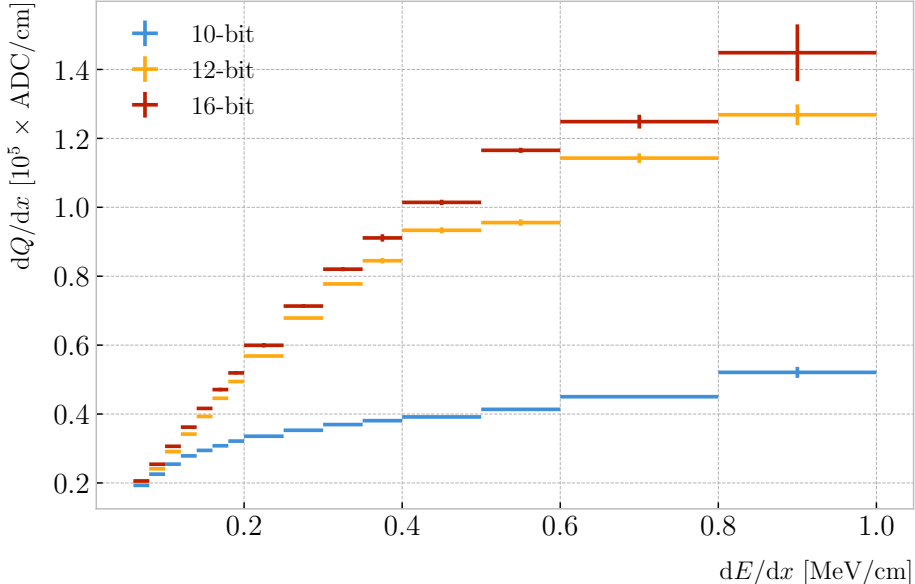


Figure 8.5: Fitted most probable dQ/dx values for each dE/dx bin for three different ADC bit limits, 10 (blue points), 12 (default, yellow points) and 16-bit (red points).

Table 8.1: Calibration parameters obtained from the fit of the ND-GAr simulated stopping proton sample to the calibration function from Eq. (8.5). The fits were performed for the 10, 12, and 16-bit ADC limits.

	χ^2/ndf	Best fit $\pm 1\sigma$		
		A	B (cm/MeV)	C (ADC/e)
10-bit	$1.83 \times 10^{-6}/12$	-9.3 ± 3.9	270 ± 69	27.1 ± 5.4
12-bit	$2.67 \times 10^{-5}/12$	0.883 ± 0.064	5.6 ± 1.3	4.94 ± 0.49
16-bit	$1.44 \times 10^{-5}/12$	0.949 ± 0.024	3.53 ± 0.58	4.52 ± 0.29

2520 By default, GArSot applies a 12-bit ADC limit, which can be changed in the
 2521 simulation configuration. However, it can only be increased up to 16-bit, as we represent
 2522 the ADC collection as a `std::vector<short>`. This way, I tried to change the saturation
 2523 parameter to see how it affects the relation between reconstructed charge and energy.
 2524 Figure 8.5 shows a comparison between the most probable dQ/dx for 10, 12 and 16-
 2525 bit ADC limits. As expected, the lower the limit is the sooner the charge saturates.
 2526 For higher ADC limits the relation between energy and charge remains linear up to
 2527 higher dE/dx values, but even for the 16-bit limit the saturation is noticeable for values
 2528 $\gtrsim 0.5$ MeV/cm.

Chapter 8. Particle ID in GArSoft

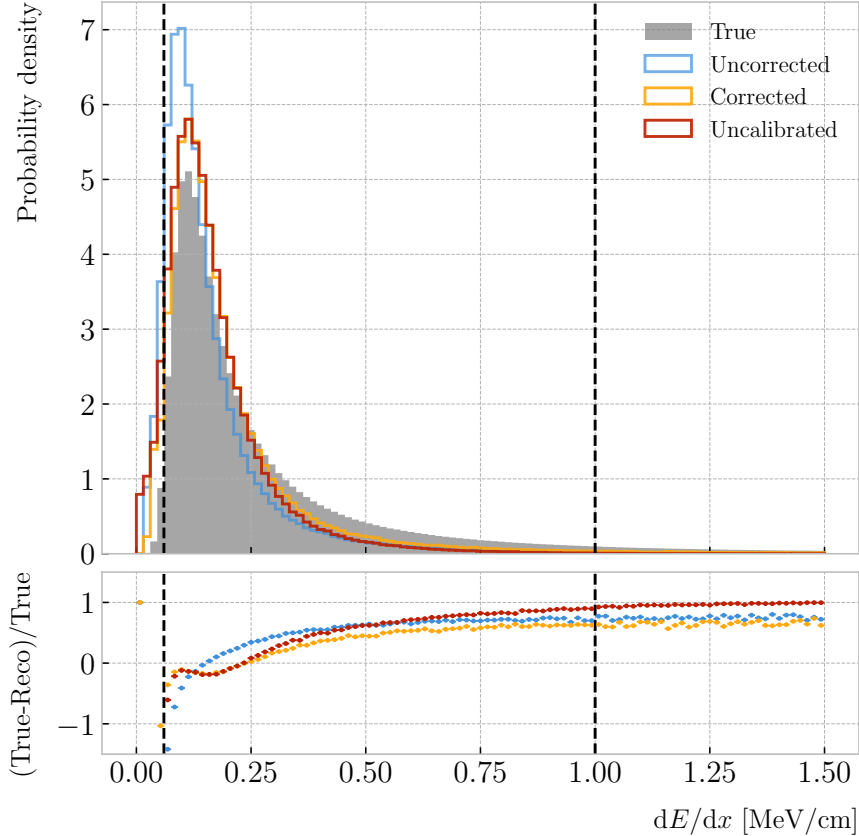


Figure 8.6: Top panel: area normalised dE/dx distributions for the true (solid grey) and the reconstructed energy deposits in the stopping proton sample, both after applying the calibration (blue) and the calibration and the normalisation correction (yellow). Also shown is the distribution obtained by applying a correction factor to the dQ/dx values but not the calibration (red). Bottom panel: fractional residuals for the uncorrected (blue), corrected (yellow) and uncalibrated (red) samples.

Table 8.1 shows the results of fitting the samples with 10 and 16-bits ADC limits to the calibration function from Eq. (8.5), using the weights based on their relative error as described previously. One interesting feature to notice is how different the best fit points look for the 10-bit ADC saturation when compared to the other two, which are consistent with each other.

At this point we can compare the dE/dx distribution one gets from Geant4, i.e. the true energy loss distribution, and the distribution I found by applying the calibration function to our collection of reconstructed dQ/dx values. Figure 8.6 (top panel) shows the true (solid grey) and reconstructed (blue, labeled as uncorrected) distributions

8.1. dE/dx measurement in the TPC

2538 together. The dashed vertical lines indicate the region of validity of the calibration fit, i.e.
2539 the left and right edges of the first and last dE/dx bin respectively. Notice that these
2540 histograms are area-normalised, as the total number of true energy deposits is much
2541 higher than the number of reconstructed charge deposits. This is due to a combination
2542 of effects, like the finite spatial resolution of the detector, the hit clustering used in the
2543 track fitting and the reclustering we have applied here.

2544 The two distributions are significantly different. That can be seen clearly when
2545 looking at the fractional residuals, shown in Fig. 8.6 (bottom panel). In particular,
2546 the position of the peak is off, which could bias the mean energy loss predictions. It
2547 seems like the difference between these may be due to an overall scaling factor. One
2548 possibility is to scale the most probable value of the reconstructed distribution to
2549 the most probable value predicted by Geant4. I do this by fitting both distributions
2550 using a LanGauss function, obtaining $dE/dx_{MPV, true} = 0.1145 \pm 0.0005$ MeV/cm and
2551 $dE/dx_{MPV, reco} = 0.0928 \pm 0.0005$ MeV/cm for the true and reconstructed most probable
2552 values respectively. These can be translated into an scaling factor $S = 0.579 \pm 0.006$.

2553 The result of applying the scaling correction can be seen in Fig. 8.6 (top panel).
2554 The corrected dE/dx distribution (yellow, labeled as corrected) peaks around the same
2555 value the true distribution does, as expected. Moreover, the high energy region is also
2556 slightly better described. For low ionisations, below the lower limit of the calibration
2557 fit, the differences between true and reconstructed are still significant. This low energy
2558 excess may be migration of some events from the peak region. The overall effect of the
2559 correction can be seen in the fractional residual plot in Fig. 8.6 (bottom panel).

2560 One can also check what happens if instead of applying the logarithmic calibration we
2561 simply scale the dQ/dx distribution (post reclustering) to have the same most probable
2562 value as the true dE/dx distribution. In this case, following an analogous procedure to the
2563 one described earlier, I found the scaling factor $S_{uncalibrated} = 0.414 \pm 0.002$ MeV/ADC⁴.
2564 The resulting distribution (red, labeled as uncalibrated) is also shown in in Fig. 8.6 (top
2565 panel). The behaviour of the new distribution is similar to the corrected case at low

⁴Notice that now the scaling factor is not dimensionless, as it acts more like a conversion factor here.

Chapter 8. Particle ID in GArSoft

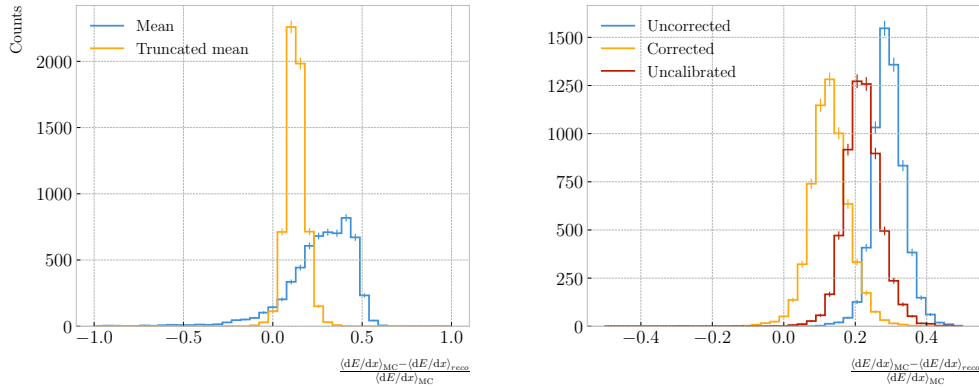


Figure 8.7: Left panel: fractional residuals between the true and the corrected dE/dx means (blue) and the 60% truncated means (yellow), for each event in the stopping proton sample. Right panel: fractional residuals between the true and the uncorrected (blue), corrected (yellow) and uncalibrated (red) dE/dx 60% truncated means, for each event in the stopping proton sample.

2566 energy losses, around the peak of the true distribution, but it is worse at describing the
 2567 high energy tail. This is expected, it is in the high ionisation regime where saturation
 2568 effects apply and therefore calibration is needed.

2569 8.1.2 Truncated dE/dx mean

2570 Once we have a collection of dE/dx values for each reconstructed track, we can compute
 2571 the corresponding most probable ionisation loss per unit length of the particle. This
 2572 is the value predicted by the Bethe-Bloch or the PAI models, and together with a
 2573 measurement of the momentum it allows for particle identification.

2574 However, estimating the most probable dE/dx value for each reconstructed track
 2575 is not a trivial task. As mentioned before, the dE/dx distributions follow Landau-like
 2576 distributions. Therefore, one should perform e.g. a LanGauss fit to correctly estimate
 2577 the most probable values. Automating this kind of fits is often problematic, as they
 2578 usually incur in convergence problems. Moreover, the reconstructed dE/dx distributions
 2579 we obtain tend to have relatively small statistics, which may also produce poor fits. In
 2580 practice, doing these unsupervised fits may degrade our performance, and a more robust
 2581 method is preferred.

8.1. dE/dx measurement in the TPC

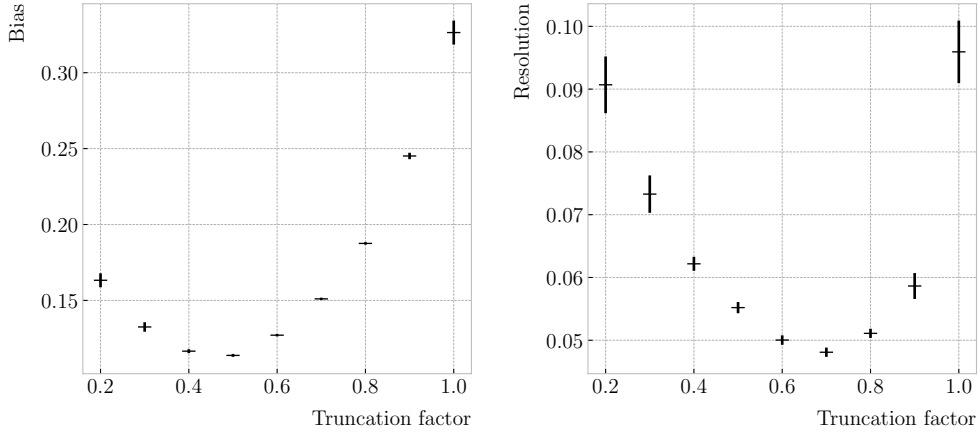


Figure 8.8: Estimated values of the mean dE/dx bias (left panel) and resolution (right panel) obtained using the corrected data from the stopping proton sample, for different values of the truncation factor.

2582 A possibility could be taking the mean of the reconstructed dE/dx distribution for
 2583 each particle. The problem with this approach is that the high energy Landau tail,
 2584 combined with our limited statistics, can induce large fluctuations in the computation
 2585 of the mean. Imagine you have two protons with the same kinetic energy, but due to
 2586 reconstruction problems in one case you did not get as many charge deposits reconstructed
 2587 in its high ionisation loss region. If you do not remove the tails the computed dE/dx
 2588 means will be significantly different.

2589 In order to avoid those fluctuations, one can compute the mean of a truncated dE/dx
 2590 distribution instead. By keeping only a given fraction of the lowest energy deposits
 2591 we obtain an estimate of the mean energy loss that is more resilient to reconstruction
 2592 inefficiencies and statistical effects. Figure 8.7 (left panel) shows a comparison between
 2593 the $\langle dE/dx \rangle$ computed by taking the mean of the full distribution (blue line) and the
 2594 60% lowest energy clusters (yellow line), for the stopping proton sample. The fractional
 2595 residuals are computed for each proton, taking the corresponding means using their
 2596 collections of true and reconstructed energy deposits. One can see that using the simple
 2597 mean translates into a high bias and uncertainty in the $\langle dE/dx \rangle$ estimation, whereas
 2598 applying the truncation reduces both significantly.

2599 Additionally, I performed a comparison between the 60% truncated mean dE/dx

Chapter 8. Particle ID in GArSoft

2600 obtained using the different calibration methods discussed earlier, namely the uncorrected
 2601 (blue), corrected (yellow) and uncalibrated (red) distributions. The results are shown
 2602 in Fig. 8.7 (right panel). While the widths of these distributions are similar, the bias
 2603 obtained for the corrected sample, i.e. calibration function and correction factor applied,
 2604 is a factor of ~ 2 lower than in the uncalibrated case and almost three times smaller
 2605 than for the uncorrected sample.

2606 The next step is to optimise the level of truncation we are going to apply to our
 2607 data. To do so, I used different truncation factors, i.e. the percentage of energy-ordered
 2608 reconstructed energy deposits we keep to compute the mean, on the corrected dE/dx
 2609 sample of the stopping protons. Then, following the same procedure of computing the
 2610 fractional residuals as before, I fitted the resulting histograms using a double Gaussian
 2611 function. This is simply the sum of two Gaussian functions of the type:

$$g(x; \mu, \sigma, A) = A e^{-\frac{(x-\mu)^2}{2\sigma^2}}. \quad (8.6)$$

2612 I do not add the classical normalisation factor of the Gaussian, $1/\sqrt{2\pi}\sigma$, therefore
 2613 the amplitude A simply represents the maximum of the function. One of the two
 2614 Gaussian functions describes the core part of the distribution, while the other captures
 2615 the behaviour of the tails.

2616 For each truncation factor, I look at the bias and the resolution I obtain. I define
 2617 these as the weighted means of the corresponding parameters in the fits:

$$\bar{x} = \frac{A_{core} x_{core} + A_{tail} x_{tail}}{A_{core} + A_{tail}}, \quad (8.7)$$

2618 where A_{core} and A_{tail} are the amplitudes of the core and tail distributions respectively
 2619 and x is either the mean μ or the width σ of said distributions.

2620 Figure 8.8 shows the bias (left panel) and the resolution (right panel) I obtained
 2621 for the stopping proton sample, using different values of the truncation. From these, it
 2622 can be seen that a truncation factor of 50% minimises the bias in the estimation, while

8.1. dE/dx measurement in the TPC

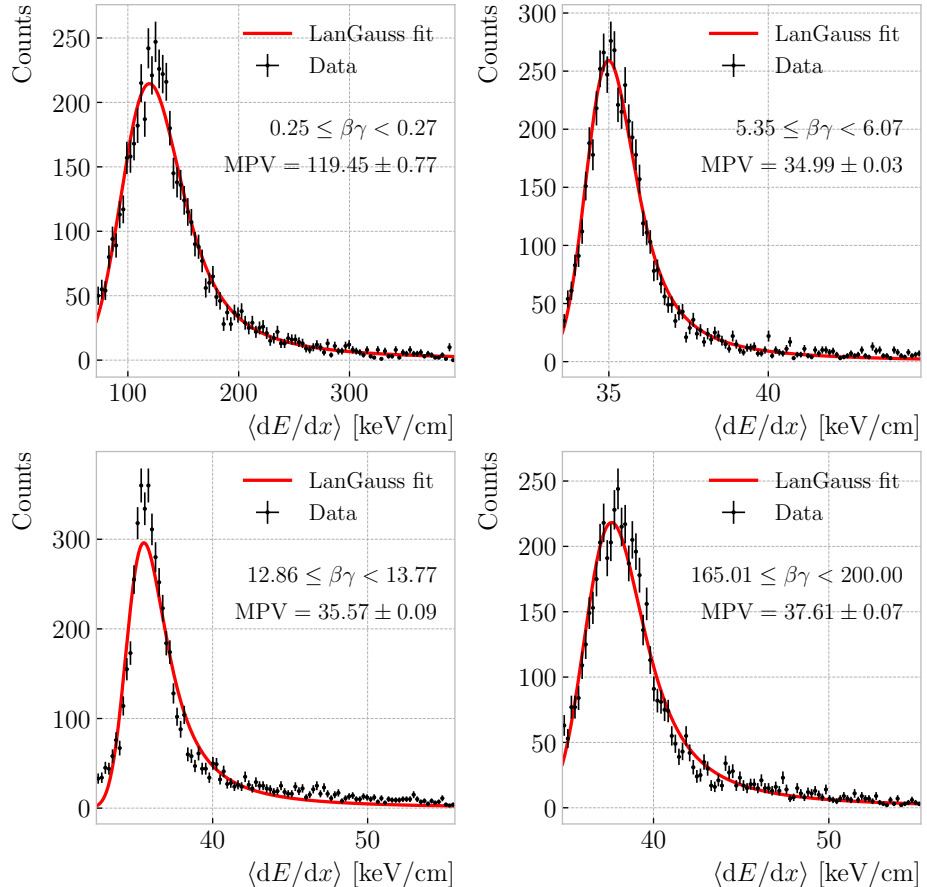


Figure 8.9: Examples of the truncated mean dE/dx LanGauss fits for various $\beta\gamma$ bins, from a simulated FHC neutrino sample.

2623 70% gives the best resolution. That way, I settled on the intermediate value of 60%
 2624 truncation, which yields a $\langle dE/dx \rangle$ resolution of 5.00 ± 0.08 % for stopping protons.

2625 8.1.3 Mean dE/dx parametrisation

2626 Now that we have a way to estimate the mean energy loss of a particle in the HPgTPC,
 2627 we can determine the value of the free parameters in the ALEPH formula, Eq. (8.3).
 2628 For this, I used a sample of 10^5 reconstructed FHC neutrino events inside ND-GAr. In
 2629 this case I cannot use the stopping proton sample, as we need to cover the full kinematic
 2630 range of interest for the neutrino interactions in our detector.

2631 The original data does not contain an estimation of the velocity of the tracks, instead
 2632 the tracks have a value for the reconstructed momentum and the associated PDG code

Chapter 8. Particle ID in GArSoft

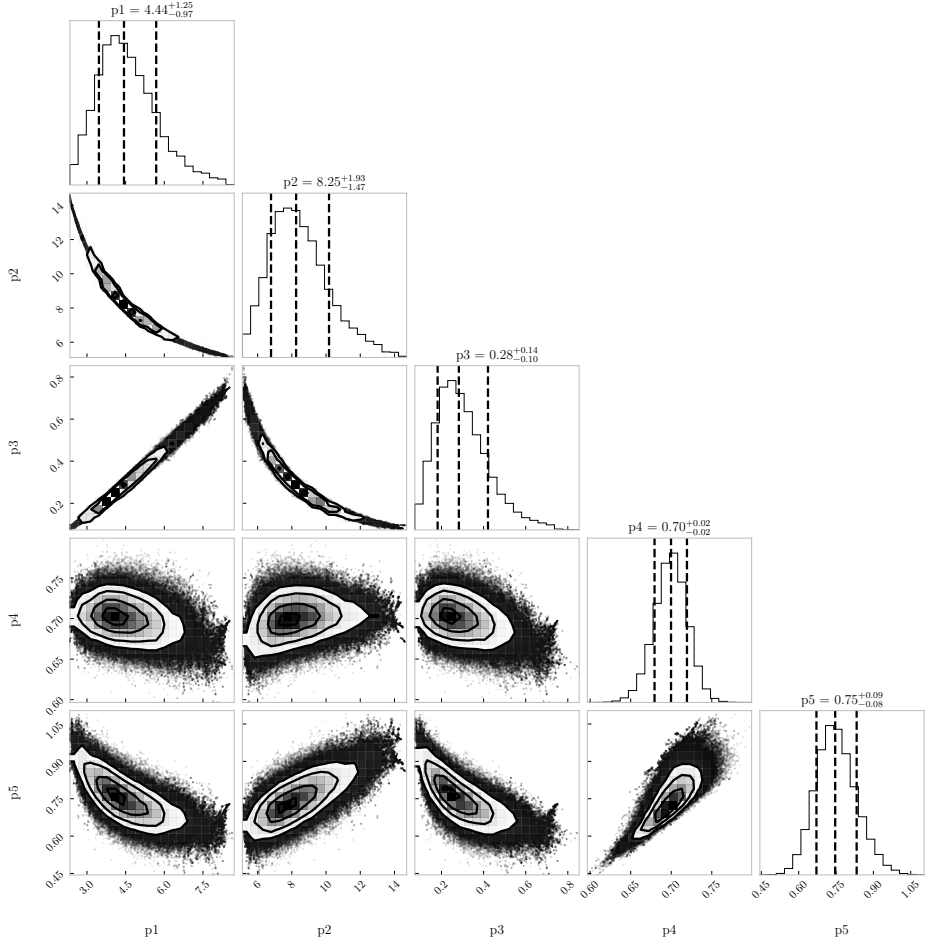


Figure 8.10: Resulting one and two dimensional projections of the posterior probability distributions of the ALEPH $\langle dE/dx \rangle$ parameters obtained by fitting the 60% truncated mean dE/dx values from a FHC neutrino sample in ND-GAr. The vertical dashed lines in the 1D distributions represent the 16th, 50th and 84th percentiles.

of the Geant4-level particle that created the track. Therefore, one can select some of the particles in the data, in this case I selected electrons, muons, pions and protons, and compute β and γ using the reconstructed momentum and their mass. In terms of $\beta\gamma$ the mean dE/dx does not depend on the particle species, so one can consider all the dataset as a whole. For this fit, I will express β in terms of the $\beta\gamma$ product as:

$$\beta = \frac{\beta\gamma}{\sqrt{1 + (\beta\gamma)^2}}, \quad (8.8)$$

which can be easily proven from the definition of γ .

8.1. dE/dx measurement in the TPC

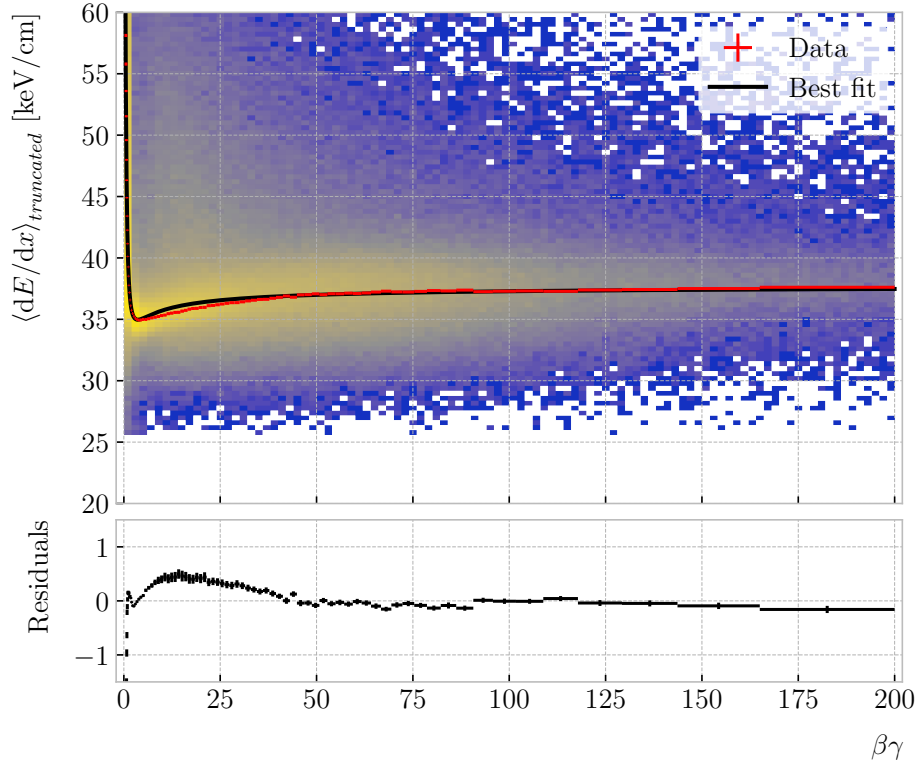


Figure 8.11: Truncated mean dE/dx obtained for the FHC neutrino sample as a function of the $\beta\gamma$ product (upper panel). Also shown are the fitted most probable values for each $\beta\gamma$ bin (red points) and the best fit obtained using the ALEPH parametrisation (black line). The residuals resulting from the fit are shown in the lower panel.

2639 Next, I bin the data in $\beta\gamma$. I chose a fine binning so as to capture the different
 2640 features of the ionisation curve. Instead of fixing the bin width, I select them so each one
 2641 has approximately the same statistics. Then, for each $\beta\gamma$ slice, I compute the median
 2642 and the interquartile range (IQR) of the $\langle dE/dx \rangle$ distribution. Using these, I make a
 2643 histogram in the range [median – IQR, median + 5 IQR], which I fit to a LanGauss
 2644 function in order to extract the MPV. Using this range accounts for the asymmetric
 2645 nature of the distributions, while also helps avoiding a second, lower maximum present
 2646 at low $\beta\gamma$, probably a result of reconstruction failures.

2647 A few examples of these fits are shown in Fig. 8.9. The chosen values of $\beta\gamma$ sit in
 2648 very distinct points along the $\langle dE/dx \rangle$ curve, going from the high ionisation region at
 2649 low velocities (top left panel), to the minimum point (top right panel), the beginning of

Chapter 8. Particle ID in GArSoft

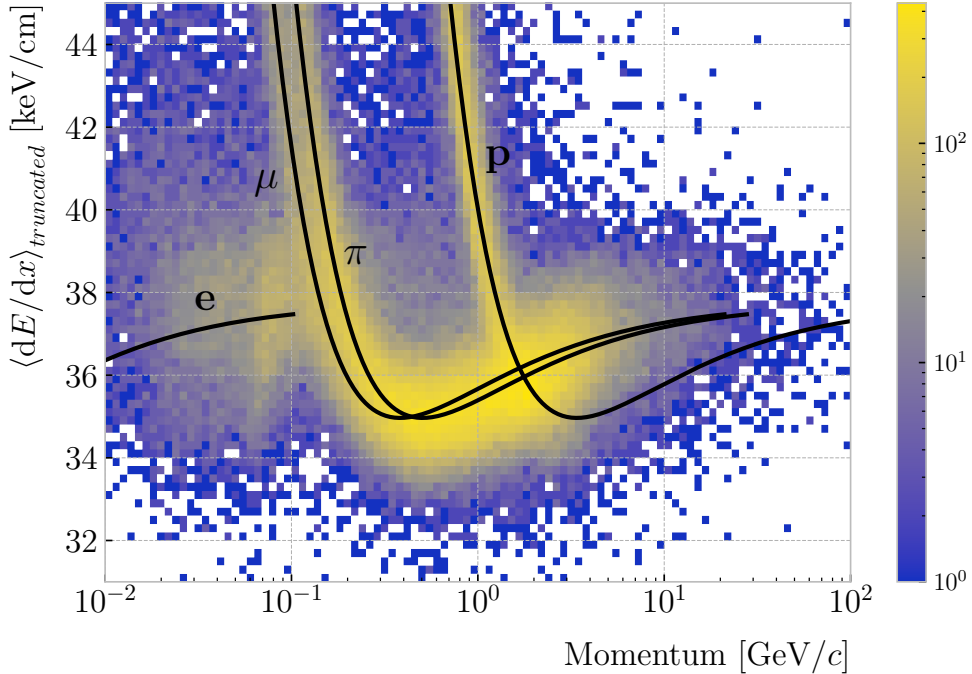


Figure 8.12: Distribution of the 60% truncated mean $\langle dE/dx \rangle$ versus reconstructed momentum for the FHC neutrino sample. The black lines indicate the predictions of the ALEPH parametrisation for electrons, muons, charged pions and protons.

the relativistic rise (bottom left panel), and the plateau produced by the density effect (bottom right panel).

I used the resulting most probable $\langle dE/dx \rangle$ values and the centres of the $\beta\gamma$ bins as the points to fit to the ALEPH formula. For this particular fit I used the least-squares method to get a first estimation of the ALEPH parameters. Applying some uniform priors, I then used these values as the starting point of a 100000 steps MCMC. Figure 8.10 shows the posterior probability distributions I obtain for each parameter. The reported best fit points are based on the 16th, 50th, and 84th percentiles in the marginalised distributions.

The resulting fit (black line), compared to the data points (red points) and the underlying distribution is shown in Fig. 8.11 (top panel). The overall fit is good, with a reduced chi-squared of $\chi^2/ndf = 1.02$. However, there are some regions where the fit does not describe the data correctly, like the very low $\beta\gamma$ regime, where the fit severely underestimates for energy losses $\gtrsim 50$ keV/cm, and the start of the relativistic raise,

8.2. Muon and pion separation in the ECal and MuID

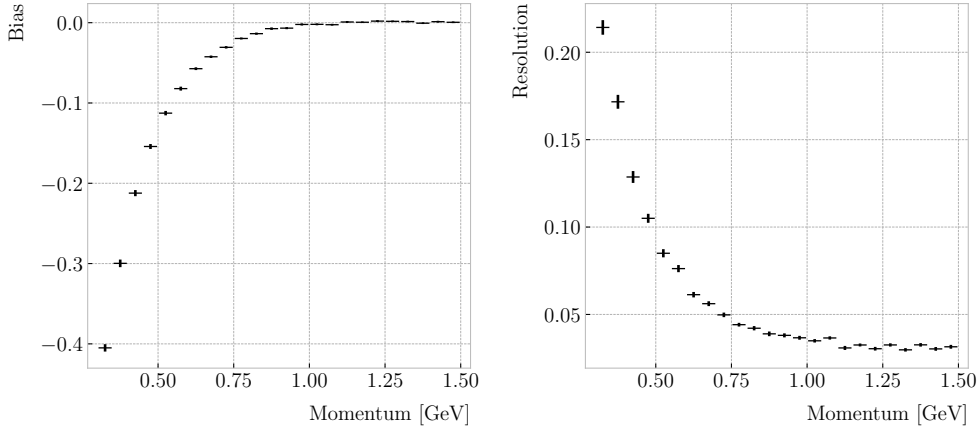


Figure 8.13: Estimated values of the mean dE/dx bias (left panel) and resolution (right panel) obtained for the true protons in a FHC neutrino sample.

where we have a slight overestimation. This is a result of those points having a larger uncertainty when compared to the ones around the dip or the plateau areas. These differences can be better seen in the residual plot, Fig. 8.11 (bottom panel).

8.1.4 Particle identification

8.2 Muon and pion separation in the ECal and MuID

As it could be seen from Fig. 8.12, it is not possible to separate muons and charged pions in the HPgTPC using dE/dx for momenta $\gtrsim 300 \text{ MeV}/c$. In ND-GAr, approximately 70% of the interactions in FHC mode will be ν_μ CC (compared to the 47% of $\bar{\nu}_\mu$ CC interactions when operating in RHC mode), while 24% are neutral currents. Out of these, around 53% and 47% of them will produce at least one charged pion in the final state, respectively. Figure 8.14 shows a comparison between the spectra of the primary muons and the charged pions for ν_μ CC interactions in ND-GAr producing one or more charged pions. From this, one can see that (i) the majority of muons and charged pions are not going to be distinguishable with a $\langle dE/dx \rangle$ measurement, and that (ii) particle identification is necessary both to classify correctly the ν_μ CC events and identify the primary muon within them.

ND-GAr features two other subdetectors which can provide additional information

Chapter 8. Particle ID in GArSoft

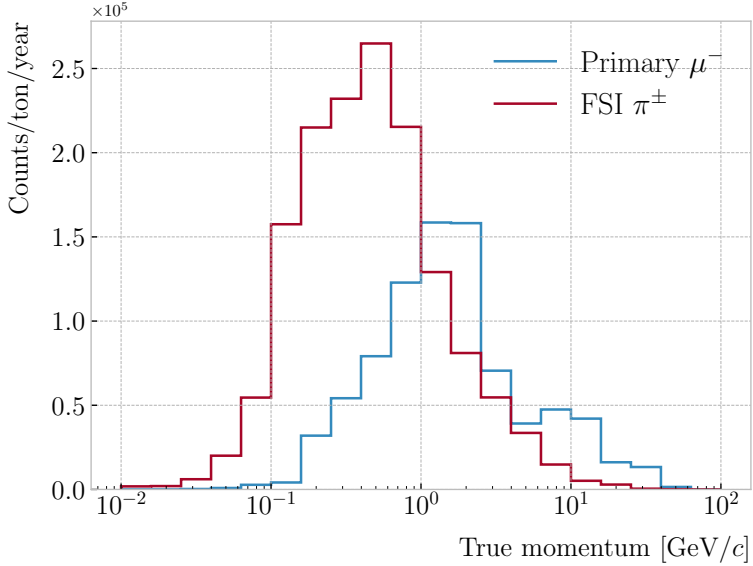


Figure 8.14: True momentum distribution for the primary muon in ν_μ CC $N\pi^\pm$ interactions inside the fiducial volume of ND-GAr (blue line), compared to the post FSI charged pion spectrum (red line).

for this task, namely the ECal and MuID. The current ECal design, described in (ref section), consists of 42 layers, made of 5 mm of Pb, 7 mm of plastic scintillator and a 1 mm PCB board. The total thickness of this calorimeter is 1.66 nuclear interaction lengths or 1.39 pion interaction lengths. The MuID design is in a more conceptual stage, however it is envisioned to feature layers with 10 cm of Fe and 2 cm of plastic scintillator⁵. With its three layers, it will have a thickness of 1.87 or 1.53 nuclear or pion interaction lengths, respectively.

Because pion showers are dominated by inelastic nuclear interactions, the signatures of these particles in the calorimeter will look significantly different from those of muons. Although our ECal is not thick enough to fully contain the hadronic showers of the charged pions at their typical energies in FHC neutrino interactions, they can still be used to understand whether the original particle was more hadron-like or MIP-like. In Fig. 8.15 I show two examples of energy distributions created by a muon (left panel) and a charged pion (right panel) of similar momenta interacting in the ECal. These

⁵It is not mentioned anywhere, but I assume that there should also be another layer of PCB board of 1 mm. However, in this case its contribution to the total thickness of the sampling calorimeter would be negligible.

8.2. Muon and pion separation in the ECal and MuID

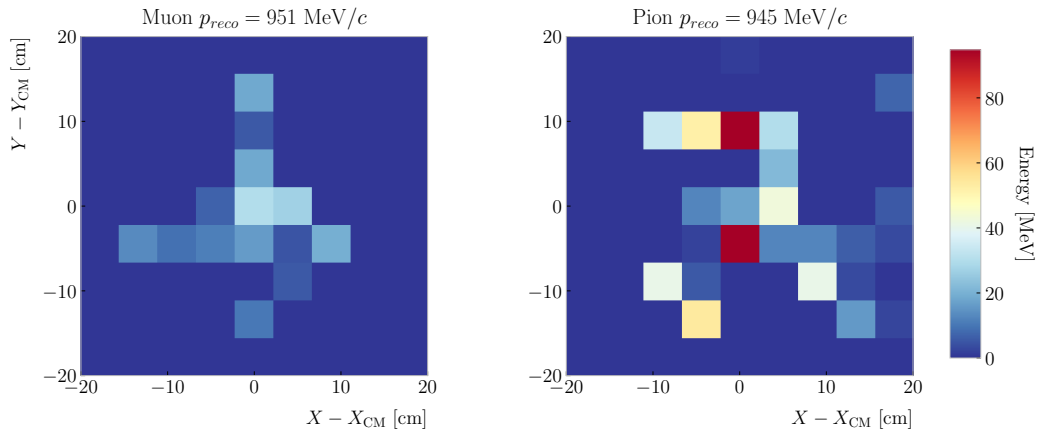


Figure 8.15: Distributions of energy deposits in the ECal for a muon (left panel) and a charged pion (right panel) with similar momenta. The energy is projected onto the plane perpendicular to the principal component of the hits, and the positions are relative to the center of the interaction.

2695 figures represent the transverse development of the interactions. For each of them, I
 2696 computed the principal component and centre of mass of the interaction, projecting
 2697 the position of the hits onto the plane perpendicular to that direction, and taking the
 2698 distances relative to the centre. It can be seen that the muon follows an almost MIP-like
 2699 behaviour, being the central bin in the histogram the one with the highest deposited
 2700 energy. On the other hand, the pion not only deposits more energy overall, but also this
 2701 energy is more spread-out among the different hits. It is this kind of information that
 2702 would allow us to tell apart muons from pions.

2703 This way, I identify three main action points that need to be addressed if one wants
 2704 to use these detectors to distinguish between muons and charged pions. These are:

- 2705 1. the way we make the associations between tracks in the HPgTPC to the activities
 2706 (what in GArSoft we call clusters) in the ECal and the MuID,
- 2707 2. what variables or features one can extract from the calorimeters that encapsulate
 2708 the information we are interested about,
- 2709 3. and how to carry out the classification problem.

Chapter 8. Particle ID in GArSoft

2710 8.2.1 Track-ECal matching

2711 One of the main players in the muon and pion separation is the way we associate clusters
2712 in the ECal to reconstructed tracks in the TPC. Missing some associations or making
2713 wrong ones can bias the ECal quantities that we can use for classifying particles. The
2714 current algorithm in GArSoft provides precise associations, i.e. most of the associations
2715 that it produces are correct, but it appears to miss an important number of associations
2716 (at least when using the default configuration).

2717 The current TPC track-ECal cluster association algorithm is divided in four parts.
2718 It first checks whether the track end point fulfils certain conditions to be extrapolated.
2719 There are two cut values in this step, one for the drift direction and other radial.

2720 If the point can be extrapolated, the code computes the coordinates of the centre
2721 of curvature using the Kalman fit estimates at the track end ($y, z, 1/R, \phi, \tan\lambda$). It
2722 then compares the distance between this and the cluster in the (z, y) plane with R . This
2723 introduces another cut in the perpendicular direction.

2724 The next step is different for clusters in the barrel or in one of the end caps. If it
2725 is a barrel cluster the algorithm extrapolates the track up to the radial distance of the
2726 cluster. There are three possible outcomes, the extrapolated helix can cut the cylinder
2727 of radius r_{clus} two, one or zero times. I get the cut point that is closer to the cluster and
2728 check that it is either in the barrel or the end caps. Computing the difference between
2729 the x coordinates of the cluster and the extrapolated point, the module checks that this
2730 is not greater than a certain cut. If the cluster is in an end cap, I propagate the track
2731 up to the x position of the cluster. Then, the algorithm computes the angle in the (z, y)
2732 plane between the centre of curvature and the cluster, α , and the centre of curvature
2733 and the propagated point, α' . A cut is applied to the quantity $(\alpha - \alpha')R$.

2734 If the cluster contains more than a certain number N of hits, I apply an extra cut to
2735 the dot product of the direction of the track at the propagated x value and the cluster
2736 direction.

2737 The code makes sure to only associate one end of the track (if any) to a cluster.

8.2. Muon and pion separation in the ECal and MuID

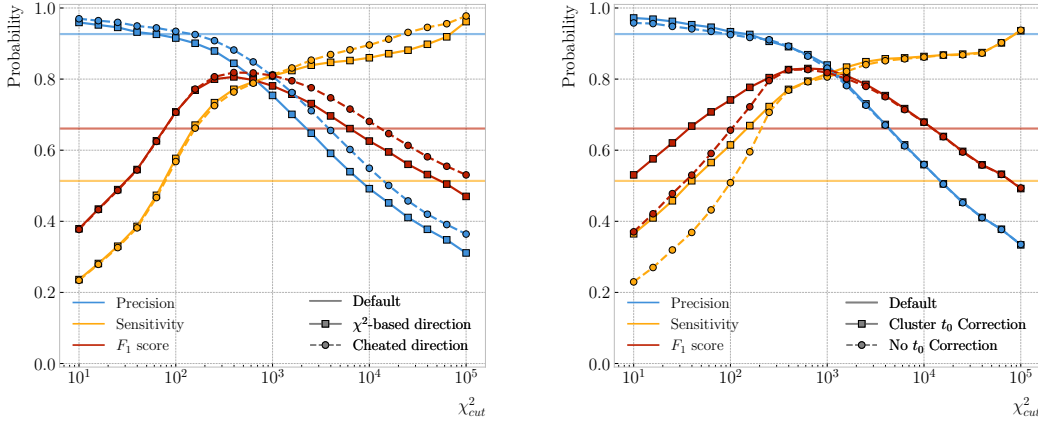


Figure 8.16: Left panel: comparison between the precision (blue), sensitivity (yellow) and F_1 score (red) obtained for the default (horizontal lines) and new algorithms, both with the χ^2 -based direction estimator (squares) and cheating the directions (circles), for different values of the χ^2 cut. Right panel: comparison of the performance of the new algorithm when applying the cluster t_0 correction (squares) and when (circles).

2738 However, it can associate more than one track to the same cluster. This makes sense,
2739 as different particles can contribute to the same cluster in the ECal, but it makes it
2740 difficult to quantify the relative contributions of the tracks to a certain cluster.

2741 As a way of comparing the performance of this algorithm, a new, simpler association
2742 module was written. The goal was to have a simple and robust algorithm, which depends
2743 on as few parameters as possible and that can produce a one-to-one matching between
2744 tracks and ECal clusters.

2745 For each reconstructed track, the new algorithms applies the same procedure to the
2746 forward and the backward fits irrespective of their end point positions. It first gets the
2747 Kalman fit parameters at the corresponding end point together with the X position, x_0 ,
2748 (y_0 , z_0 , $1/R$, ϕ_0 , $\tan\lambda$).

2749 For each ECal cluster, I compute the radial distance to the centre of the TPC and
2750 find the ϕ value in the range $[\phi_0, \phi_0 + \text{sign}(R)\phi_{max}]$ that makes the propagated helix
2751 intersect with the circle defined with such radius. The (x, y, z) position of the helix for
2752 the ϕ value found (if any) is then computed. In case there are two intersections, I keep
2753 the one that minimises the distance between (y, z) and (y_c, z_c) .

2754 I then calculate χ^2 value based on the Euclidean distance between the propagated

Chapter 8. Particle ID in GArSoft

2755 point and the cluster:

$$\chi^2/ndf = \frac{\sum_{n=0}^2 (x^{(n)} - x_c^{(n)})^2}{3}. \quad (8.9)$$

2756 If there was no intersection I store a -1 instead. In the end, for each reconstructed track
2757 in the event one ends up with two collections of χ^2 values, one for each ECal cluster
2758 and fit directions.

2759 The current code only supports having ECal clusters associated to one end of each
2760 track. We have two options to decide what track end to keep. The first one tries to
2761 cheat the selection, looking at the distance between the two track ends and the true
2762 start position of the associated MC particle. The second one keeps the track end with
2763 more χ^2 entries below the cut.

2764 This feature of only considering one track end limits the algorithm, making it not
2765 suitable for reconstructing events with particles originating outside the TPC. However,
2766 as for the moment the main concern of the group is the study of neutrino interactions
2767 off the gaseous argon, this is an acceptable assumption.

2768 In order to associate a cluster to a track, I take all clusters with a χ^2 value in the
2769 range $[0, \chi_{cut}^2]$. If a cluster has been assigned to more than one track we leave it with
2770 the one with the lowest χ^2 .

2771 This default behaviour of the algorithm can be modified to associate more than one
2772 track to each cluster. Not only that, but the χ^2 values can be used to assign relative
2773 weights to the different contributions.

2774 To evaluate the performance of the association method, I use a binary classification
2775 approach. In this case, I check the leading MC Track IDs associated to the reconstructed
2776 tracks and ECal clusters. I count an association as true positive (TP) if both Track
2777 IDs coincide. An association is considered false positive (FP) when the Track IDs are
2778 different. If a cluster has not been associated to any track but it shares the Track ID
2779 with a reconstructed track it is counted as a false negative (FN).

2780 For the testing, I used a sample of 10000 FHC neutrino events inside the HPgTPC.
2781 Figure 8.16 (left panel) shows the precision (blue line), sensitivity (yellow line), and F_1

8.2. Muon and pion separation in the ECal and MuID

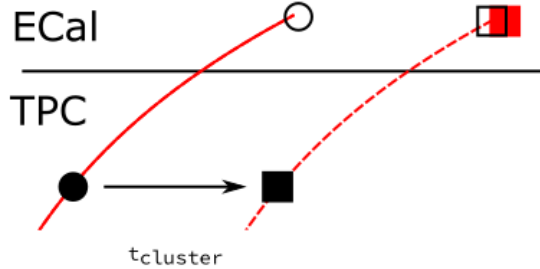


Figure 8.17: Schematics of a possible option to deal with track-ECal associations in non-zero t_0 neutrino interaction events, trying to correct for the drift direction uncertainty in a cluster-by-cluster basis using the cluster time, $t_{cluster}$.

2782 score (red line) I obtained for different values of χ^2_{cut} . For comparison, the same metrics
 2783 computed for the default algorithm with the current configuration are also shown (dashed
 2784 lines). In the case of the new algorithm, I used both the χ^2 -based method to estimate
 2785 the track direction described earlier (square markers) and the cheated direction from the
 2786 Geant-level information (circle markers). For either of these we achieve similar values of
 2787 the precision compared to the old code, while having a considerably higher sensitivity.
 2788 It can be seen that cheating the direction of the tracks only makes a difference at high
 2789 χ^2_{cut} , past the optimal value of the cut around the F_1 score maximum. Therefore, I set
 2790 the χ^2 method as the default.

2791 One of the possible weak points of this approach is that it relies on the position along
 2792 the drift direction to make the decisions. Within the current ND-GAr design implemented
 2793 in GArSoft, the timing information is provided by the ECal. That effectively means
 2794 that prior to make the track-ECal associations the reconstructed x positions of the track
 2795 trajectories differ from the simulated ones by an amount:

$$x_{reco}^{(n)} - x_{sim}^{(n)} = v_{drift} t_0, \quad (8.10)$$

2796 where v_{drift} is the mean drift velocity in our medium and the initial time is in the range
 2797 $t_0 \in [0, t_{spill}]$ where t_{spill} is the spill length. For a 10 μs spill this translates into a
 2798 maximum 30 cm uncertainty on the drift direction position.

2799 The current default in GArSoft sets $t_0 = 0$, but the functionality to randomly sample

Chapter 8. Particle ID in GArSoft

2800 this within the spill time is in place. Therefore, we need to understand what is the impact
2801 of a non-zero t_0 on the associations algorithm and foresee possible ways of minimising a
2802 loss in performance.

2803 Figure 8.17 represents a possible option to tackle the association problem when
2804 having events with a non-zero initial time t_0 . The black and white circles represent the
2805 original points, whereas the squares indicate the corrected positions. The end points of
2806 the track and the propagated points up to the cluster radius are indicated using filled
2807 and unfilled markers respectively. The red square represents the position of the cluster.

2808 Here I try to correct for the drift coordinate position using the time associated to the
2809 cluster. Assuming that the drift time is much larger than the propagation time, $t_{cluster}$
2810 could be used as a good estimation of the t_0 . An alternative can be using the earliest
2811 time associated to a hit in said cluster. Doing this for each cluster before computing
2812 the χ^2 value could be used as an alternative to knowing the specific value of the t_0 , as
2813 when the association is correct this will provide the right correction but its impact is
2814 small enough to not change the position significantly in the case the cluster does not
2815 correspond to a given track.

2816 I tested the effect of this correction again using a sample of 10000 FHC neutrino
2817 events. Figure 8.16 (right panel) shows the precision (blue line), sensitivity (yellow line),
2818 and F_1 score (red line) for the case the cluster t_0 correction is applied (square markers)
2819 and for the no correction case (circle markers), as a function of χ^2_{cut} . In this case, the
2820 differences are particularly notorious at low values of the cut. It makes sense, as the t_0
2821 effect becomes subdominant when the distance we consider grows large. Overall, the
2822 correction increases the sensitivity while keeping the precision almost unchanged. As a
2823 result, I apply the t_0 correction to the generated samples as the default.

2824 8.2.2 Classification strategy

2825 The problem of the muon and charged pion separation has to be viewed in the broader
2826 context of the particle identification in our detector. Focusing on the beam neutrino
2827 interactions, it is clear that we are going to have muons and pions spanning a broad

8.2. Muon and pion separation in the ECal and MuID

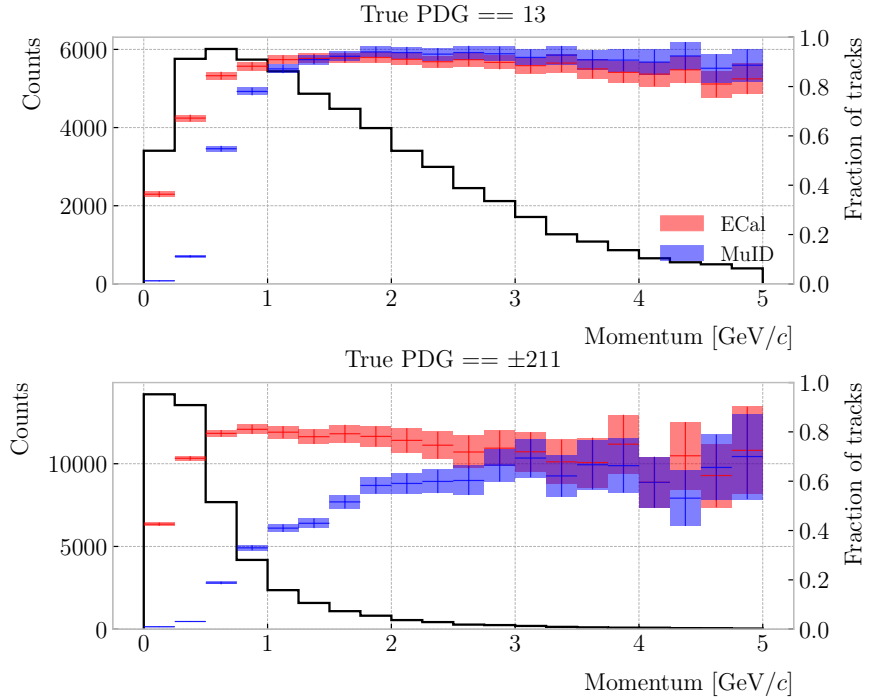


Figure 8.18: Momentum distribution for the reconstructed muons (top panel) and charged pions (bottom panel) in a FHC neutrino sample, together with the fraction of them reaching the ECal (red) and MuID (blue). Each entry corresponds to a reconstructed track, backtracked to a true muon or pion which has not produced any other reconstructed track.

momentum range. Not only that, but we will also have other particles with similar characteristics that will make the classification even more challenging. Therefore, we are presented with a task that will depend heavily on the kinematic range we are looking at each time, as both the available information and the possible impurities of other particle species vary.

For instance, distinguishing muons from pions could be difficult at low momenta, as a great number of them do not reach the ECal. Therefore, we could think of tailoring a version of the classification for that particular case, which could be complemented with a dE/dx measurement. Likewise, for momenta $\gtrsim 1$ GeV muons and pions reach the calorimeters efficiently, but so do protons. Because of this, one can try to train another classifier for this energy range, and rely on other methods to remove as many of the protons as possible.

Chapter 8. Particle ID in GArSoft

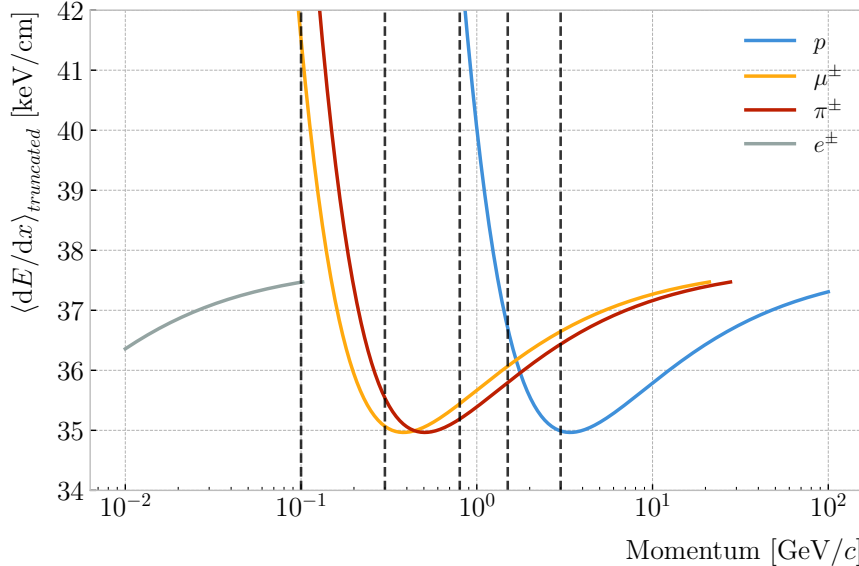


Figure 8.19: Predicted truncated mean dE/dx versus momentum, for electrons, muons, charged pions and protons, obtained using the ALEPH parametrisation. The vertical dashed lines represent the boundaries of the six regions used for the muon and pion classification training.

2840 Figure 8.18 shows the momentum distribution of the reconstructed muons (top) and
 2841 pions (bottom) in a FHC sample. It also contains the fraction of particles reaching the
 2842 ECal (red) and MuID (blue), for the different momentum bins. In Fig. 8.19 I show the
 2843 mean dE/dx of different particles as a function of the momentum, computed using the
 2844 ALEPH parametrisation with the best fit parameters found in Subsec. 8.1.2.

2845 Using these two figures as references, I decided to approach the classification by
 2846 dividing the problem into six different momentum regions. A summary of these can be
 2847 found in Tab. 8.2. The basic idea is to exploit all the information that is available in
 2848 each region and . For the problem at hand, I prepared separated samples of isotropic
 2849 single muons and pions, with momenta uniformly distributed along the corresponding
 2850 momentum range. I did not generate samples for the first region, as it is assumed
 2851 that the separation can be achieved using dE/dx only. For the last region, I generated
 2852 particles up to a momentum of 10 GeV/c, as that is well above the typical energies of
 2853 muons and pions from FHC neutrino interactions in ND-GAr.

2854 To tackle this classification problem, I make use of Boosted Decision Trees (BDT). A

8.2. Muon and pion separation in the ECal and MuID

Table 8.2: Momentum ranges and description of the PID approach assumed for the muon and pion classification task.

Momentum range	Description
< 0.1 GeV/c	All tracks can be separated with dE/dx
[0.1, 0.3) GeV/c	Use ECal for reaching muons and pions, dE/dx for the rest
[0.3, 0.8) GeV/c	Use ECal for muons and pions, dE/dx for protons
[0.8, 1.5) GeV/c	Use ECal and MuID for muons and pions, dE/dx for protons
[1.5, 3.0) GeV/c	Use ECal and MuID for muons and pions, ToF for protons
≥ 3.0 GeV/c	Use ECal and MuID for muons and pions, dE/dx and ToF for protons

2855 decision tree uses a flowchart-like structure to make decisions based on some input data.
 2856 It starts from a root node, which represents the complete dataset, and then it splits
 2857 this based on the variable or feature which gives the best separation between classes,
 2858 creating two new nodes. The process repeats for each node until it reaches a certain
 2859 limit, like a maximum number of splits or some tolerance criteria. The last set of nodes
 2860 are often called leave nodes, and represent the final prediction of the classifier.

2861 Boosting refers to a family of methods to combine the predictions from multiple
 2862 classifiers, following a sequential approach where each new model learns from the errors
 2863 of the previous one. The process starts with a simple decision tree, which is used to
 2864 make predictions on the training data. Then, the data points misclassified by the first
 2865 model are assigned higher weights, and another decision tree is trained on the data with
 2866 adjusted weights. The predictions of the two trees are then combined, and the cycle
 2867 repeats for a predefined number of iterations. Gradient boosting uses the direction of
 2868 the steepest error descent to guide the learning process and improve the accuracy with
 2869 each iteration.

2870 8.2.3 Feature selection and importance

2871 Using the reconstructed tracks as a starting point, I compute a number of ECal and
 2872 MuID variables for each of them. As there can be more than one cluster associated to a
 2873 track, what I do is collect all associated clusters and compute these variables from the

Chapter 8. Particle ID in GArSoft

2874 complete collection of associated hits. For the MuID, because it only features three layers
2875 and typically there will be less hits, I also allow single hits to be associated with tracks⁶.
2876 I can roughly divide the variables in three types: energy-related, geometry-related and
2877 statistical. In the following, I briefly describe the variables related exclusively to the
2878 ECal:

2879 • **Energy-related ECal**

- 2880 – ECal total energy (ClusterTotalEnergy): sum of the energy of all the ECal
2881 hits.
- 2882 – Mean ECal hit energy (HitMeanEnergy): mean of the hit energy distribution.
- 2883 – Standard deviation ECal hit energy (HitStdEnergy): standard deviation of
2884 the hit energy distribution.
- 2885 – Maximum ECal hit energy (HitMaxEnergy): maximum of the hit energy
2886 distribution.

2887 • **Geometry-related ECal**

- 2888 – Mean distance hit-to-cluster (DistHitClusterMean): mean of the distance
2889 distribution between the hits and the corresponding cluster's main axis.
- 2890 – RMS distance hit-to-cluster (DistHitClusterRMS): root mean square of the
2891 distance distribution between the hits and the corresponding cluster's main
2892 axis.
- 2893 – Maximum distance hit-to-centre (DistHitCenterMax): maximum of the
2894 distance distribution between the hits and the centre of the TPC.
- 2895 – Time-of-Flight velocity (TOFVelocity): slope obtained when fitting a straight
2896 line to the hit time versus hit distance to the centre (i.e. $d = v \times t$).

2897 • **Energy and geometry ECal**

⁶At the reconstruction level what happens is that non-clustered hits are put into single hit clusters, instead of being thrown away. This is necessary to keep the consistency of the track-cluster association code.

8.2. Muon and pion separation in the ECal and MuID

- 2898 – Radius 90% energy (Radius90E): distance in the hit-to-cluster distribution
2899 for which 90% of the total energy is contained in the hits that are closer to
2900 the axis (i.e. radius that contains 90% of the energy).

2901 • Statistical ECal

- 2902 – Number of hits (NHits): total number of hits associated to the track.
2903 – Number of layers with hits (NLayers): not really a count of all layers with
2904 hits but the difference between the last and the first layer with hits.

2905 Figure 8.20 shows the distributions of three different ECal variables, separating true
2906 muons (blue) and charged pions (red), for the five momentum ranges considered. I chose
2907 to show one feature from each category, namely the mean energy per hit (left column),
2908 the mean distance between the hits and the centre of the cluster (middle column), and
2909 the number of ECal layers with hits (right column). These give an idea of the separating
2910 power of the different features, and how it changes considerably with the energy. In
2911 the number of layers with hits distributions, the peak at 6 is due to the fact that the
2912 first six ECal layers sit inside the pressure vessel⁷. Therefore, some of the particles get
2913 stopped crossing it, never making it to the seventh layer.

2914 In the case of the MuID, because at low momenta a significant fraction of the particles
2915 do not make it past the ECal, I only consider the information coming from this detector
2916 for momenta $\geq 0.8 \text{ GeV}/c$, i.e. for the last three momentum regions. The variables I
2917 extract from it are the following:

2918 • Energy-related MuID

- 2919 – MuID total energy (ClusterMuIDTotalEnergy): sum of the energy of all the
2920 MuID hits.
2921 – Mean MuID hit energy (HitMuIDMeanEnergy): mean of the MuID hit energy
2922 distribution.

⁷Note to self: check this. I thought the ECal barrel had 8 layers of tiles, and that all of them were inside the pressure vessel.

Chapter 8. Particle ID in GArSoft

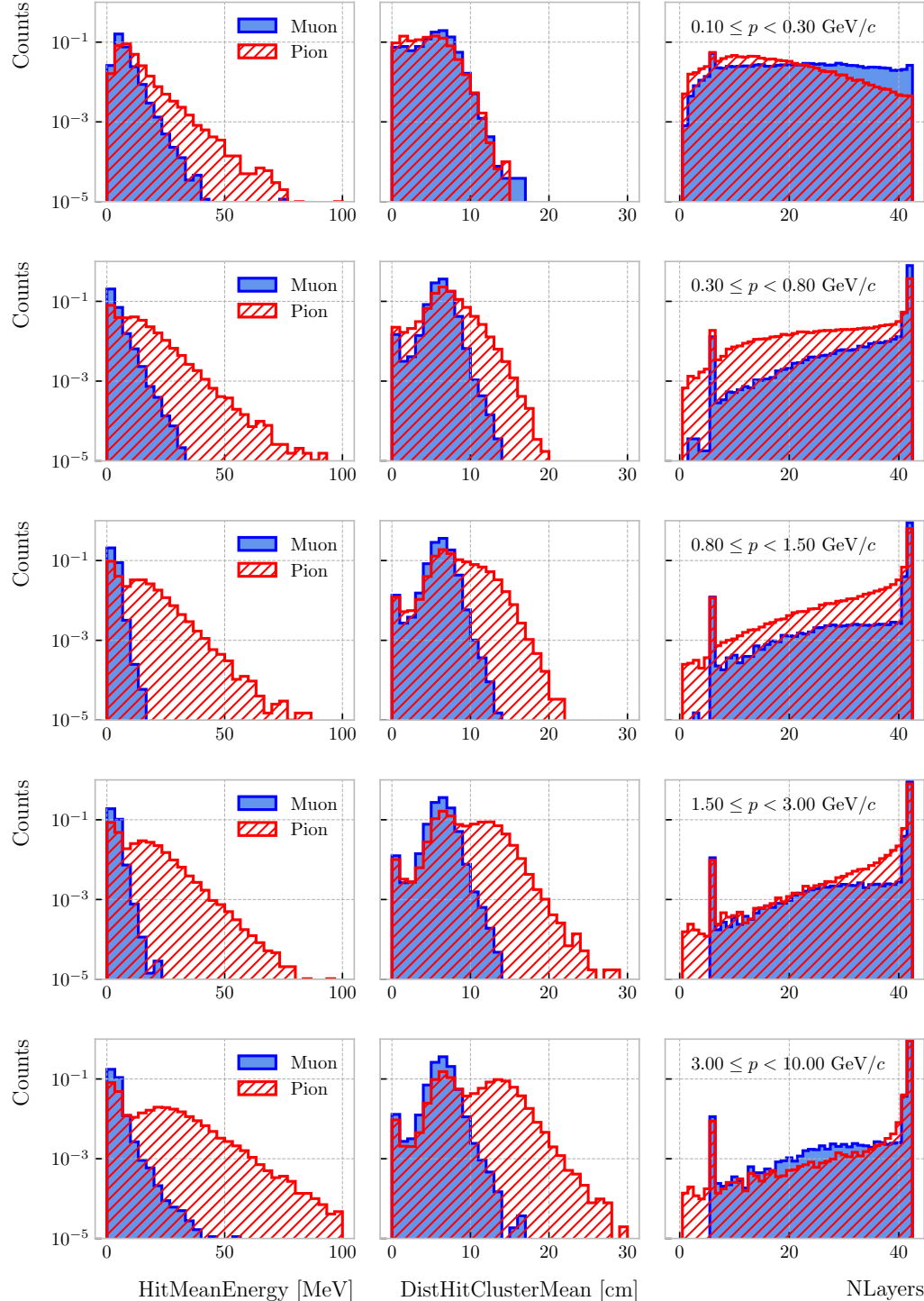


Figure 8.20: Example ECal feature distributions for muons (blue) and charged pions (red) in the five different momentum ranges considered (from top to bottom, in ascending momentum order). From left to right: mean hit energy, mean distance hit-to-cluster, and number of layers with hits.

8.2. Muon and pion separation in the ECal and MuID

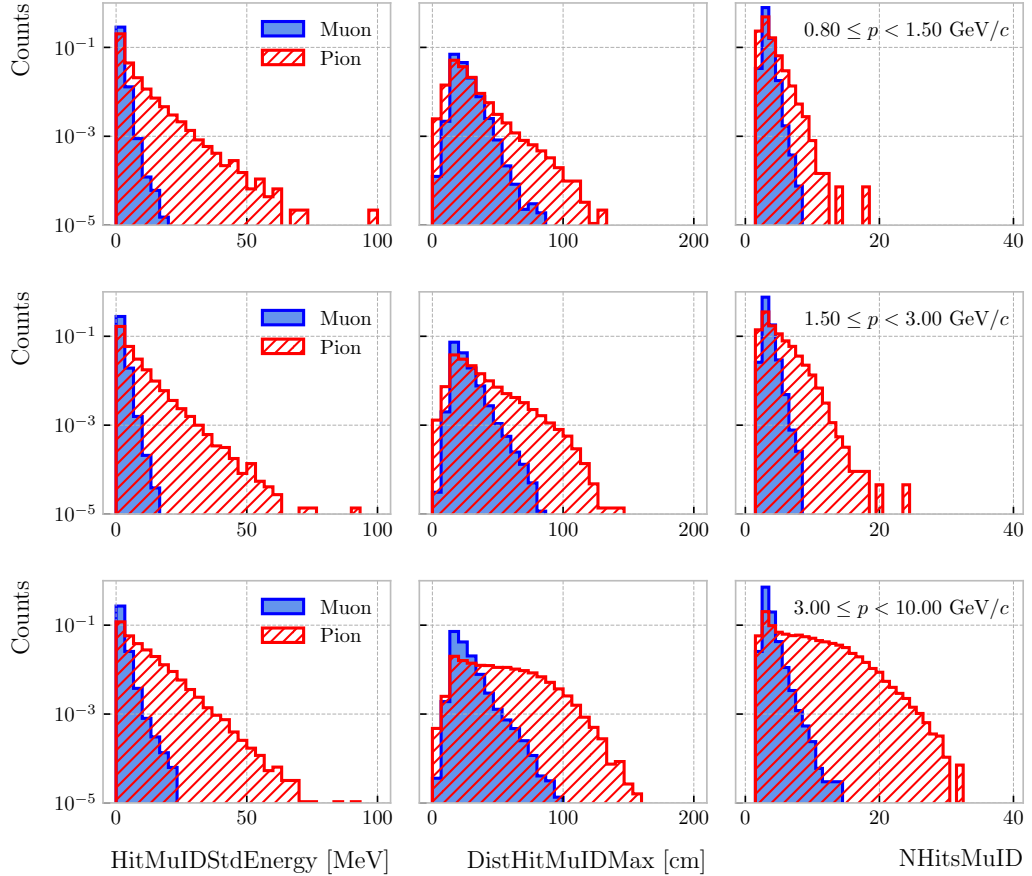


Figure 8.21: Example MuID feature distributions for muons (blue) and charged pions (red) in the three different momentum ranges considered (from top to bottom, in ascending momentum order). From left to right: standard deviation hit energy, maximum distance hit-to-hit, and number of hits.

- 2923 – Standard deviation MuID hit energy (HitMuIDStdEnergy): standard deviation
- 2924 of the MuID hit energy distribution.
- 2925 – Maximum MuID hit energy (HitMuIDMaxEnergy): maximum of the MuID
- 2926 hit energy distribution.

2927 • **Geometry-related MuID**

- 2928 – Maximum distance MuID hit-to-hit (DistHitMuIDMax): maximum distance
- 2929 between pairs of MuID hits (not sure this is a good variable, distribution
- 2930 looks nuts).
- 2931 – Maximum distance MuID hit-to-centre (DistHitCenterMuIDMax): maximum

Chapter 8. Particle ID in GArSoft

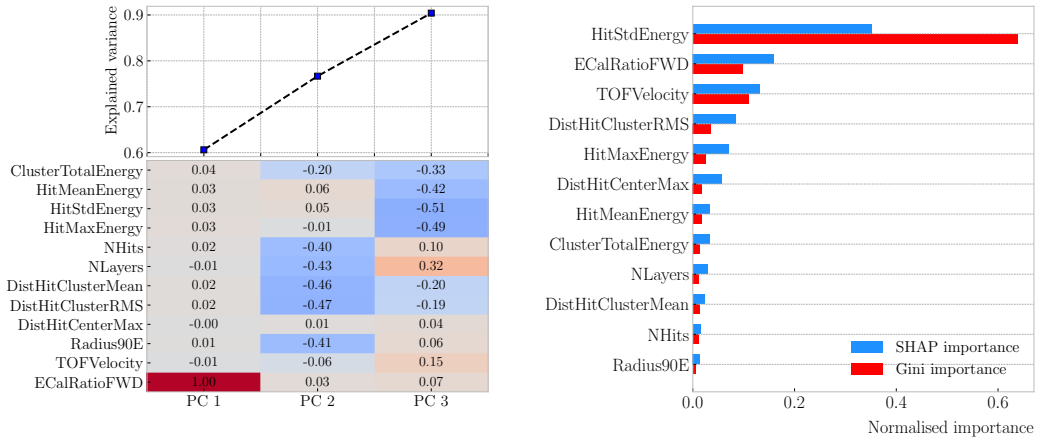


Figure 8.22: Left panel: cumulative explained variance for the first three principal components (top panel) and contribution of the different features to the principal axes in feature space (bottom panel). Right panel: Shapley (blue) and Gini (red) feature importances for the different input features. Both figures correspond to the samples in the momentum range $0.3 \leq p < 0.8$ GeV/c.

2932 of the distance distribution between the MuID hits and the centre of the
2933 TPC.

2934 • Statistical MuID

- 2935 – Number of hits (NHitsMuID): total number of MuID hits associated to the
2936 track.
2937 – Number of layers with hits (NLayersMuID): not really a count of all layers
2938 with MuID hits but the difference between the last and the first layer with
2939 MuIDhits.

2940 Figure 8.21 shows the distributions of three different MuID variables, separating true
2941 muons (blue) and charged pions (red), for the three momentum ranges which use the
2942 muon tagger information. In this case I decided to standard deviation of the MuID hit
2943 energy distribution (left column), the maximum distance between the MuID hit pairs
2944 (middle column), and the number of MuID hits (right column). These variables are used
2945 together with the ECal features at high momenta, providing additional disambiguation
2946 power.

8.2. Muon and pion separation in the ECal and MuID

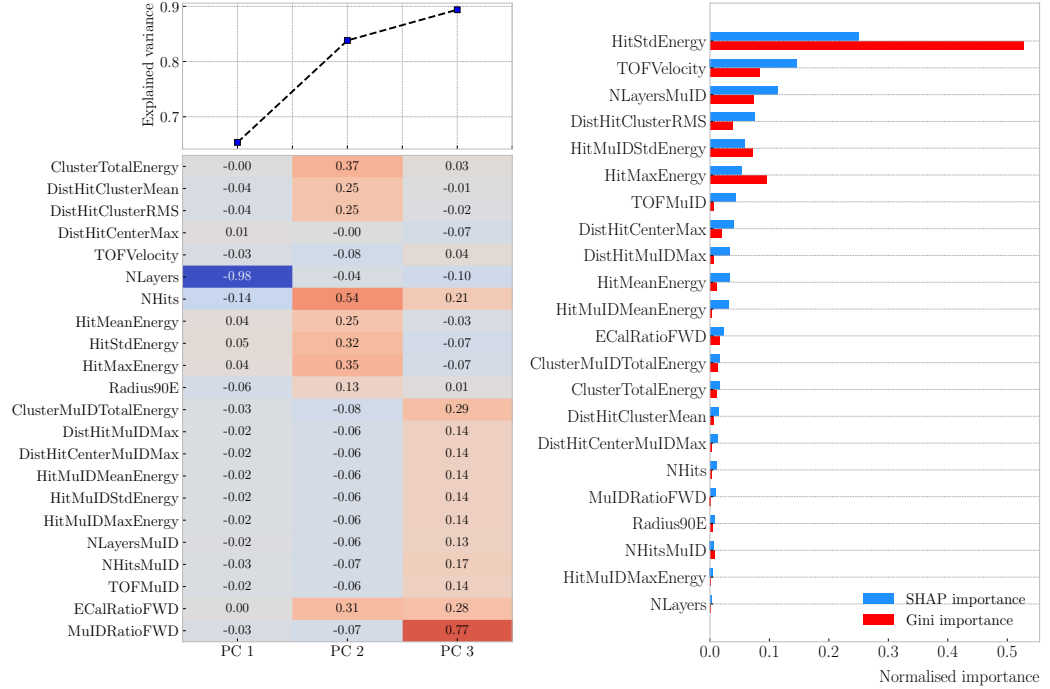


Figure 8.23: Left panel: cumulative explained variance for the first three principal components (top panel) and contribution of the different features to the principal axes in feature space (bottom panel). Right panel: Shapley (blue) and Gini (red) feature importances for the different input features. Both figures correspond to the samples in the momentum range $0.8 \leq p < 1.5$ GeV/c.

Once our features have been defined, one can do some exploratory analysis to understand how well the variables describe the target class, and avoid the black-box approach by what features are most relevant for the learning process. This way, I performed a feature analysis for each of the momentum ranges I divided this classification problem into. It follows three steps: first a principal component analysis (PCA), followed by a feature importance study using Gini and Shapley values, and finally a feature permutation importance analysis.

The PCA is useful to understand the variance of the feature space. It is an unsupervised machine learning technique that allows the user to perform a dimensionality reduction. It uses a singular value decomposition of the input features to project them into a lower dimensional space. The idea is to find the matrix \mathbf{C}_m , whose columns are the first m orthonormal eigenvectors of the input covariance matrix. Consider the $n \times p$

Chapter 8. Particle ID in GArSoft

2959 real matrix of input data \mathbf{X} , where n is the number of samples and p the number of
 2960 features. If \mathbf{X} is centred, i.e. the means of its columns are equal to zero, we can write the
 2961 covariance matrix of \mathbf{X} as $\mathbf{C} = \mathbf{X}^\top \mathbf{X} / (n - 1)$. This matrix can be diagonalised, yielding:

$$\mathbf{C} = \mathbf{V} \mathbf{L} \mathbf{V}^\top, \quad (8.11)$$

2962 where \mathbf{V} is a matrix of eigenvectors and \mathbf{L} a diagonal matrix with eigenvalues λ_i . Then,
 2963 performing SVD on \mathbf{X} gives us:

$$\mathbf{X} = \mathbf{U} \mathbf{S} \mathbf{W}^\top, \quad (8.12)$$

2964 where \mathbf{U} is a unitary matrix, whose columns are called left singular vectors, \mathbf{S} is a
 2965 diagonal matrix of single values s_i , and \mathbf{W} is another unitary matrix, its columns known
 2966 as right singular vectors. This way, we can write:

$$\mathbf{C} = \mathbf{W} \mathbf{S} \mathbf{U}^\top \mathbf{U} \mathbf{S} \mathbf{W}^\top / (n - 1) = \mathbf{W} \frac{\mathbf{S}^2}{n - 1} \mathbf{W}^\top. \quad (8.13)$$

2967 meaning that the right singular vectors are also the eigenvectors of the covariance matrix.
 2968 The SVD can be computed numerically following an iterative approach.

2969 This way, taking an input data vector $X \in \mathbb{R}^n$, the resulting feature vector $Y \in \mathbb{R}^m$
 2970 is given by:

$$Y = \mathbf{C}_m^\top X. \quad (8.14)$$

2971 The new features capture most of the variance of the original sample, while being lower
 2972 dimensional, as $m < n$.

2973 Before applying the PCA reduction one needs to centre and scale the input data.
 2974 Centring is necessary when using SVD to obtain the eigenvectors of the covariance
 2975 matrix, as only in that case we can do the identification with the right singular vectors
 2976 from the input data. Scaling is needed when variables are on different scales, as some
 2977 can then dominate the PCA procedure.

2978 I used the PCA module of `scikit-learn`, together with the `RobustScaler`, which
 2979 centres the data and scales it based on the interquartile range. In Fig. 8.22 (left panel)

8.2. Muon and pion separation in the ECal and MuID

and Fig. 8.23 (left panel) I show the results I obtained from the PCA for the momentum ranges $0.3 \leq p < 0.8$ GeV/c and $0.8 \leq p < 1.5$ GeV/c, respectively. Notice that in the second case the number of features increases considerably, as this is the first region which uses the MuID variables. I found that, in all the cases, adding a fourth PC does not add additional information. As it can be seen in the top panels of the figures, the cumulative explained variance is already over 80% with three PCs.

The bottom panels show the contribution of the variables to the principal axes. For the two first momentum regions, I observe a tendency of the energy-related and the geometry-related ECal variables to be clustered together. For the other ranges, when I include the MuID variables, there seems to be a division between ECal and MuID variables. For these, it seems like the number of ECal layers with hits also plays an important role.

The next step in the analysis is to quantify the importance of the features based on two additional metrics, namely the Gini and the Shapley values. The Gini importance, often called mean decrease impurity, is based on how much a feature contributes to the purity improvement at the splits in each decision tree. The purity is measured in terms of the Gini impurity index, defined as:

$$I_G = 1 - \sum_i f_i, \quad (8.15)$$

where f_i is the fractional abundance of the i -th class. Then, for each split one can compute the weighted decrease in impurity as:

$$\Delta_G = \frac{N_t}{N} \left(I_G - \frac{N_t^R}{N_t} I_G^R - \frac{N_t^L}{N_t} I_G^L \right), \quad (8.16)$$

where N represents the total number of samples, N_t the number of samples at the current node, N_t^R and N_t^L the number of samples in the right and left children respectively, I_G is the Gini impurity at the current node, and I_G^R and I_G^L the Gini impurities of the resulting right and left children.

Chapter 8. Particle ID in GArSoft

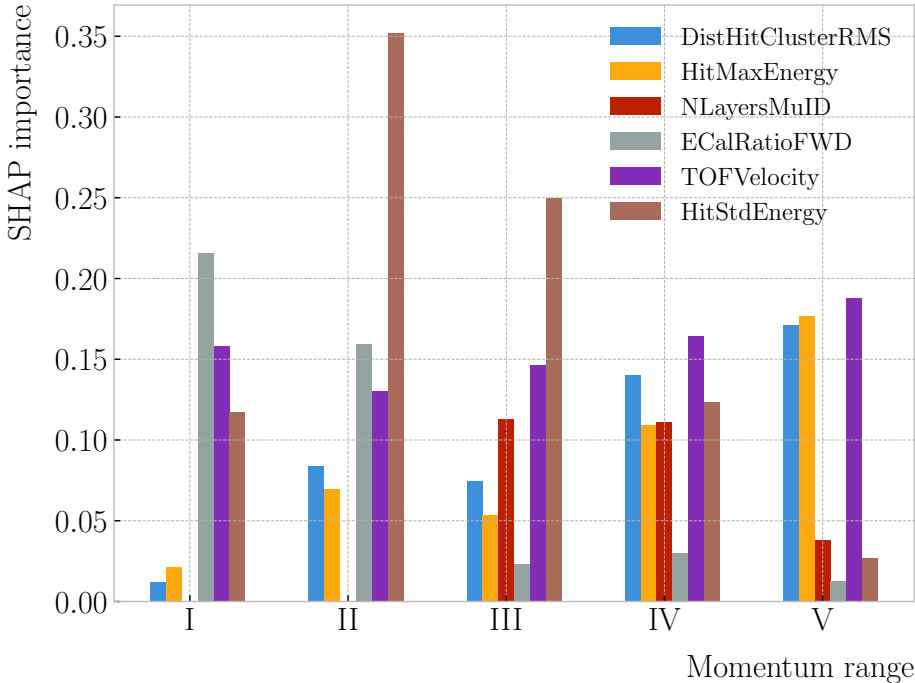


Figure 8.24: Evolution of the SHAP importance for the top six most important features across all five momentum ranges.

3003 For each decision tree, one will have a normalised vector with the accumulated
 3004 decrease in Gini impurity for each feature. In the case of a BDT, the feature importances
 3005 are simply the mean for all the estimators in the ensemble⁸.

3006 The concept of Shapley values originated in the context of game theory, and it
 3007 measures the marginal contribution of a feature in enhancing the accuracy of a classifier.
 3008 Take F to be the set of all features in a problem, and $S \subseteq F$ the subset of features. To
 3009 compute the Shapley value of the i -th feature, one has to train a model with that feature
 3010 present, $f_{S \cup \{i\}}$, and another model trained without it, f_S . This has to be repeated for
 3011 all possible combinations of subsets $S \subset F \setminus \{i\}$, and evaluating the models predictions
 3012 on the appropriate sets of data x_S . This way, the Shapley value results:

$$\varphi_i = \sum_{S \subset F \setminus \{i\}} \frac{|S|! (|F| - |S| - 1)!}{|F|!} [f_{S \cup \{i\}}(x_{S \cup \{i\}}) - f_S(x_S)]. \quad (8.17)$$

⁸Note to self: this appears not to be the case. If you get the `feature_importance` for each tree in the BDT and take the average, the result is not the same to be one reported in the `feature_importance` attribute of the BDT.

8.2. Muon and pion separation in the ECal and MuID

3013 I trained the `GradientBoostingClassifier` from `scikit-learn` with the default
3014 configuration in order to evaluate both the Gini and Shapley importances. The Gini
3015 scores are automatically computed by `scikit-learn`, using the training data. For the
3016 Shapley importance, I used the implementation from the `SHAP` package, computing
3017 it using the test sample. The results can be seen in Fig. 8.22 (right panel) and
3018 Fig. 8.23 (right panel), again for the momentum ranges $0.3 \leq p < 0.8 \text{ GeV}/c$ and
3019 $0.8 \leq p < 1.5 \text{ GeV}/c$. The length of the bars denote either the SHAP (blue) or the Gini
3020 (red) importance of the feature. One interesting thing to notice is that, when looking at
3021 the Gini importance, there is always one feature that dominates over the rest. This is
3022 not the case for the SHAP importance, where importances tend to be more balanced.

3023 Across all momentum ranges, I observe that the most important features are. For
3024 the five momentum ranges considered, only six variables sit in the top five at least once.
3025 Figure 8.24 shows the evolution of the SHAP importance of these six features. It is
3026 interesting to see that the time-of-flight variable keeps its importance almost unchanged
3027 for all momenta. Also, it looks like the ECal energy ratio gets less relevant the higher the
3028 momentum is, but the RMS of the hit-to-cluster distance distribution and the maximum
3029 ECal hit energy become more important in the last momentum ranges.

3030 The last step in the feature selection analysis is the feature permutation. This
3031 technique measures the contribution of each feature to the performance of a model by
3032 randomly shuffling its values and checking how some scores degrade. For the present
3033 case, I am interested in the precision or purity, and the sensitivity or efficiency, as these
3034 two are the most relevant metrics from a physics point of view. The `scikit-learn`
3035 module provides the user with a method to perform the permutation scans.

3036 The results of these are shown in Fig. 8.25. For the different momentum ranges
3037 I show the permutation importances for the ten most important features. For each
3038 of the variables I report the effect the permutations have on the precision (blue) and
3039 sensitivity (yellow) of the models. The bars indicate the importance value, with the
3040 lighter part representing one standard deviation around the mean (hinted as an additional
3041 vertical line). Something to notice is that, in the first momentum region, the feature

Chapter 8. Particle ID in GArSoft

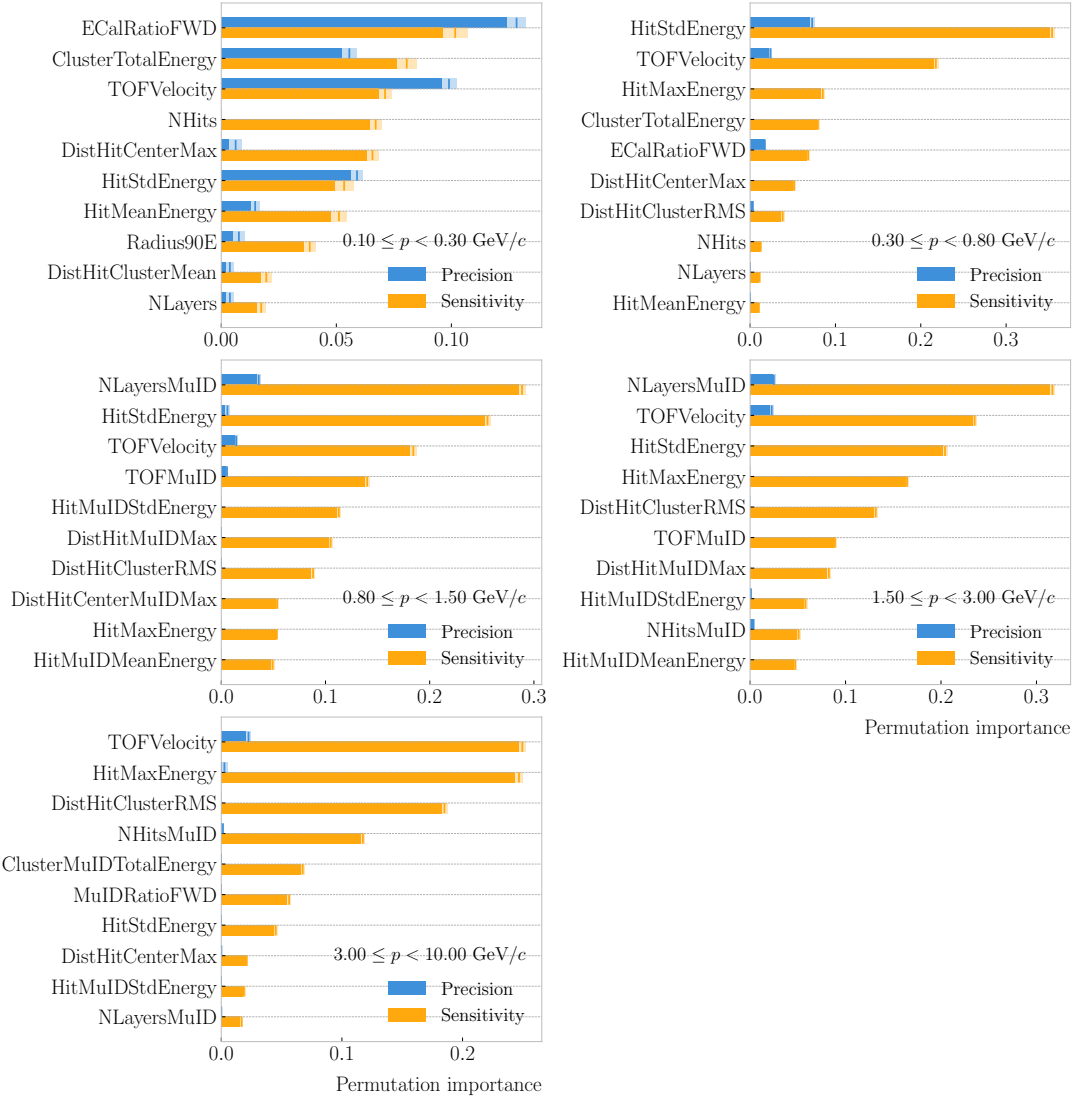


Figure 8.25: Permutation importances for the ten most important features in the different momentum ranges (from left to right, top to bottom, in increasing momentum order). The bars indicate the effect that permutations of each feature have on the purity (blue) and the sensitivity (yellow), the translucent regions representing one standard deviation around the central value.

8.2. Muon and pion separation in the ECal and MuID

3042 permutations have an effect on both the precision and the sensitivity. However, for the
3043 rest the precision is almost unaffected, while the sensitivity changes are considerably
3044 larger.

3045 It is also interesting to see that most of the variables identified as important here
3046 are the same I found when looking at the Shapley values. The behaviour of these across
3047 the momentum ranges is also similar, with the same patterns of some features being
3048 important at low momenta and then dropping in importance for the high momentum
3049 ranges.

3050 Wit this, I conclude the study of the features. I have prepared the training and
3051 testing datasets and understood what features are likely to have the largest impact on
3052 the performance of the classifiers.

3053 8.2.4 Hyperparameter optimisation

3054 Any BDT requires the user to specify a number of parameters that will dictate its
3055 behaviour. They can be divided into two categories: (i) tree-specific parameters, which
3056 affect each individual tree in the model, and (ii) boosting parameters, which control the
3057 boosting operation in the model. The value of these so-called hyperparameters affect the
3058 performance and predictive power of the models. Therefore, one needs to carefully select
3059 their optimal values in order to extract as much information as possible from the data.

3060 From all the parameters used to define a tree in the `scikit-learn` implementation
3061 of the BDT classifier, I only consider a subset of them. This is due to the fact that some
3062 are mutually exclusive, but also because I noticed that others have little effect on the
3063 problem at hand. Therefore, the parameters I investigate are the following:

3064 • `min_samples_split`: defines the minimum number of samples required in a node
3065 to be considered for splitting. Higher values prevent a model from learning relations
3066 which might be highly specific to the particular sample, but may led to under-fitting
3067 if the value is too low.

3068 • `min_samples_leaf`: defines the minimum samples required in a leaf node. For

Chapter 8. Particle ID in GArSoft

3069 imbalanced problems it should take a low value, as there will not be many cases
3070 where the minority class dominates.

3071 • `max_depth`: maximum depth of a tree. Useful to prevent over-fitting, as higher
3072 depth will allow a model to learn relations specific to the training sample.

3073 In the case of the boosting parameters, the ones I look at are:

3074 • `learning_rate`: determines the impact of each tree on the final outcome. Low
3075 values make the model robust to the specific characteristics of a tree, and thus
3076 allow it to generalise well. However, that usually requires a large number of trees
3077 to model the data properly.

3078 • `n_estimators`: number of sequential trees to be trained. In general, BDTs are
3079 fairly robust at higher number of trees but it can still overfit at a point.

3080 • `subsample`: fraction of observations to be selected for each tree. Values slightly
3081 less than 1 make the model robust by reducing the variance.

3082 In general, hyperparameters depend on each other. Thus, it is not possible to
3083 optimise them independently. In the literature, we find two main strategies to explore
3084 the hyperparameter space. We could use a grid search, in which one discretises a
3085 portion of the space of hyperparameters and evaluates the model at each point. Another
3086 approach is the randomised search, where a certain number of random configurations of
3087 hyperparameters are explored.

3088 In this case, I used the random search to scan the hyperparameter space. Also,
3089 because it is not guaranteed that a set of hyperparameters can be efficiently applied
3090 across different datasets, I perform the optimisation for each of the momentum ranges
3091 considered. Table 8.3 shows the list of hyperparameters considered, and the range within
3092 which I let them vary. I decided to fix the number of estimators to 400 in all cases, as
3093 its value is correlated with that of the learning rate.

3094 The performance of the models was assessed using a stratified 3-fold cross-validation
3095 with replacement. Cross-validation involves dividing a dataset in a number of subsets,

8.2. Muon and pion separation in the ECal and MuID

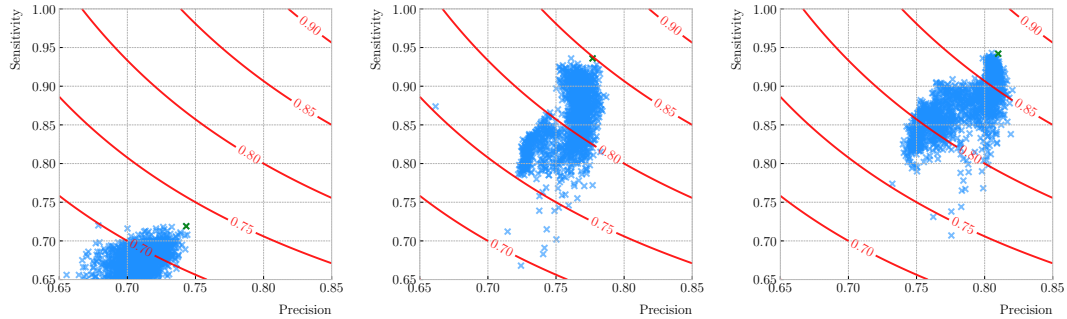


Figure 8.26: Values of the precision and sensitivity obtained for 10000 BDT hyperparameter configurations, for the momentum regions I, III and V. The red contours indicate the curves of equal F_1 -score, while the green crosses are the selected configurations.

Table 8.3: Optimal values of the hyperparameters used by the BDT, for each momentum range.

Hyperparameter	Range	Best value				
		I	II	III	IV	V
<code>min_samples_split</code>	[0.001, 1]	0.10	0.06	0.05	0.27	0.06
<code>min_samples_leaf</code>	[0.001, 1]	0.02	0.03	0.01	0.02	0.07
<code>max_depth</code>	{2, 3, ..., 8}	8	2	4	2	7
<code>learning_rate</code>	[0.05, 1]	0.10	0.23	0.07	0.13	0.09
<code>subsample</code>	[0.01, 1]	0.75	0.65	0.79	0.86	0.95

3096 training the model using some of them, and testing it with the rest. In our case, I divide
 3097 the data in 3 equal-sized subsets, maintaining the class proportions of the complete
 3098 dataset. Then, for 3 iterations, I train the models using 2 of the subsets while I compute
 3099 the precision and sensitivity scores with the other. This approach provides a more robust
 3100 estimate of the performance on unseen data.

3101 Figure 8.26 shows the results of evaluating 10000 hyperparameter configurations in
 3102 the precision versus sensitivity plane, for the momentum regions I, III and V (from left
 3103 to right). The contours represent the curves of equal F_1 -score, i.e. the harmonic mean of
 3104 the precision and the sensitivity. In order to select the optimal configurations (indicated
 3105 in the plots with a green cross), I chose the point with the highest F_1 -score.

Chapter 8. Particle ID in GArSoft

3106 The results for the different momentum ranges are summarised in Tab. 8.3. One
3107 can see some consistency in hyperparameter choices, with models generally preferring
3108 small values for the tree-specific parameters, small learning rate, and relatively large
3109 subsample sizes.

3110 8.2.5 Probability calibration

3111 8.2.6 Performance

3112 8.3 ECal time-of-flight

3113 8.3.1 Arrival time estimations

3114 8.3.2 Proton and pion separation

3115 8.4 Charged pion decay in flight

3116 As discussed previously, in GArSoft the TPC tracks are formed after a pattern recognition
3117 algorithm and a Kalman filter are applied to the TPC clusters. These two steps can
3118 find discontinuities in the track candidates (e.g. due to a particle decay) when these
3119 so-called breakpoints are large enough. However, for some, more subtle, cases they may
3120 miss them and form a single reconstructed track. It has been noted in the literature
3121 that Kalman filters offer, as a by-product, additional information to form test statistics
3122 to identify these breakpoints [?, ?].

3123 Considering the mean life of the charged pion, $\tau = (2.6033 \pm 0.0005) \times 10^{-8}$ s, one
3124 can estimate that about 12% of the pions with momentum $p \sim \mathcal{O}(500 \text{ MeV})$ (roughly
3125 the peak of the pion momentum distribution in ν_μ CC interactions off argon) decay
3126 inside the TPC. Figure 8.27 (left panel) shows the amount of charged pions decaying
3127 in the full TPC and fiducial volumes from an isotropic, monoenergetic sample of 10^5
3128 negatively charged pions with $p = 500 \text{ MeV}$. We see that about 10% of those decayed,
3129 with more than half of them decaying inside the TPC fiducial volume.

3130 Figure 8.27 (right panel) shows an example event display of a charged pion (magenta

8.4. Charged pion decay in flight

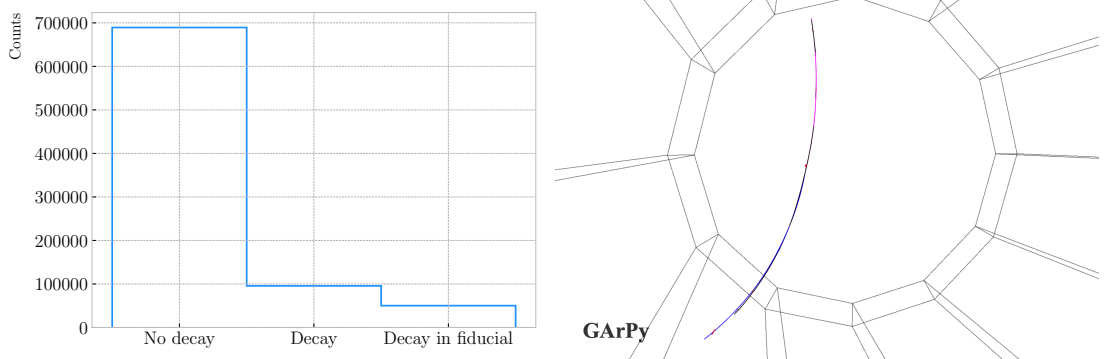


Figure 8.27: Left panel: number of non-decaying, decaying and decaying in the fiducial volume pions for a MC sample of 10^5 , $p = 500$ MeV isotropic positively charged pions inside the TPC. Right panel: event display for a positive pion decaying inside the fiducial volume, with a single reconstructed track for the pion and muon system.

line) decays in flight inside the TPC, but because the angle of the muon (blue line) is small both were reconstructed as one single track (black line). In this case, the composite track reaches the ECal, where it undergoes a muon-like interaction, thus being classified as a muon.

A way to understand what decaying pion tracks were totally or partially reconstructed together with the daughter muon is looking at the relative energy contributions to the reconstructed track. In order to select a sample of such events, I require that a minimum 50% of the total energy comes from the pion and at least 20% from the muon.

To identify potential decays we can use the information we obtain from the Kalman filter at each step of the fitted track. The simplest test we can think about is computing the χ^2 of the mismatch between all the parameters in the forward and the backward fits:

$$\chi_k^{(FB)} = (\hat{x}_k^B - \hat{x}_k^F)^T [V^{(\hat{x}_k, B)} + V^{(\hat{x}_k, F)}]^{-1} (\hat{x}_k^B - \hat{x}_k^F), \quad (8.18)$$

where \hat{x}_k^F , \hat{x}_k^B are the Kalman filter state vector estimates at step k in the forward and backward fits and $V^{(\hat{x}_k, F)}$, $V^{(\hat{x}_k, B)}$ the covariance matrices of \hat{x}_k^F and \hat{x}_k^B respectively. Using the values of the χ^2 at measurement k for the forward and backward fits we can

Chapter 8. Particle ID in GArSoft

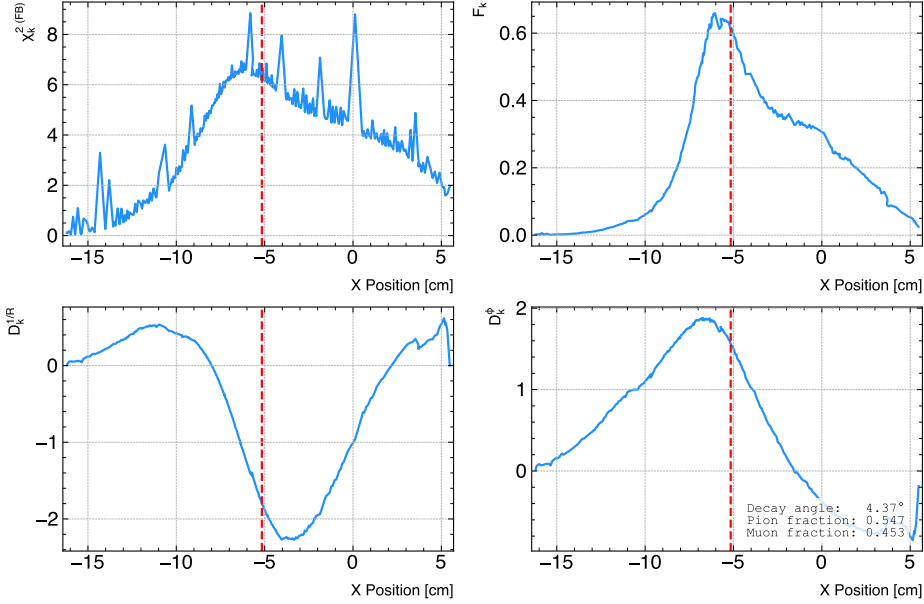


Figure 8.28: Values of $\chi_k^2(FB)$ (top left panel), F_k (top right panel), $D_k^{1/R}$ (bottom left panel) and D_k^ϕ (bottom right panel) versus position along the drift direction for a reconstructed track in a positive pion decay event. The vertical red dashed line indicates the true location of the decay point.

3145 compute another χ^2 value that characterises the overall track fit:

$$\chi_{track}^2 = \chi_k^2(F) + \chi_k^2(B) + \chi_k^2(FB), \quad (8.19)$$

3146 which remains approximately constant for all k .

3147 An alternative approach proposed in the context of the NOMAD experiment was
 3148 using a fit with a more elaborate breakpoint hypothesis, so we can perform a comparison
 3149 of the χ^2 with and without breakpoints. This can be achieved by using some alternative
 3150 parametrisation with extra parameters, which allows some of the track parameters to
 3151 be discontinuous at certain points. A decay changes the momentum magnitude and
 3152 direction, so we can use the new state vector:

$$\alpha = \begin{pmatrix} y, & z, & 1/R_F, & 1/R_B, & \phi_F, & \phi_B, & \tan\lambda_F, & \tan\lambda_B \end{pmatrix}^T. \quad (8.20)$$

3153 As we already have the estimates from the standard Kalman filter and their

8.4. Charged pion decay in flight

3154 covariance matrices at each point, we do not need to repeat the Kalman fit for the new
 3155 parametrisation. Instead, I can compute the values of α at each point k that minimise
 3156 the χ^2 resulting from comparing them to $\{\hat{x}_k^B, \hat{x}_k^F\}$. Introducing the two 5×8 matrices:

$$H^F = \begin{pmatrix} 1 & 0 & 0 & 0 & 0 & 0 & 0 & 0 \\ 0 & 1 & 0 & 0 & 0 & 0 & 0 & 0 \\ 0 & 0 & 1 & 0 & 0 & 0 & 0 & 0 \\ 0 & 0 & 0 & 0 & 1 & 0 & 0 & 0 \\ 0 & 0 & 0 & 0 & 0 & 0 & 1 & 0 \end{pmatrix}, \quad H^B = \begin{pmatrix} 1 & 0 & 0 & 0 & 0 & 0 & 0 & 0 \\ 0 & 1 & 0 & 0 & 0 & 0 & 0 & 0 \\ 0 & 0 & 0 & 1 & 0 & 0 & 0 & 0 \\ 0 & 0 & 0 & 0 & 0 & 1 & 0 & 0 \\ 0 & 0 & 0 & 0 & 0 & 0 & 0 & 1 \end{pmatrix}, \quad (8.21)$$

3157 we can write this as:

$$\begin{aligned} \chi_k^{2(FB)}(\alpha) &= (\hat{x}_k^F - H^F \alpha)^T [V^{(\hat{x}_k, F)}]^{-1} (\hat{x}_k^F - H^F \alpha) \\ &\quad + (\hat{x}_k^B - H^B \alpha)^T [V^{(\hat{x}_k, B)}]^{-1} (\hat{x}_k^B - H^B \alpha). \end{aligned} \quad (8.22)$$

3158 The minimum of $\chi_k^{2(FB)}(\alpha)$ is found when the measured new state vector takes the
 3159 value:

$$\hat{\alpha}_k = V^{(\hat{\alpha}_k)} H^T (V^{(\hat{x}_k)})^{-1} \hat{X}, \quad (8.23)$$

3160 where $\hat{X} = \{\hat{x}_k^B, \hat{x}_k^F\}$, $V^{(\hat{x}_k)}$ is the block diagonal matrix formed by $V^{(\hat{x}_k, F)}$ and $V^{(\hat{x}_k, B)}$
 3161 and $V^{(\hat{\alpha}_k)}$ is the covariance matrix of $\hat{\alpha}_k$, given by:

$$V^{(\hat{\alpha}_k)} = \left(H^T (V^{(\hat{x}_k)})^{-1} H \right)^{-1}. \quad (8.24)$$

3162 From these new fit estimates we can compute the F statistic, which tells us whether
 3163 the model with breakpoint provides a statistically significant better fit:

$$F_k = \left(\frac{\chi_{track,k}^2 - \chi_{full,k}^2}{8 - 5} \right) / \left(\frac{\chi_{full,k}^2}{N - 8} \right). \quad (8.25)$$

3164 One can also compute the signed difference of the duplicated variables divided by
 3165 their standard deviation at each point. These represent how significant the discontinuity

Chapter 8. Particle ID in GArSoft

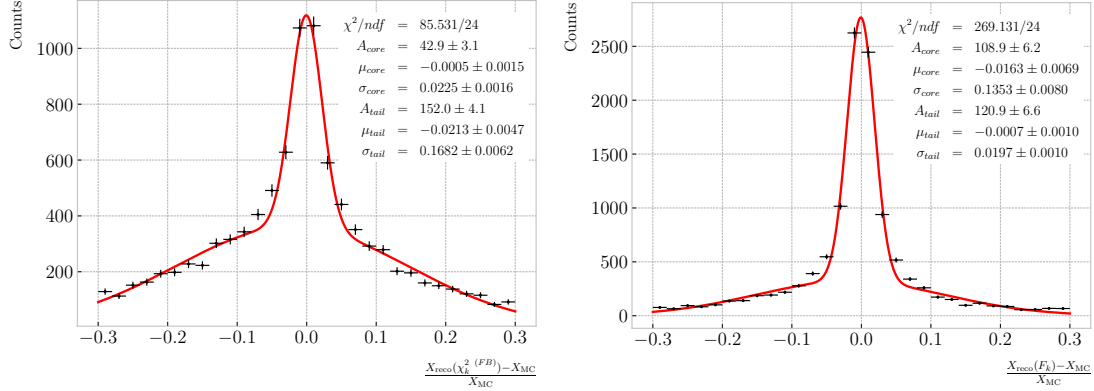


Figure 8.29: Fractional residual distributions of the true and reconstructed decay position along the drift coordinate, using the position of the maximum of $\chi_k^{2(FB)}$ (left panel) and F_k (right panel) as estimates of the decay position. Also shown are double Gaussian fits to these points (red lines).

in each variable is. For any variable η we can write it as:

$$D_k^\eta = \frac{\hat{\eta}_k^B - \hat{\eta}_k^F}{\sqrt{\text{Var}[\hat{\eta}_k^F] + \text{Var}[\hat{\eta}_k^B] - 2\text{Cov}[\hat{\eta}_k^F, \hat{\eta}_k^B]}}. \quad (8.26)$$

In our case, the relevant ones to look at are $D_k^{1/R}$ and D_k^ϕ .

Figure 8.28 shows the values of $\chi_k^{2(FB)}$, F_k , $D_k^{1/R}$ and D_k^ϕ as functions of the position along the drift direction, for an example reconstructed track with 55.5% of the energy coming from the charged pion and 45.5% from the daughter muon. The true position of the decay is indicated (dashed red lines). Notice how $\chi_k^{2(FB)}$ and F_k , $D_k^{1/R}$ reach their maxima near the decay point. In the former case this indicates a large forward-backward difference in the track fit. In the later it represents that the extended state vector improves the fit particularly around that point.

I can estimate the decay position finding resolution by computing the difference between the X position of the maxima of $\chi_k^{2(FB)}$ and F_k and the X position of the true decay. Figure 8.29 represent the the fractional residual distributions for both cases, from the sample of tracks containing pion decays. Fitting a double Gaussian to the distributions (red lines) I find a resolution of 13.62% and 7.45% respectively.

In principle, the F -statistic should follow a Fisher distribution with (8 – 5) and

8.4. Charged pion decay in flight

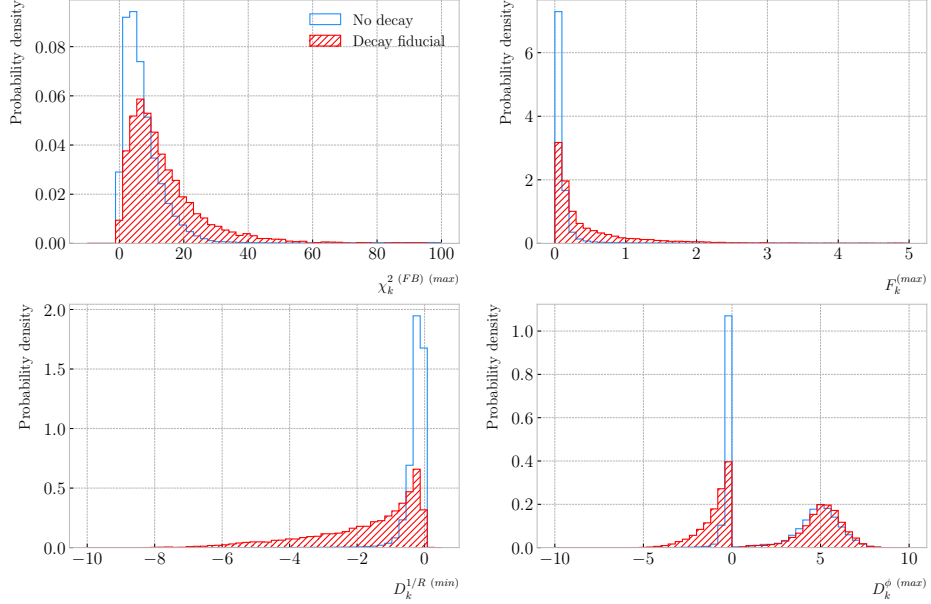


Figure 8.30: Distributions of the extreme values of $\chi_k^2(FB)$ (top left panel), F_k (top right panel), $D_k^{1/R}$ (bottom left panel) and D_k^ϕ (bottom right panel) for non-decaying reconstructed pion tracks (blue) and tracks which include the decay inside the fiducial volume (red).

3181 $(N - 8)$ degrees of freedom under the null hypothesis. In most of our cases $N \sim \mathcal{O}(100)$,
 3182 so the probability density functions will look very similar. In this case, it is safe to take
 3183 the limit $N \rightarrow \infty$ in the Fisher PDF:

$$\begin{aligned}\tilde{f}(x; a - b) &= \lim_{N \rightarrow \infty} f(x; a - b, N - a) \\ &= \frac{2^{-\frac{a-b}{2}}}{\Gamma(\frac{a-b}{2})} (a - b)^{\frac{a-b}{2}} x^{\frac{a-b}{2}-1} e^{-\frac{a-b}{2}x}.\end{aligned}\tag{8.27}$$

3184 In our case $a - b = 8 - 5 = 3$, so we would obtain a p-value of 0.05 at $x = 2.60$.

3185 Figure 8.30 contains the distributions of the maxima of $\chi_k^2(FB)$, F_k and D_k^ϕ and the
 3186 minima of $D_k^{1/R}$ for a sample of non-decaying pion tracks (blue) and another sample of
 3187 reconstructed tracks containing part of the pion and the daughter muon from a decay
 3188 inside the fiducial volume (red). Notice that, even though the values of $F_k^{(max)}$ for the
 3189 decay sample are typically larger than for the non-decaying one, just a small fraction of
 3190 the events go beyond the aforementioned value of $F = 2.60$. Therefore, from a practical

Chapter 8. Particle ID in GArSoft

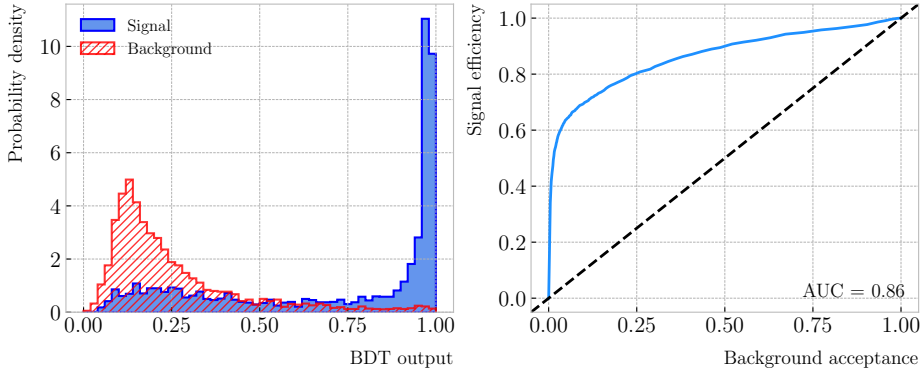


Figure 8.31: Left panel: distributions of the predicted probabilities assigned by the BDT classifier to a test sample of decaying pion+muon tracks (blue) and non-decaying pion tracks (red). Left: signal efficiency versus background acceptance (ROC curve) obtained from the BDT for the test sample.

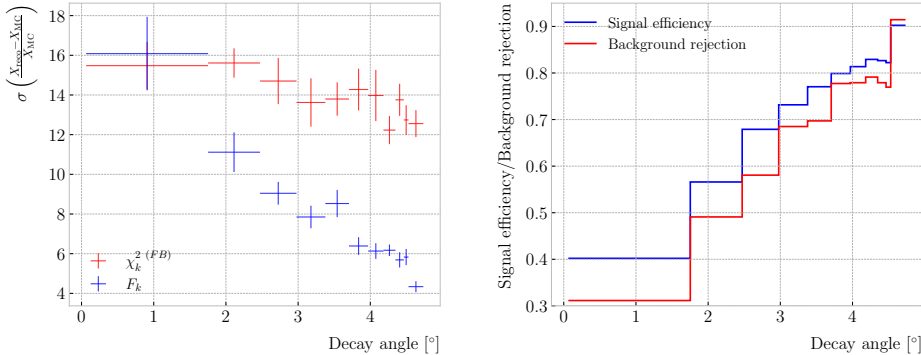


Figure 8.32: Left panel: dependence of the decay position finding resolution on the true value of the decay angle for the $\chi_k^2(FB)$ (red) and F_k (blue) methods. Right panel: signal efficiency (blue line) and background rejection (red line) from the BDT classifier versus true decay angle.

3191 point of view, it is not the most efficient variable to use for selecting the decay events.

3192 However, looking at the $D_k^{1/R \text{ (min)}}$ distribution we can see there is a big difference
 3193 between non-decaying and decaying events in this variable. One can use a combination
 3194 of these four variables to distinguish between the pion decay events (signal) and the
 3195 non-decaying pions (background).

3196 An approach to this classification could be using a boosted decision tree (BDT). One
 3197 of the advantages of BDTs is that they are easy to interpret and identify the relative
 3198 importance of the different input variables. Training a BDT with 400 estimators and a
 3199 maximum depth of 4 I can obtain an efficient classification without overtraining. Figure

8.5. Neutral particle identification

3200 8.31 (left panel) shows the distribution of probabilities predicted by the BDT for a test
3201 sample. The signal efficiency as a function of background acceptance, the so-called ROC
3202 curve, is shown in Fig. 8.31 (right panel). With a relative importance of 0.83, the most
3203 important variable turned out to be $D_k^{1/R \text{ (min)}}$.

3204 One thing we can check is how the resolution to the decay and the signal efficiency in
3205 the classification changes with the true decay angle. Using an equal-frequency binning
3206 for the decay angles, we can repeat the previous steps for each bin.

3207 Figure 8.32 (left panel) shows the dependence on the decay angle of the decay finding
3208 resolution. We can see that for the $\chi_k^2 \text{ (FB)}$ maximum location method the resolution
3209 consistently lies between 12 to 16%. However, the $F_k^{(max)}$ approach gives a significantly
3210 better resolution for high angle values, reaching the 4 – 6% range for decay angles $\geq 4^\circ$.

3211 For the classification dependence on the angle, I use the same classifier I trained
3212 before but evaluating the test sample for each individual angular bin. I compute the
3213 signal efficiency in each bin for a fixed value of the background rejection, in this case
3214 90%. Similarly, for the background rejection estimation I use a fixed signal efficiency
3215 value of 90%. Figure 8.32 (right panel) represents the change in signal efficiency (blue)
3216 and background rejection (red) with the value of the true decay angles.

3217 8.4.1 Track breakpoints

3218 8.5 Neutral particle identification

3219 8.5.1 ECal clustering

3220 Another important reconstruction item is the clustering algorithm of ECal hits in
3221 GArSoft. The default module features a NN algorithm that treats all hits in the same
3222 way, independently of the layer each hit comes from. However, the current ECal design
3223 of ND-GAr has two very different types of scintillator layers. The inner layers are made
3224 out of tiles, which provide excellent angular and timing resolutions. On the other hand,
3225 the outer layers are cross scintillator strips. That way, an algorithm that treats hits
3226 from both kinds of layers differently may be able to improve the current performance.

Chapter 8. Particle ID in GArSoft

3227 Inspired by the reconstruction of T2K’s ND280 downstream ECal [?], the idea was
3228 to put together a clustering module that first builds clusters for the different ECal views
3229 (tiles, strips segmented in the X direction and strips segmented in Y direction), and
3230 then tries to match them together to form the final clusters.

3231 Working on a module-by-module basis, the algorithm first separates the hits depending
3232 on the layer type they come from. Then, it performs a NN clustering for the 3 sets of
3233 hits separately. For the tile hits it clusters together all the hits which are in nearest-
3234 neighbouring tiles and nearest-neighbouring layers, for strip hits it looks at nearest-
3235 neighbouring strips and next-to-nearest-neighbouring layers (as the layers with strips
3236 along the two directions are alternated). For strip clusters an additional cut in the
3237 direction along the strip length is needed.

3238 After this first clustering I then apply a recursive re-clustering for each collection
3239 of strip clusters based on a PCA method. In each case, we loop over the clusters with
3240 $N_{hits} \geq 2$, computing the centre of mass and three principal components. Propagating
3241 these axes up to the layers of the rest of the clusters, we check if the propagated point
3242 and the centre of mass of the second cluster are within next-to-nearest-neighbouring
3243 strips. An additional cut in the direction along the strip length is also needed. Moreover,
3244 I require that the two closest hits across the two clusters are at most in next-to-nearest-
3245 neighbouring strips. I merge the clusters if these three conditions are satisfied. The
3246 re-clustering is repeated until no more cluster pairs pass the cuts.

3247 The clusters in each strip view are combined if their centres of mass are close enough
3248 and they point in the same direction. An alternative approach for the strip cluster
3249 merging could be to compute the overlap between the ellipsoids defined by the principal
3250 axes of the clusters, and then merge the pair if the overlap exceeds some threshold.
3251 Further study is needed to understand if this change would have an impact in the overall
3252 clustering performance.

3253 To merge the tile clusters to the combined strip clusters I propagate the principal
3254 axis of the strip cluster towards the inner layers, up to the centre of mass layer of the
3255 tile cluster. I merge the clusters if the distance between the propagated point and the

8.5. Neutral particle identification

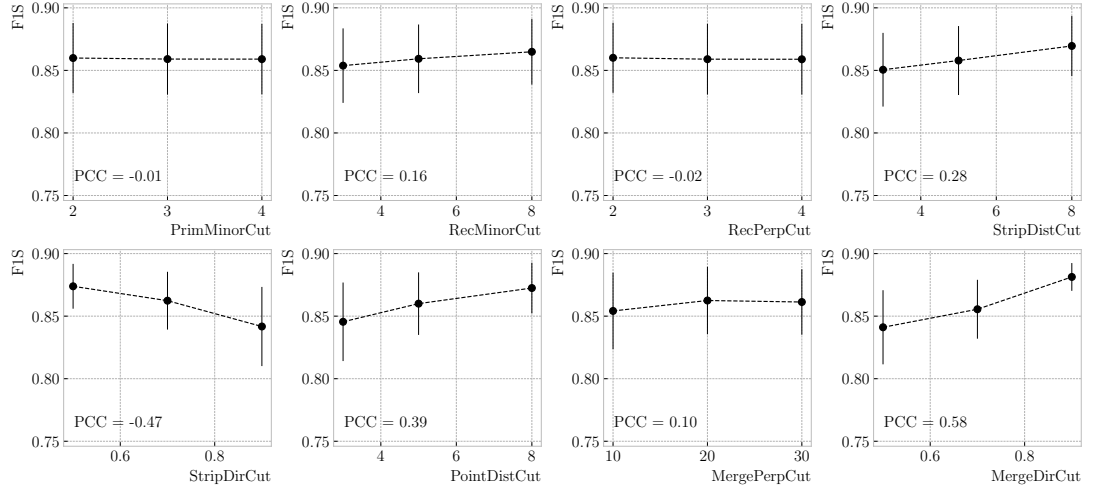


Figure 8.33: Mean values of the F_1 -score marginal distributions for the different free parameters of the new clustering algorithm, with the error bars representing one standard deviation around the mean. The F_1 -score values were computed for the 6561 possible parameter configurations using 1000 ν_μ CC interaction events.

3256 centre of mass is bellow a certain cut.

3257 The last step is to check if clusters in neighbouring modules should be merged
 3258 together, both across two barrel modules, across end cap modules and between barrel
 3259 end cap modules. I check the distance between the two closest hits in the pair of clusters
 3260 and merge them if it passes this and an additional direction cut.

3261 Figure ?? presents an example of the clustering steps relevant for strip layer hits, from
 3262 the input hits (top left panel) to the NN clustering (top right panel) and re-clustering
 3263 (bottom left panel) for each strip view and the final merging strip clusters (bottom
 3264 right panel). It shows the hits from a single ECal barrel module in a ν_μ CC interaction
 3265 event with a neutral pion and a proton in the final state. The two clusters on the left
 3266 correspond to the photon pair from the π^0 decay and the one on the upper right corner
 3267 is associated to the proton.

3268 This algorithm has a total number of eight free parameters that need to be optimised.
 3269 I used a sample of 1000 ν_μ CC interactions in order to obtain the optimal configuration of
 3270 clustering parameters. This sample was generated up to the default ECal hit clustering
 3271 level, so then I could run the new clustering algorithm each time with a different

Chapter 8. Particle ID in GArSoft

Table 8.4: Summary of parameters and sampled values used in the optimisation of the clustering algorithm.

Name	Units	Sampled values	Description
PrimMinorCut	strips	2, 3, 4	Distance along strip length in NN clustering
RecMinorCut	strips	3, 5, 8	Distance between propagated point and CM along strip length in re-clustering
RecPerpCut	strips	2, 3, 4	Closest hit pair distance in re-clustering
StripDistCut	strips	3, 5, 8	Distance between CMs in strip cluster merging
StripDirCut	cos	0.5, 0.7, 0.9	Main axes direction cut in strip cluster merging
PointDistCut	tiles	3, 5, 8	Distance between propagated point and CM in strip-tile matching
MergePerpCut	cm	10, 20, 30	Closest hit pair distance in module merging
MergeDirCut	cos	0.5, 0.7, 0.9	Main axes direction cut in module merging

3272 configuration of parameters. As the number of parameters is relatively large, I only
 3273 performed a coarse-grained scan of the parameter space. Sampling each of the eight
 3274 parameters at three different points each I obtain 6561 different configurations. These
 3275 parameters, together with the used values, are summarised in Tab. 8.4.

3276 In order to measure the performance of the clustering, I use a binary classification
 3277 approach. For each formed cluster, I identify the Geant4 Track ID of the matching MC
 3278 particle and the energy fraction of each hit. Then, I assign to each cluster the Track ID
 3279 with the highest total energy fraction. For each of the different Track IDs associated to
 3280 the clusters, I select the cluster with the highest energy (only from the hits with the
 3281 same Track ID). I identify such a cluster as the main cluster for that Track ID. I count
 3282 as true positives (TPs) the hits with the correct Track ID in each main cluster. False
 3283 positives (FPs) are the hits with the incorrect Track ID for the cluster they are in, not
 3284 only main clusters. The false negatives (FNs) are the hits with the correct Track ID in
 3285 clusters other than the main.

3286 Figure 8.33 shows the computed F_1 -score values for the different cuts. In each case,
 3287 the central value represents the mean of the F_1 -score distribution for the specified value
 3288 of the corresponding variable and the vertical error bar represents one standard deviation

8.5. Neutral particle identification

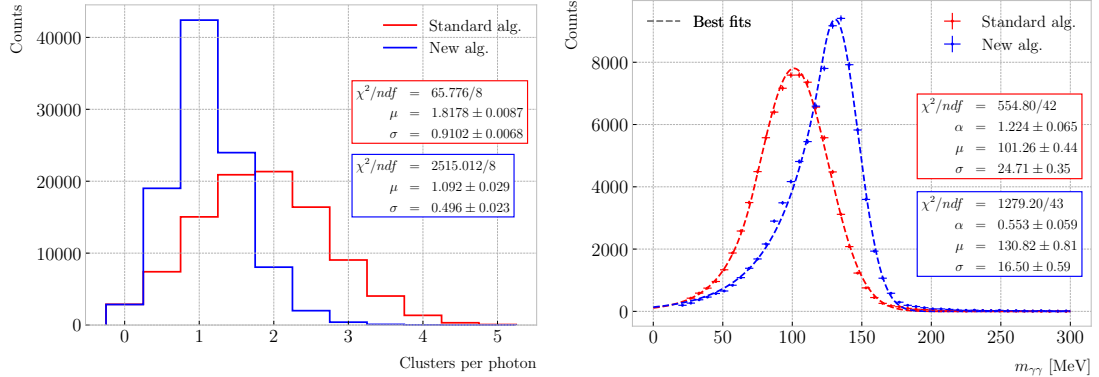


Figure 8.34: Left panel: distributions of the number of ECal clusters per photon from π^0 decays for the standard (red) and new (blue) clustering algorithms. Right panel: reconstructed invariant mass distributions for photon pairs from single π^0 events using the standard (red) and new (blue) ECal clustering algorithms.

3289 around the mean. Also shown are the Pearson correlation coefficients of these central
 3290 values. We can see that five of the variables have a sizeable effect on the F_1 -score, with
 3291 an absolute difference between the last and first values as big as 4%.

3292 The working configuration is obtained as follows. I first select all configurations
 3293 with purity $\geq 90\%$. Among those, I choose the combinations that yield the maximum
 3294 F_1 -score. If more than one configuration remains I select the one with the highest
 3295 sensitivity. Doing so, I end up with a parameter configuration with an efficiency of 88%
 3296 and a 90% purity. Compared with the default algorithm, which gives an efficiency of
 3297 76% and a purity of 91% for the same sample, I have managed to improve the efficiency
 3298 by a factor of 1.16.

3299 8.5.2 π^0 reconstruction

3300 One of the potential applications of the new ECal hit clustering is the reconstruction of
 3301 neutral particles, in particular pions. Neutral pions decay promptly after being produced,
 3302 through the $\pi^0 \rightarrow \gamma\gamma$ channel ($98.823 \pm 0.034\%$) of the time. The photon pair does
 3303 not leave any traces in the HPgTPC (unless one or both of them converts into an
 3304 electron-positron pair), but each of them will produce an electromagnetic shower in
 3305 the ECal.

Chapter 8. Particle ID in GArSoft

3306 To test the potential impact of the new algorithm in π^0 reconstruction, I generated
3307 a MC sample of single, isotropic neutral pions inside the HPgTPC. All pions were
3308 generated with a momentum $p = 500$ MeV and their initial positions were uniformly
3309 sampled inside a $2 \times 2 \times 2$ m box aligned with the centre of the TPC. I ran both the
3310 default and the new clustering algorithms, using for the latter the optimised configuration
3311 discussed above.

3312 The first thing to notice is that the number of clusters produced per photon has
3313 decreased. Figure 8.34 (left panel) shows these distributions for the default (red) and
3314 new (blue) algorithms. Using a simple Gaussian fit, we see that the mean number of
3315 ECal clusters per photon went from 1.82 ± 0.01 to 1.09 ± 0.03 . This effectively means that
3316 with the new algorithm the ECal activity of one true particle is typically reconstructed
3317 as a single object. From the reconstruction point of view this can be an advantage. As
3318 now most of the photon energy ends up in a single ECal cluster, I can simply use cluster
3319 pairs to identify the π^0 decay.

3320 In general, one calculates the invariant mass of the photon pair as:

$$m_{\gamma\gamma} = \sqrt{2E_1E_2(1 - \cos \theta)}, \quad (8.28)$$

3321 where E_i are the energies of the photons and θ the opening angle between them. In this
3322 case I can use the energies deposited in the ECal and their incident directions. This
3323 quantity is computed for all possible pairs of clusters, using their position together with
3324 the true decay point. In a more realistic scenario, e.g. ν_μ CC interaction, one could use
3325 the position of the reconstructed primary vertex instead. I also tried to use the principal
3326 direction of the clusters, but that approach gave considerably worse results. For each
3327 event I only keep the pair with an invariant mass closer to the true π^0 mass value.

3328 Figure 8.34 (right panel) shows the invariant mass distributions for the photon pairs
3329 we get using the default (red) and the new (blue) ECal clustering algorithms. For the fit
3330 I used a modified version of the Crystal Ball function [?], obtained by taking the limit

8.5. Neutral particle identification

3331 where the parameter controlling the power-law tail goes to infinity:

$$f(x; N, \mu, \sigma, \alpha) = N \cdot \begin{cases} e^{\frac{\alpha(2x-2\mu+\alpha\sigma)}{2\sigma}}; & x \leq \mu - \alpha\sigma, \\ e^{-\frac{(x-\mu)^2}{2\sigma^2}}; & x > \mu - \alpha\sigma. \end{cases} \quad (8.29)$$

3332 Comparing the fitted mean and standard deviation values for the Gaussian cores, we
3333 see that the distribution for the new algorithm is a 67% narrower and also peaks much
3334 closer to the true m_{π^0} value, going from 101.3 ± 0.4 MeV to 130.8 ± 0.6 MeV.

3335 Chapter 9

3336 Event selection in ND-GAr

3337 9.1 CAFs and CAFAna

3338 9.2 Event selection

3339 9.2.1 ν_μ CC selection

3340 9.2.2 Charged pion multiplicity

3341 Chapter 10

3342 Conclusions

₃₃₄₃ Appendix A

₃₃₄₄ An appendix

³³⁴⁵ Bibliography

- ³³⁴⁶ [1] DUNE collaboration, *Deep Underground Neutrino Experiment (DUNE), Far*
³³⁴⁷ *Detector Technical Design Report, Volume I Introduction to DUNE*, JINST **15**
³³⁴⁸ (2020) T08008 [2002.02967]. 15, 43, 44, 45, 48, 49, 50, 56, 57, 58, 65, 66
- ³³⁴⁹ [2] DUNE collaboration, *Deep Underground Neutrino Experiment (DUNE), Far*
³³⁵⁰ *Detector Technical Design Report, Volume IV: Far Detector Single-phase*
³³⁵¹ *Technology*, JINST **15** (2020) T08010 [2002.03010]. 15, 53
- ³³⁵² [3] J.N. Bahcall, A.M. Serenelli and S. Basu, *New solar opacities, abundances,*
³³⁵³ *helioseismology, and neutrino fluxes*, *Astrophys. J. Lett.* **621** (2005) L85
³³⁵⁴ [[astro-ph/0412440](#)]. 21, 113, 115
- ³³⁵⁵ [4] R. Garani and S. Palomares-Ruiz, *Dark matter in the Sun: scattering off electrons*
³³⁵⁶ *vs nucleons*, JCAP **05** (2017) 007 [[1702.02768](#)]. 21, 111, 112, 114, 115, 116, 139
- ³³⁵⁷ [5] M. Honda, M. Sajjad Athar, T. Kajita, K. Kasahara and S. Midorikawa,
³³⁵⁸ *Atmospheric neutrino flux calculation using the NRLMSISE-00 atmospheric model*,
³³⁵⁹ *Phys. Rev. D* **92** (2015) 023004 [[1502.03916](#)]. 22, 119, 120
- ³³⁶⁰ [6] M. Colom i Bernadich and C. Pérez de los Heros, *Limits on Kaluza-Klein dark*
³³⁶¹ *matter annihilation in the Sun from recent IceCube results*, Eur. Phys. J. C, **80** 2
³³⁶² (2020) 129 **80** (2019) [[1912.04585](#)]. 22, 124
- ³³⁶³ [7] ANTARES collaboration, *Search for Dark Matter in the Sun with the ANTARES*
³³⁶⁴ *Neutrino Telescope in the CMSSM and mUED frameworks*, Nucl. Instrum. Meth. A
³³⁶⁵ **725** (2013) 76 [[1204.5290](#)]. 22, 124

BIBLIOGRAPHY

- 3366 [8] N. Deutschmann, T. Flacke and J.S. Kim, *Current LHC Constraints on Minimal*
3367 *Universal Extra Dimensions*, *Phys. Lett. B* **771** (2017) 515 [[1702.00410](#)]. 22, 124,
3368 125
- 3369 [9] ICECUBE collaboration, *Search for GeV-scale dark matter annihilation in the Sun*
3370 *with IceCube DeepCore*, *Phys. Rev. D* **105** (2022) 062004 [[2111.09970](#)]. 24, 136,
3371 137
- 3372 [10] C.-S. Chen, F.-F. Lee, G.-L. Lin and Y.-H. Lin, *Probing Dark Matter*
3373 *Self-Interaction in the Sun with IceCube-PINGU*, *JCAP* **10** (2014) 049 [[1408.5471](#)].
3374 24, 136, 137
- 3375 [11] N.F. Bell, M.J. Dolan and S. Robles, *Searching for dark matter in the Sun using*
3376 *Hyper-Kamiokande*, *JCAP* **11** (2021) 004 [[2107.04216](#)]. 24, 136, 137
- 3377 [12] E. Behnke et al., *Final Results of the PICASSO Dark Matter Search Experiment*,
3378 *Astropart. Phys.* **90** (2017) 85 [[1611.01499](#)]. 24, 136, 137
- 3379 [13] PICO collaboration, *Dark Matter Search Results from the Complete Exposure of*
3380 *the PICO-60 C₃F₈ Bubble Chamber*, *Phys. Rev. D* **100** (2019) 022001
3381 [[1902.04031](#)]. 24, 136, 137
- 3382 [14] DARKSIDE collaboration, *Constraints on Sub-GeV Dark-Matter–Electron*
3383 *Scattering from the DarkSide-50 Experiment*, *Phys. Rev. Lett.* **121** (2018) 111303
3384 [[1802.06998](#)]. 24, 140, 141
- 3385 [15] XENON collaboration, *Light Dark Matter Search with Ionization Signals in*
3386 *XENON1T*, *Phys. Rev. Lett.* **123** (2019) 251801 [[1907.11485](#)]. 24, 140, 141
- 3387 [16] P.F. de Salas, D.V. Forero, S. Gariazzo, P. Martínez-Miravé, O. Mena, C.A. Ternes
3388 et al., *2020 global reassessment of the neutrino oscillation picture*, *JHEP* **02** (2021)
3389 071 [[2006.11237](#)]. 29, 40, 45
- 3390 [17] W. Pauli, *Dear radioactive ladies and gentlemen*, *Phys. Today* **31N9** (1978) 27. 35

BIBLIOGRAPHY

- 3391 [18] F. Reines and C.L. Cowan, *Detection of the free neutrino*, *Phys. Rev.* **92** (1953) 830. 35
- 3392
- 3393 [19] ALEPH, DELPHI, L3, OPAL, SLD, LEP ELECTROWEAK WORKING GROUP, SLD ELECTROWEAK GROUP, SLD HEAVY FLAVOUR GROUP collaboration, *Precision electroweak measurements on the Z resonance*, *Phys. Rept.* **427** (2006) 257 [[hep-ex/0509008](#)]. 36
- 3394
- 3395
- 3396
- 3397 [20] SUPER-KAMIOKANDE collaboration, *Evidence for oscillation of atmospheric neutrinos*, *Phys. Rev. Lett.* **81** (1998) 1562 [[hep-ex/9807003](#)]. 36
- 3398
- 3399 [21] B. Pontecorvo, *Inverse beta processes and nonconservation of lepton charge*, *Zh. Eksp. Teor. Fiz.* **34** (1957) 247. 36
- 3400
- 3401 [22] Z. Maki, M. Nakagawa and S. Sakata, *Remarks on the unified model of elementary particles*, *Prog. Theor. Phys.* **28** (1962) 870. 36
- 3402
- 3403 [23] L. Wolfenstein, *Neutrino Oscillations in Matter*, *Phys. Rev. D* **17** (1978) 2369. 38
- 3404
- 3405 [24] B.T. Cleveland, T. Daily, R. Davis, Jr., J.R. Distel, K. Lande, C.K. Lee et al., *Measurement of the solar electron neutrino flux with the Homestake chlorine detector*, *Astrophys. J.* **496** (1998) 505. 39
- 3406
- 3407 [25] F. Kaether, W. Hampel, G. Heusser, J. Kiko and T. Kirsten, *Reanalysis of the GALLEX solar neutrino flux and source experiments*, *Phys. Lett. B* **685** (2010) 47 [1001.2731]. 39
- 3408
- 3409
- 3410 [26] SAGE collaboration, *Measurement of the solar neutrino capture rate with gallium metal. III: Results for the 2002–2007 data-taking period*, *Phys. Rev. C* **80** (2009) 015807 [0901.2200]. 39
- 3411
- 3412
- 3413 [27] G. Bellini et al., *Precision measurement of the ^{7}Be solar neutrino interaction rate in Borexino*, *Phys. Rev. Lett.* **107** (2011) 141302 [1104.1816]. 39
- 3414

BIBLIOGRAPHY

- 3415 [28] SUPER-KAMIOKANDE collaboration, *Solar neutrino measurements in*
3416 *super-Kamiokande-I*, *Phys. Rev. D* **73** (2006) 112001 [[hep-ex/0508053](#)]. 39
- 3417 [29] SNO collaboration, *Combined Analysis of all Three Phases of Solar Neutrino Data*
3418 *from the Sudbury Neutrino Observatory*, *Phys. Rev. C* **88** (2013) 025501
3419 [[1109.0763](#)]. 39
- 3420 [30] SUPER-KAMIOKANDE collaboration, *Atmospheric neutrino oscillation analysis with*
3421 *external constraints in Super-Kamiokande I-IV*, *Phys. Rev. D* **97** (2018) 072001
3422 [[1710.09126](#)]. 39
- 3423 [31] ICECUBE collaboration, *Measurement of Atmospheric Neutrino Oscillations at*
3424 *6–56 GeV with IceCube DeepCore*, *Phys. Rev. Lett.* **120** (2018) 071801
3425 [[1707.07081](#)]. 39
- 3426 [32] KAMLAND collaboration, *Reactor On-Off Antineutrino Measurement with*
3427 *KamLAND*, *Phys. Rev. D* **88** (2013) 033001 [[1303.4667](#)]. 39
- 3428 [33] RENO collaboration, *Measurement of Reactor Antineutrino Oscillation Amplitude*
3429 *and Frequency at RENO*, *Phys. Rev. Lett.* **121** (2018) 201801 [[1806.00248](#)]. 39
- 3430 [34] DAYA BAY collaboration, *Measurement of the Electron Antineutrino Oscillation*
3431 *with 1958 Days of Operation at Daya Bay*, *Phys. Rev. Lett.* **121** (2018) 241805
3432 [[1809.02261](#)]. 39
- 3433 [35] K.J. Kelly, P.A.N. Machado, S.J. Parke, Y.F. Perez-Gonzalez and R.Z. Funchal,
3434 *Neutrino mass ordering in light of recent data*, *Phys. Rev. D* **103** (2021) 013004. 40
- 3435 [36] P. Dunne, “Latest Neutrino Oscillation Results from T2K.” Jul, 2020. 40
- 3436 [37] MINOS collaboration, *Combined analysis of ν_μ disappearance and $\nu_\mu \rightarrow \nu_e$*
3437 *appearance in MINOS using accelerator and atmospheric neutrinos*, *Phys. Rev. Lett.*
3438 **112** (2014) 191801 [[1403.0867](#)]. 40

BIBLIOGRAPHY

- 3439 [38] K2K collaboration, *Measurement of Neutrino Oscillation by the K2K Experiment*,
3440 *Phys. Rev. D* **74** (2006) 072003 [[hep-ex/0606032](#)]. 40
- 3441 [39] DUNE collaboration, *Long-baseline neutrino oscillation physics potential of the*
3442 *DUNE experiment*, *Eur. Phys. J. C* **80** (2020) 978 [[2006.16043](#)]. 40
- 3443 [40] HYPER-KAMIOKANDE collaboration, *Physics potential of Hyper-Kamiokande for*
3444 *neutrino oscillation measurements*, *PoS NuFact2019* (2019) 040. 40
- 3445 [41] DUNE collaboration, *Snowmass Neutrino Frontier: DUNE Physics Summary*,
3446 [2203.06100](#). 45, 46
- 3447 [42] DUNE collaboration, *Deep Underground Neutrino Experiment (DUNE), Far*
3448 *Detector Technical Design Report, Volume II: DUNE Physics*, [2002.03005](#). 45, 47,
3449 61, 63, 119, 128, 132
- 3450 [43] SUPER-KAMIOKANDE collaboration, *Search for Proton Decay via $p \rightarrow e^+ \pi_0$ and*
3451 *$p \rightarrow \mu^+ \pi_0$ in a Large Water Cherenkov Detector*, *Phys. Rev. Lett.* **102** (2009)
3452 [141801](#) [[0903.0676](#)]. 46
- 3453 [44] S. Raby, *Grand Unified Theories*, in *2nd World Summit: Physics Beyond the*
3454 *Standard Model*, 8, 2006 [[hep-ph/0608183](#)]. 46
- 3455 [45] KAMIOKANDE-II collaboration, *Observation of a Neutrino Burst from the*
3456 *Supernova SN 1987a*, *Phys. Rev. Lett.* **58** (1987) 1490. 47
- 3457 [46] R.M. Bionta et al., *Observation of a Neutrino Burst in Coincidence with Supernova*
3458 *SN 1987a in the Large Magellanic Cloud*, *Phys. Rev. Lett.* **58** (1987) 1494. 47
- 3459 [47] DUNE collaboration, *The DUNE Far Detector Vertical Drift Technology*,
3460 *Technical Design Report*, [2312.03130](#). 51, 52
- 3461 [48] DUNE collaboration, *Deep Underground Neutrino Experiment (DUNE) Near*
3462 *Detector Conceptual Design Report, Instruments* **5** (2021) 31 [[2103.13910](#)]. 55, 56,
3463 59, 63, 143

BIBLIOGRAPHY

- 3464 [49] J. Strait, E. McCluskey, T. Lundin, J. Willhite, T. Hamernik, V. Papadimitriou
3465 et al., *Long-baseline neutrino facility (lbnf) and deep underground neutrino*
3466 *experiment (dune) conceptual design report volume 3: Long-baseline neutrino*
3467 *facility for dune june 24, 2015*, 1601.05823. 60
- 3468 [50] DUNE DAQ, “dtp-firmware.”
3469 <https://gitlab.cern.ch/dune-daq/readout/dtp-firmware>, 2020. 75
- 3470 [51] DUNE DAQ, “dtp-simulation.”
3471 <https://gitlab.cern.ch/dune-daq/readout/dtp-simulation>, 2020. 78
- 3472 [52] DUNE DAQ, “dtpemulator.”
3473 https://github.com/DUNE-DAQ/dtpemulator/tree/fmlopez/filter_ana, 2022.
3474 78
- 3475 [53] J. McClellan and T. Parks, *A personal history of the Parks-McClellan algorithm*,
3476 *IEEE Signal Processing Magazine* **22** (2005) 82. 79
- 3477 [54] G. Turin, *An introduction to matched filters*, *IEEE Transactions on Information*
3478 *Theory* **6** (1960) 311. 82
- 3479 [55] J.W. Goodman, *Statistical Optics*, Wiley (1985). 84
- 3480 [56] B. Dwork, *Detection of a pulse superimposed on fluctuation noise*, *Proceedings of*
3481 *the IRE* **38** (1950) 771. 85
- 3482 [57] L. Wainstein and V. Zubakov, *Extraction of Signals from Noise*, Prentice-Hall
3483 (1962). 85
- 3484 [58] E.D. Church, *Larsoft: A software package for liquid argon time projection drift*
3485 *chambers*, 1311.6774. 88, 89
- 3486 [59] S.V. Stehman, *Selecting and interpreting measures of thematic classification*
3487 *accuracy*, *Remote Sensing of Environment* **62** (1997) 77. 102

BIBLIOGRAPHY

- 3488 [60] A.A. Taha and A. Hanbury, *Metrics for evaluating 3d medical image segmentation: analysis, selection, and tool*, *BMC Medical Imaging* **15** (2015) . 103
- 3489
- 3490 [61] J. Silk, K.A. Olive and M. Srednicki, *The Photino, the Sun and High-Energy Neutrinos*, *Phys. Rev. Lett.* **55** (1985) 257. 109
- 3491
- 3492 [62] M. Srednicki, K.A. Olive and J. Silk, *High-Energy Neutrinos from the Sun and Cold Dark Matter*, *Nucl. Phys. B* **279** (1987) 804. 109
- 3493
- 3494 [63] J.S. Hagelin, K.W. Ng and K.A. Olive, *A High-energy Neutrino Signature From Supersymmetric Relics*, *Phys. Lett. B* **180** (1986) 375. 109
- 3495
- 3496 [64] T.K. Gaisser, G. Steigman and S. Tilav, *Limits on Cold Dark Matter Candidates from Deep Underground Detectors*, *Phys. Rev. D* **34** (1986) 2206. 109
- 3497
- 3498 [65] N. Bernal, J. Martín-Albo and S. Palomares-Ruiz, *A novel way of constraining WIMPs annihilations in the Sun: MeV neutrinos*, *JCAP* **08** (2013) 011
- 3499
- 3500 [1208.0834]. 109, 110, 111, 117
- 3501 [66] C. Rott, J. Siegal-Gaskins and J.F. Beacom, *New Sensitivity to Solar WIMP Annihilation using Low-Energy Neutrinos*, *Phys. Rev. D* **88** (2013) 055005
- 3502
- 3503 [1208.0827]. 109, 116
- 3504 [67] C. Rott, S. In, J. Kumar and D. Yaylali, *Dark Matter Searches for Monoenergetic Neutrinos Arising from Stopped Meson Decay in the Sun*, *JCAP* **11** (2015) 039
- 3505
- 3506 [1510.00170]. 109
- 3507 [68] DUNE collaboration, *Searching for solar KDAR with DUNE*, *JCAP* **10** (2021) 065
- 3508 [2107.09109]. 109
- 3509 [69] G. Busoni, A. De Simone and W.-C. Huang, *On the Minimum Dark Matter Mass Testable by Neutrinos from the Sun*, *JCAP* **07** (2013) 010 [1305.1817]. 110
- 3510
- 3511 [70] V.A. Bednyakov and F. Simkovic, *Nuclear spin structure in dark matter search: The Zero momentum transfer limit*, *Phys. Part. Nucl.* **36** (2005) 131
- 3512
- 3513 [hep-ph/0406218]. 111

BIBLIOGRAPHY

- 3514 [71] A. Gould, *WIMP Distribution in and Evaporation From the Sun*, *Astrophys. J.* **321**
3515 (1987) 560. 112
- 3516 [72] J.N. Bahcall, M.H. Pinsonneault and S. Basu, *Solar models: Current epoch and*
3517 *time dependences, neutrinos, and helioseismological properties*, *Astrophys. J.* **555**
3518 (2001) 990 [[astro-ph/0010346](#)]. 114
- 3519 [73] T. Golan, J.T. Sobczyk and J. Zmuda, *NuWro: the Wroclaw Monte Carlo*
3520 *Generator of Neutrino Interactions*, *Nucl. Phys. B Proc. Suppl.* **229-232** (2012)
3521 499. 118
- 3522 [74] G. Cowan, K. Cranmer, E. Gross and O. Vitells, *Asymptotic formulae for*
3523 *likelihood-based tests of new physics*, *Eur. Phys. J. C* **71** (2011) 1554 [[1007.1727](#)].
3524 119
- 3525 [75] T. Kaluza, *Zum Unitätsproblem der Physik, Sitzungsber. Preuss. Akad. Wiss.*
3526 *Berlin (Math. Phys.)* **1921** (1921) 966 [[1803.08616](#)]. 121
- 3527 [76] O. Klein, *Quantum Theory and Five-Dimensional Theory of Relativity. (In*
3528 *German and English)*, *Z. Phys.* **37** (1926) 895. 121
- 3529 [77] T. Appelquist, H.-C. Cheng and B.A. Dobrescu, *Bounds on universal extra*
3530 *dimensions*, *Phys. Rev. D* **64** (2001) 035002 [[hep-ph/0012100](#)]. 121
- 3531 [78] N. Arkani-Hamed, S. Dimopoulos and G.R. Dvali, *The Hierarchy problem and new*
3532 *dimensions at a millimeter*, *Phys. Lett. B* **429** (1998) 263 [[hep-ph/9803315](#)]. 121
- 3533 [79] L. Randall and R. Sundrum, *A Large mass hierarchy from a small extra dimension*,
3534 *Phys. Rev. Lett.* **83** (1999) 3370 [[hep-ph/9905221](#)]. 121
- 3535 [80] G. Servant and T.M.P. Tait, *Is the lightest Kaluza-Klein particle a viable dark*
3536 *matter candidate?*, *Nucl. Phys. B* **650** (2003) 391 [[hep-ph/0206071](#)]. 121
- 3537 [81] H.-C. Cheng, K.T. Matchev and M. Schmaltz, *Radiative corrections to*
3538 *Kaluza-Klein masses*, *Phys. Rev. D* **66** (2002) 036005 [[hep-ph/0204342](#)]. 123

BIBLIOGRAPHY

- 3539 [82] M. Blennow, J. Edsjö and T. Ohlsson, *Neutrinos from WIMP annihilations using a*
3540 *full three-flavor Monte Carlo*, *JCAP* **01** (2008) 021 [[0709.3898](#)]. 123, 126
- 3541 [83] J. Edsjö, J. Elevant and C. Niblaeus, *WimpSim Neutrino Monte Carlo*. 123, 126
- 3542 [84] U. Haisch and A. Weiler, *Bound on minimal universal extra dimensions from*
3543 *anti-B → X(s)gamma*, *Phys. Rev. D* **76** (2007) 034014 [[hep-ph/0703064](#)]. 125
- 3544 [85] A. Freitas and U. Haisch, *Anti-B → X(s) gamma in two universal extra*
3545 *dimensions*, *Phys. Rev. D* **77** (2008) 093008 [[0801.4346](#)]. 125
- 3546 [86] C. Rott, D. Jeong, J. Kumar and D. Yaylali, *Neutrino Topology Reconstruction at*
3547 *DUNE and Applications to Searches for Dark Matter Annihilation in the Sun*,
3548 *JCAP* **07** (2019) 006 [[1903.04175](#)]. 128
- 3549 [87] F. Pedregosa, G. Varoquaux, A. Gramfort, V. Michel, B. Thirion, O. Grisel et al.,
3550 *Scikit-learn: Machine learning in Python*, *Journal of Machine Learning Research*
3551 **12** (2011) 2825. 134
- 3552 [88] J. Kopp, V. Niro, T. Schwetz and J. Zupan, *DAMA/LIBRA and leptонically*
3553 *interacting Dark Matter*, *Phys. Rev. D* **80** (2009) 083502 [[0907.3159](#)]. 138
- 3554 [89] PARTICLE DATA GROUP collaboration, *Review of Particle Physics*, *PTEP* **2020**
3555 (2020) 083C01. 139
- 3556 [90] M. Beltran, D. Hooper, E.W. Kolb and Z.C. Krusberg, *Deducing the nature of dark*
3557 *matter from direct and indirect detection experiments in the absence of collider*
3558 *signatures of new physics*, *Phys. Rev. D* **80** (2009) 043509 [[0808.3384](#)]. 139
- 3559 [91] PLANCK collaboration, *Planck 2018 results. VI. Cosmological parameters*, *Astron.*
3560 *Astrophys.* **641** (2020) A6 [[1807.06209](#)]. 140